Deeply Virtual Compton Scattering off an Unpolarized Hydrogen Target at the HERMES Experiment

Der Naturwissenschaftlichen Fakultät
der Friedrich-Alexander-Universität Erlangen-Nürnberg
zur
Erlangung des Doktorgrades Dr. rer. nat.

vorgelegt von
Dietmar Zeiler

aus Nürnberg

Als Dissertation genehmigt
von der Naturwissenschaftlichen Fakultät
der Universität Erlangen-Nürnberg

Tag der mündlichen Prüfung: 06.10.2009

Vorsitzender der
Prüfungskommission: Prof. Dr. Eberhard Bänsch

Erstberichterstatter: Prof. Dr. K. Rith

Zweitberichterstatter: Prof. Dr. M. Düren

Dedicated to my wife.

Contents

1 Introduction

How is matter composed? This is one of the most basic, yet not (completely) answered question in natural sciences. In the current most established picture a restricted group of smallest entities exists that are the building blocks of all matter. One member of this group are the quarks forming e.g. the two nucleon states, proton and neutron, that in turn form the nuclei of the large variety of existing atoms.

The HERMES collaboration examines the spin structure of the nucleon at the **H**adron–**E**lektron–**R**ing–**A**nlage (HERA) in Hamburg in high–energetic scattering processes. The abbreviation HERMES stands for '**HER**A **me**asurement of **s**pin'.

In the constituent quark model the nucleon consists of three valence quarks describing its basic properties like charge and spin. A proton is formed by two quarks with flavor up and charge $e_u = +2/3\,e$ and one quark with flavor down and charge $e_u = -1/3\,e$, with the elementary charge e. The neutron consists of one up– and two down–quarks. Quarks and nucleons are both spin–1/2 particles and thus fermions. Assuming that the two quarks with the same flavor enter with the same spin in the nucleons, the properties of the nucleon are easily explained in this model. Other properties of the nucleons require the existence of quark–antiquark pairs and gluons as mediators of the strong interaction.

In the 1980s the European Muon Collaboration published results on the double–spin asymmetry of a longitudinally polarized muon beam off a longitudinally polarized proton target suggesting that the total quark spin contributes with a rather small fraction of $14 \pm 9 \pm 21\,\%$ to the spin of the nucleon [A+88]. The z–component of the nucleons spin s_z can be decomposed into

$$s_z = \frac{1}{2}\Delta\Sigma + L_z^q + \Delta g + L_z^g = \frac{1}{2}. \tag{1.1}$$

In this equation $\Delta\Sigma$ denotes the contribution of the spin of the valence and sea quarks in the nucleon, Δg the gluon spin contribution and L^q (L^g) the orbital angular momenta of quarks (gluons).

Within the constituent quark model the quarks were expected to carry the whole spin of the nucleons. After measuring this small contribution from the spin of the quarks the other contributions of the spin decomposition were expected to be sizeable. In 1997 Ji showed that the total angular momenta of both quarks and gluons can be accessed within the framework of **G**eneralised **P**arton **D**istributions (GPD) [Ji97b]. They are generalizations of the successfull concepts of form factors and parton distribution functions as will be discussed in chapter 2.4.

The most promising access to these new distributions functions is the **D**eeply **V**irtual **C**ompton **S**cattering (DVCS) process. In contrast to the famous real Compton scatte-

ring process depicted in figure 1.1, where a real photon scatters off a lepton inside the atomic system, in DVCS a virtual photon is scattering off a quark inside the nucleon. In both cases a real photon is emitted by either the lepton or the quark. One advantage of this process is the existence of the experimentally indistinguishable and well known Bethe–Heitler process that offers in a interferometric picture a reference beam to allow to image the nucleon [RP02, Bel02a]. Both, the DVCS and Bethe–Heitler process will be discussed in detail in the following chapter.

The structure of this thesis is as follows: In the second chapter the theoretical basis needed for the description of the exclusive electro–production of photons in the framework of GPDs is explained. Three different models are discussed and experimental observables are defined. The third chapter includes a description of the HERMES experiment and its components. The data analysis is discussed in chapter four, along with various studies both on real and Monte Carlo data and the derivations of the systematic uncertainties. In chapter five the present results will be given and interpreted both from an experimental point of view, and in comparison to existing models. Conclusion from the results will be drawn. Furthermore the calibration of the Recoil Silicon Detector and the performance of the complete Recoil Detector is outlined in chapter six. In chapter seven an outlook is presented followed by the summary.

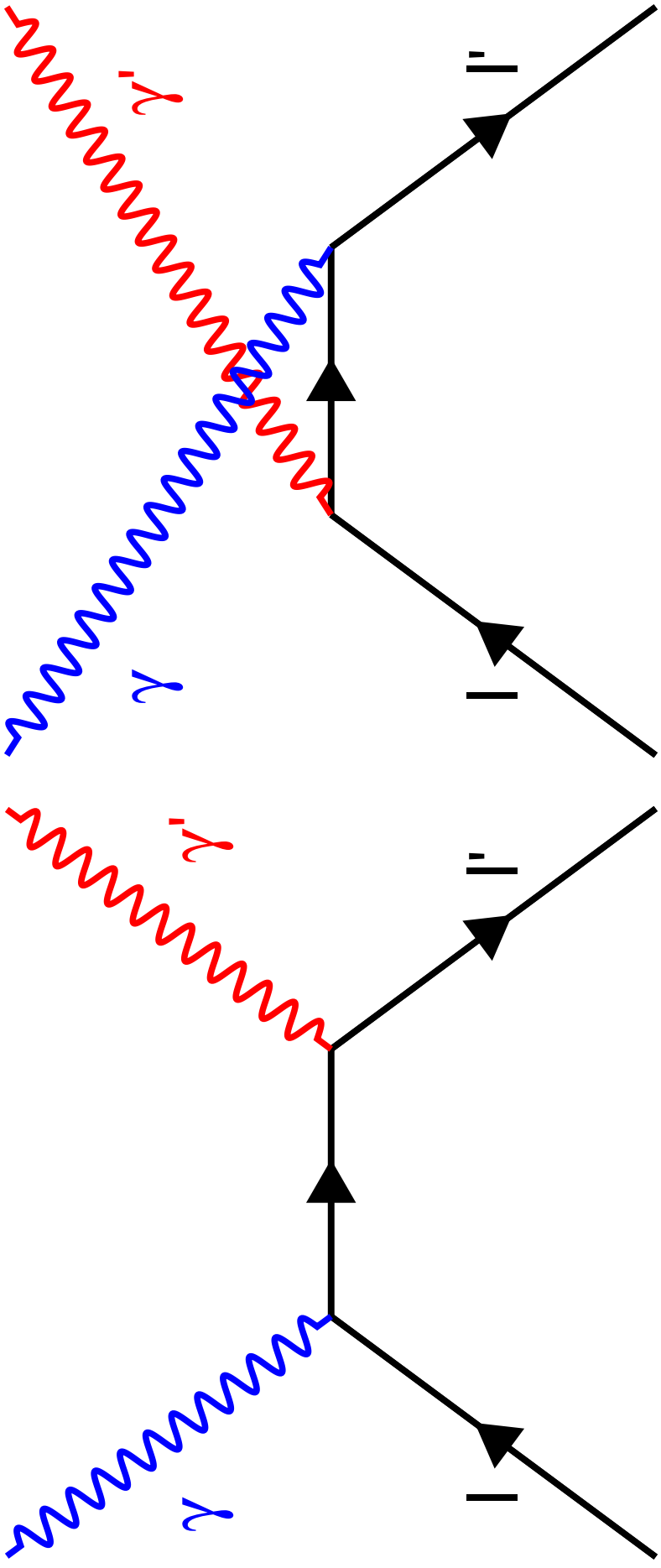

Figure 1.1: The two Feyman–graphs for the description of real Compton scattering in leading order perturbation theory: A real photon γ scatters off a quasi–free lepton l and is re–emitted as a photon γ' with a reduced energy. The energy

2 Theory

This chapter gives a short review over the theoretical basis needed for examining the DVCS process like in the present analysis. First the exclusive lepto–production of real photons will be introduced and its description using the framework of GPDs will be outlined. Three different theoretical models will be discussed. Finally various experimental observables will be defined to allow for an evaluation of the obtained results in comparison to models.

2.1 Exclusive lepto–production of a real photon

The exclusive lepto–production of a photon γ in scattering off a nucleon N

$$l(k) + N(p) \rightarrow l(k') + N(p') + \gamma(q') \tag{2.1}$$

with the initial and final state's lepton l momenta k and k', the initial and final state's proton momenta p and p', and the momentum of the produced photon γ involves contributions from two processes: The **B**ethe–**H**eitler (BH) where the real photon is emitted from either the initial or final state lepton (see figure 2.1) and the **V**irtual **C**ompton **S**cattering (VCS) process. In the latter the real photon is emitted from (a parton inside) the nucleon. The interaction between the lepton and the nucleon is mediated by a virtual photon γ^* in both processes.

The 'handbag–diagram' of the VCS process is depicted in figure 2.2, in which the same quark both absorbs the virtual and emits the real photon. It was shown in [Mul94, Rad96, Ji97a] that in the Bjorken–limit where the energy and momentum of the virtual photon are going to infinity at the same rate, the handbag–diagram describes the leading contribution to the VCS process. In this kinematic region the process is called **D**eeply **V**irtual **C**ompton **S**cattering (DVCS).

The orange blobs in figures 2.1 and 2.2 illustrate the propagation of the nucleon during the process. Their description is subject to section 2.4.

2.2 Kinematic definitions

The inclusive part of the DVCS process can be described with the known formulae from the **D**eep **I**nelastic **S**cattering (DIS) framework. Note, that the interpretation of the kinematic variables differ in the BH and DVCS processes. In the following the meaning in the DVCS case will be outlined.

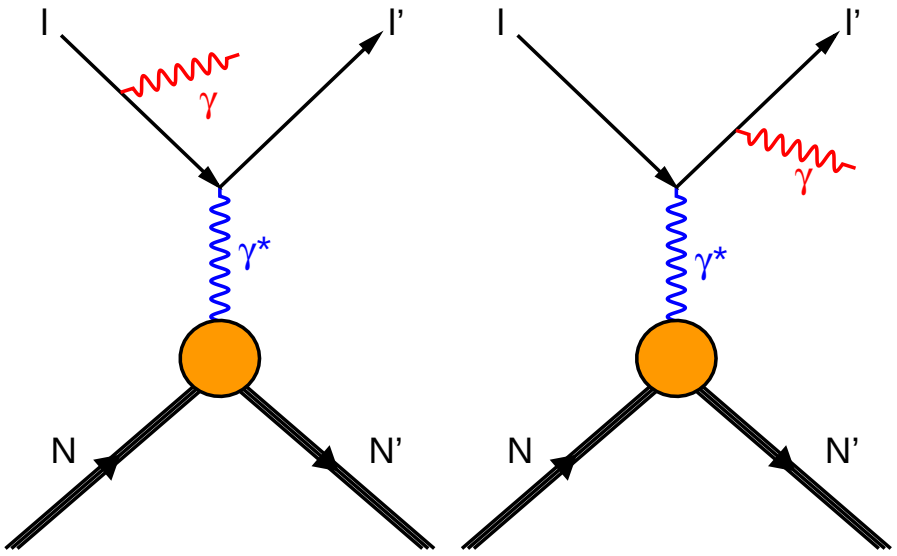

Figure 2.1: The leading diagrams of the Bethe–Heitler process, i.e. the scattering off a lepton l of a nucleon N mediated by a virtual photon γ^* with the emission of a real photon γ from either the initial or final state lepton l'.

The four–momentum of the virtual photon q is defined as the difference of the four–momenta of the incoming and outgoing lepton

$$-q^2 \equiv Q^2 \equiv -(k-k')^2 \tag{2.2}$$
$$= 2EE'(1-cos\ \theta). \tag{2.3}$$

In the laboratory frame of a fixed–target experiment like HERMES the negative squared momentum transfer Q^2 can be expressed as a function of the energy of the incoming and outgoing lepton (E and E') and the scattering angle of the lepton with respect to the beam axis θ (Eq. 2.3).

The dimensionless Bjorken scaling variable x_B is defined by:

$$x_B \equiv \frac{Q^2}{2p\cdot q} = \frac{Q^2}{2M_N\nu}. \tag{2.4}$$

It relates to the virtuality of the photon, the mass of the nucleon M_N and the variable ν defined as

$$\nu \equiv \frac{p\cdot q}{M_N} = E - E', \tag{2.5}$$

which turns out to be the difference of the lepton's energy before and after the scattering process $\nu = E - E'$ in the above defined rest frame of the nucleon. Another dimensionless variable

$$y \equiv \frac{p\cdot q}{p\cdot k} = \frac{\nu}{E} \tag{2.6}$$

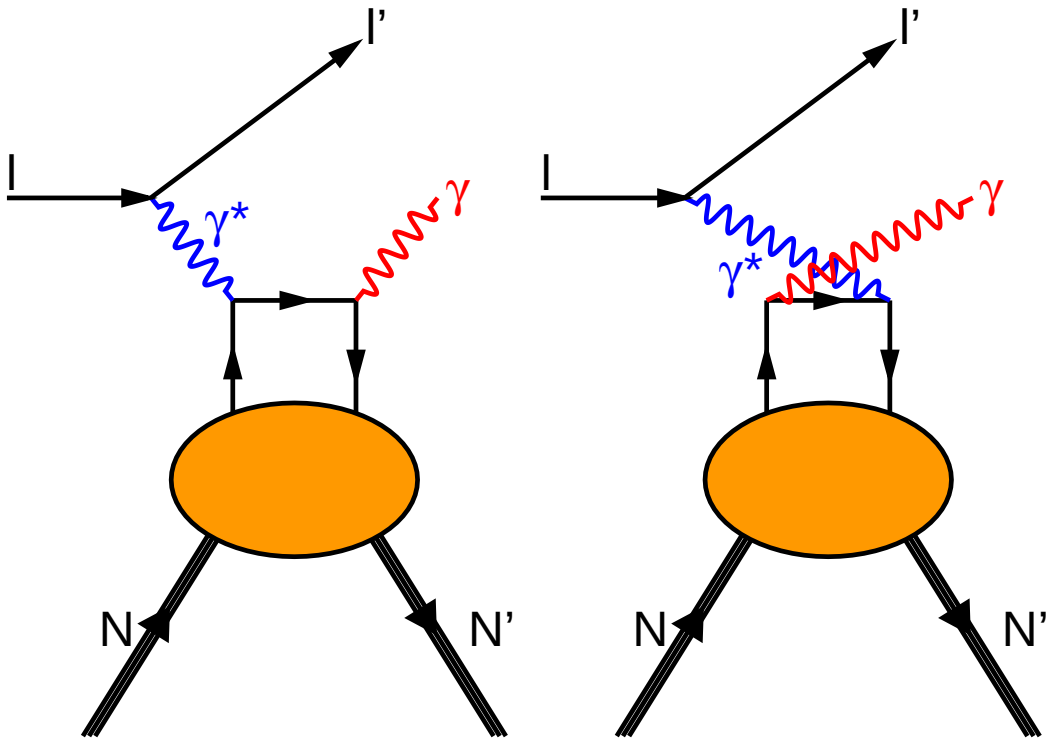

Figure 2.2: The leading–order DVCS handbag–diagrams. An incoming lepton l couples with a quark inside the nucleon N mediated by a virtual photon γ^*. The quarks emits a real photon γ.

can be interpreted as the fraction between the energies of the virtual photon and the incoming lepton in the rest frame of the nucleon. The squared invariant mass of the photon–nucleon system W^2 is defined as:

$$W^2 \equiv (P+q)^2 = M_N^2 + 2M_N\nu - Q^2. \tag{2.7}$$

The above defined variables are all inclusive variables that can be deduced from the detected scattered lepton exclusively.

Besides that another variable is needed for the description of the exclusive photon leptoproduction. Usually the squared four–momentum transfer t from the initial to the final state nucleon is chosen:

$$t \equiv (p'-p)^2 \tag{2.8}$$

$$= 2M_{\mathrm{N}}\,(M_{\mathrm{N}} - E_{N'}) < 0. \tag{2.9}$$

In equation 2.9 it is assumed that the target mass is unchanged in the scattering process.

2.3 Cross section of the exclusive lepto–production of a real photon

The four–fold differential cross section of the exclusive lepto–production of a real photon is given by [DGPR97, Bel02b]

$$\frac{d\sigma}{dx_B dQ^2 dt d\phi} = \frac{\alpha^3 x_B y}{16\pi^2 Q^2 e^3} \frac{2\pi y}{Q^2} \frac{|\mathcal{T}|^2}{\sqrt{1 + 4x_B^2 M_N^2/Q^2}}, \tag{2.10}$$

with the coupling constant of the electromagnetic interaction α and the elementary charge e. The azimuthal angle ϕ is spanned by the lepton scattering plane and the photon production plane (see figure 2.3).

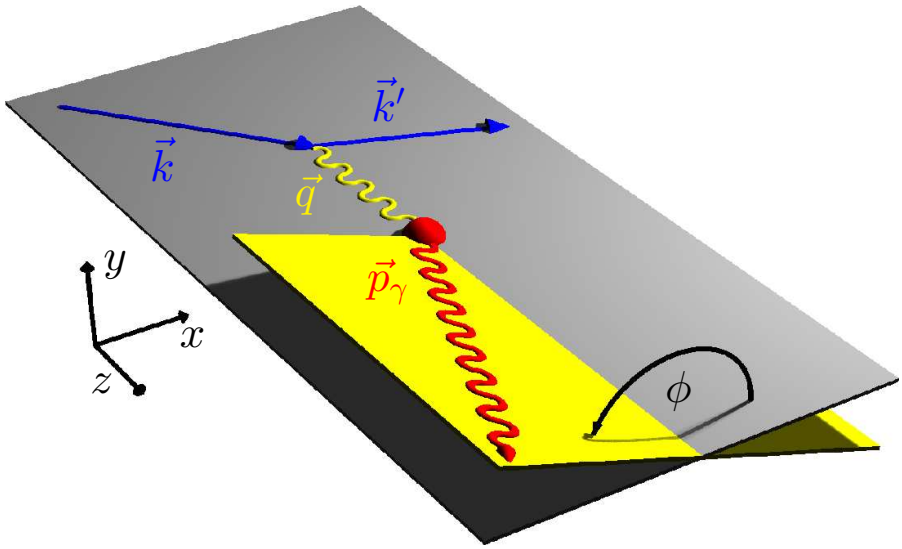

Figure 2.3: Definition of the azimuthal angle ϕ between the lepton scattering in grey (defined by the spatial coordinates of the momentum vectors of the two leptons) and the photon production plane in yellow (defined by the spatial coordinates of the momentum vectors of the virtual and the real photon).

As the BH and DVCS processes have the same final state, the squared amplitude $|\mathcal{T}|^2$ contains the coherent sum of the BH and DVCS amplitudes $\mathcal{T}_{BH}$ and $\mathcal{T}_{DVCS}$

$$\begin{aligned} |\mathcal{T}|^2 &= |\mathcal{T}_{BH} + \mathcal{T}_{DVCS}|^2 \\ &= |\mathcal{T}_{BH}|^2 + |\mathcal{T}_{DVCS}|^2 + \mathcal{T}_{DVCS}\mathcal{T}_{BH}^* + \mathcal{T}_{DVCS}^*\mathcal{T}_{BH} \\ &= |\mathcal{T}_{BH}|^2 + |\mathcal{T}_{DVCS}|^2 + I \end{aligned} \tag{2.11}$$

producing an interference term I.

In the Bjorken–limit ($Q^2 \to \infty$, $P \cdot q \to \infty$ and x_B finite) of large photon virtuality the leading contribution to the DVCS process is the handbag–diagram shown in

figure 2.2 [Mul94, Rad96, Ji97a]. In this approximation the squared amplitudes are given by the contraction of the DVCS hadronic tensor $T_{\mu\nu}$, the electromagnetic current J_μ and a leptonic tensor $L^{\mu\nu}$ [Bel01]:

$$|\mathcal{T}_{\mathrm{DVCS}}|^2 = \frac{e^6}{q^4}(-g^{\alpha\beta})L^{\mu\nu}_{\mathrm{DVCS}}\sum_{S'} T_{\alpha\mu}(T_{\beta\nu})^\dagger, \tag{2.12}$$

$$|\mathcal{T}_{\mathrm{BH}}|^2 = \frac{e^6}{t^4}L^{\mu\nu}_{\mathrm{BH}}\sum_{S'} J_\mu(J_\nu)^\dagger, \tag{2.13}$$

$$I = \frac{\pm e^6}{q^2t^2}L^{\alpha\mu\nu}\sum_{S'}[J_\mu(T_{\alpha\nu})^\dagger + h.c.]. \tag{2.14}$$

The signs (±) denote the charge of the incoming lepton, $g^{\alpha\beta}$ is the metric tensor and the summation index S' the polarization of the final state nucleon. These equations were summed over the photon and lepton polarization states.

The DVCS tensor $T_{\mu\nu}$ can be expressed as the time–ordered product of two electromagnetic currents

$$j_\alpha(x) = \sum_{i=u,d,s} e_i\bar{\psi}(x)\gamma_\alpha\psi(x) \tag{2.15}$$

of quarks, expressed by quark fields with flavour i and charge e_i between hadron states that exhibit (in contrast to the DIS process) different momenta and possibly also spin states

$$T_{\mu\nu} = \frac{i}{e^2}\int dx\cdot e^{i/2\ x\cdot(q+q')}\left\langle p',S'\left|Tj_\mu\left(\frac{x}{2}\right)j_\nu\left(\frac{-x}{2}\right)\right|p,S\right\rangle, \tag{2.16}$$

where q' denotes the four–momentum of the final state real photon. The tensor has to be evaluated in orders of the strong coupling constant α_s and orders of twist (starting at twist–two). The latter is defined by the dimension minus spin of the operators describing the propagation of the partonic components of the nucleon and is more commonly identified with the order in M_N/Q [Jaf96].

In leading twist and leading order perturbation theory the DVCS tensor can be expressed in a basis of four so–called **C**ompton **F**orm **F**actors (CFF)

$$T_{\mu\nu} = \left[\mathcal{H},\mathcal{E},\widetilde{\mathcal{H}},\widetilde{\mathcal{E}}\right](\xi,t,Q^2), \tag{2.17}$$

where ξ is the dimensionless skewness variable defined by $\xi \equiv -q^2/(q\cdot(p+p'))$ reducing to $\xi \approx x_B/(2-x_B)$ in the Bjorken–limit. It has been shown in [Rad96, CF99, JO98] that the DVCS tensor can be factorized in leading twist into a hard scattering part calculable in perturbative **Q**uantum **C**hromo–**D**ynamics (QCD) and a soft part described by Generalized Parton Distributions

$$\mathcal{F}(\xi,t,Q^2) = \int_{-1}^{1} dx\ C^-(\xi,x)\ F(x,\xi,t,Q^2), \tag{2.18}$$

$$\widetilde{\mathcal{F}}(\xi,t,Q^2) = \int_{-1}^{1} dx\ C^+(\xi,x)\ \widetilde{F}(x,\xi,t,Q^2), \tag{2.19}$$

where $C^{\pm}$ denote hard scattering amplitudes and F ($\widetilde{F}$) stand for the different GPDs each related to one CFF. The hard scattering amplitudes have been calculated in next–to leading order in α_s in [JO98, MPW98, Bel98]. In a frame where the nucleon moves fast x and ξ can be interpreted as longitudinal momentum fractions of the involved partons (see figure 2.4). Note, that the GPDs enter in a convolution integral over the momentum fraction x. At leading order the imaginary part of the CFFs is given by the GPDs evaluated at $x = \xi$. The full x–range is only contained in the real part. Moreover the variable x is not accessible in the DVCS process. Therefore, in DVCS the full x and ξ dependence of the GPD cannot be accessed. In an experimentally challenging process known as 'Double DVCS', where the final state contains a lepton anti–lepton pair from a decaying virtual photon [GV03] the region $|x| < \xi$ can be explored.

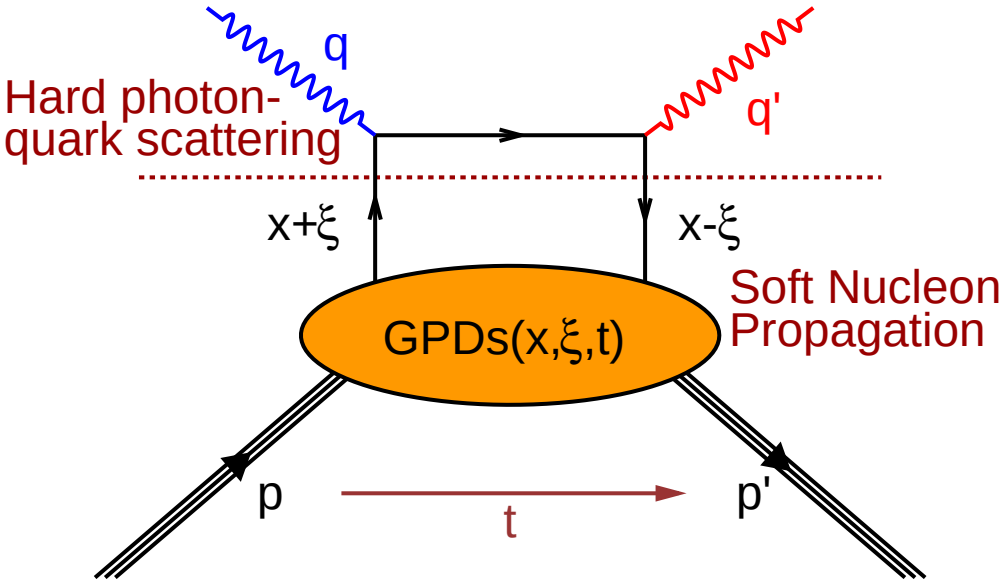

Figure 2.4: An illustration of the factorization of the DVCS process and the meaning of GPDs.

In the following section the concept and properties of GPDs are explained.

2.4 Generalized Parton Distributions

Compared to quark distributions GPDs depend on two additional variables, namely t and ξ. The latter demonstrates the more general aspect of the new distributions as it is formed by the scalar product of the longitudinal momentum fraction x and the momentum transfer to the nucleon t.

This is illustrated in figure 2.5, where the concepts of form factors, parton density functions and GPDs are compared. In the infinite momentum frame the GPDs can

be interpreted as a simultaneous measurement of the longitudinal momentum and transverse position of the partons inside the nucleon [Bur00].

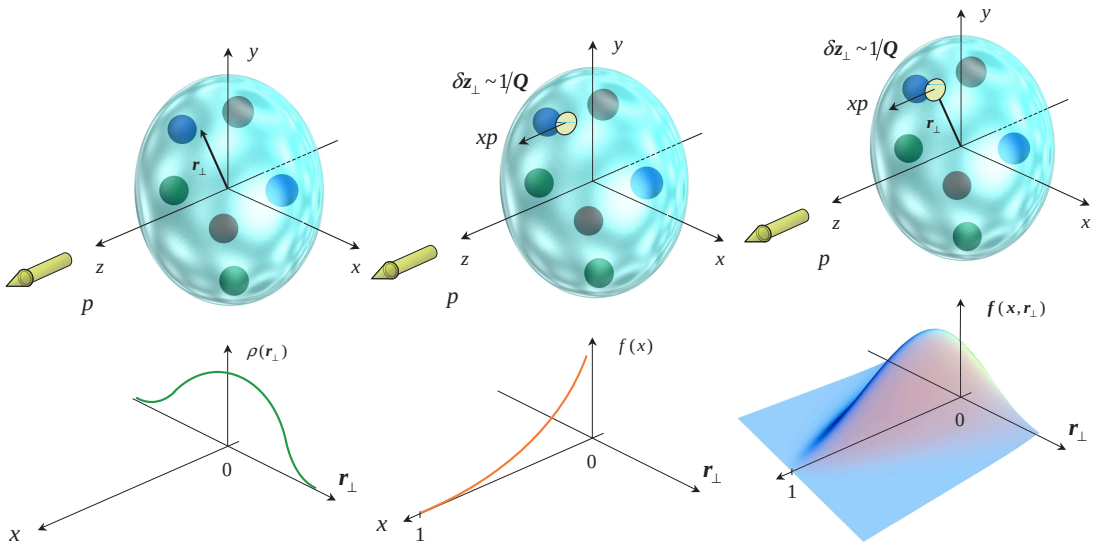

Figure 2.5: An illustration of the meaning of form factors describing the charge distribution as a function of the impact parameter $r_\perp$ on the left; the parton density functions as a function of the longitudinal momentum fraction x in the middle; on the right GPDs are displayed, which combine both sensitivities (taken from [Bel02a]).

In addition, GPDs are subject to evolution and thus depend on the squared momentum transfer to the quark Q^2. Their evolution was calculated in leading order in α_s in references [Mul94, Ji97a, Rad99, Blu99] and in references [Bel00d, Bel00a, Bel00b] in next–to leading order.

In the following the Q^2–dependence will be omitted.

2.4.1 Properties of GPDs

In contrast to CFFs, GPDs are real functions. For a spin–1/2 particle like the nucleon four GPDs are needed for the description in leading twist and leading order perturbation theory. Two of them, namely H and $\widetilde{H}$, conserve the nucleon helicity, while E and $\widetilde{E}$ flip the nucleon helicity.

In the forward limit of vanishing momentum transfer to the final state nucleon ($t \to 0$) the GPDs reduce to the quark momentum and quark helicity distribution q and Δq [Mul94, Rad96, Ji97a]:

$$H(x, \xi = 0, t = 0) = q(x), \tag{2.20}$$

$$\widetilde{H}(x, \xi = 0, t = 0) = \Delta q(x). \tag{2.21}$$

The first moments of the twist–two GPDs are related to corresponding form factors by [Ji97a]

$$\int_{-1}^{1} dx\, H(x,\xi,t) = F_1(t), \tag{2.22}$$

$$\int_{-1}^{1} dx\, E(x,\xi,t) = F_2(t), \tag{2.23}$$

$$\int_{-1}^{1} dx\, \widetilde{H}(x,\xi,t) = G_{\mathrm{A}}(t), \tag{2.24}$$

$$\int_{-1}^{1} dx\, \widetilde{E}(x,\xi,t) = G_{\mathrm{P}}(t), \tag{2.25}$$

where F_1 and F_2 are the Dirac and Pauli form factors and G_{A} and G_{P} are the axial–vector and the pseudo–scalar form factors for each parton.

In [Ji97b] it was shown that the quark contribution to the nucleon spin is measurable through the second x–moment of the GPDs H and E in the limit of t going to zero, expressed in the so–called Ji relation:

$$J = \lim_{t\to 0} \frac{1}{2} \int_{-1}^{1} dx\, x[H(x,\xi,t) + E(x,\xi,t)]. \tag{2.26}$$

Note, that this angular momentum operator differs from the one defined in [JM90]. This needs to be taken care of when, e.g. combining different experimental results in order to draw conclusions on the spin decomposition of the nucleon.

Another property of the GPDs is the polynomiality of their Mellin moments and can be expressed as [Ji98, GPV01]:

$$\int_{-1}^{1} dx\, x^N H(x,\xi) = h_0^N + h_2^N \xi^2 + \ldots + h_{N+1}^N \xi^{N+1}, \tag{2.27}$$

$$\int_{-1}^{1} dx\, x^N E(x,\xi) = e_0^N + e_2^N \xi^2 + \ldots + e_{N+1}^N \xi^{N+1}. \tag{2.28}$$

In these equations only even powers of ξ enter because of hermicity and time reversal invariance [Ji98, MPW98]. From the above equations different additional conditions for models describing GPDs can be deduced, e.g. [Ji98]

$$e_{N+1}^N = -h_{N+1}^N \tag{2.29}$$

relating the GPDs H and E in a non–trivial way [GPV01].

In [Mul94, Rad96] two–variable **d**ouble **d**istributions were proposed to fulfill the polynomiality conditions

$$H_{\mathrm{DD}}(x,\xi) = \int_{-1}^{1} d\beta \int_{-1+|\beta|}^{1-|\beta|} d\alpha\ \delta(x-\beta-\alpha\xi)\ F(\beta,\alpha), \tag{2.30}$$

where the dependencies on both variables are projected out by the use of delta functions. An equivalent relation exists for the GPD E, while the only difference for the polarized GPDs $\widetilde{H}$ and $\widetilde{E}$ is that the highest power of ξ is N or $N-1$ for even and odd N, respectively. In this ansatz the highest power of ξ for odd N is zero, but can be completed by the inclusion of a D–term as proposed by [PW99]:

$$H(x,\xi) = \int_{-1}^{1} d\beta \int_{-1+|\beta|}^{1-|\beta|} d\alpha\ \delta(x-\beta-\alpha\xi)\ F(\beta,\alpha) + \theta\left(1-\frac{x^2}{\xi^2}\right) D\left(\frac{x}{\xi}\right). \tag{2.31}$$

The D–term contribution to the GPD H and E are of the same magnitude, but opposite sign and thus cancel in Ji's relation. The polarized GPDs do not have a D–term. As is discussed in [GPV01] the D–term plays an essential role in extracting the angular momentum carried by quarks even though it drops out in Ji's relation (Eq. 2.26) as it is needed in understanding the data on each of the contributing GPDs alone. In an observable proportional to the sum of $H + E$ the situation would be different.

The preceding discussion focused on leading–twist quark GPDs, which are usually labeled by another superscript q. In analogy gluon and higher–twist quark and gluon GPDs are needed in the description of the DVCS process (see, e.g. [Bel02b] for review). Note, that higher twist quark GPDs can be expressed in leading–twist GPDs in the Wandzura–Wilczek approximation [WW77] as deduced in e.g. [Bel00c] and [KM01]. Another class of GPDs describes the transition from the initial state nucleon into a resonant state and are hence called 'transition GPDs'.

In the last decade several theoretical models were suggested to describe GPDs with a phenomenological ansatz. Recently also attempts have started to directly fit experimental data on the level of CFFs. In the following sections three models will be discussed that were compared to the results of the present analysis.

2.4.2 The 'VGG model'

In [VGG99, GPV01] the Vanderhaeghen–Guichon–Guidal model ('VGG model') is described. It is based on the framework of double distributions (see Eq. 2.30) with the polynomiality property ensured by the inclusion of a D–term (see Eq. 2.31). The model for the double distributions was taken from [Rad99] as

$$F^q(\beta,\alpha) = h(\beta,\alpha)\ q(\beta), \tag{2.32}$$

where $h(\beta,\alpha)$ stands for a profile function and $q(\beta)$ for the quark density of quark flavor q in the case of the GPD H. In this way the model's implementation satisfies the

requirements of Eq. 2.21. The parameterization of the quark distributions was taken from [MRST98]. The same author [Rad99] suggested to use a one–dimensional profile function of the form:

$$h(\beta,\alpha) = \frac{\Gamma(2b+2)}{2^{2b+1}\Gamma^2(b+1)} \frac{\left[\left(1-\left|\beta\right|\right)^2 - \alpha^2\right]^b}{\left(1-\left|\beta\right|\right)^{2b+1}}. \tag{2.33}$$

The b–parameter thus controls the dependence of the GPD to the skewness variable ξ in this model. With increasing b the skewness dependence of the model decreases. For both, valence and sea contributions the parameter (b_{val} or b_{sea}) can be chosen freely in a reasonable range.

In order to also satisfy the requirements from Eqs. 2.25 the t–dependence can be chosen easiest in the 'factorized ansatz'

$$H^u(x,\xi,t) = H^u(x,\xi)\, F_1^u(t)/2, \tag{2.34}$$
$$H^d(x,\xi,t) = H^d(x,\xi)\, F_1^d(t), \tag{2.35}$$
$$H^s(x,\xi,t) = 0, \tag{2.36}$$

with the quark form factors F_1^q deduced from the proton and neutron Pauli and Dirac form factors under the assumption of isospin symmetry. However, the factorized t–dependence is not supported by comparisons to results from the quark soliton model [GPV01]. Therefore a Regge theory motivated ansatz was proposed

$$H^q(x,\xi,t) = h(\beta,\alpha)\, q(\beta)\, \frac{1}{\left|\beta\right|^{\alpha' t}} \tag{2.37}$$

with the slope α' of the Regge trajectory.

The D–term was expanded in odd Gegenbauer polynomials using an estimate from the quark soliton model for the moments of the individual terms [GPV01].

The GPD E does not have a comparable DIS constraint in the forward limit. Though its moment is related to the form factor F_2 and the constraint from the polynomiality condition (Eq. 2.29) exist. These requirements are met by parameterizing the GPD E in a double distribution ansatz with an additional D–term and a factorized t–dependence.

While the GPD $\widetilde{H}$ can be constructed in complete analogy to the GPD H without a D–term, $\widetilde{E}$ only gets a contribution from the pion pole in the discussed model. This ansatz is again motivated by findings from the quark soliton model that the GPD $\widetilde{E}$ is dominated by the pion pole in a wide range of t and ξ [GPV01]. Note, that like in the case of the GPD E also in the parameterization of $\widetilde{H}$ the b–parameters are fixed to unity and a factorized t–dependence is chosen.

In addition, the model contains contributions from the twist–three sector in a Wandzura–Wilczek approximation [WW77, Bel00c].

2.4.3 The 'Dual–GT model'

Another model was derived by Guzey and Teckentrup in [GT06] describing the GPDs in a 'dual parameterization' ('Dual–GT'). In this ansatz the unpolarized GPDs H and E are decomposed into an infinite sum of t–channel exchanges, which is similar to the idea of duality [PS02].

The unknown form factors entering the infinite sum are derived as the Mellin moments of a newly defined set of generating functions. In the minimal version of this model only the first two even terms of the sum (with index $k = [0, 2]$) are kept, because of a prefactor ξ^k and ξ being small in HERA kinematics ($\xi_{\text{HERMES}} \approx 0.05$). The functions with $k = 0$ are completely determined by the known relations to the quark distributions in the forward limit (see Eq. 2.21). In the case of the GPD E the unknown forward limit is chosen like in the VGG approach. The generating function with index $k = 2$ are less constraint and can be used to introduce the D–term as proposed by [PS02] for the prize of an additional unknown function. The chosen form of this function and the D–term parameters can be found in [GT06].

The t–dependence of the GPDs was either included in a factorized or a Regge motivated ansatz. The Regge slope parameters are determined in a comparison to DVCS cross section measurements from H1 [A$^+$05] and ZEUS [C$^+$03], which yielded in larger values compared to expectations from Regge theory [Die06].

Note, that in the original version of the model a factor of two in the DVCS amplitude was missing, which was corrected in [GT09]. In the present analysis only curves obtained from the corrected version are shown.

In [PSTS09] the relation between the double distribution and the dual representation is discussed for some models. For a particular double distribution model the first three generating functions in a dual representation are derived.

2.4.4 The 'CFF–KM ansatz'

In recent years more and more experimental data became available on various DVCS observables. These results can be used to fit GPDs (or CFFs) in a given parameterization. In this section the approach from [Kum09] will be explained, which has been adopted in this analysis to fit the obtained experimental results.

The twist–2 photon–helicity conserving amplitude $M^{1,1}$ is given by a linear combination of three CFFs

$$M^{1,1} = F_1(t)\mathcal{H}(\xi, t) + \frac{x_B}{2 - x_B}(F_1(t) + F_2(t))\widetilde{\mathcal{H}}(\xi, t) - \frac{t}{4M^2}F_2\mathcal{E}(\xi, t), \tag{2.38}$$

where the superscripts of the amplitude denote the helicity state of the initial and final state photon. At HERMES kinematics (x_B and $|t|$ of order 0.1) the contributions of the CFFs $\widetilde{\mathcal{H}}$ and $\mathcal{E}$ with respect to the CFF $\mathcal{H}$ can be neglected. Hence, in the following fit approach only the GPD H is taken into account. In addition, the evolution of this GPD is neglected, which is supported by the success of the ansatz in the comparison to experimental data.

Making use of the dispersion relation

$$Re\mathcal{H}(\xi,t) = \frac{1}{\pi}\mathrm{PV}\int_0^1 d\xi' \frac{2\xi'}{\xi^2-\xi'^2} Im\mathcal{H}(\xi',t) - C(t), \tag{2.39}$$

both real and imaginary part of the CFF $\mathcal{H}$ can be fitted together as was suggested in [Kum08a]. Here, PV denotes a principal value integral, which can be solved numerically. Analogous expressions are valid for other CFFs and allow to extend the approach to other observables.

The imaginary part of the CFF can be expressed in leading order on the crossover line given by $\xi = x$ as

$$Im\mathcal{H}(\xi = x, t) = \pi H(x,x,t), \tag{2.40}$$

linking it to the respective GPD. Thus a parameterization of the GPD and an ansatz for the additional t–dependent term $C(t)$ are needed as input to the fit procedure. The latter is taken as

$$C(t) = \frac{C}{(1-\frac{t}{M_C^2})^2} \tag{2.41}$$

with a normalization parameter C and a cut–off parameter M_C^2. It is entirely related to a GPD term that completes polynomiality [Kum08b] and can be identified with the D–term in the double distribution representation, utilized above.

The GPD H can be decomposed into a simplified charge–weighted sum of valence and sea quark contributions:

$$H(\xi = x, t) = \frac{4+1}{9}H^{\mathrm{val}}(x,x,t) + \frac{2}{9}H^{\mathrm{sea}}(x,x,t). \tag{2.42}$$

The ansatz for the GPD on the cross-over line arises from a double distribution model with a t–dependence inspired from the quark spectator model and reads:

$$H^i(x,t) = \frac{2^{\alpha_i}N_i(1+s_i)}{\left(1-\frac{1-x}{1+x}\frac{t}{M_i^2}\right)^{p_i}}\left(\frac{2x}{1+x}\right)^{-\alpha_i(t)}\left(\frac{1-x}{1+x}\right)^{b_i}. \tag{2.43}$$

The complete parameterization includes 14 parameters, out of which eight were fixed [Kum09]. In table 2.1 both the meaning and the set values are given. The values of the parameters describing the sea quark sector are mainly inspired from fits to DVCS data at low x. From the remaining set of free parameters only two enter in the description of the real part of the CFF. The finally obtained parameterization is given by:

$$Im\mathcal{H}(x,t) = \pi\left[\frac{1.35(1+s_{\mathrm{val}})\left(\frac{2x}{1+x}\right)^{-0.43-0.85t/\mathrm{GeV}^2}\left(\frac{1-x}{1+x}\right)^{b_{\mathrm{val}}}}{\left(1-\frac{1-x}{1+x}\frac{t}{M_{\mathrm{val}}^2}\right)} + \frac{\frac{2}{9}1.5\left(\frac{2x}{1+x}\right)^{-1.13-0.15t/\mathrm{GeV}^2}\left(\frac{1-x}{1+x}\right)^{b_{\mathrm{sea}}}}{\left(1-\frac{1-x}{1+x}\frac{t}{0.5\mathrm{GeV}^2}\right)^2}\right]. \tag{2.44}$$

parameter	meaning	valence	sea
α_i	Regge trajectories compatible with PDF parameterization.	$\alpha_{\text{val}} = 0.43 + 0.85t/\text{GeV}^2$	$\alpha_{\text{sea}} = 1.13 + 0.15t/\text{GeV}^2$
N_i	Residue parameters compatible with PDF parameterization.	$N_{\text{val}} = 1.35$	$N_{\text{sea}} = 1.5$
s_i	Quantify the skewness effect.	s_{val} free	$s_{\text{sea}} = 0$
b_i	Control large x behavior.	b_{val} free	b_{sea} free
p_i	Determine the number of poles in t–dependence.	$p_{\text{val}} = 1$	$p_{\text{sea}} = 2$
M_i	Cut–off mass parameters controls also t–dependence.	M^2_{val} free	$M^2_{\text{sea}} = 0.5\,\text{GeV}^2$

Table 2.1: The meaning and the settings of the parameters inherit in the discussed parameterization of the GPD H.

Note, that the functional form of this parameterization controls the experimentally unconstrained region for $x = \xi$ in the large ξ region. The relation of the fit to experimental observables with the presented approach will be given in the next section.

2.5 Experimental observables

The measurement of absolute cross sections requires a precise knowledge of the luminosity of the experiment. More promising observables include asymmetries, e.g. the ratios of differential cross sections, where acceptance effects approximately cancel. Moreover in HERMES kinematics the cross section of the BH process dominates the one from the DVCS process. However, the interference of both processes provides access to the GPDs via various azimuthal asymmetries.

The three contributions entering the differential photon production cross section (see Eq. 2.10) can be expanded in a Fourier series in the azimuthal angle ϕ. For an

unpolarized nucleon target they read [Bel02b]

$$
\begin{aligned}
|\mathcal{T}_{\mathrm{BH}}|^2 &= \frac{e^6}{x_{\mathrm{B}}^2\, y^2\, t\, (1+\epsilon^2)^2\, \mathcal{P}_1(\phi)\, \mathcal{P}_2(\phi)} \left\{ c_0^{\mathrm{BH}} + \sum_{n=1}^{2} c_n^{\mathrm{BH}} \cos(n\phi) \right\}, \\
|\mathcal{T}_{\mathrm{DVCS}}|^2 &= \frac{e^6}{y^2\, Q^2} \left\{ c_0^{\mathrm{DVCS}} + \sum_{n=1}^{2} c_n^{\mathrm{DVCS}} \cos(n\phi) + \lambda\, s_1^{\mathrm{DVCS}} \sin(\phi) \right\}, \qquad (2.45) \\
I &= \frac{\pm\, e^6}{x_{\mathrm{B}}\, y^3\, t\, \mathcal{P}_1(\phi)\, \mathcal{P}_2(\phi)} \left\{ c_0^{I} + \sum_{n=1}^{3} c_n^{I} \cos(n\phi) + \sum_{n=1}^{2} \lambda\, s_n^{I} \sin(n\phi) \right\}, \qquad (2.46)
\end{aligned}
$$

where λ represents the beam polarization and the ± symbols denote the sign of the beam charge. The Fourier coefficients c_n^{BH} and propagators $\mathcal{P}_1(\phi)$, $\mathcal{P}_2(\phi)$ of the BH term can be calculated within the framework of **Q**uantum **E**lectro–**D**ynamics (QED). Their explicit dependencies are given in [Bel02b] and include a dependence on the well–measured Dirac and Pauli form factors F_1 and F_2 of the nucleon. Note, that the virtual lepton propagators in the BH term introduce an additional dependence on the cosine of ϕ:

$$
\begin{aligned}
\mathcal{P}_1 &\approx 1 - \frac{1 + 2k\, cos(\phi) + (\ldots)}{y\left(1 + (2x_{\mathrm{B}}M_{\mathrm{N}}/Q)^2\right)}, \qquad (2.47) \\
\mathcal{P}_2 &\approx \frac{t}{Q^2} + \frac{1 + 2k\, cos(\phi) + (\ldots)}{y\left(1 + (2x_{\mathrm{B}}M_{\mathrm{N}}/Q)^2\right)}. \qquad (2.48)
\end{aligned}
$$

The kinematical factor k is proportional to $\sqrt{-t}/Q$.

Thus, azimuthal asymmetries with respect to beam charge and/or beam helicity provide an access to Fourier coefficients appearing in both the interference and the squared DVCS term.

2.5.1 Beam–helicity related azimuthal asymmetries

The single–charge beam–helicity asymmetry, formerly known as **B**eam–**S**pin **A**symmetry (BSA), reads

$$
\begin{aligned}
\mathcal{A}_{\mathrm{LU}}(\phi) &\equiv \frac{\sigma^{\rightarrow}(\phi) - \sigma^{\leftarrow}(\phi)}{\sigma^{\rightarrow}(\phi) + \sigma^{\leftarrow}(\phi)} \\
&= \frac{\frac{K_{\mathrm{I}} e_\ell}{\mathcal{P}_1(\phi)\mathcal{P}_2(\phi)} \left[\sum_{n=1}^{2} s_n^{\mathrm{I}} \sin(n\phi) \right] + K_{\mathrm{DVCS}} s_1^{\mathrm{DVCS}} \sin(\phi)}{\frac{1}{\mathcal{P}_1(\phi)\mathcal{P}_2(\phi)} \left[K_{\mathrm{BH}} \sum_{n=0}^{2} c_n^{\mathrm{BH}} \cos(n\phi) \pm K_{\mathrm{I}} \sum_{n=0}^{3} c_n^{\mathrm{I}} \cos(n\phi) \right] + K_{\mathrm{DVCS}} \sum_{n=0}^{2} c_n^{\mathrm{DVCS}} \cos(n\phi)}
\end{aligned} \qquad (2.49)
$$

with the normalized yields $\sigma^{\rightarrow}$ ($\sigma^{\leftarrow}$) for a beam with positive (negative) helicity. The factors K_{I}, K_{DVCS} and K_{BH} include solely kinematic dependencies. In the numerator of this asymmetry the leading–twist coefficient s_1^{I} dominates, but it includes an additional sine contribution from the the squared DVCS amplitude.

This entanglement can be avoided by defining a 'charge–averaged' beam–helicity asymmetry:

$$\begin{aligned}\mathcal{A}_{\mathrm{LU}}^{\mathrm{I}}(\phi) &\equiv \frac{(d\sigma^{+\rightarrow} - d\sigma^{+\leftarrow}) - (d\sigma^{-\rightarrow} - d\sigma^{-\leftarrow})}{(d\sigma^{+\rightarrow} + d\sigma^{+\leftarrow}) + (d\sigma^{-\rightarrow} + d\sigma^{-\leftarrow})} \\ &= \frac{-\frac{K_{\mathrm{I}} e_\ell}{\mathcal{P}_1(\phi)\mathcal{P}_2(\phi)} \left[\sum_{n=1}^{2} s_n^{\mathrm{I}} \sin(n\phi) \right]}{\frac{K_{\mathrm{BH}}}{\mathcal{P}_1(\phi)\mathcal{P}_2(\phi)} \sum_{n=0}^{2} c_n^{\mathrm{BH}} \cos(n\phi) + K_{\mathrm{DVCS}} \sum_{n=0}^{2} c_n^{\mathrm{DVCS}} \cos(n\phi)}.\end{aligned} \tag{2.50}$$

In this asymmetry the normalized yields are grouped according to the sign of the beam charge (denoted by superscripts ±). Because the squared DVCS term does not include a dependence on the sign of the beam charge, its coefficients cancel both in the numerator and denominator. In leading twist the asymmetry simplifies to

$$\mathcal{A}_{\mathrm{LU}}^{\mathrm{I}}(\phi) \approx \frac{-K_{\mathrm{I}} s_1^{\mathrm{I}} \sin\phi}{K_{\mathrm{BH}} c_0^{\mathrm{BH}}}, \tag{2.51}$$

where also the higher cosine modulations from the squared BH term were neglected. This asymmetry is linearly related to the imaginary part of the leading–twist photon–helicity conserving amplitude $M^{1,1}$ and thus in Hermes kinematics mainly to the CFF $\mathcal{H}$ [Bel02b]:

$$s_1^{\mathrm{I}} = 8k \cdot \lambda y(2-y)\, Im M^{1,1} \tag{2.52}$$

$$\approx 8k \cdot \lambda y(2-y) F_1\, Im\mathcal{H}. \tag{2.53}$$

The analogous 'charge–difference' beam–helicity asymmetry is defined by

$$\begin{aligned}\mathcal{A}_{\mathrm{LU}}^{\mathrm{DVCS}}(\phi) &\equiv \frac{(d\sigma^{+\rightarrow} - d\sigma^{+\leftarrow}) + (d\sigma^{-\rightarrow} - d\sigma^{-\leftarrow})}{(d\sigma^{+\rightarrow} + d\sigma^{+\leftarrow}) + (d\sigma^{-\leftarrow} + d\sigma^{-\rightarrow})} \\ &= \frac{K_{\mathrm{DVCS}}\, s_1^{\mathrm{DVCS}} \sin(\phi)}{\frac{K_{\mathrm{BH}}}{\mathcal{P}_1(\phi)\mathcal{P}_2(\phi)} \sum_{n=0}^{2} c_n^{\mathrm{BH}} \cos(n\phi) + K_{\mathrm{DVCS}} \sum_{n=0}^{2} c_n^{\mathrm{DVCS}} \cos(n\phi)}.\end{aligned} \tag{2.54}$$

The sinusoidal modulation in the numerator originating from the squared DVCS term enters in twist–three. It is mainly related to the GPDs H and $\widetilde{H}$ in a bilinear form. Measuring this asymmetry allows to quantify the influence of this twist–suppressed contribution in the single–charge BSA measured at Hermes and CLAS[1] [M+03]. The

[1] **C**EBAF **L**arge **A**cceptance **S**pectrometer

comparison of the three asymmetries is complicated by the additional term in the denominator of Eq. 2.49. Neglecting this contribution the three beam helicity–dependent azimuthal asymmetries can be related via

$$\mathcal{A}_{\mathrm{LU}} \approx e_\ell \cdot \mathcal{A}_{\mathrm{LU}}^{\mathrm{I}} + \mathcal{A}_{\mathrm{LU}}^{\mathrm{DVCS}}. \tag{2.55}$$

2.5.2 Beam–charge azimuthal asymmetry and relations between Fourier coefficients

In addition, the **B**eam–**C**harge **A**symmetry (BCA) is defined by

$$\begin{aligned}\mathcal{A}_{\mathrm{C}}(\phi) &\equiv \frac{d\sigma^+(\phi) - d\sigma^-(\phi)}{d\sigma^+(\phi) + d\sigma^-(\phi)} \\ &= \frac{-\frac{K_{\mathrm{I}}}{\mathcal{P}_1(\phi)\mathcal{P}_2(\phi)} \sum_{n=0}^{3} c_n^I \cos(n\phi)}{\frac{K_{\mathrm{BH}}}{\mathcal{P}_1(\phi)\mathcal{P}_2(\phi)} \sum_{n=0}^{2} c_n^{\mathrm{BH}} \cos(n\phi) + K_{\mathrm{DVCS}} \sum_{n=0}^{2} c_n^{\mathrm{DVCS}} \cos(n\phi)},\end{aligned} \tag{2.56}$$

and provides access to the real part of the interference term. In leading twist and by neglecting the higher cosine modulations from the squared BH term the asymmetry simplifies to

$$\mathcal{A}_{\mathrm{C}}(\phi) \approx \frac{-K_{\mathrm{I}} \left(c_0^I + c_1^I \cos\phi\right)}{K_{\mathrm{BH}} c_0^{\mathrm{BH}}}. \tag{2.57}$$

Both, the constant c_0^I and cosine c_1^I coefficients in the numerator are related to the real part of the leading–twist photon helicity–conserving amplitude $M^{1,1}$

$$c_0^{\mathrm{I}} \approx -8(2-y)\left(\frac{k^2(2-y)^2}{1-y} + \frac{t}{Q^2}(1-y)(2-x_{\mathrm{B}})\right) ReM^{1,1}, \tag{2.58}$$

$$c_1^{\mathrm{I}} = 8k \cdot (2 - 2y + y^2)\, ReM^{1,1}, \tag{2.59}$$

and thus can be approximately related by

$$r \equiv \frac{c_0^{\mathrm{I}}}{c_1^{\mathrm{I}}} \approx -\frac{2-y}{2-2y+y^2}\left[\frac{(2-y)^2}{1-y}k + \frac{t}{kQ^2}(1-y)(2-x_B)\right]. \tag{2.60}$$

The definition of the azimuthal angle ϕ here is in accordance to the Trento convention [BDDM04] and differs from that in [Bel02b]: $\phi = \pi - \phi^{[\mathrm{Bel02b}]}$.

Besides c_0^{I}, c_1^{I} and s_1^{I} only the Fourier coefficient c_0^{DVCS} is related to the amplitude $M^{1,1}$, but is not accessible in scattering off an unpolarized nucleon target. The coefficients s_2^I, c_2^I, s_1^{DVCS} and c_1^{DVCS} are related to twist–3 GPDs. In contrast, the Fourier coefficients c_3^I and c_2^{DVCS} arise in twist–two gluon helicity–flip GPDs and from quark twist–four GPDs.

The observables defined in this section will be extracted from HERMES data taken off an unpolarized hydrogen target and presented in chapter 5.5 of this thesis. Before that the HERMES experiment and DVCS analysis will be explained in detail.

3 The HERMES experiment

The HERMES experiment was one of three experiments located at the HERA storage ring provided by the german institute **D**eutsches **E**lektronen–**Sy**nchrotron (DESY). It was designed to study polarized DIS processes. This chapter explains all parts of the HERA and HERMES facilities exploited in the scope of this work.

3.1 The HERA storage ring

The HERA storage ring including its system of pre–accelerators is depicted in figure 3.1. It provided a lepton beam of 27.57 GeV energy and an anti–parallel running proton beam that was not made use of at the fixed target experiment HERMES. The charge of the leptons was switched five times during the operation of the HERA facility, resulting in three data periods with positrons and electrons. The beam was structured into bunches of 27 ps length, separated by around 96 ns.

An asymmetry in the spin–flip probabilities of the emission of synchrotron radiation in the arcs of the HERA ring led to a natural transverse polarization of the lepton beam [BDS+75]. This so–called Sokolov–Ternov mechanism exhibits an exponential time dependence

$$P(t) = P_0 \left(1 - e^{\frac{-t}{\tau}}\right). \tag{3.1}$$

Even though the mechanism allowed for a maximum polarization of 92.4 %, depolarization effects reduced this number to around 50 % with a time constant τ of around 30 minutes (see figure 3.2), while a typical duration of a lepton fill in the HERA storage ring was about ten hours.

An array of bending magnets in front of the HERMES experiment rotated the spin of the beam into the longitudinal direction. Another spin rotator behind the experiment transformed the orientation of the spins back to the transverse direction.

The polarization direction was usually reversed every few months. Two polarimeters [B+94, B+02b] were installed to continuously monitor the magnitude of the beam polarization. They exploited the spin–dependent cross section of the Compton scattering process for circularly polarized photons off polarized leptons. Comparing both polarimeters shows a reasonable agreement except for shorter periods (see again figure 3.2). The two measurements were each smoothed via a spline interpolation and then combined. Requiring one of both polarimeters to be working removes only very little data (< 1 %). The deviations were added in quadrature into the total systematic uncertainty of e.g. 3.4 % on the determination of the magnitude of the longitudinal

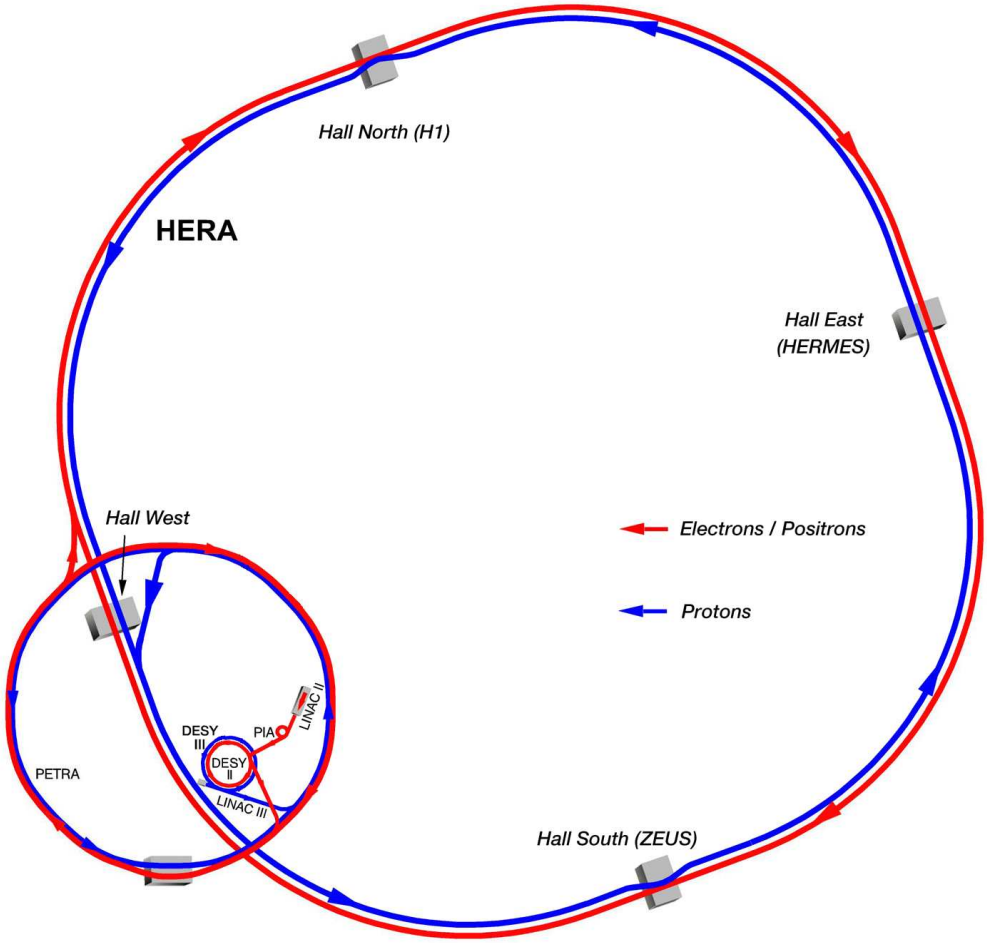

Figure 3.1: The Hera storage ring and its system of pre–accelerators, which are located in the south–west section of the facility. The lepton beam is depicted in red and the proton beam in blue. The three experiments are located in the East (Hermes), South (Zeus) and North Hall (H1).

beam polarization in the year 2005, containing also the individual systematic errors from both polarimeters [A$^+$07b].

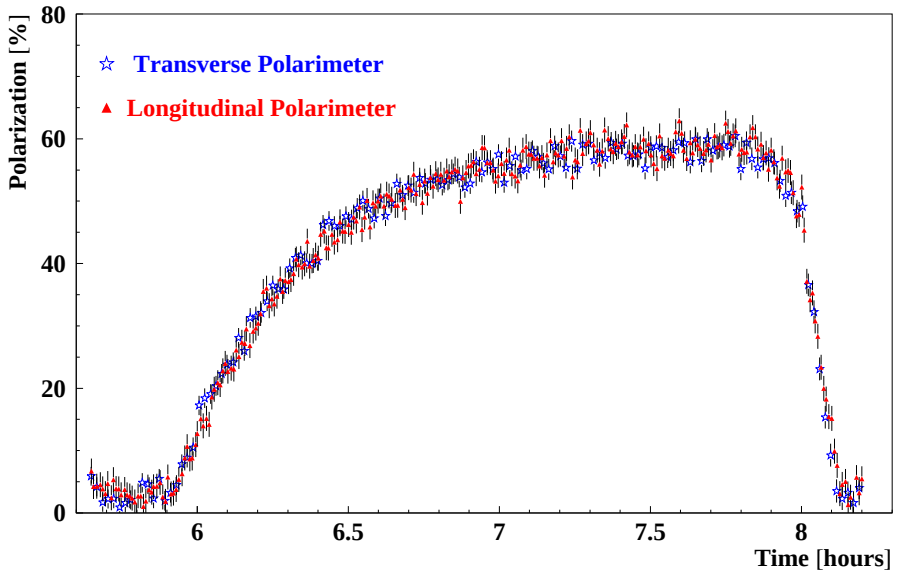

Figure 3.2: One example of the polarization build–up of a positron fill in the HERA facility measured from both, the longitudinal and transverse polarimeters.

3.2 The HERMES target

The HERMES target cell was located inside the beam vacuum and could be filled with several polarized (H, D, ^{3}He) or unpolarized (H, D, N, ...) gas types (see figure 3.3). It consisted of an open–ended elliptically formed aluminum tube of 75 μm wall thickness. The width and height of the cell were decreased from 29.0 mm to 21.0 mm and from 9.8 mm to 8.9 mm during a major shutdown in 1999 in order to increase the achievable target density. Its length of 400 mm was kept unchanged until the installation of the **R**ecoil **D**etector (RD) in 2005. The cell was centered around the origin of the HERMES coordinate system, in which the z–axis pointed along the lepton beam and the y–axis pointed upwards.

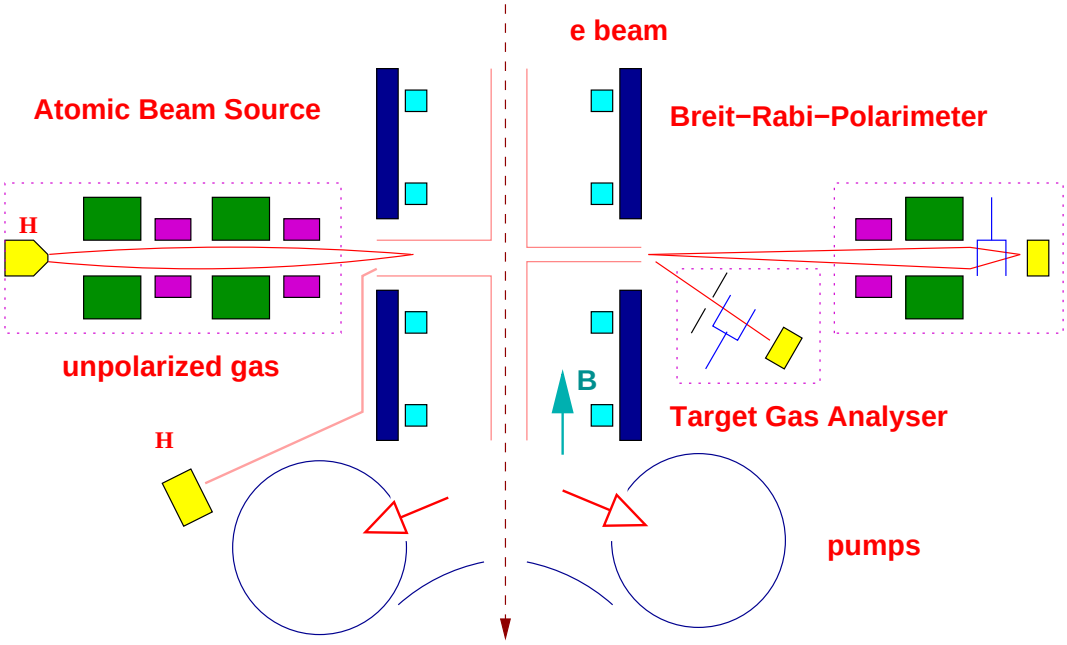

Figure 3.3: A schematical drawing of the HERMES target viewed from the top. The gas was inserted from the Atomic Beam Source on the left, a small fraction was analyzed with the Breit–Rabi–Polarimeter and a Target–Gas–Analyzer on the right and was pumped away towards the lower part of the drawing.

An **A**tomic **B**eam **S**ource (ABS) based on Stern–Gerlach separation provided the polarized gas types [N$^+$03]. The alignment of the nuclear polarization was defined by a longitudinal target magnetic field in the years 1995 until 2000 and thereafter by a transverse magnetic field replaced by the Recoil Detector. The enhanced spin state was reversed in periods of 60 s or 90 s depending on the data taking year. This ensured a negligible net target polarization and compensated for possible emerging systematic detector effects. Thus this data could be analyzed together with the unpolarized data. To monitor the polarization a Breit–Rabi–Polarimeter [B$^+$02a] was used, while the

dilution from not dissociated molecules in the cell was measured by the Target–Gas–Analyzer [B+03]. It was found to be less than 5 % [Tai05]. An additional connection to the target cell allowed to feed in unpolarized gas types.

The realized densities in the storage cell depended on the dimensions of the target cell, the produced flux from the ABS and was limited by the negotiated contribution to the life time of the lepton beam. Typical values of 10^{14} nucleons/cm^2 in the polarized case and around a factor of two orders of magnitude more in the unpolarized case were achieved. Through small rectangular holes in the rear part of the target cell, the gas was pumped away by a differential pumping system.

3.3 The HERMES Forward Spectrometer

The forward spectrometer of the HERMES experiment (see figure 3.4) consisted of symmetric halves above and below the plane defined by the two beams. A dipole magnet with an integrated field of 1.3 Tm bent all charged particles, but was separated from the beams by a horizontal septum plate made of iron. This plate limited the angular acceptance of the experiment to ±170 mrad horizontally and 40 – 140 mrad vertically. A correction coil was mounted inside the shielding of the positron beam pipe to correct for fringe fields and to compensate the transverse holding field of the target when operating with transverse polarization.

During the years of operation certain components had been added or removed. In the following only those spectrometer parts used in the scope of this work will be discussed. A more complete description of the apparatus can be found in Ref. [A+98a].

The different detector's purposes fell into three main subjects: To track, to identify and to reconstruct the momentum of the ejectiles.

3.3.1 Tracking system

After exiting the target region through a stainless steel foil of 300 μm thickness, the particles first passed the **D**rift **V**ertex **C**hamber (DVC) and the two **F**ront **C**hambers (FC). In combination with the **B**ack **C**hambers (BC) behind the magnet, both front and back partial tracks could be reconstructed. Three additional proportional chambers in the magnet (**M**agnet **C**hambers (MCs)) allowed to reconstruct charged particles not reaching the rear part of the spectrometer in combination with the information from the FCs. The spatial resolution of the different chambers varied between 200 and 300 μm [A+98a].

The information from the tracking detectors was combined in the **H**ERMES **r**econstruction **c**ode (HRC). To match the position information from the single detector layers a tree–search algorithm was implemented that increased the resolution of the detectors in each iteration up to the real value [Wan97].

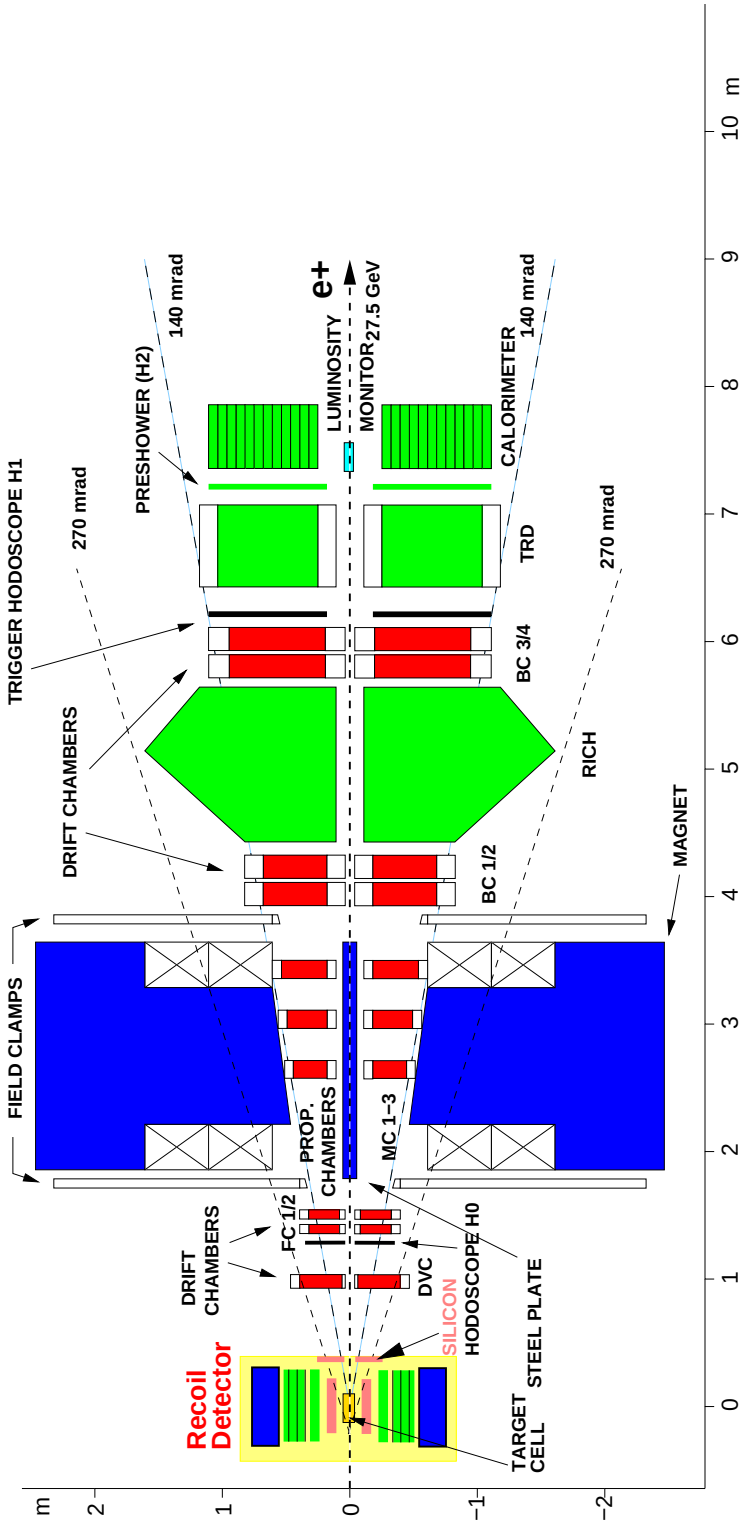

Figure 3.4: The HERMES setup used in the years 2006 and 2007. The components colored in red built the tracking system, the green parts were used for the particle identification and the magnets are shown in blue. The Recoil Detector replaced the target polarization apparatus in december 2005, while the Forward Spectrometer was not changed.

3.3.2 Momentum reconstruction

To determine the momentum of a found track from its deflection in the inhomogeneous magnetic field in a fast way, HRC used a look-up table. For high momentum leptons between 3.5 and 27 GeV/c the achieved momentum resolution $\delta p/p$ was between 0.7 and 1.3 % in the first three years of data taking [A+98a]. After the installation of the **R**ing **I**mage **Č**erenkov Counter (RICH) in 1998 it decreased to 1.5 – 2.5 % (see figure 3.5). This resolution was determined by **M**onte **C**arlo (MC) simulation with the geometry description for the years 2006/2007. The angular resolution $\delta\vartheta$ was better than 0.6 mrad for small opening angles.

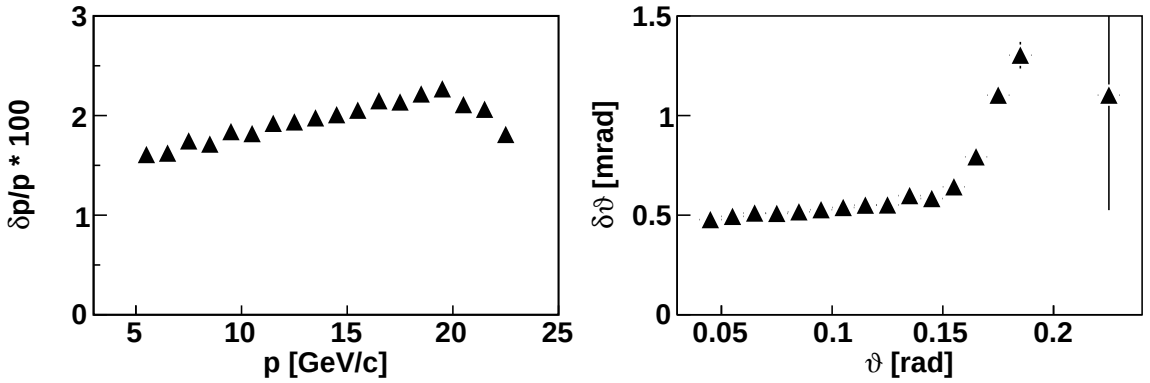

Figure 3.5: The momentum (left panel) and angular resolution (right panel) for identified leptons from elastic DVCS/BH events. The points represent the mean of a Gaussian fit function, while the errors are calculated from the number of events in each bin.

3.3.3 Particle identification system

The HERMES **P**article **I**dentification (PID) system consisted of four detectors: the RICH, a **T**ransition **R**adiation **D**etector (TRD), a preshower and a lead-glass calorimeter.

The concept of Čerenkov detectors bases on the emission of a cone of Čerenkov radiation from charged particles moving with a velocity faster than the in–medium speed of light. For the separation of leptons and hadrons the RICH only contributed to particles with less than 4 GeV energy (as did the threshold Čerenkov detector that was installed in the years 1996 and 1997) and was therefore not used in this analysis. However it was a powerful tool for the separation of different hadron types.

A TRD exploits the emission of transition radiation from relativistic charged particles at the boundary of two materials with different dielectric constants. The radiated energy is proportional to the γ–factor of the particle and therefore allows to separate between particles with different masses.

The preshower consisted of two radiation lengths of lead and a hodoscope (a scintillator array) and was located directly in front of the electromagnetic calorimeter.

Both detector concepts base on the different probabilities for leptons and hadrons to start producing electromagnetic showers. Thus the deposited energy from leptons is usually smaller than those from hadrons. Therefore the ratio of the deposited energy and the momentum obtained from the deflection in the magnet should be unity for leptons in contrast to the hadronic ratio.

The energy depositions dE_i of the traversing particles in the different detector layers (i) are translated into probability distributions P for a specific particle hypothesis. These functions are called parent distributions and are recalculated for each data production, thus always using the best knowledge of the detector calibrations. The distributions from the PID detectors are combined into one fractional quantity comparing the likelihoods for two different particle (or particle family) types

$$P = \sum_{\text{PID detector}} \log_{10} \frac{P_i^l(p, dE_i)}{P_i^h(p, dE_i)}, \tag{3.2}$$

where l (h) stands for lepton (hadron). In principal, this probability needs to be corrected for the ratio of the initial lepton flux ϕ_l compared to the hadron flux ϕ_h, which is typically around 1 at HERMES. This correction shifts the black dashed line onto the red dotted line in figure 3.6) that depicts the currently used cut in the DVCS analysis, but recovers only very little data and was therefore omitted.

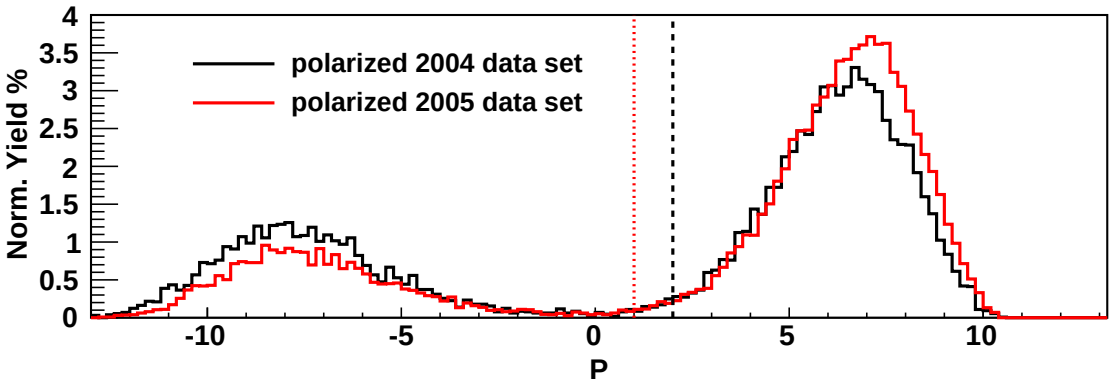

Figure 3.6: A comparison of the normalized PID distributions for DIS events with an additional single photon detected from the polarized data sets of the years 2004 and 2005 is shown. The dashed line indicates the cut used in the analysis.

Real photons were identified in the data as a cluster in the preshower and the electromagnetic calorimeter without a track pointing towards it. Both, energy and position of the trackless cluster are defined from the signal in the calorimeter, whose calibration is therefore crucial for the present analysis.

The recoiling particles were not detected until the installation of the RD in the year 2006 (see chapter 3.4).

3.3.4 Trigger system

In order to distinguish events of physics interest from background, an efficient trigger system for different event topologies was installed at HERMES. In this analysis only the so–called trigger 21 is of interest that required a signal in the hodoscopes H0, H1 and H2 (the preshower counter) as well as a cluster in the calorimeter coinciding with a bunch of HERA. By requiring the hits in the hodoscopes to arrive in the correct time order, background originating from the proton beam was suppressed as those circulated the ring in the opposite direction. The threshold for the signal in the calorimeter was chosen to be sufficiently larger (at least 1.4 GeV) than the minimum ionizing energy to suppress signals from any produced hadrons. In about 65 % of the triggered events, tracks could be reconstructed that originated with a probability of 95 % from the target. Around one third of these events included a lepton with the charge of the beam [A+98a].

3.3.5 Luminosity monitor

A luminosity monitor [B+01] consisting of two small radiation hard calorimeters was located 7.2 m behind the target region, measuring Bhabha scattering and annihilation processes (or Møller scattering) for positron (or electron) beams, respectively. These processes left high energy depositions in both detector halves, making them distinguishable from background signals. The luminosity of the experiment was deduced by

$$\mathcal{L} = \frac{R_{\text{Bhabha/Møller}}}{\sigma_{\text{Bhabha/Møller}}}, \tag{3.3}$$

where the rate R was measured from the detector and the cross section σ was simulated within the acceptance taking into account the efficiency of the experimental environment. A precise knowledge of the beam position at the target and at the luminosity monitor was needed. The resulting systematic uncertainty varied between 7.2 % and 8.4 % for the years 1996 until 2000 and between 3.0 % and 5.3 % for the rest of the running period. In the calculation of an asymmetry the large uncertainties cancelled each other.

The luminosity must be corrected for the trigger deadtime. This quantity describes the fraction of the trigger rate that was lost, because the data acquisition could not record the event. The deadtime was determined by counting and comparing the number of generated and accepted triggers.

3.3.6 Alignment procedure

A high resolution track reconstruction needs an exact knowledge of the position of the various detector components. In order to monitor possible shifts of the tracking system, alignment data were taken typically once per year with the spectrometer magnet switched off. In this case the straight tracks from the particles could be used to align the detectors. This procedure only allowed for a relative positioning of the

spectrometer parts. In addition the relative alignment of the detectors was monitored by a laser alignment system with a precision of better than 60 mrad [S+98].

In order to achieve an absolute alignment and to cross–check the laser alignment system, further optical surveys have been performed starting in the year 2004. In addition, beam position monitors on either side of the HERMES spectrometer measured both the offset from the nominal beam axis and the slopes of the beam. This information was combined to externally align the detector system. The relative shifts between the top and bottom halves of the tracking detectors were found to be smaller than 1 mm with an accuracy of around 0.1 mm, while the relative slopes were determined to be 60 ± 30 μrad (-340 ± 40 μrad) in x(y)–direction [Kis07].

3.4 The HERMES Recoil Detector

The detecting system for the recoiling particles was realized in two steps. First, in the year 2002 a wheel–shaped silicon micro–strip telescope, the so–called Lambda Wheels, have been installed [Dem07]. They were located inside the target chamber to reduce the material between them and the target (see SILICON in figure 3.4) and were mainly intended to detect decay particles from secondary vertices, e.g. the Λ particle.

Second, in beginning of the year 2006 the complete target polarization apparatus was removed and the HERMES **R**ecoil **D**etector installed instead. Its purpose was to detect, identify and reconstruct the recoiling particles from exclusive processes, which were typically out of the HERMES front spectrometer acceptance [TDR02]. It therefore consisted of different detector types, namely a **S**ilicon **D**etector (SD), a **S**cintillating **F**iber **T**racker (SFT) and a **P**hoton **D**etector (PD) (see figure 3.7). All three sub–detectors were mounted inside a super–conducting solenoid providing a magnetic field of 1 T. In order to increase the angular acceptance covered by the RD the target cell length was shortened to 15 cm. In a shorter cell the flux needs to be increased to achieve the same areal density. Therefore the length was limited by the amount of gas the pumping system could still handle and thus maintain the vacuum in the target chamber. In addition, the cell was moved a little closer towards the spectrometer (the center was moved by 12.5 cm in positive z–direction).

3.4.1 Recoil Silicon Detector

The SD was located around the target cell inside the beam vacuum to reduce the lower momentum cut–off determined by the amount of material between the detector and the target. It was organized in four quadrants called modules arranged in a diamond–like shape, each consisting of two layers of double–sided silicon strip detectors (see figure 3.8) mounted into a holding structure consisting of aluminum.

It has been chosen to use the TTT sensors designed from Micron Semiconductors for the TIGRE experiment[1] with a thickness of 300 μm. One layer included two active

[1] **T**racking and **I**maging **G**amma **R**ay **E**xperiment

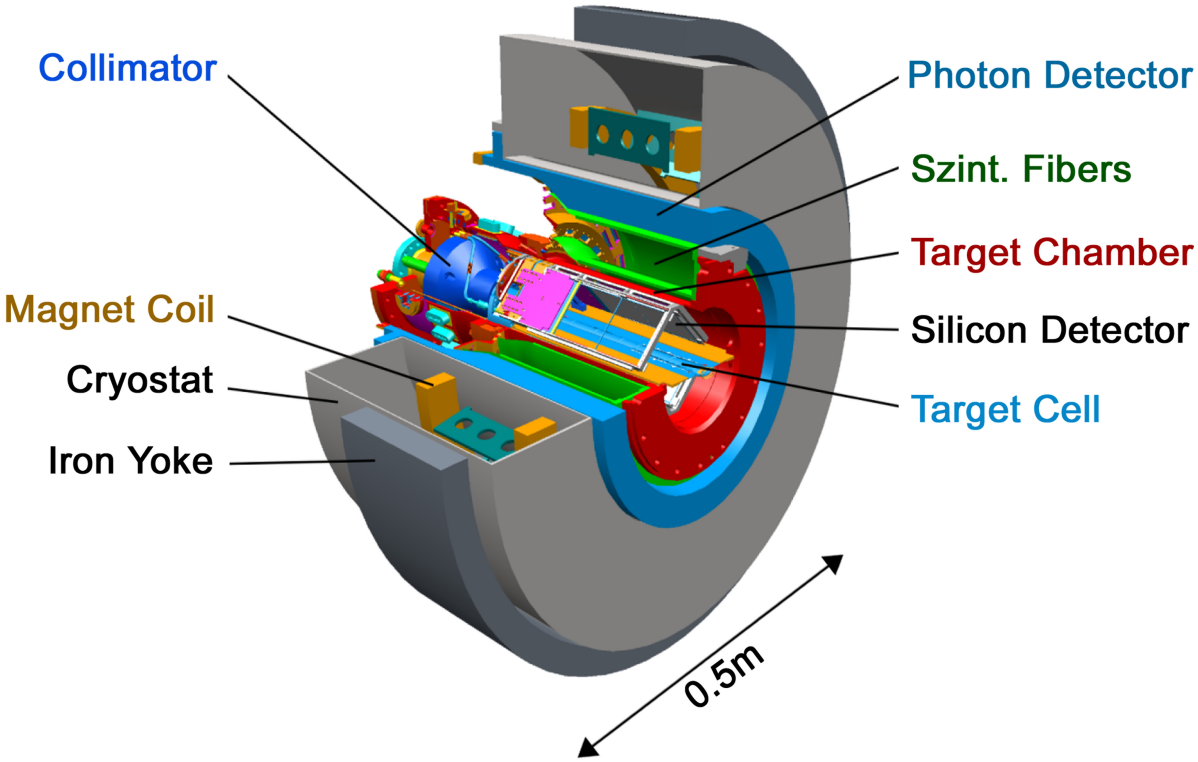

Figure 3.7: A CAD drawing of the Hermes target region and the Recoil Detector. See text for further details.

areas of $99 \cdot 99$ mm^2 called sensors, mounted into a ceramic support frame with a gap of 1.3 mm. The strip pitch was 758 μm leading to 128 strips per sensor. The strips on the n–side of the modules were orientated parallel to the beam axis, while the p–side strips were rotated by 90 degrees.

A flexible Kapton foil with a thickness of 50 μm and conducting pathes of 5 μm copper, 5 μm nickel and 100 nm gold connected the strips with the readout chips. An arrangement with the minimum possible coverage of the sensors with passive material was intended, but was only feasible for the p–side. Hence the two p–sides were installed facing each other to reduce the amount of passive material between the two modules to improve the momentum reconstruction. The vicinity to the beam dictated various conditions for the electronics. The HELIX 3.0 chip was chosen as it was also used for the Lambda Wheels [Dem07] and matched all technical constraints. It had been developed for the HERA-B experiment and could therefore store all 128 channels per chip within the 96 ns between two Hera bunches.

The energy deposits of the traversing particles of interest ranges from a **M**inimum **I**onizing **P**article (MIP) (with a mean energy deposit of 116 keV in 300 μm of silicon) and protons depositing up to 6.2 MeV energy. To cover this very large dynamic range, each signal was fed to two separate helix chips; directly to the so–called high–gain

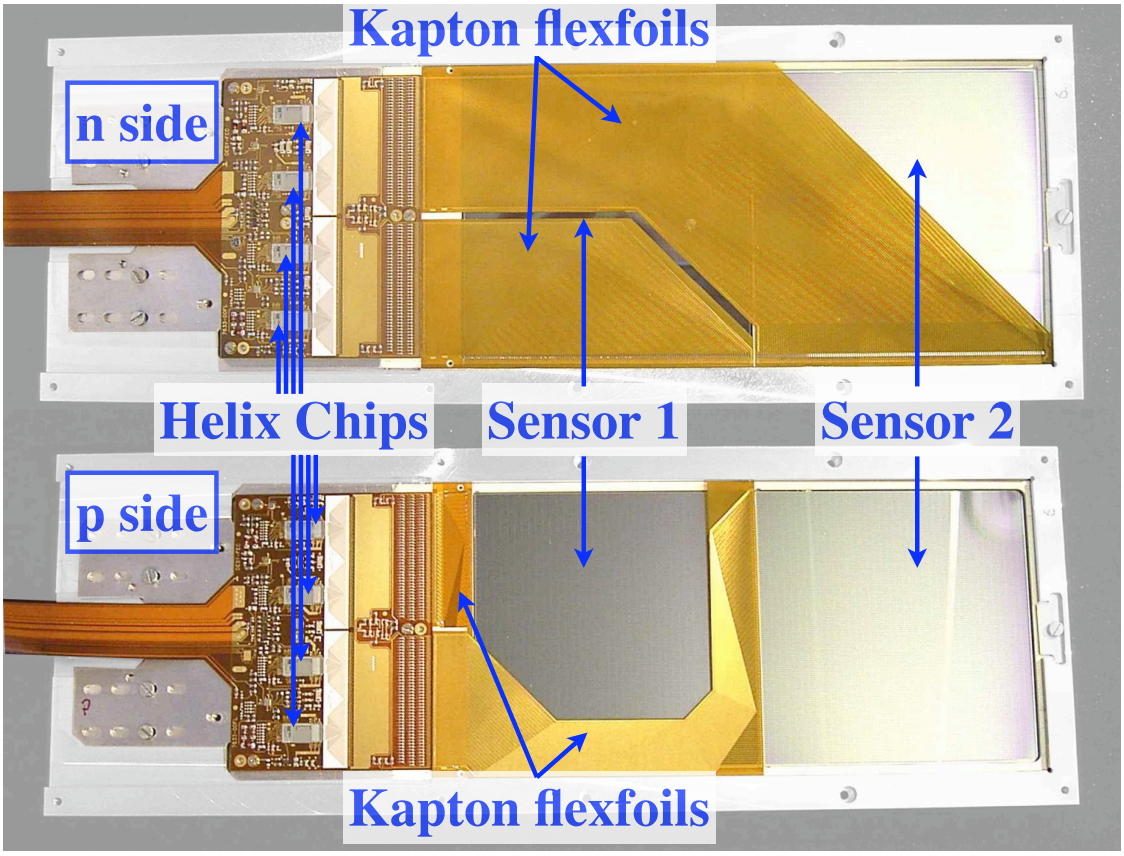

Figure 3.8: A picture of the n– and p–side of one module of the HERMES Recoil Silicon Detector. The active areas, called sensors, are divided into strips connected by flex foils made of Kapton to the read–out HELIX chips.

and attenuated by a 10 pF capacitor to the so–called low–gain (for a scheme compare with figure 3.9; plots of the high-low–gain ratio are shown in chapter 6.3).

The HERA lepton beam was a source of huge radio frequency power and thus the SD electronics placed within the vacuum needed to be shielded. Therefore a Faraday cage was installed around the silicon modules, using a copper vaporized Kapton foil and a simple holding structure (see figure 6.1).

The digitization of the signal was performed in the **H**ELIX **a**nalog–to–**d**igital **c**onverters (HADCs) developed for the Lambda Wheels. Each of the four units was used for four HELIX chips, resulting in 512 channels per unit. The HADC internally subtracted the pedestal level. It also determined the **C**ommon **M**ode **N**oise (CMN) by averaging those 16 out of the first 32 strips of a sensor whose signal was below the so–called high threshold. The data taking and processing is explained in more detail in chapters 6.1 and 6.2.2.

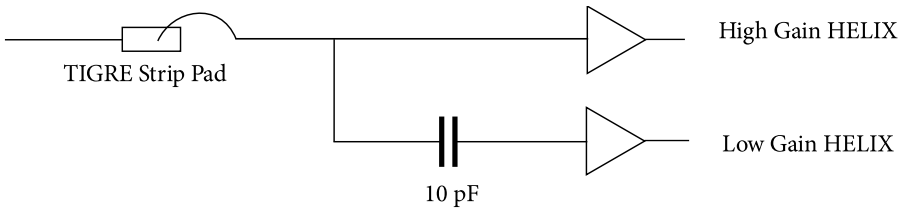

Figure 3.9: A simplified scheme of the SD read out. The ratio of the two gains is approximately 1/5 determined by the 10 pF capacitance.

3.4.2 Recoil Scintillating Fiber Tracker

The SFT [Hoe06, Ker08] was located directly outside the target chamber. It consisted of two barrels with each four layers of scintillating fibers (see figure 3.10), two of which were oriented parallel to the beam axis and two tilted by an angle of 10° to be able to reconstruct coordinates in three dimensions. The layers were constructed using more than 600 (1000) fibers, where always four (two) fibers were connected via one light guide fiber of 4 m length to one channel of the multi–anode **P**hoto**m**ultiplier **T**ubes (PMTs). Thus, the PMTs only needed an additional μ–metal shielding from the magnetic field. Each barrel had an active length of 280 mm.

The SFT had an ϕ–acceptance of 2π with a lower efficiency in the regions, where the Silicon Detector holding structure was located. The θ–acceptance contained the interval between 0.7 – 1.35 rad, thus increasing the coverage of the Lambda Wheels to angles greater than 90°. For a particle passing through both SFT modules, two coordinates could be reconstructed. Combined with the vertex position this allowed to obtain the particles track and from its bending radius the momentum was deduced. Using also the energy deposits in the individual layers a particle identification between pions and protons starting from a momentum of 250 MeV/c was possible.

3.4.3 Recoil Photon Detector

The Photon Detector consisted of six alternating layers of segments of tungsten as converter material and scintillating strips [vH07]. The first tungsten layer was 6.3 mm thick, the other two tungsten layers only 3.5 mm, which corresponds to one radiation length. While the strips of the inner PD layer were parallel to the beam axis, the other two layers were inclined by around ±45°. All scintillator strips were connected to two wave–length shifters, which were coupled by 2 m long light guides to photomultipliers that were read out by **A**nalog **D**igital **C**onverter (ADCs). The PMTs were mounted into a soft steel case and additionally shielded with thin μ–metal plates from the magnetic field. A picture of the PD before installation is shown in figure 3.11.

The PD had a ϕ–acceptance of 2π and a θ–acceptance between 0.78 – 1.90 rad. Thus additional information on the separation between higher energetic pions and protons was collected. Its main purpose was to detect one or both decay photons from excited

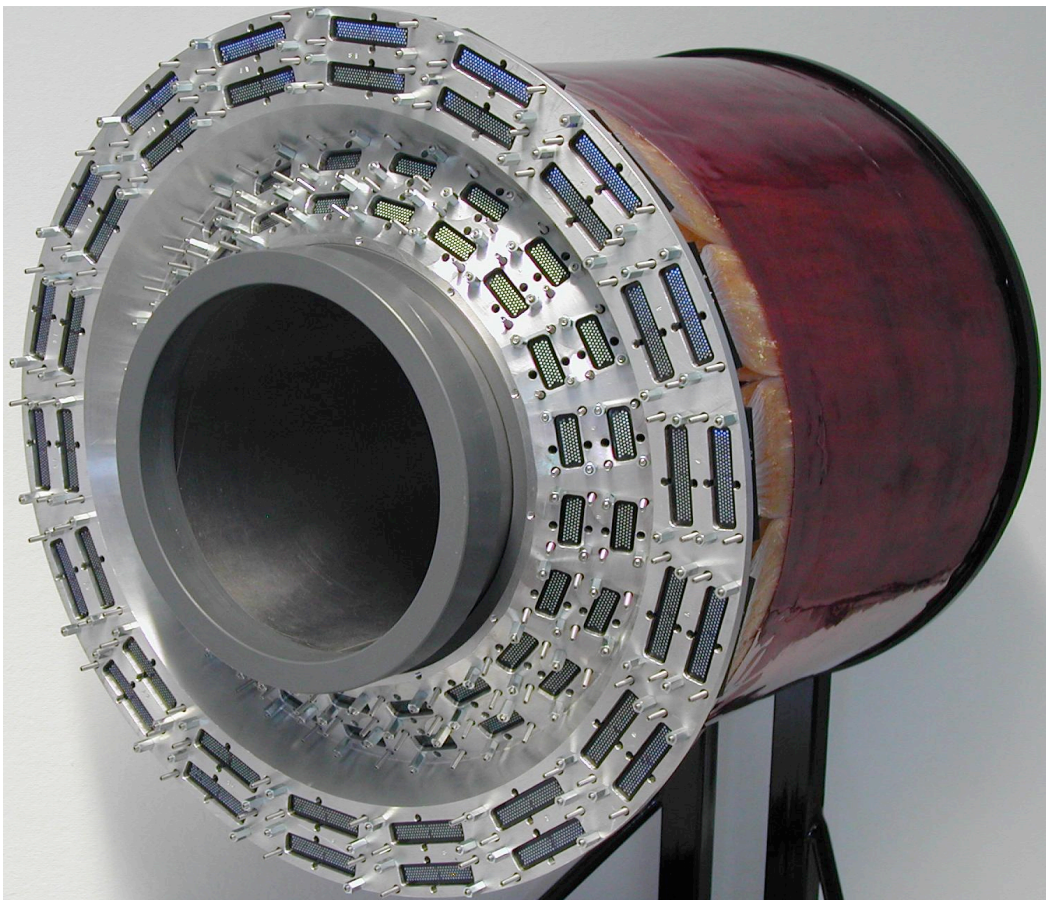

Figure 3.10: A picture of the fully mounted HERMES Recoil Scintillating Fiber Tracker. The light guide connectors are visible on the front side.

Δ–resonances from the associated DVCS/BH processes. For this aim a rather low polar resolution of 8° was found to be sufficient and determined the dimensions of the individual scintillator strips. Moreover, the Photon Detector provided a trigger for cosmic data, which were needed to align the different RD components.

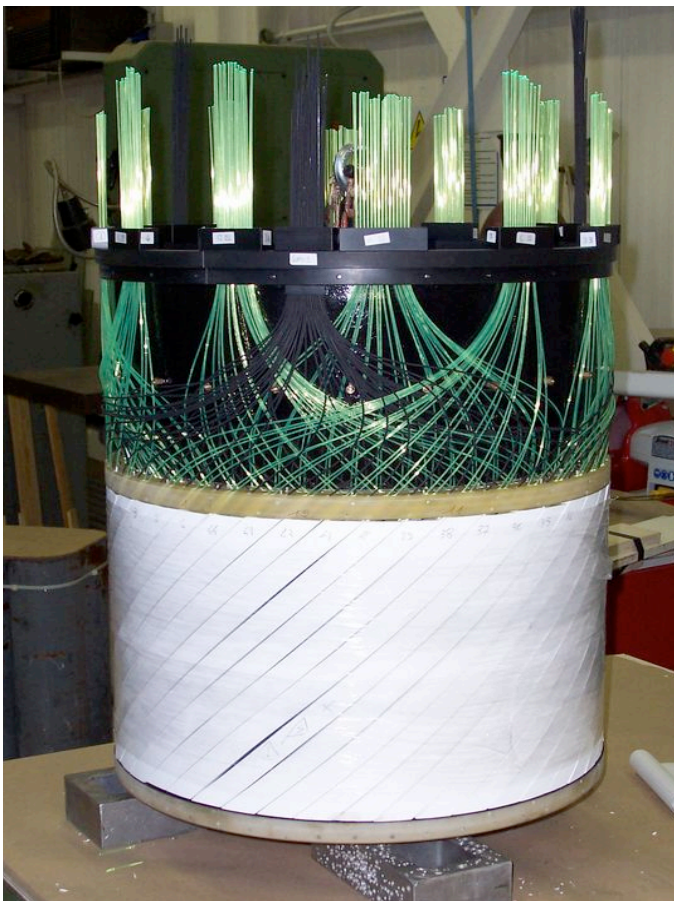

Figure 3.11: A picture of the fully mounted HERMES Recoil Photon Detector.

4 DVCS analysis

This chapter will give a description of the DVCS analysis performed on all hydrogen data taken before the RD was installed. Besides technical requirements to ensure high–quality data it will focus on the analysis cuts and various studies to check the validity of the analysis techniques, both on real and MC data. Throughout this chapter the term DVCS will be used to describe both DVCS and BH events, unless stated otherwise.

4.1 Data quality requirements

The HERMES spectrometer consisted of many different parts. Experts were constantly checking the performance for each individual component. This information was collected and encoded into two 32–bit status words, one for each detector half. For a specific analysis not all parts of the experiment are employed and thus different bit patterns were chosen for different analysis topics. For the present analysis the bit pattern was chosen as 0x501e03dc. It contained checks on the data taking (dead time) and on the performance of the beam facility (beam current and polarization), and various detectors. In the DVCS analysis the tracking chambers, the calorimeter and the TRD were crucial in the lepton-hadron separation. In addition an operating luminosity detector was required. In the year 1996 the calorimeter performance was encoded in a different bit (22), leading to a bit pattern of 0x505e03dc. A more detailed description of the meaning of the bits can be found in Ref. [ZL08].

In addition several criteria were checked directly in the data. For this analysis no lower limit on the beam polarization was applied, making it necessary to explicitly request the existence of a polarization measurement and the combined result from both polarimeters to be physically meaningful. The count rate of the luminosity monitors and the life time of the data taking system was checked to be reasonable.

4.2 Event selection

The event selection contained three steps:

- Select a single lepton event satisfying DIS kinematics.
- Select an additional high–energetic single photon.
- Select DVCS events.

quantity	meaning	limits [cm]
$\lvert x_{\text{Calo}}\rvert$	The x–coordinate of the cluster position in the calorimeter.	$[0, 175]$
$\lvert y_{\text{Calo}}\rvert$	The y–coordinate of the cluster position in the calorimeter.	$[30, 108]$
$\lvert x_{\text{FFC}}\rvert$	The x–coordinate of the track at the front field clamp.	$[0, 31]$
$\lvert y_{\text{SP}}\rvert$	The y–coordinate of the track at the beginning of the septum plate.	> 7
$\lvert x_{\text{RFC}}\rvert$	The x–coordinate of the track at the rear field clamp.	$[0, 100]$
$\lvert y_{\text{RFC}}\rvert$	The y–coordinate of the track at the rear field clamp.	$[0, 54]$

Table 4.1: The explicit requirements on the geometry of DIS track candidates. The abbreviations stand for: Calorimeter (Calo), front field clamp (FFC), septum plate (SP) and rear field clamp (RFC).

The first step was needed for normalization purposes. The intermediate step served to reduce the amount of data. In the final step an as pure as possible DVCS event sample was created. This step was hampered because of the missing detection of the recoiling proton. The single steps will be explained in the next three sections.

4.2.1 Selection of DIS events

The selection criteria for DIS events were separated into requirements on the lepton track and the kinematics of the process.

The algorithm searched for events with a trigger 21 (see section 3.3.4) and at least one long track producing a signal in the tracking system both in front of and behind the target magnet. The likelihood of the combined PID detector responses from the TRD, the preshower and calorimeter was required to be larger than 2 corresponding to a lepton sample with a hadronic contamination of less than 1 %. The charge of the lepton needed to correspond to the charge of the beam in the considered data year.

The lepton's vertex position in the z–coordinate was required to lie between -18 cm and 18 cm, and the closest transverse distance to the beam axis was below 0.75 cm to suppress tracks not originating from the target cell. (This cut was discarded for data taken with a transversely polarized target.) The center of the cluster position in the calorimeter belonging to the track was restricted to make sure the whole shower energy was deposited into the lead–glas blocks. In addition the so–called fiducial volume cuts were applied. This group of requirements assured that the track did not hit or scatter off passive detector parts like field clamps, the septum plate or frames of the tracking chambers. The explicit numbers are given in table 4.1.

In the case of data taken on a transversely polarized target the track was corrected for the impact of the target magnet. If none of the (two existing) correction methods was available the event was discarded.

From the reconstructed scattered lepton the so–called inclusive variables can be calculated. To ensure the validity of the factorization theorem, a hard virtual photon with a squared momentum Q^2 larger than 1 GeV^2 is required. The cut on the squared invariant mass of the photon–nucleon system ($W^2 > 9$ GeV^2) was increased to not only remove data from the resonance region (below 4 GeV^2), but also improve the compatibility of data and MC [Ell04]. In the same reference a cut on the energy transfer from the incoming lepton to the virtual photon $\nu < 22$ GeV was proposed to improve the agreement of data taken in the years 1998 and 2000. The loss of data due to this cut is negligible as the threshold on the cluster energy in the calorimeter was set to 3.5 GeV.

Events fulfilling all listed requirements will be called ***DIS events*** in the following.

4.2.2 Selection of the real photon

Besides the scattered lepton, the DVCS final state consists of the real photon and the undetected recoiling proton. In order to maximize the statistics of such event topologies in the data sample, only events with exactly one charged track and one untracked cluster in the calorimeter were considered. These events will be called ***single photon event candidates*** in the following.

The identification of the untracked cluster to originate from a photon was realized by requiring the cluster signal in the preshower to be larger than 1 MeV and in the calorimeter larger than 5 GeV. The former cut was introduced to suppress photons not showering in the preshower detector. Such photons are known to be miscalibrated by 10 % at a photon energy of 15 GeV [Ely02]. A more sophisticated energy calibration of the calorimeter taking into account the preshower signal is under investigation. The cut reduced the statistics by about 20 %.

The lower limit on the cluster amplitude in the calorimeter improved the exclusivity of the analysis (see figure 4.1). The two–dimensional distribution showing the squared missing mass M_X^2 distribution (will be defined in the following section) as a function of the photon energy E_γ was obtained from the whole data sample of the year 2000. In the exclusive region ($M_X^2 \approx m_p^2$) only very few photons with an energy below 5 GeV^2 are observed, because of the lower limit on the squared photon–nucleon invariant mass.

The position of the photon cluster on the surface of the calorimeter was restricted according to table 4.2. The limits in the vertical direction were chosen such that the cluster was fully contained inside the sensitive volume. The horizontal coverage was limited by the dimensions of the target magnet.

The shower profiles created from a lepton and a photon differ. Because the calorimeter was calibrated on the quantity E/p (for leptons), this discrepancy has to be accounted for. This is done using a different z–position of the cluster in the calorimeter.

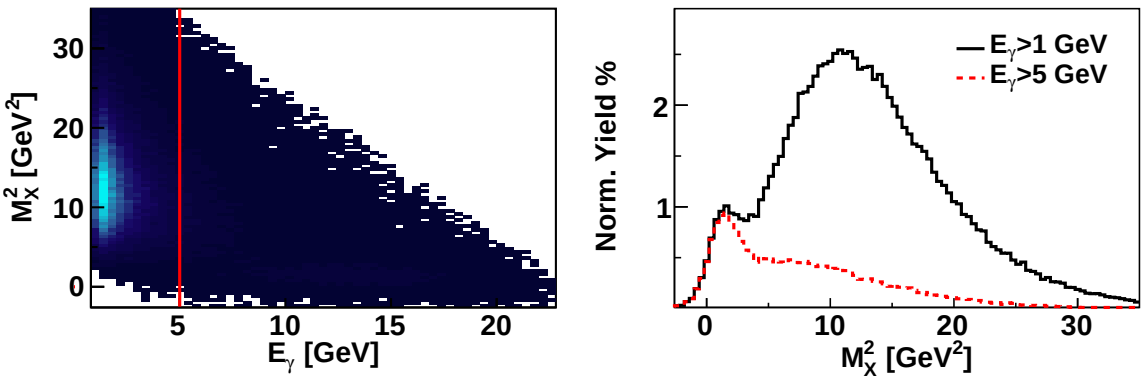

Figure 4.1: On the left side the squared missing mass distribution is shown as a function of the photon energy. The red dashed line visualizes the cut used in the analysis. On the right side the squared missing mass distribution for two different lower limits on the photon energy is given. The black curve is normalized to unity.

quantity	meaning	limits [cm]
$\lvert x_{\text{Calo}}\rvert$	The x–coordinate of the cluster position in the calorimeter.	$[0, 125]$
$\lvert y_{\text{Calo}}\rvert$	The y–coordinate of the cluster position in the calorimeter.	$[33, 105]$

Table 4.2: The explicit requirements on the position of the photon clusters on the calorimeter (Calo) surface.

A MC study with the latest geometry based on all alignment survey measurements performed gave an optimal value of $z = 729$ cm for photons.

4.2.3 Selection of exclusive events

A further reduction of events from other than the DVCS channels was possible by exploiting the angular information on the real photon with respect to the virtual photon. The opening angle $\theta_{\gamma^*\gamma}$ describes the radius of the circle around the hit position of the virtual photon in the calorimeter plane, on which the photon lies. For $\theta_{\gamma^*\gamma} = 0$ mrad no azimuthal angle ϕ can be defined. A lower limit on this quantity was needed because of the finite detector resolution and was chosen in [Kra05] as 5 mrad. The upper limit was constrained to 45 mrad for two reasons: The acceptance in ϕ depended on the magnitude of $\theta_{\gamma^*\gamma}$ as can be seen from figure 4.2. In addition, the background contribution increased with increasing $\theta_{\gamma^*\gamma}$ (see chapter 4.4.2).

The correlation between $\theta_{\gamma^*\gamma}$ and the squared momentum transfer to the proton t

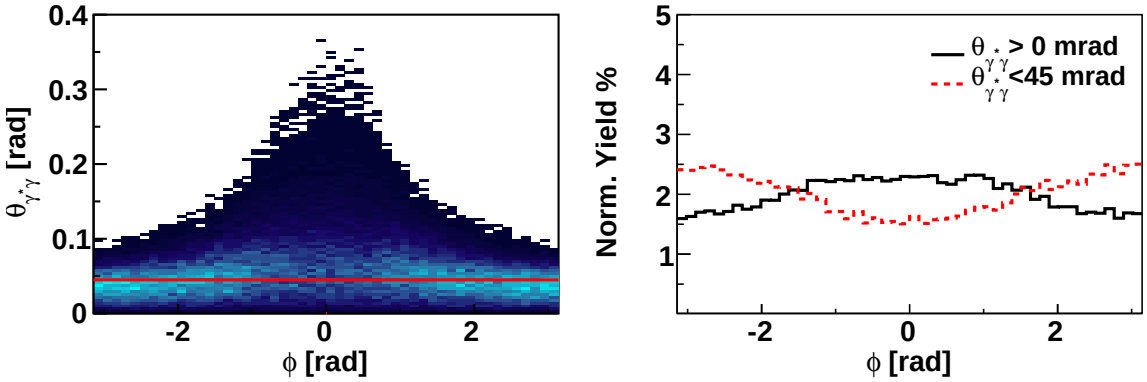

Figure 4.2: On the left side the $\theta_{\gamma^*\gamma}$–ϕ–distribution of single photon event candidates is plotted. The red dashed line represents the chosen cut. On the right side the normalized ϕ–distribution is shown, comparing all single photon events and those fulfilling the requirement $\theta_{\gamma^*\gamma} < 45$ mrad.

suggested an upper limit on the latter variable as well. This suited the requirement $|t| \ll Q^2$ of the DVCS factorization theorem.

The comparison of the extracted asymmetry moments as a function of t was one of the main goals of this analysis. The resolution of the variable t:

$$\begin{aligned} t &\equiv (q - q')^2 \\ &= -Q^2 - 2E_\gamma(\nu - \sqrt{\nu^2 + Q^2}\ \cos\ \theta_{\gamma^*\gamma}) \end{aligned} \tag{4.1}$$

suffered from the photon energy resolution, which is typically a few per cent. Assuming the elastic process (and hence $M_X = m_p$) t can be calculated without using the photon energy:

$$t_c = \frac{-Q^2 - 2\nu(\nu - \sqrt{\nu^2 + Q^2}\ \cos\ \theta_{\gamma^*\gamma})}{1 + \frac{1}{m_p}(\nu - \sqrt{\nu^2 + Q^2}\ \cos\ \theta_{\gamma^*\gamma})}. \tag{4.2}$$

This variable is usually called constrained t in the literature. Although this redefinition is only valid for the elastic process, the improvement in the resolution of t by one order of magnitude to about 0.01 GeV^2 in the full exclusive sample [Ell04] was decisive. However, the impact on the extracted asymmetry amplitudes will be difficult to judge: First, the calculation of the relative contributions of the associated process in different t–bins suffered from the introduction of the constrained variable. Second, the knowledge on the asymmetry amplitudes of the resonance processes is limited. The upper limit ($t < 0.7$ GeV^2) was finally set to the point, where the background contribution started to dominate the data sample. Here and in the following, t will stand for the constrained variable.

Finally, the allowed intervals in Q^2 and x_B were restricted to

$$\begin{aligned} 1\,\mathrm{GeV}^2 &< Q^2 < 10\,\mathrm{GeV}^2, \\ 0.03 &< x_B < 0.35. \end{aligned} \tag{4.3}$$

These requirements removed only very few outlying events (see, e.g. figure 4.4) and served to define the covered phase space. The remaining data sample after applying the discussed constraints is called ***single photon events*** in the HERMES jargon.

The best tool to further improve the exclusiveness of the data sample was found to be the missing mass technique. The squared missing four–momentum should be equal to the squared mass of the missing particle; in the studied process the mass of a undetected recoiling proton.

The squared missing mass is defined as

$$\begin{aligned} M_x^2 &= (q + p - q')^2 \\ &= m_p^2 + 2m_p(\nu - E_\gamma) + t. \end{aligned} \tag{4.4}$$

Thus also the missing mass resolution was limited by the resolution on the photon energy leading to a distribution reaching negative values (see figure 4.5). Therefore the missing mass was calculated according to:

$$M_X = \mathrm{sgn}(M_X^2) \cdot \sqrt{|M_X^2|}. \tag{4.5}$$

The selected range in the squared missing mass defined the final data sample, thus determining its exclusiveness. More detailed discussions on the choice of the cuts and their implications will be explained in the chapters 4.3.3 and 4.6.3. As a starting point the limits from the first published DVCS analysis were chosen:

$$-2.25\,\mathrm{GeV}^2 < M_X^2 < 2.89\,\mathrm{GeV}^2. \tag{4.6}$$

These cuts were obtained from a MC simulation that resulted in a resolution of $\delta M_X^2 = 1.840\,\mathrm{GeV}^2$ at a peak position of $1.502\,\mathrm{GeV}^2$ [Ely02]. This error was propagated according to:

$$\delta M_X = \frac{dM_X}{M_X^2} \cdot \delta M_X^2 = \frac{1}{2M_X} \cdot \delta M_X^2 = 0.8\,\mathrm{GeV}. \tag{4.7}$$

As the missing mass values of the background processes were larger compared to the elastic DVCS events, an asymmetric exclusive window $\left[m_p^2 - 3\sigma,\ m_p^2 + 1\sigma\right]$ was chosen around the squared proton mass. The events passing all described cuts will be called ***exclusive events*** in the following.

4.3 Studies based on real data

The cross section of the electro–production of real photons off an unpolarized target depends in a complicated form on the four kinematic variables x_B, Q^2, t and ϕ (compare chapter 2.3). This leads to acceptance holes in the azimuthal angle ϕ in the HERMES environment for certain regions in the other three variables.

The distribution of these three variables in the analyzed data is shown in figure 4.3 for the 2000 data. In the upper panel the correlation between the Bjorken scaling variable x_B and Q^2 in the HERMES acceptance is visible. There is no correlation between either of these two inclusive variables with t (lower two panels). All three variables show a steep fall–off towards higher absolute amplitudes.

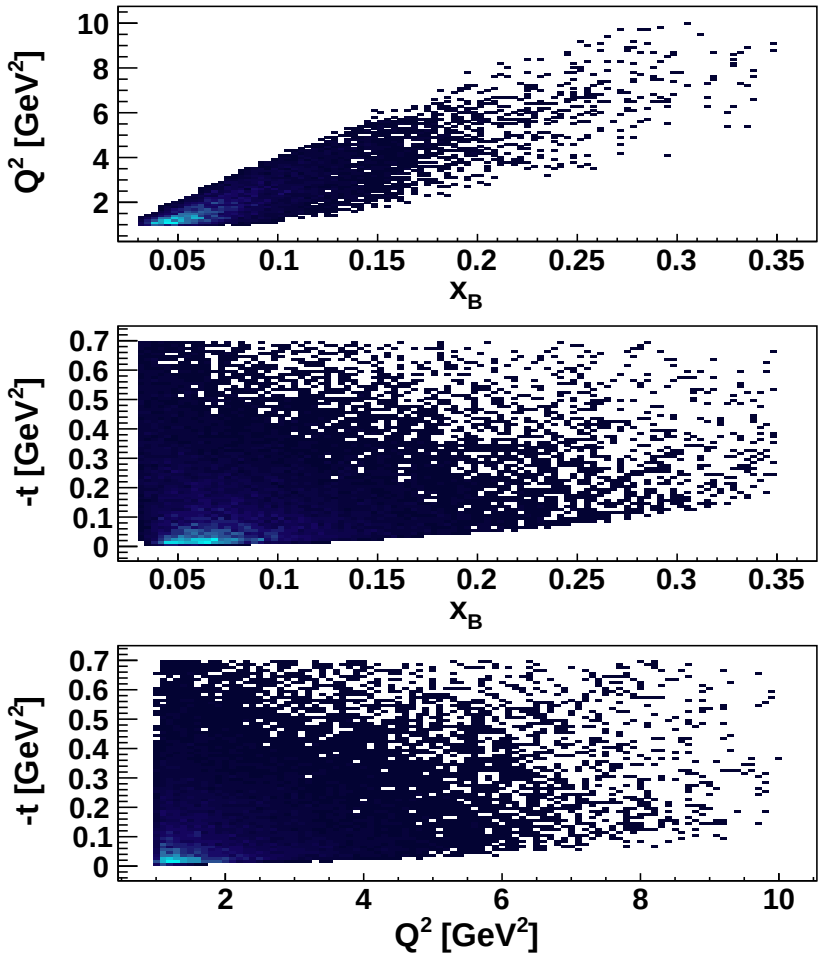

Figure 4.3: The phase space in the three kinematic variables x_B, Q^2 and t covered in the discussed analysis.

In the following sections consistency checks performed on the real data will be illustrated. Those studies include the cross–check between different analysors, the

Year	Target State	Beam Charge	Beam Helicity	$N_{\text{exclusive}}$	N_{DIS}	P_{Beam}
1996	unpolarized	+	+	1236	829628	50.15 %
1996	unpolarized	+	-	–	–	–
1996	polarized	+	+	563	366465	51.28 %
1996	polarized	+	-	–	–	–
1997	unpolarized	+	+	–	–	–
1997	unpolarized	+	-	1675	1168530	-52.48 %
1997	polarized	+	+	395	317888	49.68 %
1997	polarized	+	-	1680	1213566	-53.08 %
1998	unpolarized	-	+	–	–	–
1998	unpolarized	-	-	733	479389	-30.15 %
2000	unpolarized	+	+	2791	1887579	53.69 %
2000	unpolarized	+	-	4905	3187375	-55.03 %
2003	polarized	+	+	396	277064	32.15 %
2003	polarized	+	-	–	–	– %
2004	unpolarized	+	+	161	109725	33.86 %
2004	unpolarized	+	-	–	–	– %
2004	polarized	+	+	1794	1207353	32.56 %
2004	polarized	+	-	1433	928162	-40.27 %
2005	unpolarized	-	+	400	232497	21.09 %
2005	unpolarized	-	-	296	181052	-28.32 %
2005	polarized	-	+	2740	1748896	33.53 %
2005	polarized	-	-	3961	2466635	-28.52 %

Table 4.3: The numbers for DIS and exclusive events split into each data year and target state. The averaged beam polarizations values are also given.

comparison of different data productions and efficiency checks.

4.3.1 Cross–check

At HERMES, each result needs to be analyzed in parallel from two independent co–workers. The cross–check was performed on different stages of the analysis. First, the numbers of extracted events in the various introduced categories like DIS or exclusive events were compared. The agreement was perfect on the exclusive level and better than 0.05 % on the DIS level. The explicit numbers are compiled in table 4.3. Note, that in some years only data for one helicity state was collected. The accumulated luminosity for the electron (positron) beam was 106 (292) pb^{-1}. For both beam charge states less data was taken with positive beam helicity which made a beam helicity balancing essential in the extraction of beam–helicity dependent asymmetries.

In this table all data productions included in the analysis are explicitly mentioned, disentangled for different target polarization, beam charge and beam helicity states. From the DVCS analysis point of view the data can be divided into two periods:

Before and after 1998, when the RICH detector was installed. In each period the beam charge was changed once. The main data samples for the positive (negative) beam charge were collected in 2000 (2005). The magnitude of the longitudinal beam polarization was higher for the positron compared to the electron data sample.

In this analysis data taken with an unpolarized, a longitudinally and transversely polarized hydrogen target were combined. The target polarization values for the latter two are not stated, as the spin orientation of the longitudinal (transverse) polarized target was flipped in periods of 60 (90) s resulting in an effectively unpolarized target polarization. Thus also no systematic errors were calculated for possible occurring double spin asymmetries.

The second step of the cross–check was performed on the asymmetry level. Again the results agreed within the per–mille level for each extracted data point [ZL08].

4.3.2 Year–by–year data comparison

During the years 1996 until 2005 many detector components were replaced, removed or added. This made it essential to compare the performance from different years and productions. In addition, possible effects from the target magnet had to be considered.

Therefore the year–by–year distributions in different kinematic variables have been compared. An example is shown in figure 4.4 comparing the yields in Q^2 and x_B between the years 2000 and 2005. Apart from a small discrepany at very low x_B the distributions agree very well. In addition a small slope in the y–distribution was found [ZL08]. These discrepancies occur mainly between data samples taken with different beam charges. A new track reconstruction is being developed including the latest knowledge on the beam and detector positions and is hoped to solve the differences. Apart from that the other yields matched very well, independent of the target state.

In the DVCS analysis the number of DIS events is only used for the normalization. In order to study the impact of the slopes in the ratios of different data sets on this analysis, also the yields of the exclusive variable t (M_X^2) has been compared for different data samples. This study has been performed on single photon events. Again, as in the DIS case, several pairs of data years have been studied. All t–distributions seem to be flat within the statistical fluctuations (see figure 4.5). However, in the same figure a shift in the exclusive region of the missing mass distribution between the positron data from 2000 and the electron data from 2005 is visible. Again this deviation only occurs between data sets taken with different beam charge. An additional slight discrepancy between the years before and after 1998 can be related to the influence of the RICH detector. The reason for the observed deviations will be discussed in the next section along with the treatment of the effect in the present analysis.

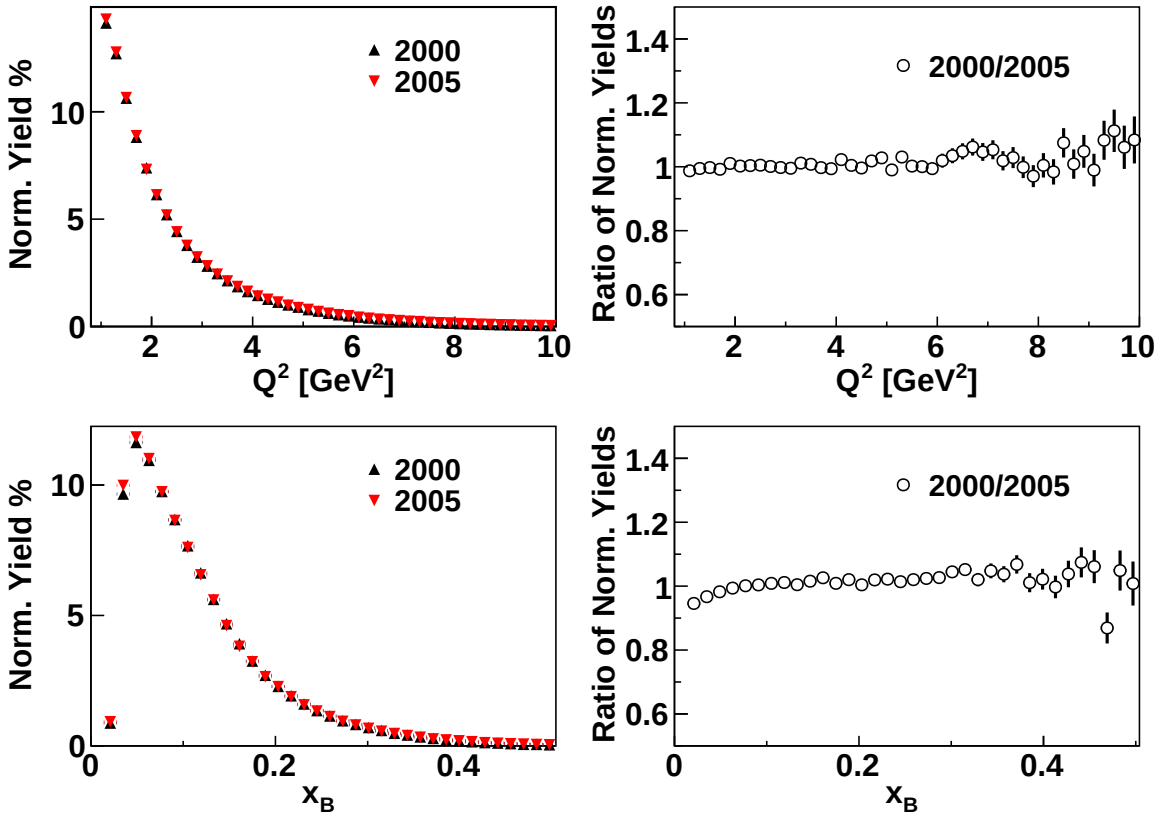

Figure 4.4: The left upper (lower) plot compares the normalized yields of DIS events in Q^2 (x_B) for the unpolarized data set from the year 2000 (black triangles) and the polarized one from 2005 (red triangles). The plots on the right show the ratio of these normalized data sets.

4.3.3 Calorimeter calibration and the missing mass shift

The missing mass is the only remaining variable, where the photon energy enters after making the choice of using the constrained Mandelstam variable t. Thus the observed shift was evaluated with respect to the calorimeter calibration.

The calibration of the calorimeter is based on the ratio between the energy measurement in the calorimeter and the momentum obtained from the bending in the magnetic field for leptons [A$^+$98b]. This quantity is shown on the left side in figure 4.6 for all DIS positrons from the data of the year 2000. A fit with the sum of a Gaussian function and a first order polynomial resulted in a peak position with a small offset of 0.1 % from unity (and a width of 4.8 %).

On the right side of the figure the same ratio is given as a function of the positrons' momentum. In each bin the distribution was fit with the above described function and the position of the Gaussian is given by the red points. The correction worked for the whole momentum range with a deviation from unity of less than 1 %. The same behavior was found for the largest electron data sample from the year 2005.

Even though the calibration for leptons worked stable, the photon energy recon-

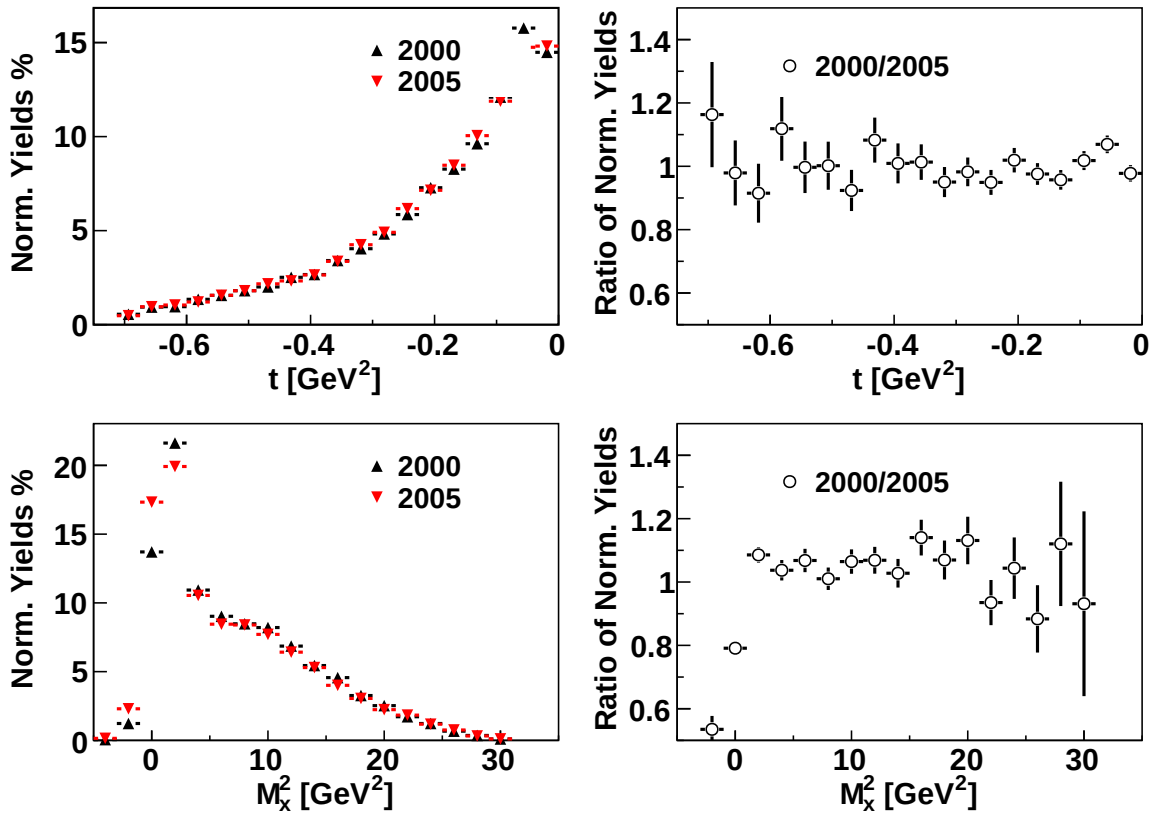

Figure 4.5: The left upper (lower) plot compares the normalized yields of single photon events in t (M_X^2) for the polarized data set from the year 2005 (black triangles) and the unpolarized one from 2000 (red triangles). The plots on the right show the ratio of these normalized data sets.

struction can be off. The energy of photons not showering in the preshower detector are known to be miscalibrated and the corresponding events were therefore suppressed by the requirement on the preshower energy deposit (see section 4.2.2). An offset in the remaining photon sample can explain the missing mass shift. In this analysis it was decided to apply a correction on the final data selection instead of correcting the photon energy reconstruction. Therefore the data has been split into four periods, dividing into electron and positron data on the one hand and before and after 1998 on the other hand. This has two reasons: Firstly, the RICH that degraded the momentum resolution of the DIS lepton has been installed before the 1998 data taking. Secondly, the two electron data years 1998 and 2005 are separated by a long time with one major access to the experiment in 2000/2001.

For these four data sets, the mean of the distribution of the DVCS events has been calculated in the window between $-2.25\ \text{GeV}^2 < M_x^2 < 2.89\ \text{GeV}^2$ (see table 4.4). The lower limit is displaced from the squared proton mass by three times the resolution

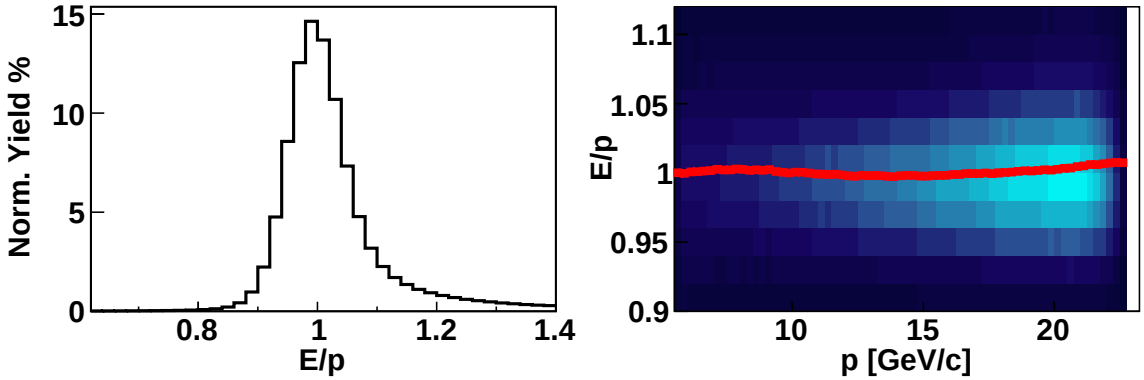

Figure 4.6: On the left side the energy obtained from the calorimeter is compared to the momentum calculated from the bending in the magnetic field. On the right side the same ratio is plotted versus the momentum. The red points show the mean of a bin–wise fit to the data. All DIS leptons from the 2000 data were used to extract the plots.

Data Sample	Mean [GeV^2]	Shift [GeV^2]	Window [GeV^2]
run1 e^+ (1996-1997)	1.17	0.02	$[-2.08, 2.81]$
run1 e^- (1998)	0.88	-0.27	$[-2.52, 2.62]$
run2 e^+ (2000-2004)	1.15	0.0	$[-2.25, 2.89]$
run2 e^- (2005)	0.93	-0.22	$[-2.47, 2.67]$

Table 4.4: The mean values for the Missing Mass distributions in the window between -2.25 GeV$^2 < M_X^2 < 2.89$ GeV^2 for the different data samples.

in M_X^2 of 0.8 GeV^2, whereas the upper limit is displaced by one time the missing mass resolution. Then the missing mass window has been shifted by the difference in the mean. For the data sets taken before the installation of the RICH, the width of the exclusive peak in the missing mass distribution is decreased by approximately 5 %. Therefore the width of the window for these data sets has been decreased accordingly. The final windows for all data samples are again summarized in table 4.4.

The final statistics with the shifted missing mass windows are given in table 4.5 for the different beam charge and helicity states. In total about 25000 exclusive events were identified. The electron data sample is smaller in statistics and its mean beam polarization.

The effect of the shift in the missing mass and the assigned systematics will be discussed on the asymmetry level in chapter 4.6.3.

Beam Charge	Beam Helicity	P_{Beam}	N_{DVCS}	N_{DIS}
+1	+1	45.93 %	7291	4995703
+1	−1	-52.10 %	9628	6497633
−1	+1	32.07 %	3132	1981393
−1	−1	-28.76 %	4802	3127076
+1	0	-9.49 %	16919	11493336
−1	0	-5.16 %	7934	5108469
0	+1	42.00 %	10423	6977096
0	−1	-44.52 %	14430	9624709

Table 4.5: The final statistics after applying the shift in the missing mass.

4.3.4 Efficiencies

Inefficiencies in either the tracking or the trigger system can lead to false asymmetries (see chapter 4.5.2). In order to estimate the impact of possible inefficiencies their magnitudes have to be determined.

The distribution of the tracking efficiencies of the FCs and BCs are shown in figure 4.7 for each detector half separately. The plots include all analyzed data samples. The mean efficiency values deviated only minimal from unity. Only in the data sets from 2004 some problems with the FCs have occurred, but were shown to have a negligible impact on the differential cross section distributions in [Zei05].

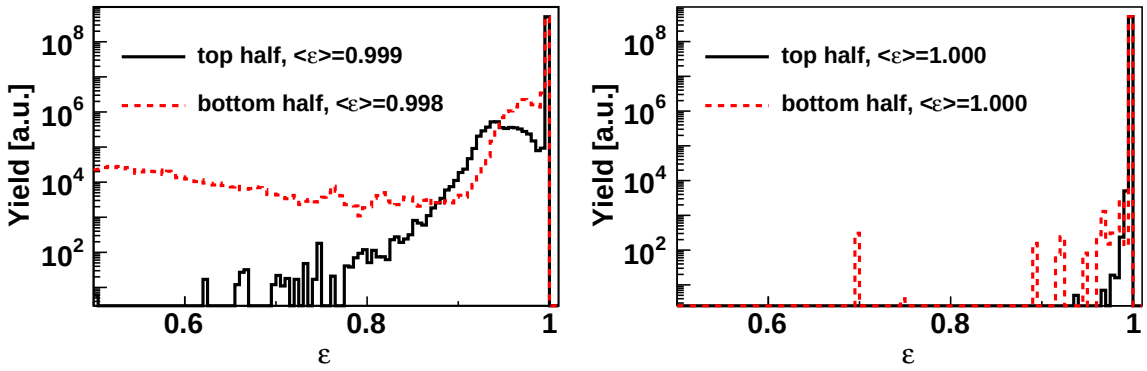

Figure 4.7: The distributions in the tracking efficiencies of the FCs (BCs) on the left (right) plot. The results were split up for the upper (black line) and lower (red dashed line) detector halves.

The used trigger 21 required a hit in the three hodoscopes H0, H1 and H2 along with a hit in the calorimeter. Therefore its efficiency was deduced from [dN01]

$$\varepsilon_{\text{Trigger 21}} = \varepsilon_{\text{H0}} \cdot \varepsilon_{\text{H1}} \cdot \varepsilon_{\text{H2}} \cdot \varepsilon_{\text{Calo}}. \tag{4.8}$$

The efficiencies of the single detector components were deduced from comparing different triggers. In case of the H0 hodoscope it was deduced from the comparison of trigger 21 and 18 events, because the latter required the same hit pattern except for a hit in H0

$$\varepsilon_{\mathrm{H0}} = \frac{N_{21\wedge 18}}{N_{18}}. \tag{4.9}$$

The other detectors entering in trigger 21 were found to be very efficient throughout the data taking [Gab08] and were not studied in further detail in the present work.

The hodoscope efficiency was studied as a function of lepton momentum and point of incident on the hodoscope surface. The lepton sample for the momentum dependent plots (see figure 4.8) was selected by only using the cut on the combined PID as introduced in chapter 4.2.1. The efficiency in the considered momentum range was higher than 99 % with a relative fluctuation of below 0.4 % for the complete data sample (left plot), thus ensuring a bias–free extraction of the asymmetry moments in the whole covered phase space. In the right panel the efficiency for the 2000 data sample is shown, which was known to have a less efficient region in the upper half of the hodoscope (see figure 4.9). This was not reflected in a less efficient range in the momentum spectrum.

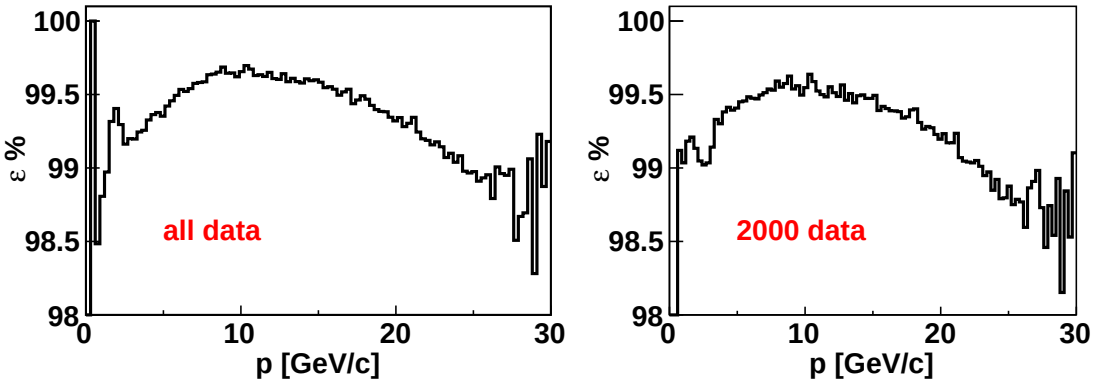

Figure 4.8: The efficiencies of the H0 hodoscope versus the momentum of the considered lepton tracks. On the left (right) panel for all analyzed (only 2000) data.

The efficiency as a function of the incident point on the hodoscope surface is shown in figure 4.9 for different data samples. The surface was subdivided into a grid with quadratic cells of 4 cm side length.

The trigger efficiency was very stable and well above 99 % as can be seen from the left upper plot. Especially in the region with high statistics ($|x_{\mathrm{H0}}| < 12$ cm $\wedge$ $|y_{\mathrm{H0}}| < 12$ cm) the fluctuations were small. In the same figure the efficiencies were split up for all analyzed data years always using the target state sample with the largest statistics. The most severe problems occurred in the year 1998 (second panel on the right), where the efficiencies in the lower half went down to around 95 % in certain bins. In the

year 2000 a small discrepany between the upper and lower detector half is visible. The effect of the observed inefficiencies was studied and the results will be given in chapter 4.6.2.

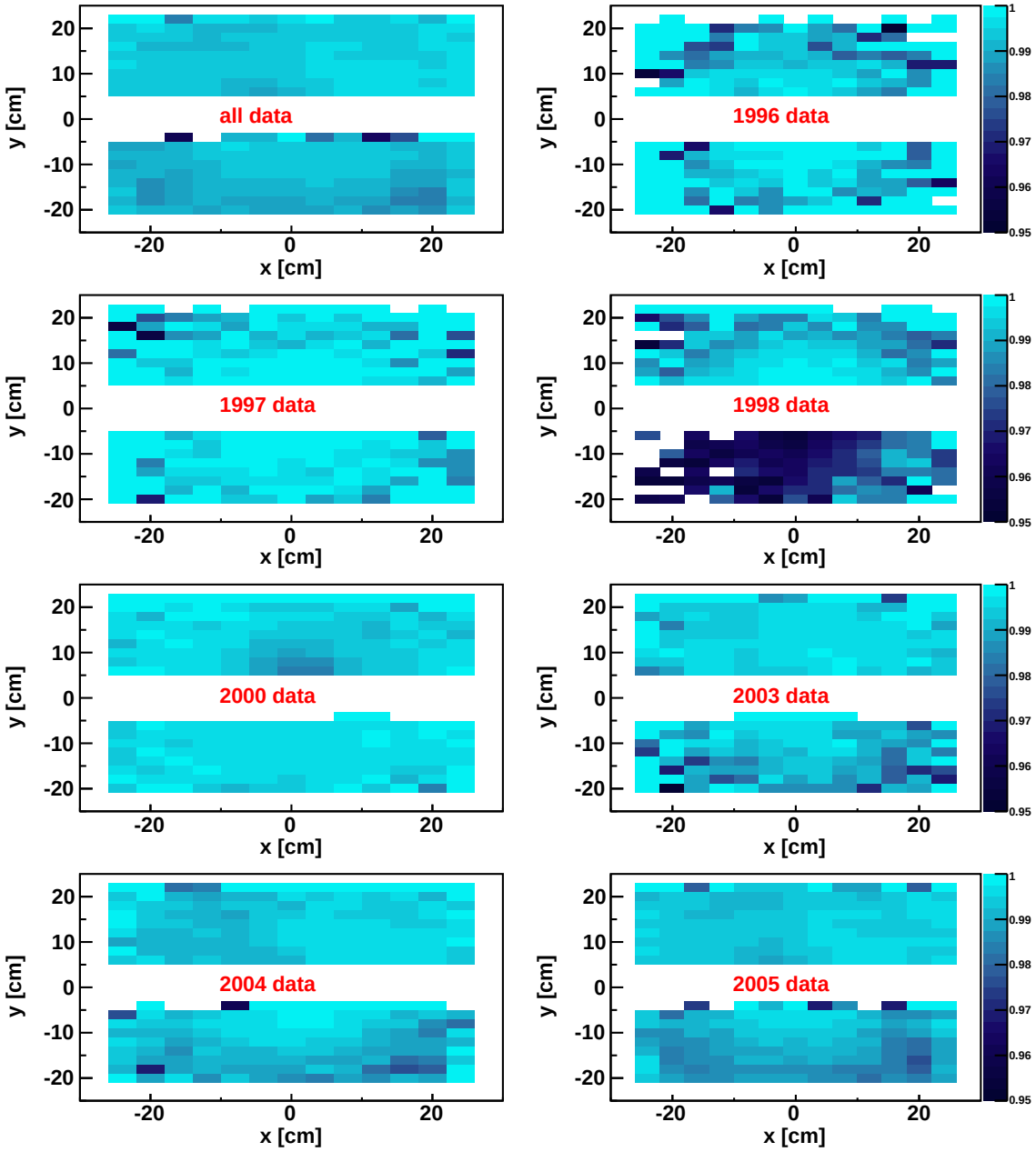

Figure 4.9: The efficiencies of the H0 hodoscope versus the hit position on the surface of the detector. The different panels show different data samples as labeled in red.

4.4 MC studies

Monte Carlo simulations are a powerful tool to understand detector responses, to verify results from physics analyzes and to apply corrections on them. In the presented analysis four different event generators were used, which will be introduced in the following section. The comparison with the results on distributions of kinematic variables will be subject of section 4.4.2, while the detector resolutions will be studied in section 4.4.3. The estimation of the background fractions and the smearing and acceptance effects will be explained in the section about systematic uncertainties.

4.4.1 MC generators

For this work two event generators were used to simulate the DVCS process, namely GMC_DVCS and GMC_DUAL. To model the main background processes two additional generators were used: GMC_DISNG to simulate the semi-inclusive production of neutral mesons and GMC_EXCLPION for the exclusive production of neutral pions.

The GMC_DVCS generator is capable of simulating the elastic BH and DVCS process and the associated BH process. The GPDs parameterization is taken from reference [VGG99] as explained in section 2.4.2. Within this formalism five model variants were included, which had been suggested in [KN02]:

- The three GPDs $\mathcal{H}, \tilde{\mathcal{H}}$ and $\mathcal{E}$ were not skewed, but factorized in x and t.
- The GPDs were skewed within the double distribution ansatz [Rad99] and the t–dependence was factorized. The slope parameter b was chosen to be 1.
- The same as the previous variant with the b–parameter set to 3.
- Again the double distributions ansatz was used expanded by a D-term [GPV01] and the t–dependence was factorized. The slope parameter b was chosen to be 1.
- The same as the previous variant with the b–parameter set to 3.

The cross section for the elastic and associated BH process is obtained from reference [MT69], while the transition form factors were taken from [Duf68]. Alternatively the resonance region can be modelled using the Brasse parameterization [B$^+$76] for the differential cross section in W, which yields better results [Kra05] and was consequently used in this analysis. Making use of a Rosenbluth separation the single meson production channels were obtained from the MAID model [DHKT99].

The GMC_DUAL generator included the elastic BH/DVCS cross section based on the dual parameterization GPD model of reference [GT06] and is shortly outlined in section 2.4.3. This ansatz assumes that the BH/DVCS scattering amplitude in the s–channel can be represented as an infinite sum of t-channel resonances [PS02]. The D–term is contained in this model. The t–dependence of the GPD H was either included in a Regge inspired or a factorized ansatz. The associated process was not implemented into the generator.

The GMC_DISNG event generator is based on LEPTO [IER97], a framework simulating leptonic DIS processes off unpolarized nucleons. The fragmentation and decay of the produced hadrons is modelled with JETSET [Sjo95], which uses the LUND string hadronization model [AGIS83] and was tuned to HERMES kinematics [Hil05]. Even though the BH process was simulated in GMC_DISNG, the standard resonance parameterization resulted in a mismatch in reproducing the missing mass distribution of the HERMES data [Kra05]. It was found that using a different parameterization option ('RESO'), the agreement improved.

The GMC_EXCLPION generator bases also on the GPD model developed in reference [VGG99]. In this analysis it was solely used to obtain the fractional contributions of the exclusive production of neutral pions, which were found to be very small.

Note that in the used MC productions the modelling of the calorimeter output was questionable. Therefore the reconstructed photon energy E_γ was taken from the calorimeter resolution obtained in a test beam experiment [A$^+$98b]

$$\frac{\sigma(E_\gamma)}{E_\gamma}\,\% = \frac{5.1 \pm 1.1}{\sqrt{E_\gamma(\mathrm{GeV})}} + (2.0 \pm 0.5) + \frac{10.0 \pm 2.0}{E_\gamma(\mathrm{GeV})}. \tag{4.10}$$

4.4.2 Data–MC–comparison

For the comparison between MC and HERMES data the output from the different generators were combined. It was decided to take both the elastic and associated BH process from the GMC_DVCS generator, as the latter process was modelled more thoroughly in it. For the comparison the DVCS processes were not included as they are subject to uncertainties because of their model dependence. The normalization with respect to the data was ensured by comparing the weighted number of DIS events from GMC_DVCS with the number of DIS events in the data.

In figure 4.10 the reconstructed MC yields of eight different kinematic variables are shown together with the corresponding data yields. The distributions in the upper three rows agree very well. Only the exclusive peak in the squared missing mass spectrum was overestimated by around 7 % in the MC and the semi–inclusive region was underestimated. A possible explanation might be missing radiative effects in the MC simulation, which would move events out of the exclusive peak into the semi–inclusive region. However, adding the weight of the DVCS process would further increase the exclusive peak.

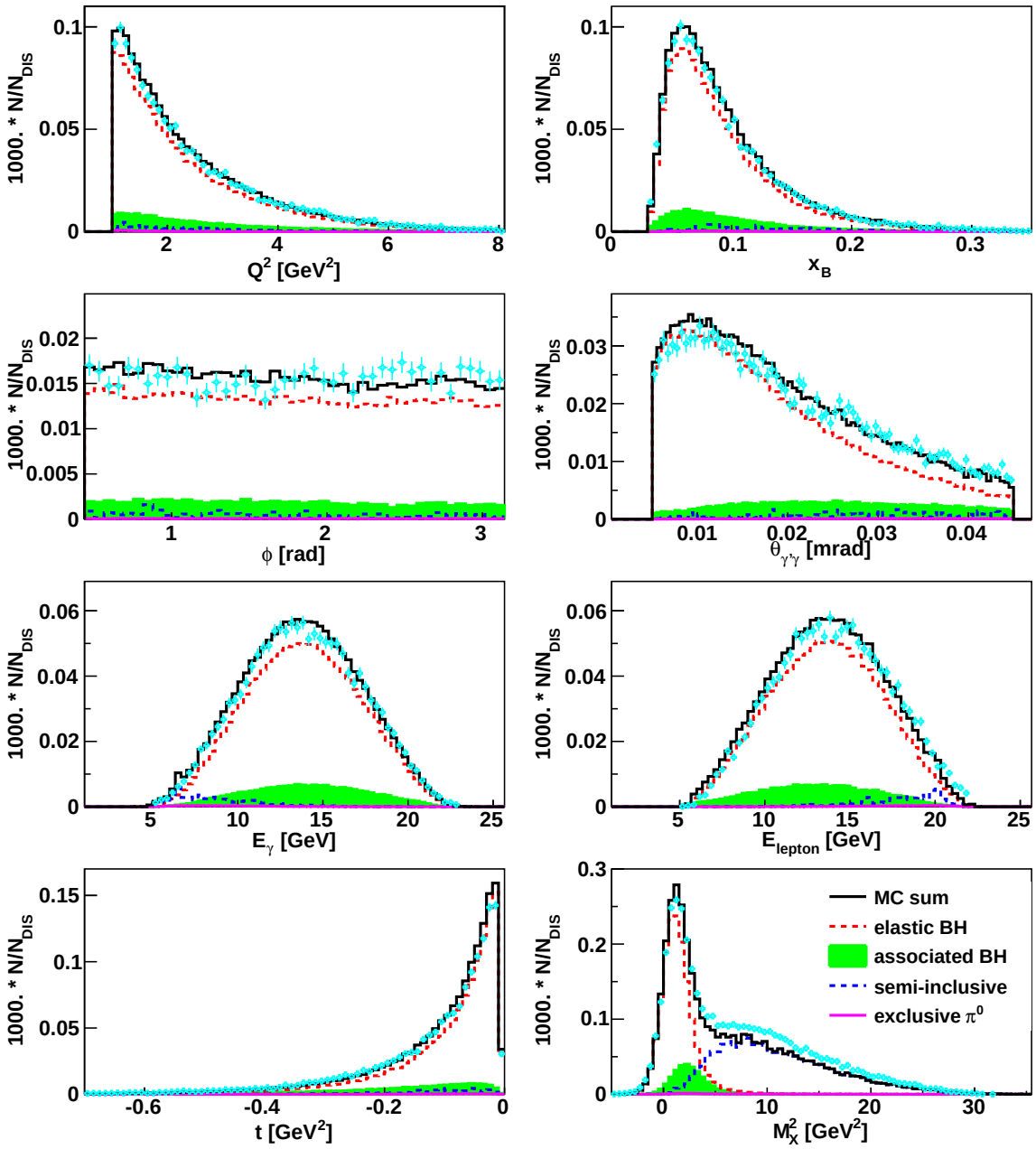

Figure 4.10: The comparison of MC (black line) and data (light blue points) in several kinematic variables. The MC contributions are split up into the underlying physics processes (see labeling in the lower right panel).

4.4.3 Kinematic resolutions and choice of binning

Compared to previous DVCS results published by the HERMES experiment [A$^+$01, A$^+$07a, A$^+$08c] more statistics was available for this analysis (see table 4.5). Hence the resolution in the three kinematic variables t, x_B and Q^2 was studied to check if a finer binning of the finally extracted asymmetry amplitudes was possible. Elastic DVCS/BH events from a GMC_DVCS MC production were used including the actual values for the beam positions, detector misalignment and the transverse magnet. In the reconstruction the target magnet correction algorithm was made use of.

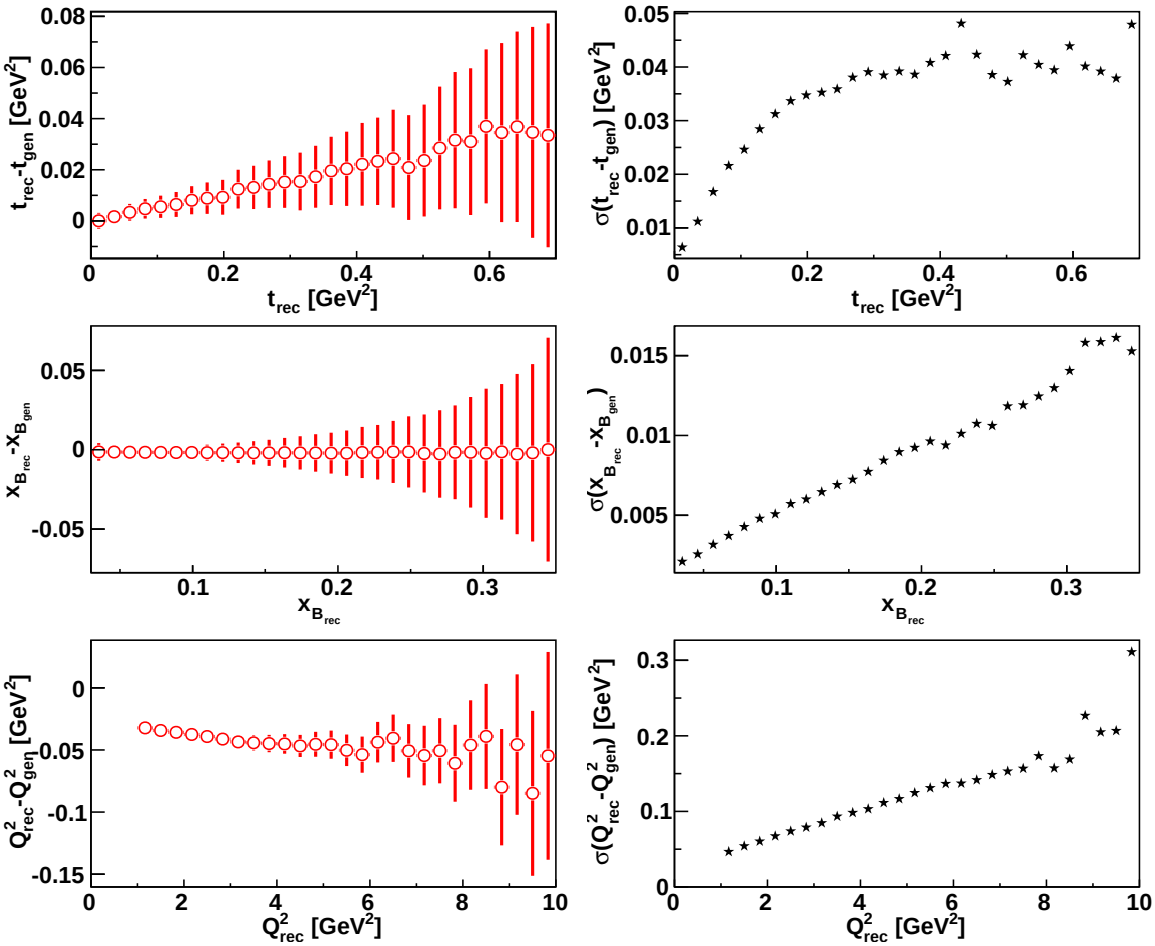

Figure 4.11: On the left side the deviations from the reconstructed variables t, x_B and Q^2 with respect to the generated ones are shown. On the right side the resolutions of the same variables are plotted.

In the left column of figure 4.11 the difference between reconstructed and generated variables are shown versus the reconstructed quantity. Generally all deviation are small, while they increase with increasing $-t$ and Q^2. On the right side of the same figure the corresponding resolutions are drawn. The resolutions are becoming

$-t$ [GeV^2]	x_B	Q^2 [GeV^2]
0.00 – 0.06	0.03 – 0.07	1.0 – 1.5
0.06 – 0.14	0.07 – 0.10	1.5 – 2.3
0.14 – 0.30	0.10 – 0.15	2.3 – 3.5
0.30 – 0.70	0.15 – 0.35	3.5 – 10.

Table 4.6: The binning used in former HERMES DVCS analysis [A$^+$01, A$^+$07a, A$^+$08c].

$-t$ [GeV^2]	x_B	Q^2 [GeV^2]
0.00 – 0.03	0.03 – 0.06	1.0 – 1.4
0.03 – 0.06	0.06 – 0.08	1.4 – 1.8
0.06 – 0.10	0.08 – 0.10	1.8 – 2.4
0.10 – 0.20	0.10 – 0.13	2.4 – 3.2
0.20 – 0.35	0.13 – 0.20	3.2 – 4.5
0.35 – 0.70	0.20 – 0.35	4.5 – 10.

Table 4.7: The new binning used in this analysis.

worse with increasing magnitude of the considered kinematic variables. Though the obtained resolutions allow for a finer binning in all three variables, the statistics are also decreasing with the magnitudes (except for the low x_B region; see the yields in figure 4.10).

The binning used in the previous HERMES DVCS publications is listed in table 4.6. The new binning is summarized in table 4.7. Especially the low–t region is theoretically very interesting due to the Ji relation (see section 2.4.1). Therefore the first t–bin was split into two. Apart from that it was ensured that the bin widths were bigger than the respective resolutions, while the statistics in each bin were kept similar. Only the highest bins in the three variables showed a significantly lower number of events.

4.5 Extraction of azimuthal amplitudes

In the present analysis the asymmetries were extracted using the **M**aximum **L**ikelihood (ML) technique. Although this fitting method is very well known in high–energy physics [A$^+$08d], it turned out to be difficult to judge which variant could be employed best in this analysis. Therefore this section gives a more general introduction to the method and its variants, and an explanation for the taken choice in the analysis.

4.5.1 Choice of the ML fitting method

The likelihood function L for a set of N independently measured data points x_i is defined as the product of the **P**robability **D**ensity **F**unctions (PDF) $f(x_i;\vartheta)$ depending on a set of unknown parameters ϑ:

$$L(\vartheta) \equiv \prod_{i=1}^{N} f(x_i;\vartheta). \tag{4.11}$$

The apriori unknown values of the parameter set ϑ_j are determined by maximizing the likelihood function (or equivalently by minimizing the negative logarithm of the likelihood function), e.g. finding those n values for the parameter set that best describe the data points. This is usually achieved by solving the likelihood equations for the logarithm of the likelihood function

$$\frac{\partial \ln L}{\partial \vartheta_j} = 0\ , \quad \text{with } j = 1, ..., n. \tag{4.12}$$

Any normalizations factors depending on ϑ need to be included in the PDFs, while additional factors may be omitted even if they depend on the data.

The PDF is normalized to unity in the standard ML method:

$$\int f(x;\vartheta)dx = 1. \tag{4.13}$$

In the so–called **E**xtended **M**aximum **L**ikelihood (EML) method the normalization of the PDF is unconstrained [Bar90].

$$\int F(x;\vartheta)dx = \mathfrak{N}(\vartheta), \tag{4.14}$$

where the new PDF is related to the standard one via the normalization

$$F(x;\vartheta) \equiv \mathfrak{N}\ f(x;\vartheta). \tag{4.15}$$

$\mathfrak{N}$ is the expected total number of events, which can differ from the observed number of events due to the nature of statistical measurements. The new likelihood function is given as

$$L = e^{-\mathfrak{N}} \prod_{i=1}^{N} F(x_i;\vartheta). \tag{4.16}$$

Thus, the logarithm can be derived to be

$$-\ln L = \mathfrak{N} - \sum_{i=1}^{N} F(x_i). \tag{4.17}$$

The advantage of the ML technique compared to a least–square fit is that it does not need a binned distribution, which is important in low–statistics analyzes. On the other side the ML method does not offer an easy goodness–of–fit test. One way to avoid this disadvantage is to perform the ML fit on a binned data sample [A$^+$08d].

Following the argument of Ref. [Bar90], the EML method was adopted for the described analysis, where the observed number of events is a consequence of experimental constraints (in luminosity, time, ...). In data studies, the EML method was shown to yield consistent results with a least–square method, while the standard ML method overestimated the uncertainty for a constant term included in the fit function [LY07]. In a MC study, the EML method gave better results compared to a least–square fit in reconstructing known input asymmetries, both for a small number of bins with a large number of events and for a limited data sample with (almost) empty bins [Ye07].

4.5.2 Application of the EML method to the DVCS analysis

In this analysis data taken with both beam charges and beam helicity states were merged and thus it was possible to access three different asymmetries simultaneously. The PDF for the EML method can be parameterized as follows:

$$\begin{aligned} &\mathcal{N}(e_\ell, P_\ell, \phi; \eta_{\mathrm{LU}}^{\mathrm{DVCS}}, \eta_{\mathrm{LU}}^{I}, \eta_{\mathrm{C}}) = \mathcal{L}(e_\ell, P_\ell)\, \epsilon(e_\ell, P_\ell, \phi)\, \sigma_{\mathrm{UU}}(\phi) \times \\ &\left[1 + P_\ell\, \mathcal{A}_{\mathrm{LU}}^{\mathrm{DVCS}}(\phi; \eta_{\mathrm{LU}}^{\mathrm{DVCS}}) + e_\ell P_\ell\, \mathcal{A}_{\mathrm{LU}}^{\mathrm{I}}(\phi; \eta_{\mathrm{LU}}^{I}) + e_\ell\, \mathcal{A}_{\mathrm{C}}(\phi; \eta_{\mathrm{C}})\right], \end{aligned} \tag{4.18}$$

where $\mathcal{L}$ is the integrated luminosity, ϵ the detection efficiency, and σ_{UU} the cross section for an unpolarized target averaged over both beam charges:

$$\begin{aligned} \sigma_{\mathrm{UU}}(\phi) \;\equiv\; & \frac{x_{\mathrm{B}} y^2}{32(2\pi)^4 Q^4} \frac{1}{\sqrt{1+\varepsilon^2}} \times \\ & \left[\frac{K_{\mathrm{BH}}}{\mathcal{P}_1(\phi)\mathcal{P}_2(\phi)} \sum_{n=0}^{2} c_n^{\mathrm{BH}} \cos(n\phi) + K_{\mathrm{DVCS}} \sum_{n=0}^{2} c_n^{\mathrm{DVCS}} \cos(n\phi)\right]. \end{aligned} \tag{4.19}$$

The estimators $\eta_{\mathrm{LU}}^{\mathrm{DVCS}}, \eta_{\mathrm{LU}}^{I}$ and η_{C} represent the sets of Fourier amplitudes decomposing the asymmetries $\mathcal{A}_{\mathrm{LU}}^{\mathrm{DVCS}}, \mathcal{A}_{\mathrm{LU}}^{\mathrm{I}}$ and $\mathcal{A}_{\mathrm{C}}$ in the azimuthal angle ϕ as defined in Eqs. 2.50-2.56. The choice of the fit function will be discussed in the chapter 4.6.1. The charge–averaged beam helicity asymmetry $\mathcal{A}_{\mathrm{LU}}^{\mathrm{DVCS}}$ originates from the squared DVCS amplitude and is calculated from the data set with a longitudinally polarized beam off an unpolarized target (LU). In contrast the charge–averaged beam helicity $\mathcal{A}_{\mathrm{LU}}^{\mathrm{I}}$ and the beam charge asymmetries $\mathcal{A}_{\mathrm{C}}$ result from the interference term and are calculated for either the two beam helicity or beam charge states (LU, C).

The corresponding negative logarithm of the likelihood function is given by

$$
\begin{aligned}
&-\ln L(e_\ell, P_\ell, \phi; \eta_{\mathrm{LU}}^{\mathrm{DVCS}}, \eta_{\mathrm{LU}}^{I}, \eta_{\mathrm{C}}) = \\
&-\sum_{i}^{N} \ln\Big[1 + P_\ell\, \mathcal{A}_{\mathrm{LU}}^{\mathrm{DVCS}}(\phi; \eta_{\mathrm{LU}}^{\mathrm{DVCS}}) + e_\ell P_\ell\, \mathcal{A}_{\mathrm{LU}}^{\mathrm{I}}(\phi; \eta_{\mathrm{LU}}^{I}) + e_\ell\, \mathcal{A}_{\mathrm{C}}(\phi; \eta_{\mathrm{C}})\Big] \\
&\qquad\qquad + \mathfrak{N}(e_\ell, P_\ell, \phi; \eta_{\mathrm{LU}}^{\mathrm{DVCS}}, \eta_{\mathrm{LU}}^{I}, \eta_{\mathrm{C}}),
\end{aligned}
\tag{4.20}
$$

where the normalization is obtained by integrating (summing) over the experimental parameters to

$$
\begin{aligned}
&\mathfrak{N}(\eta_{\mathrm{LU}}^{\mathrm{DVCS}}, \eta_{\mathrm{LU}}^{I}, \eta_{\mathrm{C}}) = \sum_{i}^{N} K(e_\ell, P_\ell, \phi) \times \\
&\quad\Big[M_1 + M_2\, P_{\ell,i}\, \mathcal{A}_{\mathrm{LU}}^{\mathrm{DVCS}}(\phi_i; \eta_{\mathrm{LU}}^{\mathrm{DVCS}}) + M_3\, e_{\ell,i} P_{\ell,i}\, \mathcal{A}_{\mathrm{LU}}^{\mathrm{I}}(\phi_i; \eta_{\mathrm{LU}}^{I}) + M_4\, e_{\ell,i}\, \mathcal{A}_{\mathrm{C}}(\phi_i; \eta_{\mathrm{C}})\Big].
\end{aligned}
\tag{4.21}
$$

The new terms appearing in Eq 4.21 are defined individually for each beam charge and helicity state

$$
K(e_\ell, P_\ell, \phi) = \begin{cases}
\dfrac{1}{2} \dfrac{1}{\mathcal{L}^{\rightarrow+}\varepsilon^{\rightarrow+}(\phi)} \dfrac{1}{1 - \langle P_\ell^{\rightarrow+}\rangle(\phi)/\langle P_\ell^{\leftarrow+}\rangle(\phi)}\,, & (P_\ell > 0, e_\ell = +1), \\
\dfrac{1}{2} \dfrac{1}{\mathcal{L}^{\leftarrow+}\varepsilon^{\leftarrow+}(\phi)} \dfrac{1}{1 - \langle P_\ell^{\leftarrow+}\rangle(\phi)/\langle P_\ell^{\rightarrow+}\rangle(\phi)}\,, & (P_\ell < 0, e_\ell = +1), \\
\dfrac{1}{2} \dfrac{1}{\mathcal{L}^{\rightarrow-}\varepsilon^{\rightarrow-}(\phi)} \dfrac{1}{1 - \langle P_\ell^{\rightarrow-}\rangle(\phi)/\langle P_\ell^{\leftarrow-}\rangle(\phi)}\,, & (P_\ell > 0, e_\ell = -1), \\
\dfrac{1}{2} \dfrac{1}{\mathcal{L}^{\leftarrow-}\varepsilon^{\leftarrow-}(\phi)} \dfrac{1}{1 - \langle P_\ell^{\leftarrow-}\rangle(\phi)/\langle P_\ell^{\rightarrow-}\rangle(\phi)}\,, & (P_\ell < 0, e_\ell = -1),
\end{cases}
\tag{4.22}
$$

and

$$
\begin{aligned}
M_1(\phi) &= \mathcal{L}^{+}\varepsilon^{+}(\phi) + \mathcal{L}^{-}\varepsilon^{-}(\phi), \\
M_2(\phi) &= \mathcal{L}^{+}\varepsilon^{+}(\phi)\langle P_\ell^{+}\rangle(\phi) + \mathcal{L}^{-}\varepsilon^{-}(\phi)\langle P_\ell^{-}\rangle(\phi), \\
M_3(\phi) &= \mathcal{L}^{+}\varepsilon^{+}(\phi)\langle P_\ell^{+}\rangle(\phi) - \mathcal{L}^{-}\varepsilon^{-}(\phi)\langle P_\ell^{-}\rangle(\phi), \\
M_4(\phi) &= \mathcal{L}^{+}\varepsilon^{+}(\phi) - \mathcal{L}^{-}\varepsilon^{-}(\phi).
\end{aligned}
\tag{4.23}
$$

The superscripts $\rightarrow$ ($\leftarrow$) indicate that the respective quantity was integrated over the complete positive (negative) beam helicity data sample. The + (−) superscripts label quantities which were summed over the positive (negative) beam charge data sample. These weights were introduced to account for luminosity imbalances with respect to beam charge and polarization. No balancing procedure was required for the target polarization, as it was flipped rapidly. Note, that the quantities labeled with a subscript i are evaluated for each event separately. The minimization was accomplished using the MINUIT package [JR75] included within the ROOT framework [BR97].

4.6 Systematics

In this chapter the systematic studies performed within the present analysis will be described. They include choosing the sets of azimuthal amplitudes, studying the photon energy calibration, any experimental inefficiencies, background processes and smearing and acceptance effects.

4.6.1 Choice of the fit function

Due to the restricted acceptance of the HERMES experiment cross section ratios, e.g. asymmetries, in which acceptance effects cancel to a certain degree, are better observables compared to cross sections. However, the extractable asymmetries as defined in Eqs. 2.50–2.56 exhibit dependencies on the azimuthal angle ϕ both in the numerator and the denominator. Thus the choice of the fit function is essential for a physical interpretation of the results in terms of the Fourier coefficients decomposing the involved process amplitudes.

The following decompositions include all ϕ–modulations appearing in the numerator and additional terms to describe the impact of the denominator in Eqs. 2.50–2.56:

$$\mathcal{A}_{\mathrm{LU}}^{\mathrm{DVCS}}(\phi;\eta_{\mathrm{LU}}^{\mathrm{DVCS}}) = \sum_{n=1}^{2} A_{\mathrm{LU,DVCS}}^{\sin(n\phi)} \sin(n\phi) + \sum_{n=0}^{1} A_{\mathrm{LU,DVCS}}^{\cos(n\phi)} \cos(n\phi), \tag{4.24}$$

$$\mathcal{A}_{\mathrm{LU}}^{\mathrm{I}}(\phi;\eta_{\mathrm{LU}}^{I}) = \sum_{n=1}^{2} A_{\mathrm{LU,I}}^{\sin(n\phi)} \sin(n\phi) + \sum_{n=0}^{1} A_{\mathrm{LU,I}}^{\cos(n\phi)} \cos(n\phi), \tag{4.25}$$

$$\mathcal{A}_{\mathrm{C}}(\phi;\eta_{\mathrm{C}}) = \sum_{n=0}^{3} A_{\mathrm{C}}^{\cos(n\phi)} \cos(n\phi) + A_{\mathrm{C}}^{\sin(\phi)} \sin(\phi). \tag{4.26}$$

The 13 coefficients of these functions are called 'azimuthal asymmetry amplitudes' and must not be identified with the Fourier coefficients in the decomposition of the process amplitudes. The asymmetry amplitudes $A_{\mathrm{LU,I}}^{\cos(0\phi)}$, $A_{\mathrm{LU,I}}^{\sin(\phi)}$ and $A_{\mathrm{C}}^{\cos(\phi)}$ relate to the twist–two coefficients defined in equations 2.53, 2.59 and 2.60. $A_{\mathrm{LU,DVCS}}^{\sin(\phi)}$, $A_{\mathrm{LU,I}}^{\sin(2\phi)}$, $A_{\mathrm{C}}^{\cos(2\phi)}$ and $A_{\mathrm{C}}^{\cos(3\phi)}$ are related to higher twist coefficients. In the following $A_{\mathrm{LU,I}}^{\cos(0\phi)}$, $A_{\mathrm{LU,I}}^{\sin(\phi)}$, $A_{\mathrm{C}}^{\cos(\phi)}$ and $A_{\mathrm{LU,DVCS}}^{\sin(\phi)}$ will be called 'leading–twist amplitudes' as their underlying Fourier coefficients have the lowest $1/Q$–dependence in the numerator of the three asymmetries.

It was checked that omitting the $\cos\phi$ ($\sin\phi$) modulations in the helicity (charge) depending asymmetries did not significantly change the other asymmetry amplitudes (see figure 4.12). This is expected, because the numerators of the BSAs (BCA) only involve sine (cosine) ϕ–modulations and the denominators in both cases only cosine ϕ–harmonics. Any cosine (sine) ϕ harmonic in the BSA (BCA) would originate from experimental limitations, like the acceptance or inefficiencies.

Nevertheless from this study it cannot be judged, if there is a higher harmonic in the data arising from the interplay between the ϕ–modulations in numerator and denominator of the asymmetries. It was checked mathematically that such contributions

from higher harmonics are not expected as long as the higher–twist coefficients do not show a larger amplitude compared to leading–twist ones. There is no indication of such a behavior found in the results.

In addition, the fit function was anti–symmetrized in order to eliminate all even modulations in the data. The result is shown in figure 4.13, where the sine amplitudes of both BSAs are plotted along with the respective constant moments. The latter ones are zero as expected, while the former agree well within the error bars with the standard extraction procedure. The larger error bars reflect the worse description of the data by the anti–symmetrized fit. The even moments of the BCA were also extracted and found to be compatible with zero (not shown here).

No systematic error was introduced for the choice of the fit function.

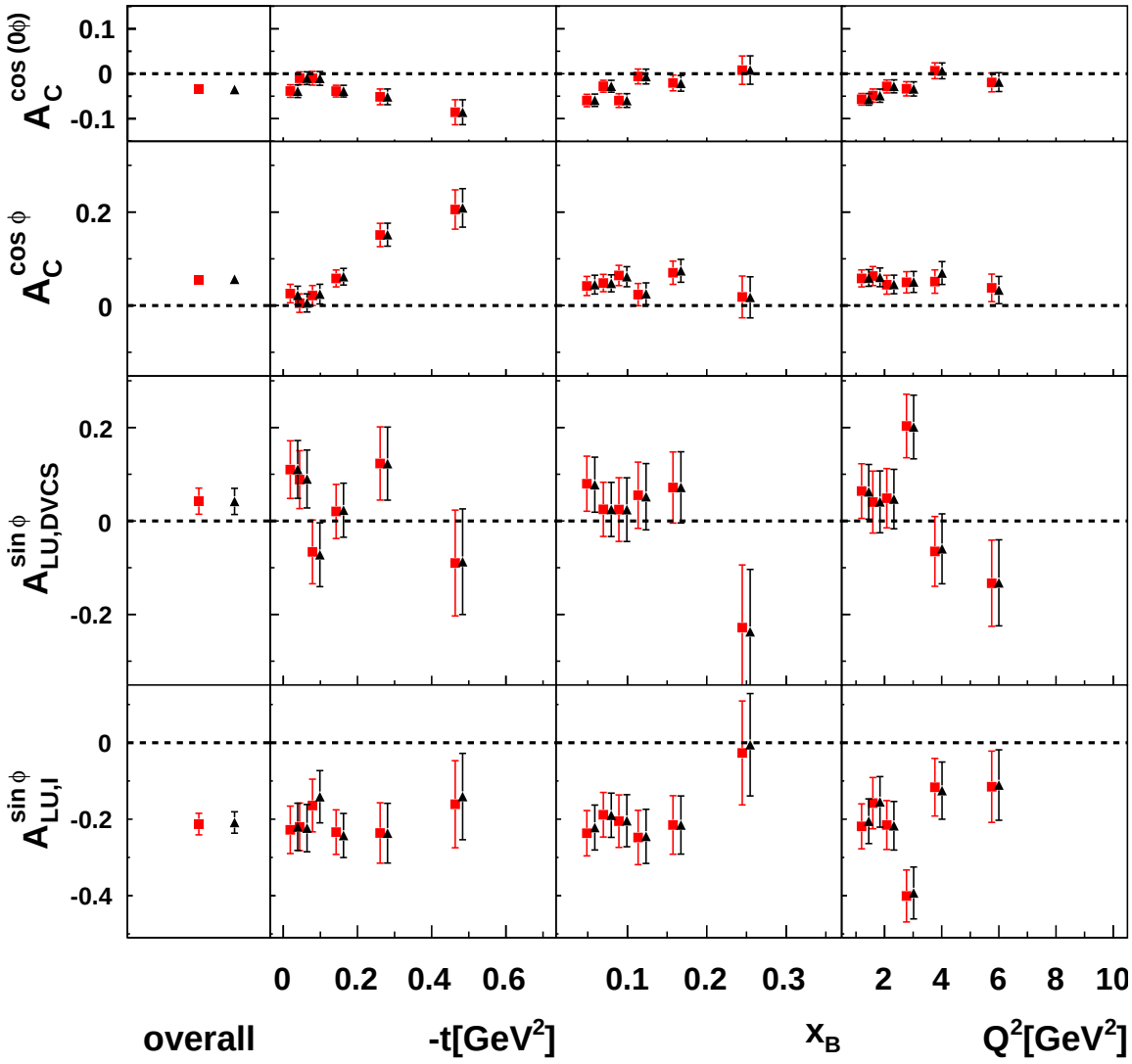

Figure 4.12: The four leading–twist amplitudes extracted with a 13–parameter fit (red squares) and a ten–parameter fit (black triangles) omitting the amplitudes $A_{\mathrm{LU,I}}^{\cos(\phi)}$, $A_{\mathrm{LU,DVCS}}^{\cos(\phi)}$ and $A_{\mathrm{C}}^{\sin(\phi)}$. The plot is displayed in the usual kinematic binning.

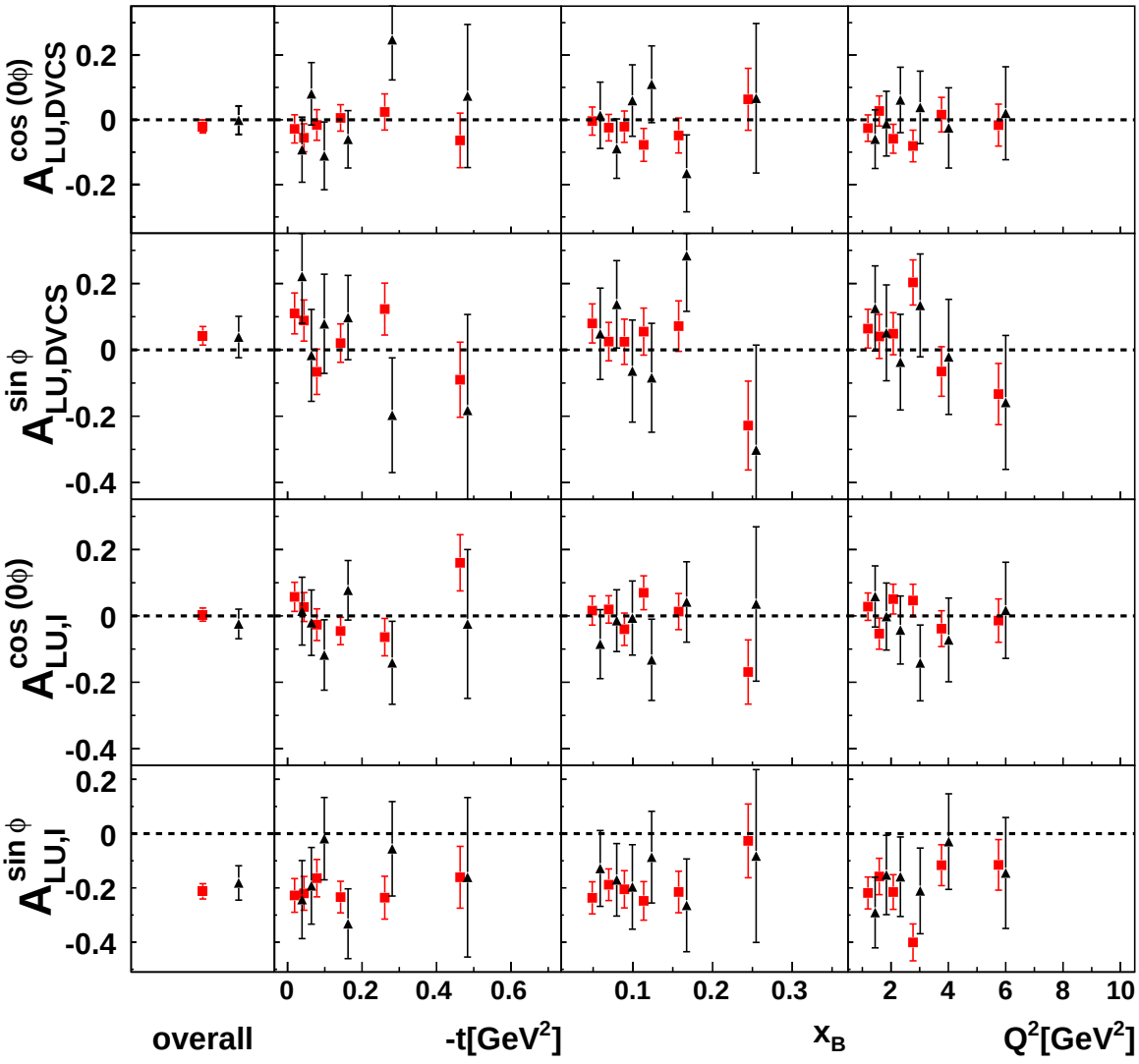

Figure 4.13: The constant and sine–modulation of the two BSAs extracted with a 13–parameter fit (red squares) and an anti–symmetrized fit function (black triangles) in the usual kinematic binning.

4.6.2 Efficiency corrections

Tracking and trigger efficiencies enter the pdf of the ML formalism and may depend on the angle ϕ. They can therefore cause false asymmetries moments and need to be evaluated thoroughly.

As the tracking efficiencies were found to be compatible with unity, they were not further considered. The trigger efficiencies were found to depend mainly on the H0 hodoscopes. In figure 4.9 the efficiency of these hodoscopes are shown separately for each analyzed data year. Especially in the years 1998 and 2000 some drops in the efficiency were observed. Therefore an efficiency correction was studied.

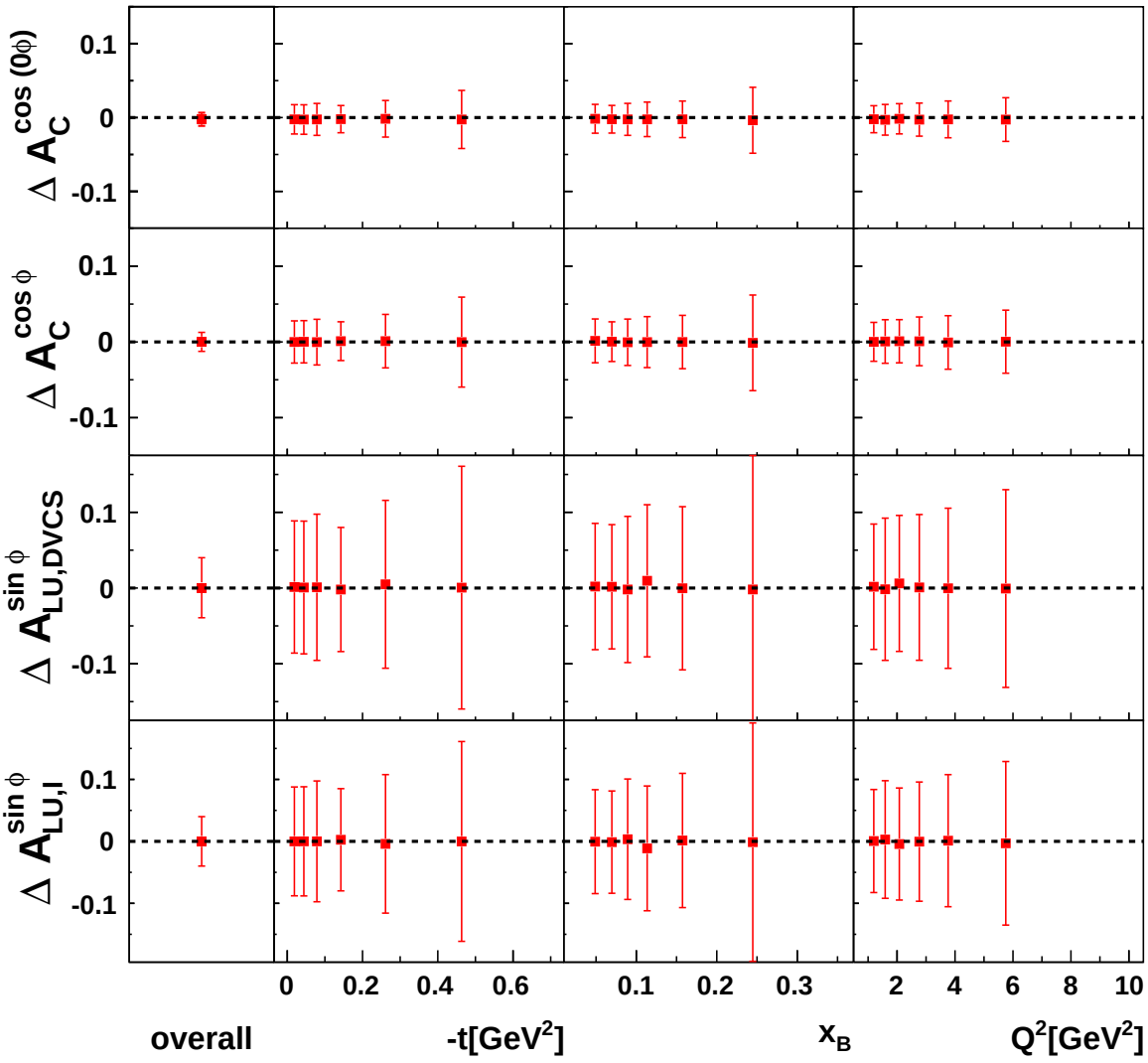

Figure 4.14: The difference of the leading–twist asymmetry amplitudes extracted with and without taking into account the H0 efficiency values. The differences are given in the usual kinematic binning.

From figure 4.9 a table was deduced for each year with a value for the H0 efficiency depending on the hit position on the surface. These tables were used to apply a weight to each DVCS event calculated as the inverse of the H0 efficiency at the position the DIS lepton hit the hodoscope. The extraction method was described in chapter 4.5.2. The result for the four leading–twist amplitudes is shown in figure 4.14, where the difference of the asymmetry amplitudes extracted with and without taking into account the H0 efficiency are displayed. The differences were very small for the main amplitudes compared to the statistical uncertainties.

For all asymmetry amplitudes and in every bin the differences due to the efficiency correction were smaller than 0.6 % with two outliers at around 1 % difference (not shown). This is understandable because of the high efficiency of the hodoscope during most of the data taking. The efficiency correction was therefore omitted for the final extraction of the result.

No systematic error was introduced for the tracking and trigger efficiencies.

4.6.3 Missing mass shift

As described in chapter 4.3.3, a relative shift of the squared missing mass spectra between the electron and positron data sample was observed. The boundaries limiting the exclusive region in the missing mass spectra were adjusted to account for this shift.

In figures 4.15–4.17 the effect of the shift on the asymmetry amplitudes is shown. The red squares visualize the amplitudes extracted from the unchanged exclusive region, while the black squares show the amplitudes for the altered exclusive regions. As expected the biggest impact is seen on the BCA and the charge–averaged BSA amplitudes. In general, the impact on the asymmetry amplitudes is small.

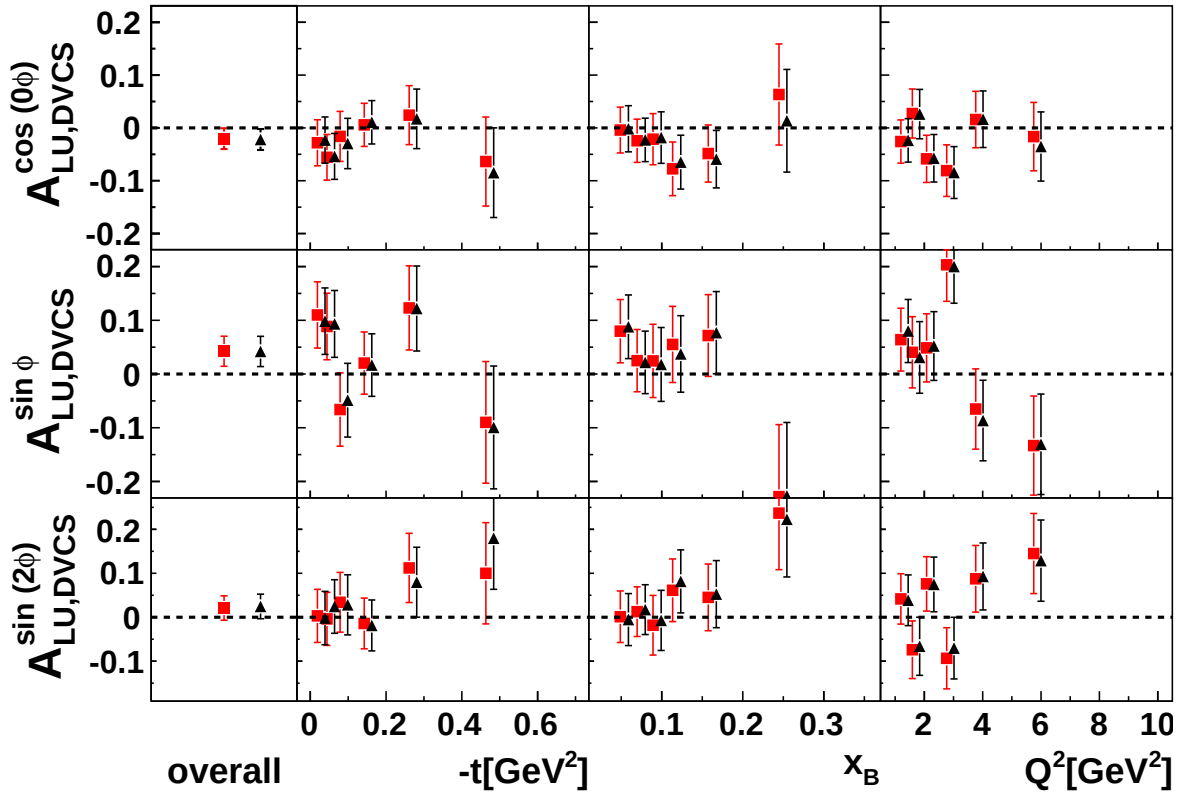

Figure 4.15: The amplitudes of the charge–difference BSA originating from the DVCS term for the standard exclusive region (red squares) and the shifted squared missing mass distribution (black triangles) in the usual kinematic binning.

For the final extraction the shifted data sample was chosen. As the reason for the shift is not understood, one quarter of the effect was added to the systematic uncertainty. The resulting systematic uncertainty for the whole data sample is smaller than 0.01 for all considered asymmetry amplitudes, except from an uncertainty of 0.016 for the constant moment of the BCA. The largest bin–wise deviations are observed in the last t–bins.

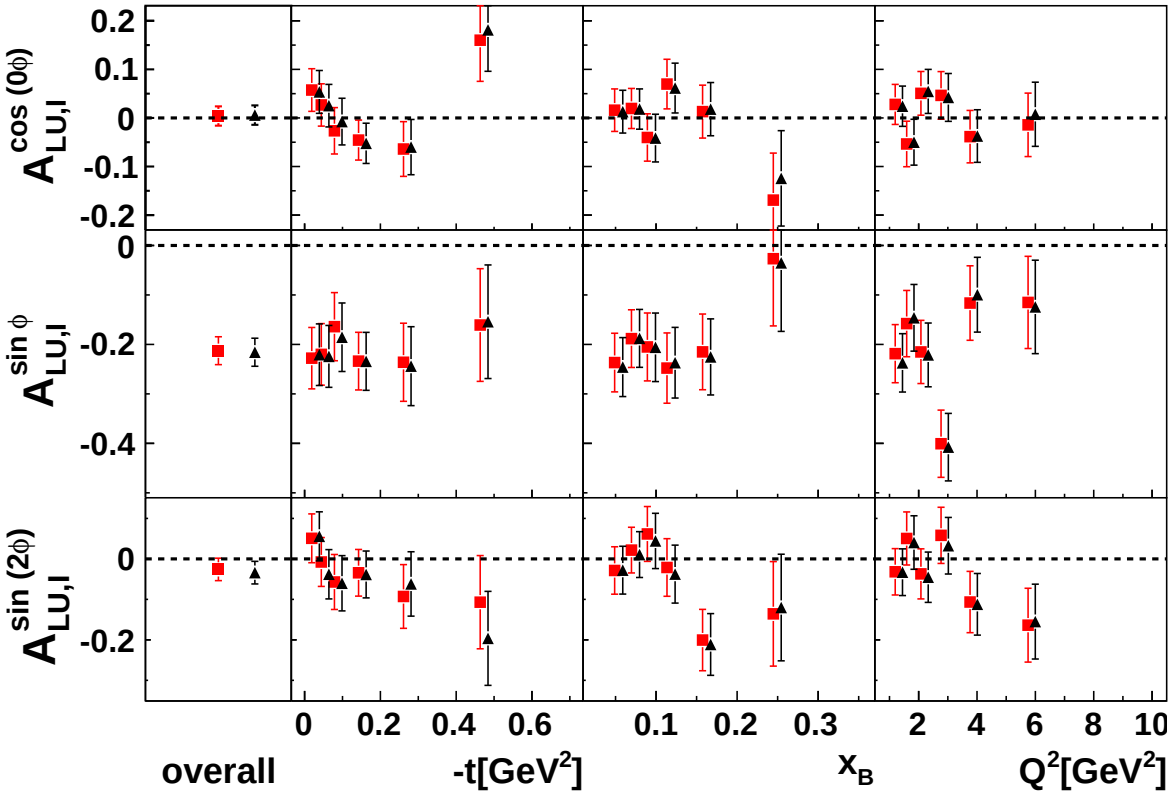

Figure 4.16: The amplitudes of the charge–averaged BSA for the standard exclusive region (red squares) and the shifted squared missing mass distribution (black triangles) in the usual kinematic binning.

For the leading–twist amplitudes the bin–wise asymmetry amplitudes along with their statistical uncertainties are listed in table 4.8. In addition, the systematic uncertainty due to the shift in the missing mass spectra is quoted.

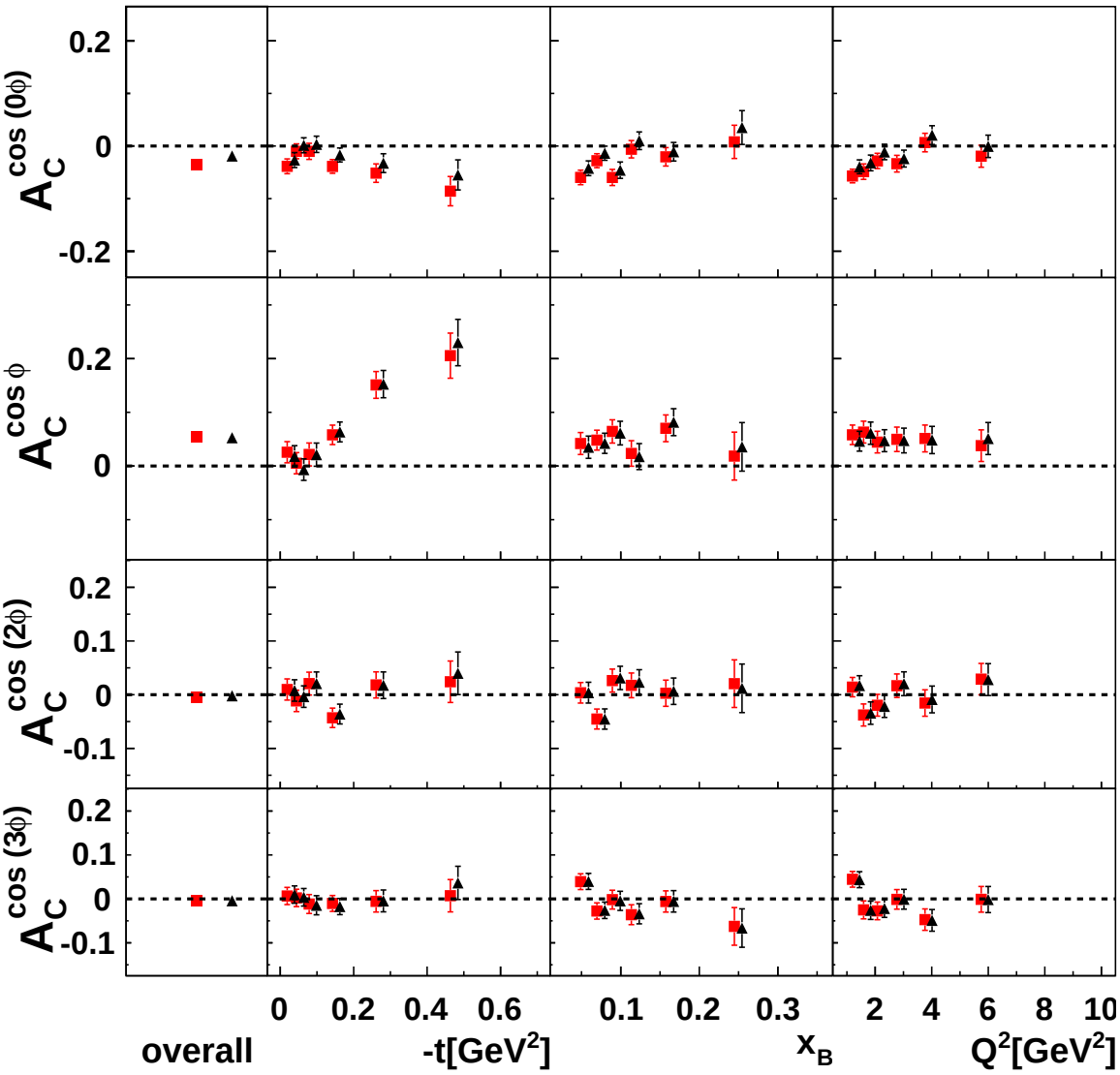

Figure 4.17: The amplitudes of the BCA for the standard exclusive region (red squares) and the shifted squared missing mass distribution (black triangles) in the usual kinematic binning.

	$A_C^{cos(0\phi)} \pm \delta_{stat} \pm \delta_{syst}$	$A_C^{cos(\phi)} \pm \delta_{stat} \pm \delta_{syst}$	$A_{LU,DVCS}^{sin(\phi)} \pm \delta_{stat} \pm \delta_{syst}$	$A_{LU,I}^{sin(\phi)} \pm \delta_{stat} \pm \delta_{syst}$
overall	$-0.019 \pm 0.006 \pm 0.004$	$0.053 \pm 0.009 \pm 0.001$	$0.042 \pm 0.028 \pm 0.000$	$-0.216 \pm 0.028 \pm 0.001$
$0.00 < -t < 0.03$	$-0.027 \pm 0.014 \pm 0.003$	$0.018 \pm 0.020 \pm 0.002$	$0.098 \pm 0.062 \pm 0.003$	$-0.221 \pm 0.062 \pm 0.002$
$0.03 < -t < 0.06$	$0.001 \pm 0.014 \pm 0.003$	$-0.007 \pm 0.020 \pm 0.003$	$0.093 \pm 0.062 \pm 0.001$	$-0.224 \pm 0.063 \pm 0.001$
$0.06 < -t < 0.10$	$0.003 \pm 0.015 \pm 0.003$	$0.021 \pm 0.022 \pm 0.000$	$-0.049 \pm 0.069 \pm 0.004$	$-0.185 \pm 0.069 \pm 0.005$
$0.10 < -t < 0.20$	$-0.017 \pm 0.013 \pm 0.005$	$0.063 \pm 0.018 \pm 0.001$	$0.017 \pm 0.058 \pm 0.001$	$-0.234 \pm 0.059 \pm 0.000$
$0.20 < -t < 0.35$	$-0.033 \pm 0.018 \pm 0.005$	$0.153 \pm 0.025 \pm 0.000$	$0.122 \pm 0.079 \pm 0.000$	$-0.244 \pm 0.080 \pm 0.002$
$0.35 < -t < 0.70$	$-0.055 \pm 0.029 \pm 0.008$	$0.230 \pm 0.043 \pm 0.006$	$-0.099 \pm 0.114 \pm 0.002$	$-0.154 \pm 0.115 \pm 0.002$
$0.03 < x_B < 0.06$	$-0.042 \pm 0.014 \pm 0.004$	$0.035 \pm 0.021 \pm 0.002$	$0.088 \pm 0.059 \pm 0.002$	$-0.246 \pm 0.060 \pm 0.002$
$0.06 < x_B < 0.08$	$-0.014 \pm 0.013 \pm 0.004$	$0.042 \pm 0.019 \pm 0.001$	$0.022 \pm 0.058 \pm 0.001$	$-0.188 \pm 0.059 \pm 0.000$
$0.08 < x_B < 0.10$	$-0.046 \pm 0.016 \pm 0.003$	$0.061 \pm 0.022 \pm 0.001$	$0.018 \pm 0.069 \pm 0.002$	$-0.206 \pm 0.069 \pm 0.000$
$0.10 < x_B < 0.13$	$0.010 \pm 0.017 \pm 0.004$	$0.018 \pm 0.024 \pm 0.001$	$0.037 \pm 0.071 \pm 0.004$	$-0.237 \pm 0.071 \pm 0.003$
$0.13 < x_B < 0.20$	$-0.011 \pm 0.018 \pm 0.002$	$0.082 \pm 0.025 \pm 0.003$	$0.077 \pm 0.077 \pm 0.001$	$-0.225 \pm 0.077 \pm 0.003$
$0.20 < x_B < 0.35$	$0.035 \pm 0.032 \pm 0.007$	$0.036 \pm 0.045 \pm 0.004$	$-0.227 \pm 0.137 \pm 0.000$	$-0.035 \pm 0.139 \pm 0.002$
$1.0 < Q^2 < 1.4$	$-0.039 \pm 0.013 \pm 0.004$	$0.046 \pm 0.018 \pm 0.003$	$0.080 \pm 0.059 \pm 0.004$	$-0.237 \pm 0.059 \pm 0.005$
$1.4 < Q^2 < 1.8$	$-0.032 \pm 0.015 \pm 0.004$	$0.061 \pm 0.021 \pm 0.001$	$0.031 \pm 0.067 \pm 0.002$	$-0.146 \pm 0.067 \pm 0.003$
$1.8 < Q^2 < 2.4$	$-0.011 \pm 0.015 \pm 0.004$	$0.047 \pm 0.020 \pm 0.001$	$0.052 \pm 0.064 \pm 0.001$	$-0.221 \pm 0.064 \pm 0.002$
$2.4 < Q^2 < 3.2$	$-0.024 \pm 0.016 \pm 0.002$	$0.047 \pm 0.023 \pm 0.001$	$0.200 \pm 0.068 \pm 0.001$	$-0.408 \pm 0.068 \pm 0.002$
$3.2 < Q^2 < 4.5$	$0.021 \pm 0.018 \pm 0.004$	$0.048 \pm 0.025 \pm 0.001$	$-0.087 \pm 0.075 \pm 0.005$	$-0.100 \pm 0.076 \pm 0.004$
$4.5 < Q^2 < 10.0$	$-0.001 \pm 0.021 \pm 0.005$	$0.051 \pm 0.030 \pm 0.003$	$-0.131 \pm 0.093 \pm 0.001$	$-0.124 \pm 0.094 \pm 0.002$

Table 4.8: The leading–twist asymmetry amplitudes for the data with the shifted squared missing mass distribution together with its statistical error and the systematic uncertainty applied on the final results. The limits in $-t$ and Q^2 are given in GeV^2.

4.6.4 Background corrections

Three different sources of background remain in the final data sample after applying all cuts used in this analysis:

- Associated BH/DVCS.
- **S**emi–**i**nclusive **DIS** processes (SIDIS).
- Exclusive production of neutral pions.

In the following sections the determination of their fractional contributions and their asymmetry amplitudes will be described and the correction procedure will be explained.

Determination of the background contributions

In figure 4.18 the contributions of the elastic BH process is compared to the sum of the background processes. The latter one starts to dominate the data sample at $M_X^2 \approx 3.0$ GeV^2, which confirms the choice of the upper cut on the squared missing mass of 2.89 GeV^2. The background itself is dominated by the associated BH/DVCS production, which cannot be separated experimentally from the elastic BH/DVCS production due to the limited resolution in the squared missing mass. Therefore it will be treated as part of the signal.

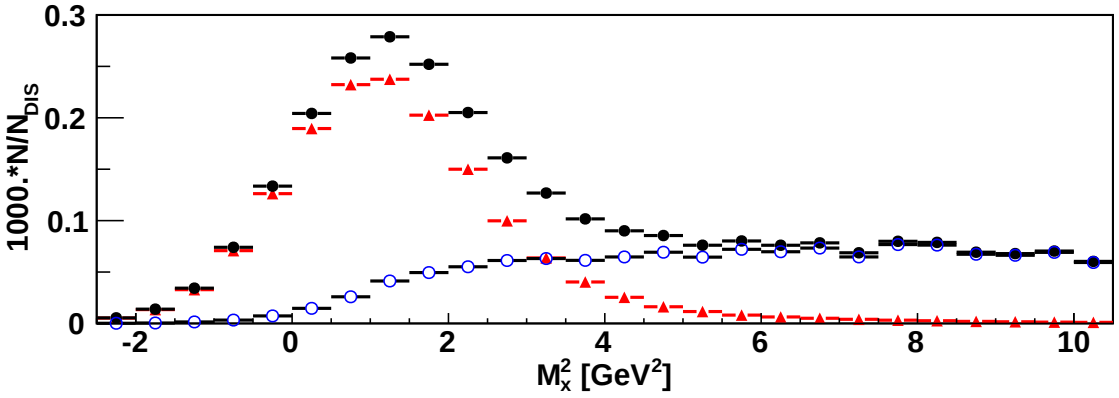

Figure 4.18: The contribution from the elastic BH process (red triangles) compared to the sum of the background processes (associated BH, semi–inclusive processes and exclusive π^0 production) depicted by the blue open circles in bins of the squared missing mass. The black circles give the sum of all processes.

The semi–inclusive background is dominated by the production of neutral pions ($\approx 80\,\%$), where either only one decay photon is detected or the decay photons cannot be resolved by the electromagnetic calorimeter [Ye07]. Another 15 % originate from the decay of η–mesons.

	BH	assoc. BH	semi-incl.	excl. π^0
overall	84.4 ± 0.3 %	11.9 ± 0.1%	3.3 ± 0.3%	0.4 ± 0.2%
$0.00 < -t < 0.03$	94.6 ± 0.6 %	3.6 ± 0.1%	1.5 ± 0.4%	0.2 ± 0.4%
$0.03 < -t < 0.06$	90.2 ± 0.7 %	7.0 ± 0.1%	2.5 ± 0.4%	0.3 ± 0.5%
$0.06 < -t < 0.10$	85.4 ± 0.9 %	10.4 ± 0.1%	3.6 ± 0.7%	0.5 ± 0.7%
$0.10 < -t < 0.20$	79.0 ± 0.8 %	15.1 ± 0.2%	5.3 ± 0.7%	0.5 ± 0.6%
$0.20 < -t < 0.35$	72.6 ± 1.0 %	22.6 ± 0.3%	4.3 ± 0.9%	0.4 ± 0.8%
$0.35 < -t < 0.70$	62.7 ± 0.9 %	35.1 ± 0.6%	2.0 ± 1.1%	0.2 ± 0.9%
$0.03 < x_B < 0.06$	88.5 ± 0.5 %	10.7 ± 0.1%	0.6 ± 0.2%	0.2 ± 0.3%
$0.06 < x_B < 0.08$	87.5 ± 0.7 %	10.8 ± 0.1%	1.3 ± 0.3%	0.4 ± 0.5%
$0.08 < x_B < 0.10$	84.3 ± 0.9 %	11.3 ± 0.2%	3.9 ± 0.7%	0.5 ± 0.7%
$0.10 < x_B < 0.13$	82.9 ± 0.9 %	12.8 ± 0.2%	3.8 ± 0.6%	0.5 ± 0.7%
$0.13 < x_B < 0.20$	78.1 ± 1.1 %	14.3 ± 0.2%	7.1 ± 0.9%	0.5 ± 0.8%
$0.20 < x_B < 0.35$	71.9 ± 2.0 %	15.0 ± 0.5%	12.7 ± 2.2%	0.4 ± 1.2%
$1.0 < Q^2 < 1.4$	87.0 ± 0.8 %	9.2 ± 0.1%	3.1 ± 0.5%	0.7 ± 0.7%
$1.4 < Q^2 < 1.8$	85.7 ± 0.8 %	11.0 ± 0.1%	2.9 ± 0.6%	0.5 ± 0.7%
$1.8 < Q^2 < 2.4$	84.8 ± 0.8 %	11.5 ± 0.1%	3.4 ± 0.6%	0.4 ± 0.6%
$2.4 < Q^2 < 3.2$	82.9 ± 0.8 %	12.9 ± 0.2%	3.9 ± 0.7%	0.3 ± 0.5%
$3.2 < Q^2 < 4.5$	82.9 ± 0.8 %	13.9 ± 0.2%	3.1 ± 0.6%	0.2 ± 0.5%
$4.5 < Q^2 < 10.$	79.3 ± 0.9 %	16.9 ± 0.3%	3.6 ± 0.9%	0.1 ± 0.5%

Table 4.9: The fractional contributions for the elastic BH ('BH'), the associated BH ('assoc. BH'), semi–inclusive DIS processes ('semi–incl.') and the exclusive π^0 production ('excl. π^0') as obtained from a MC study. The given errors are statistical ones. The limits in $-t$ and Q^2 are given in GeV^2.

The fractional contribution of the four classes of processes were obtained from a MC study using the three event generators GMC_DVCS, GMC_DISNG and GMC_EXCLPION. The bin–wise fractional contributions are listed in table 4.9. The study only included the (elastic and associated) BH processes, while ignoring the corresponding DVCS processes, which are model–dependent. Especially the associated DVCS process is theoretically difficult to understand.

The fractional contributions in the fully covered kinematics were determined to be 11.9 % for the associated production, 3.3 % for the semi–inclusive DIS processes and 0.4 % for the exclusive production of neutral pions. The amount of the associated production is increasing with increasing squared momentum transfer to the final state nucleon ($-t$). A weaker increase is observed for the contribution of the semi–inclusive processes with Bjorken–x approaching the more valence–dominated region.

Determination of the background amplitudes

Besides the fractional contributions of the background processes, also the knowledge of their asymmetry amplitudes are necessary for a correction.

As stated in the previous section, the semi–inclusive DIS processes are dominated by the production of neutral pions, which decay into real photon(s) that are detected in the electromagnetic calorimeter. The asymmetries from these decay photons were determined from HERMES data in the so–called 2–photon analysis. The following criteria were used for this extraction:

- ⋆ The same DIS cuts on the scattered lepton as used in the DVCS analysis.
- ⋆ Two trackless clusters were required that
  - pass the fiducial volume cuts,
  - give a pulse in the preshower of more than 1 MeV,
  - deposit an energy of more than 5 GeV and 1 GeV.
- ⋆ The mass of the reconstructed π^0 must fulfill: 0.1 GeV $< m_{\gamma\gamma} <$ 0.17 GeV.
- ⋆ All exclusive cuts are required on the reconstructed π^0, but the DVCS missing mass criterium.
- ⋆ The fractional energy $z \equiv E_{\pi^0}/\nu$ needs to be larger than 0.8.

The obtained statistics for these two–photon events was approximately one quarter of the DVCS statistics in each data set.

It was verified in [Ye07] that the asymmetry amplitudes from the detected two–photon events, ignoring events in which one of the photons escaped detection or both photons were reconstructed as a single cluster, correspond very well to the amplitudes from the neutral pions. The results of the extraction are shown in figures 4.19 - 4.21. The charge–difference BSA is compatible with zero, while some bins show statistical fluctuations. As there are no theory expectations the extracted numbers were used for the correction.

The beam charge–related asymmetry amplitudes are expected to be zero, because in the case of π^0 production an asymmetry can only arise from a two–photon exchange mechanism. However, both the constant and the cosine two–ϕ moment show amplitudes of the magnitude 0.04. The beam charge–averaged BSA moments are compatible with zero except for some outliers. In the correction the beam charge–related asymmetries will be treated as dilutions, e.g. the asymmetry amplitudes will be set to zero.

In [Van07] the extraction of cross section asymmetries in exclusive neutral pion production was studied. Due to large background contributions in the exclusive region, which are difficult to describe in a model, no asymmetry amplitudes are given. Therefore the asymmetry amplitudes of the neutral pions were assumed to be a dilution, i.e. $0 \pm 2/\sqrt{12}$ in the correction.

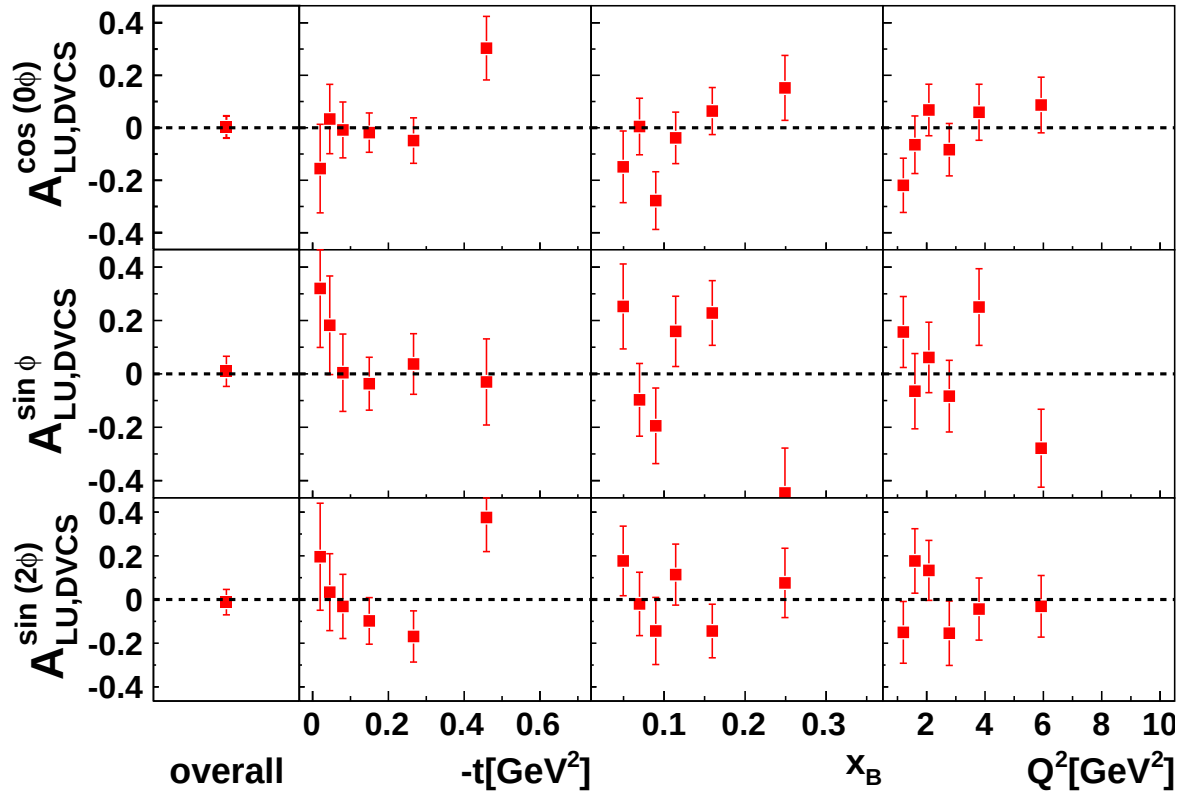

Figure 4.19: The amplitudes of the charge–difference BSA from the two–photon analysis in the usual kinematic binning.

Background correction algorithm

With the knowledge of the fractional contributions f and the asymmetry amplitudes A of all contributing processes, the background correction can be performed in the following way:

$$A_{\text{excl.}} = \frac{A_{\text{meas.}} - f_{\text{SIDIS}} A_{\text{SIDIS}} - f_{\text{excl. }\pi^0} A_{\text{excl. }\pi^0}}{1 - f_{\text{SIDIS}} - f_{\text{excl. }\pi^0}}. \tag{4.27}$$

In this equation $A_{\text{meas.}}$ denotes the extracted amplitude before the background correction and $A_{\text{excl.}}$ the corrected amplitude. Thus each asymmetry amplitude can be corrected in each kinematic bin.

The statistical uncertainty of the approach arises from the uncertainties in the back-

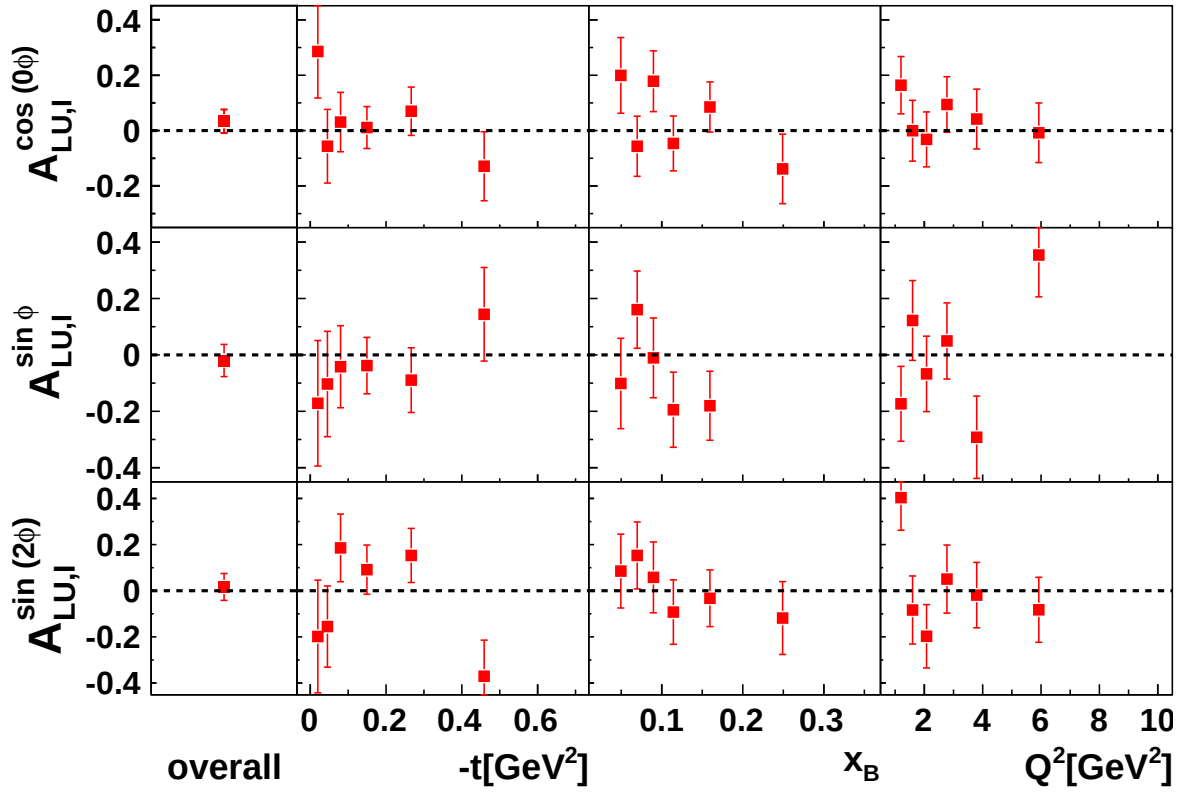

Figure 4.20: The amplitudes of the charge–averaged BSA from the two–photon analysis in the usual kinematic binning.

ground fractions and the asymmetries.

$$\delta_{f_{\mathrm{bg,i}}} = \frac{A_{\mathrm{meas.}} - A_{\mathrm{bg,i}} + A_{\mathrm{bg,i}} f_{\mathrm{bg,j}} - A_{\mathrm{bg,j}} f_{\mathrm{bg,j}}}{(1 - f_{\mathrm{bg,i}} - f_{\mathrm{bg,j}})^2} \cdot \delta f_{\mathrm{bg,i}}, \tag{4.28}$$

$$\delta_{A_{\mathrm{bg,i}}} = \frac{-f_{\mathrm{bg,i}}}{1 - f_{\mathrm{bg,i}} - f_{\mathrm{bg,j}}} \cdot \delta A_{\mathrm{bg,i}}, \tag{4.29}$$

$$\delta = \sum_i \sqrt{(\delta^2_{f_{\mathrm{bg,i}}} + \delta^2_{A_{\mathrm{bg,i}}})}, \tag{4.30}$$

where bg,i replaces the different background contributions. In this way the uncertainty is propagated to the final statistical uncertainty. In addition, half the size of the actual correction is assigned as systematic uncertainty in order to account for the assumptions and approximations in the correction.

The background–corrected leading–twist asymmetry amplitudes are listed in table 4.10 together with the corrected statistical uncertainties and the systematic uncertainties arising from the correction. The contributions to the different asymmetry amplitudes are largest for the charge–difference BSA, because here the background was not treated as dilution.

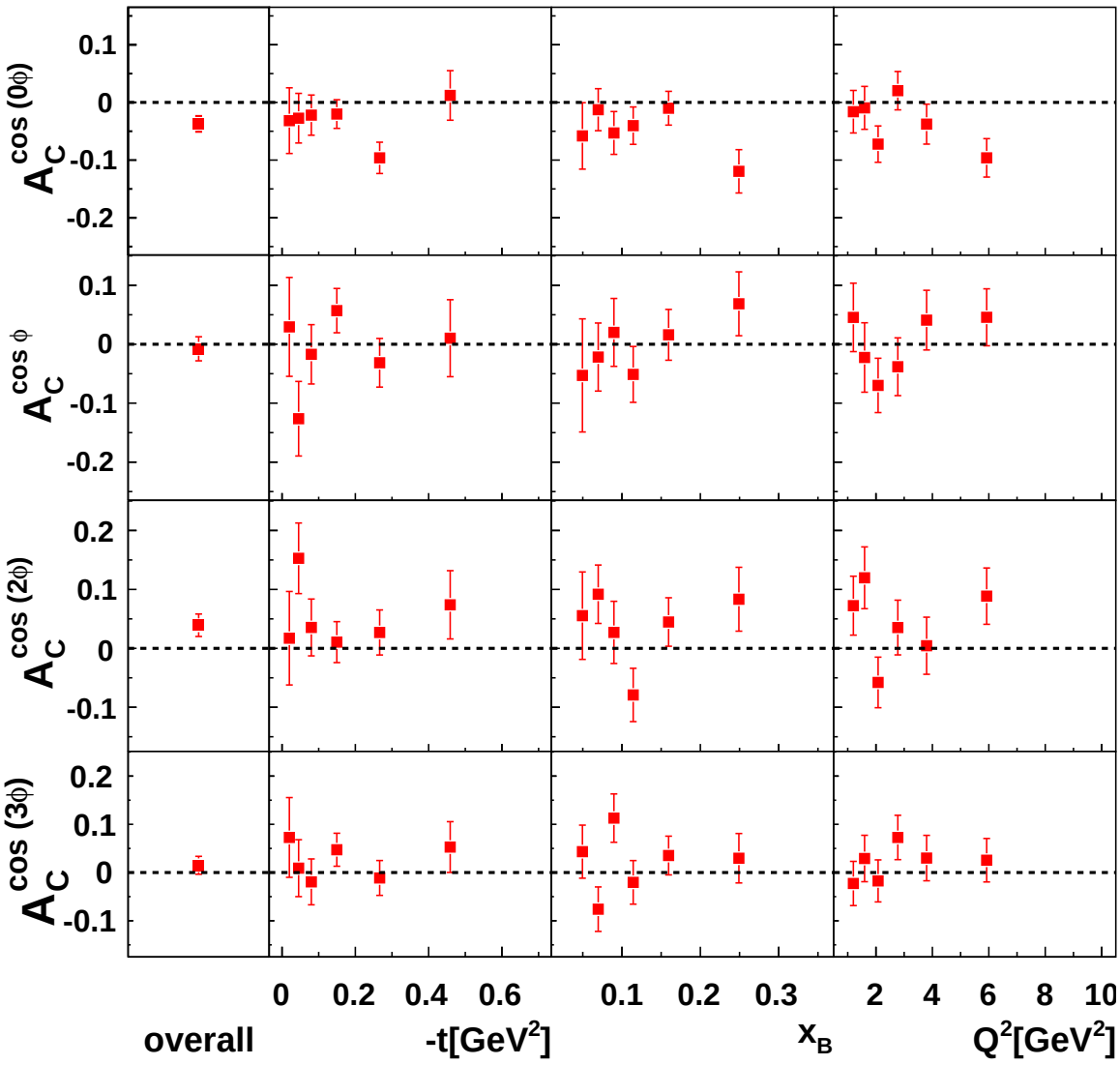

Figure 4.21: The BCA amplitudes from the two–photon analysis in the usual kinematic binning.

	$A_C^{cos(0\phi)} \pm \delta_{stat} \pm \delta_{syst}$	$A_C^{cos(\phi)} \pm \delta_{stat} \pm \delta_{syst}$	$A_{LU,DVCS}^{sin(\phi)} \pm \delta_{stat} \pm \delta_{syst}$	$A_{LU,I}^{sin(\phi)} \pm \delta_{stat} \pm \delta_{syst}$
overall	$-0.020 \pm 0.006 \pm 0.000$	$0.055 \pm 0.009 \pm 0.001$	$0.043 \pm 0.028 \pm 0.004$	$-0.224 \pm 0.028 \pm 0.005$
$0.00 < t_c < 0.03$	$-0.027 \pm 0.014 \pm 0.000$	$0.018 \pm 0.020 \pm 0.000$	$0.095 \pm 0.062 \pm 0.005$	$-0.225 \pm 0.062 \pm 0.003$
$0.03 < t_c < 0.06$	$0.001 \pm 0.014 \pm 0.000$	$-0.007 \pm 0.020 \pm 0.000$	$0.091 \pm 0.062 \pm 0.006$	$-0.231 \pm 0.063 \pm 0.005$
$0.06 < t_c < 0.10$	$0.003 \pm 0.015 \pm 0.000$	$0.022 \pm 0.022 \pm 0.001$	$-0.051 \pm 0.069 \pm 0.007$	$-0.193 \pm 0.069 \pm 0.006$
$0.10 < t_c < 0.20$	$-0.018 \pm 0.013 \pm 0.001$	$0.067 \pm 0.018 \pm 0.003$	$0.020 \pm 0.058 \pm 0.008$	$-0.249 \pm 0.059 \pm 0.010$
$0.20 < t_c < 0.35$	$-0.034 \pm 0.018 \pm 0.001$	$0.160 \pm 0.025 \pm 0.006$	$0.126 \pm 0.079 \pm 0.008$	$-0.256 \pm 0.080 \pm 0.009$
$0.35 < t_c < 0.70$	$-0.056 \pm 0.029 \pm 0.001$	$0.235 \pm 0.043 \pm 0.006$	$-0.101 \pm 0.114 \pm 0.005$	$-0.158 \pm 0.115 \pm 0.004$
$0.03 < x_B < 0.06$	$-0.043 \pm 0.014 \pm 0.000$	$0.035 \pm 0.021 \pm 0.000$	$0.087 \pm 0.059 \pm 0.002$	$-0.248 \pm 0.060 \pm 0.002$
$0.06 < x_B < 0.08$	$-0.014 \pm 0.013 \pm 0.000$	$0.043 \pm 0.019 \pm 0.001$	$0.023 \pm 0.058 \pm 0.004$	$-0.191 \pm 0.059 \pm 0.003$
$0.08 < x_B < 0.10$	$-0.048 \pm 0.016 \pm 0.002$	$0.064 \pm 0.022 \pm 0.002$	$0.026 \pm 0.069 \pm 0.011$	$-0.215 \pm 0.069 \pm 0.007$
$0.10 < x_B < 0.13$	$0.010 \pm 0.017 \pm 0.000$	$0.018 \pm 0.024 \pm 0.001$	$0.033 \pm 0.071 \pm 0.008$	$-0.248 \pm 0.071 \pm 0.008$
$0.13 < x_B < 0.20$	$-0.012 \pm 0.018 \pm 0.001$	$0.088 \pm 0.025 \pm 0.004$	$0.066 \pm 0.077 \pm 0.016$	$-0.244 \pm 0.077 \pm 0.012$
$0.20 < x_B < 0.35$	$0.040 \pm 0.032 \pm 0.004$	$0.041 \pm 0.045 \pm 0.004$	$-0.196 \pm 0.137 \pm 0.041$	$-0.040 \pm 0.139 \pm 0.004$
$1.0 < Q^2 < 1.4$	$-0.041 \pm 0.013 \pm 0.001$	$0.048 \pm 0.018 \pm 0.001$	$0.078 \pm 0.059 \pm 0.007$	$-0.247 \pm 0.059 \pm 0.007$
$1.4 < Q^2 < 1.8$	$-0.033 \pm 0.015 \pm 0.001$	$0.063 \pm 0.021 \pm 0.002$	$0.034 \pm 0.067 \pm 0.007$	$-0.151 \pm 0.067 \pm 0.004$
$1.8 < Q^2 < 2.4$	$-0.012 \pm 0.015 \pm 0.000$	$0.049 \pm 0.020 \pm 0.001$	$0.052 \pm 0.064 \pm 0.005$	$-0.230 \pm 0.064 \pm 0.006$
$2.4 < Q^2 < 3.2$	$-0.025 \pm 0.016 \pm 0.001$	$0.050 \pm 0.023 \pm 0.001$	$0.212 \pm 0.068 \pm 0.012$	$-0.425 \pm 0.068 \pm 0.013$
$3.2 < Q^2 < 4.5$	$0.021 \pm 0.018 \pm 0.001$	$0.050 \pm 0.025 \pm 0.001$	$-0.097 \pm 0.075 \pm 0.011$	$-0.103 \pm 0.076 \pm 0.002$
$4.5 < Q^2 < 10.$	$-0.001 \pm 0.021 \pm 0.000$	$0.053 \pm 0.030 \pm 0.002$	$-0.125 \pm 0.093 \pm 0.009$	$-0.129 \pm 0.094 \pm 0.004$

Table 4.10: The leading–twist asymmetry amplitudes after applying the background correction. The systematic uncertainties after applying the correction are also stated. The boundaries in $-t$ and Q^2 are given in GeV^2.

4.6.5 The 'Four–in–one' MC study

Four other sources of systematic uncertainties were determined in a dedicated MC study:

1.) The limited acceptance.

2.) The finite bin–width.

3.) The limited resolution leading to smearing effects.

4.) The misalignment of detector (components).

The limited acceptance of the HERMES spectrometer does not allow to measure any observable in 4π. In case of the BH/DVCS processes the cross section exhibits a difficult kinematic dependence. Therefore the extracted asymmetry amplitudes need to be corrected for the effect of the HERMES acceptance in order to make comparisons to models possible.

In theory the asymmetry amplitudes are calculated at the mean kinematics of an experiment, while the extracted asymmetry amplitudes are averaged over the acceptance in the corresponding kinematical region. Any discrepancies arising from the different approaches are collected into the bin–width effect.

The limited resolution of an experiment leads to a smeared signal, which can produce errors in the extraction procedure and are called smearing effects.

Finally, the detectors forming the spectrometer might be tilted or shifted relative to each other and/or relative to the beam. Such (internal and external) misalignments might produce large asymmetries and are therefore studied within the misalignment effect.

To extract the systematic uncertainties, MC data was generated in 4π and the asymmetry amplitudes were extracted in the same way as from the real data. These reconstructed asymmetry amplitudes were compared to generated asymmetry amplitudes calculated from a Fourier decomposition of the three considered asymmetries obtained with the same MC model in 4π and evaluated at the mean kinematics of each bin. This study was called 'Four–in–one' method.

The comparison of the generated and reconstructed asymmetry amplitudes is shown in figures 4.22 - 4.24. The red squares depict the reconstructed asymmetry amplitudes and the blue lines show the generated ones.

These figures were obtained from model five of the GMC_DVCS generator (see section 4.4.1). In this model only twist–two amplitudes are included and the charge–difference BSA amplitudes are all zero (see figure 4.22). Also the reconstructed amplitudes are all compatible with zero. The sine ϕ moment of the charge–averaged BSA is large in this model. The reconstructed overall value is smaller by around 16%. This is the largest absolute deviation in the integrated result observed in this study. Note the fact that the main deviations occur in the t–integrated data bins. Both, the amplitudes of the constant and cosine moments of the BCA are underestimated by 0.03 and 0.02

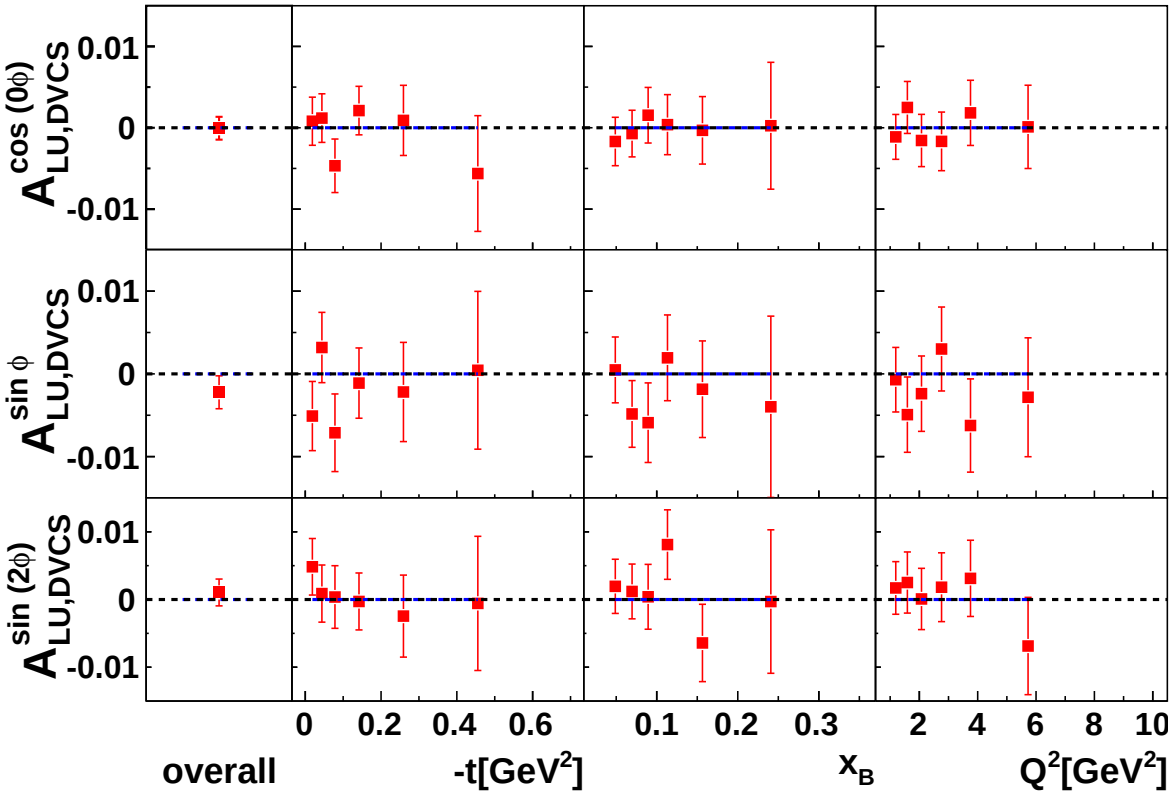

Figure 4.22: The 4–in–1 results for the charge–difference BSA amplitudes obtained from model five of the GMC_DVCS generator in the usual kinematic binning.

in the reconstruction. In the chosen model variant a D–term was included, which increases the BCA moments compared to the variants without it.

For the determination of the final systematic uncertainties from the Four–in–one method it was decided to compute the root mean square of the bin–wise differences between the generated and reconstructed amplitudes for the variants one, three and five of the GMC_DVCS generator and the Regge–inspired variant of a dual–parameterization based model [GT06]. The results for the other model variants are not shown here, but in general show a similar behavior. Note that all mentioned model (variants) miss a contribution from higher twist. This might explain, why twist–two amplitudes are usually underestimated in the reconstruction and higher twist amplitudes are overestimated.

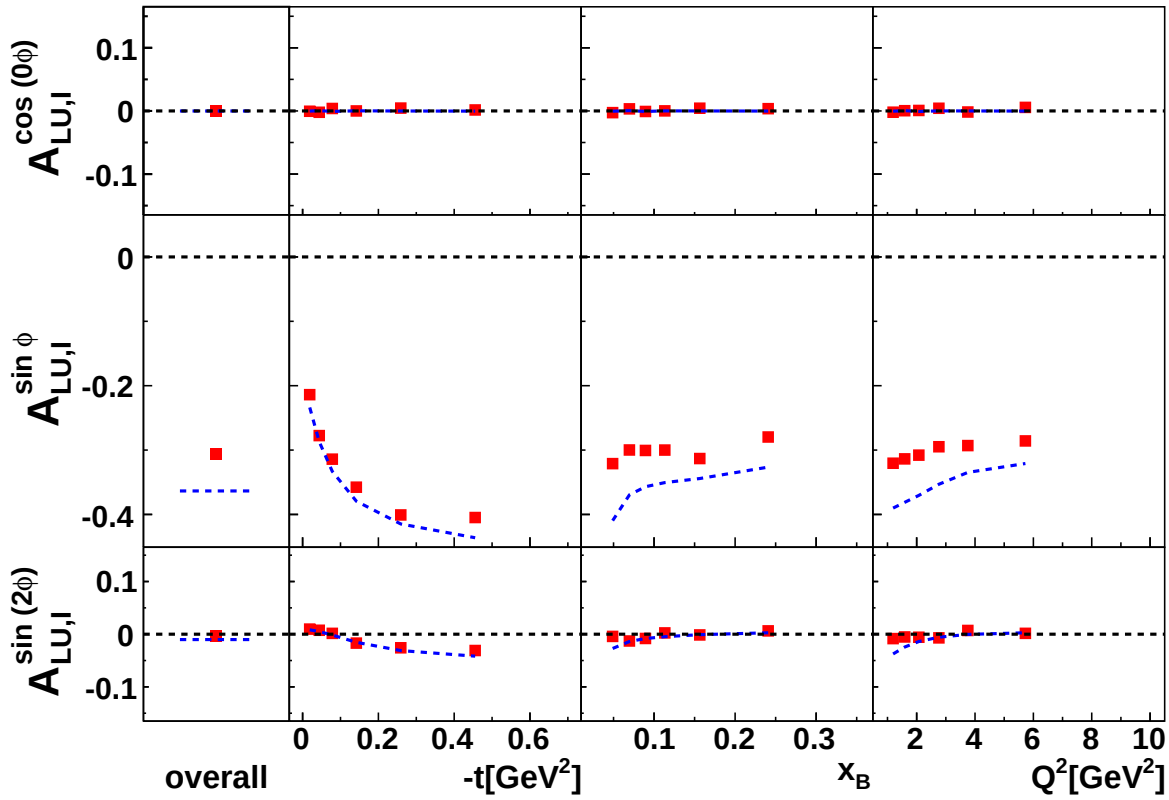

Figure 4.23: The 4–in–1 results for the charge–averaged BSA amplitudes obtained from model five of the GMC_DVCS generator in the usual kinematic binning.

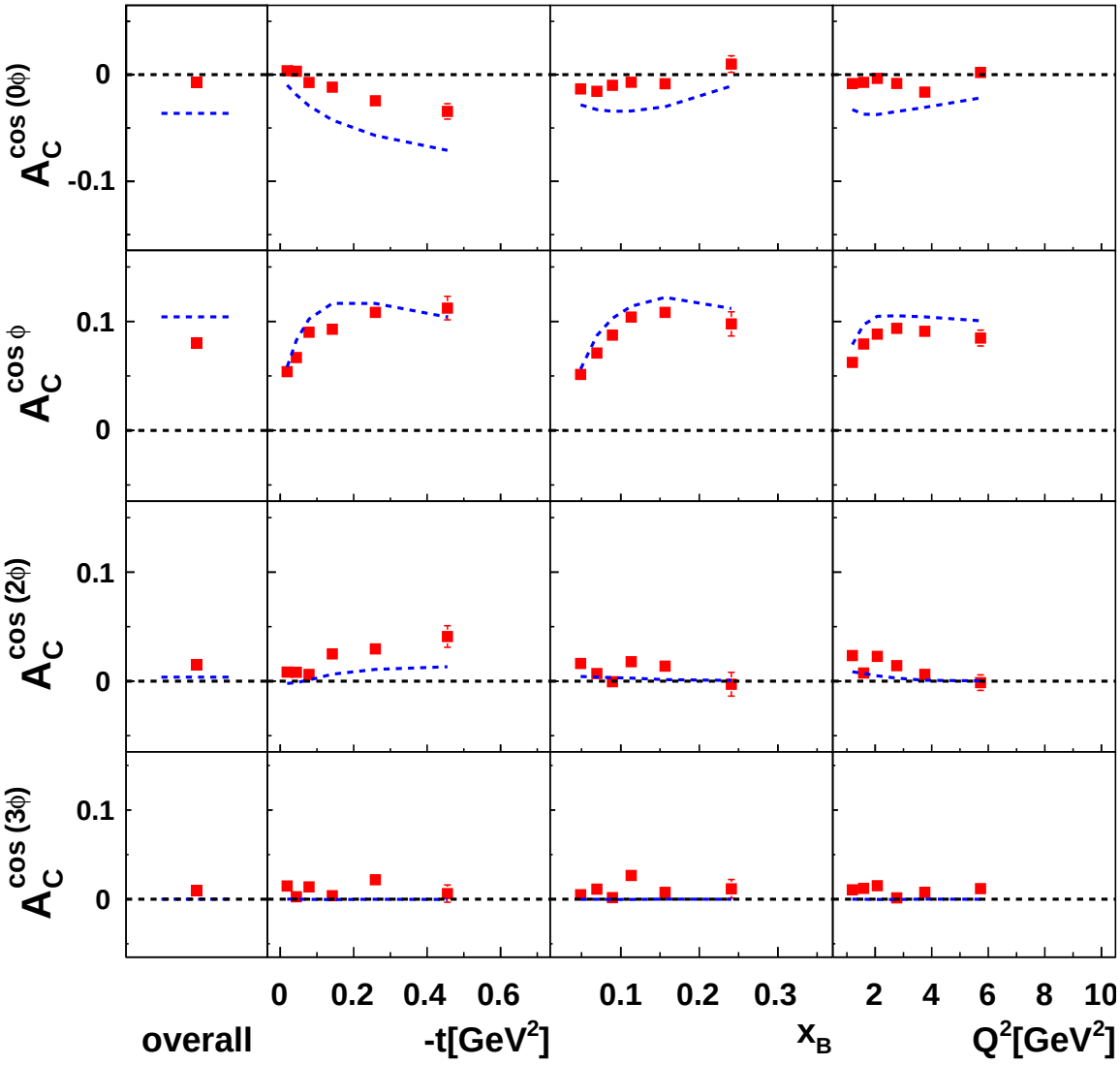

Figure 4.24: The 4–in–1 results for the BCA amplitudes obtained from model five of the GMC_DVCS generator in the usual kinematic binning.

Amplitude	$A \pm \delta(\text{stat.}) \pm \delta(\text{syst.})$	M_X^2 shift	Bg–corr.	Four–in–one error
$A_C^{cos(0\phi)}$	$-0.020 \pm 0.006 \pm 0.016$	0.004	0.000	0.015
$A_C^{cos(\phi)}$	$0.055 \pm 0.009 \pm 0.013$	0.001	0.001	0.013
$A_{LU,I}^{sin(\phi)}$	$-0.224 \pm 0.028 \pm 0.050$	0.001	0.005	0.050
$A_{LU,DVCS}^{sin(\phi)}$	$0.043 \pm 0.028 \pm 0.006$	0.000	0.004	0.002

Table 4.11: The results of the leading–twist amplitudes together with their statistical and systematic uncertainties. The latter ones are also split into the different contributions arising from the missing mass shift (M_X^2 shift), the background correction (Bg–corr.) and the Four–in–one error.

4.6.6 Summary of systematic uncertainties

In table 4.11 the systematic uncertainties of the leading–twist amplitudes are stated. The uncertainties of the charge–related asymmetry amplitudes are dominated by the Four–in–one error. The $A_{LU,DVCS}^{\sin\phi}$ amplitude is dominated by the uncertainty arising from the background correction. Note, that the BSAs receive another contribution to the systematic uncertainty from the uncertainty in the determination of the beam polarization. It amounts to a scale uncertainty of 3.4 %, which is negligible for the magnitudes in the present analysis. The systematic uncertainties are in the same order of magnitude as the statistical ones. The bin–wise systematic uncertainties are displayed in the next chapter.

5 Results

In this chapter some of the former HERMES results on DVCS are shown and compared to the results obtained from the present analysis. In addition, all asymmetry amplitudes from the current analysis are shown together with theoretical model calculations. In the following the dependence of the asymmetries on the squared missing mass are discussed and an estimate of the asymmetry from the associated processes is given. Finally, two of the twist–2 amplitudes are exploited towards an extraction of the CFF $\mathcal{H}$.

5.1 Former HERMES results on DVCS

The first DVCS data was published by the HERMES collaboration in Ref. [A+01]. All data taken off a hydrogen target in the years 1996 and 1997 was analyzed. The single–charge BSA was extracted with a least–square method and is shown in figure 5.1 as a function of ϕ. The integrated result yielded a value of:

$$A_{\mathrm{LU},e^+} = -0.23 \pm 0.04\ (\mathrm{stat.}) \pm 0.03\ (\mathrm{syst.}). \tag{5.1}$$

The systematic uncertainty includes contributions from the smearing effect and the uncertainty in the determination of the beam polarization as well as contributions from false asymmetries due to the BH process and the neutral pion contamination.

In addition, the analyzing power $A_{\mathrm{LU},e^+}^{sin\phi}$ defined as

$$A_{\mathrm{LU},e^+}^{sin\phi} \equiv \frac{2}{N^+ + N^-} \sum_{i=1}^{N} \frac{sin\phi_i}{P_{\ell,i}}, \tag{5.2}$$

where $N^+(N^-)$ denotes the number of events i with positive (negative) beam helicity, was evaluated in bins of the squared missing mass (see figure 5.1). While a significant negative amplitude was measured in the exclusive region up to approximately $M_X \approx 2.5$ GeV, the result was consistent with zero for larger M_X–values. The systematic uncertainties include only contributions from the smearing effect and the uncertainty in the determination of the beam polarization.

The first observation of a BCA amplitude was reported in Ref. [A+07a]. The results from a least–square fit with the four lowest cosine modulations is shown in figure 5.2. The integrated result after background correction yields:

$$A_{\mathrm{C}}^{cos(\phi)} = 0.063 \pm 0.029\ (\mathrm{stat.}) \pm 0.028\ (\mathrm{syst.}). \tag{5.3}$$

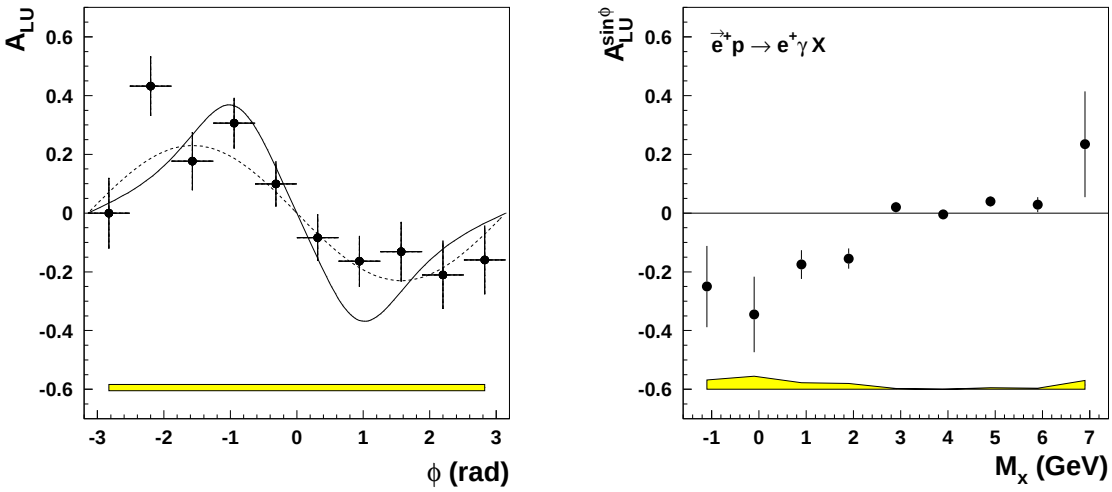

Figure 5.1: In the left panel the single–charge BSA is shown as a function of ϕ. The dashed curve represents the $sin\phi$–modulation of the data and the solid curve a model calculation taken from Ref. [KPV01]. On the right panel the analyzing power of the BSA is plotted as a function of M_X. Both plots are taken from Ref. [A$^+$01].

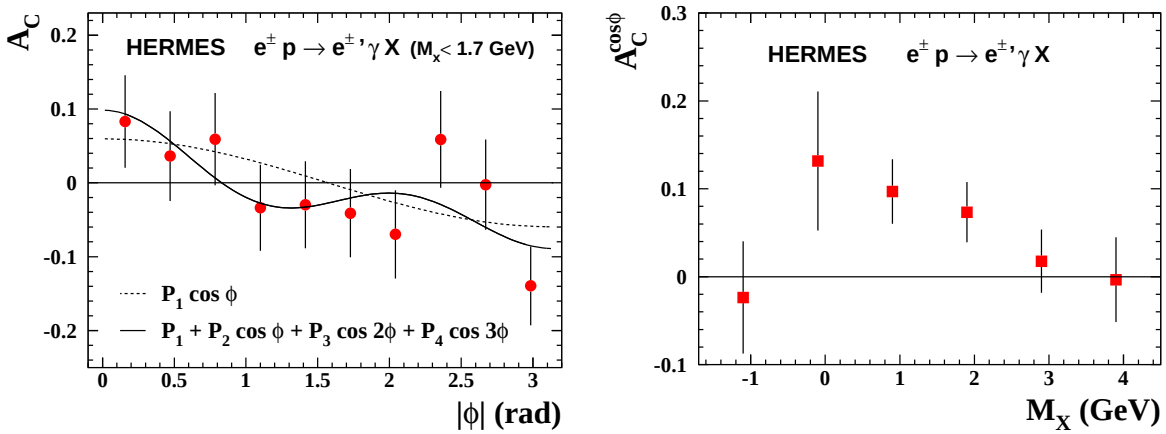

Figure 5.2: In the left panel the BCA is shown as a function of $|\phi|$. The solid curve represents a four–parameter fit and the dashed curve the $cos\phi$–dependence of the data (see labels on the plot). On the right panel the BCA is plotted as a function of M_X. Both plots are taken from Ref. [A$^+$07a].

The other harmonics were found to be compatible with zero. The systematic uncertainty consists of contributions from the background correction, the calorimeter calibration, possible detector and/or beam misalignments, and the smearing and acceptance effects.

In the right panel of figure 5.2 the cosine moment of the BCA is shown in bins of the missing mass. Again the result is compatible with zero for missing mass values larger than 2.5 GeV.

Asymmetry amplitudes with respect to the transverse target polarization have first been published by the HERMES collaboration in Ref. [A+08c]. In this analysis asymmetry amplitudes are accessible, whose dependence on the CFF $\mathcal{E}$ and the polarization dependent CFFs $\widetilde{\mathcal{H}}$ and $\widetilde{\mathcal{E}}$ are unsuppressed. For this publication the EML method was adopted for the first time.

During the last year also all HERMES data taken off an unpolarized deuterium target and other nuclear targets before the year 2006 were analyzed. In figure 5.3 the ratio of the $A_{\mathrm{LU,(I)}}^{sin\phi}$ asymmetry amplitude of the charge–averaged BSA between different nuclear targets and a hydrogen target is shown. The upper panel includes a data sample with an enriched contribution from the coherent process, where the virtual photon scatters off the whole nucleus, which stays intact in the final state. The lower panel involves an enriched contribution from the incoherent process, in which the final state nucleus breaks up. Note, that in case of the helium–4, nitrogen and neon target the single–charge BSA was used, because no electron data were available. For the hydrogen analysis only part of the data analyzed in the present work were used and the lower $\theta_{\gamma^*\gamma}$–cut was reduced from 5 mrad to 2 mrad. The ratio is flat around unity. In the case of the coherent–enriched data sample, this is in contrast to theory expectations [A+09b].

5.2 Comparison to former results

Even though the extraction method differed, the data involved in the former analyzes represented a subsample of the data evaluated for the present analysis. Therefore the obtained results need to be compatible. A comparison of the $A_{\mathrm{C}}^{cos\phi}$ asymmetry amplitude of the BCA between the present analysis and the results from Ref. [A+08c] and from Ref. [A+07a] is shown in figure 5.4.

Both the integrated results and the results in the different kinematic bins agree very well. Note, that the binning changed in the present analysis. The systematic uncertainty increased compared to the previous analyzes as new model variants were evaluated for the four–in–one error.

As will be seen in the following section, also the comparison with the published results on the single–charge BSA agree very well. The comparison to the deuterium data will be shown in the next section, as well.

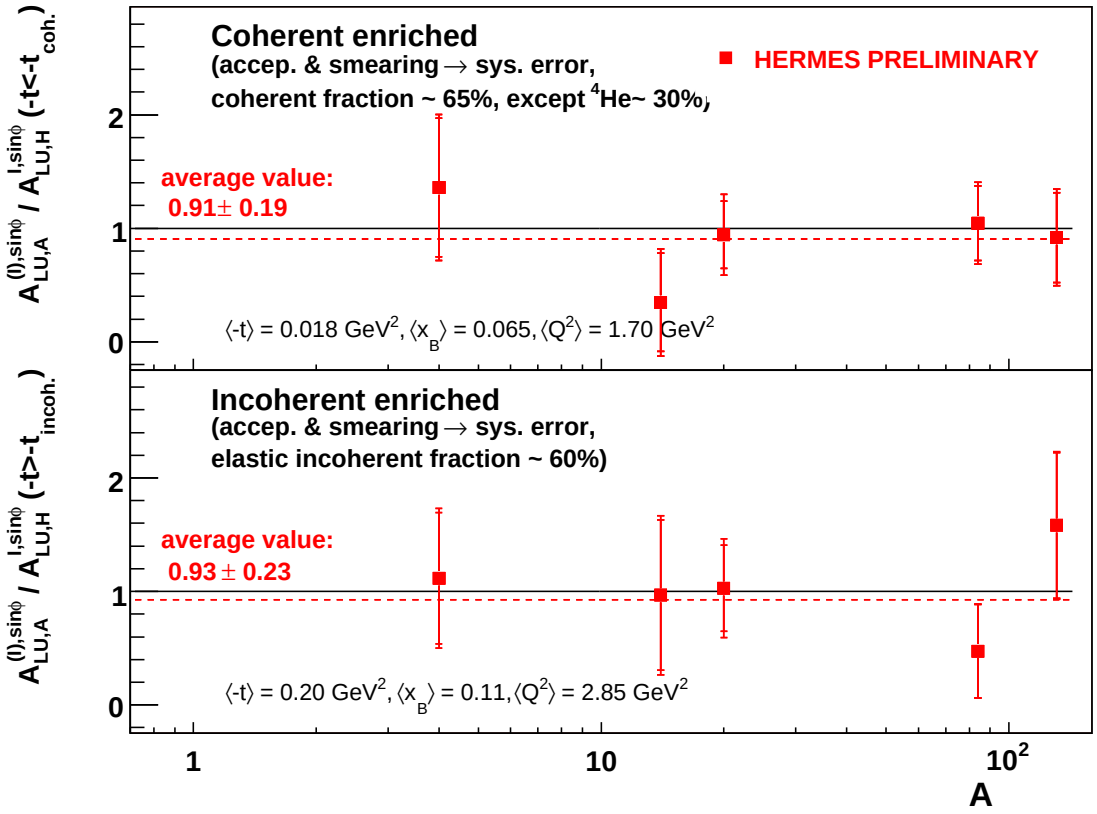

Figure 5.3: The ratios of the $A_{LU,(I)}^{sin\phi}$ asymmetry amplitude of the charge–averaged BSA between different nuclear targets and a hydrogen target. In the top (bottom) panel the (in)coherent process was enriched. Statistical and systematic uncertainties are expressed in the inner and outer error bars, while the latter does not include the Four–in–one error. To be published in [A$^+$09b]

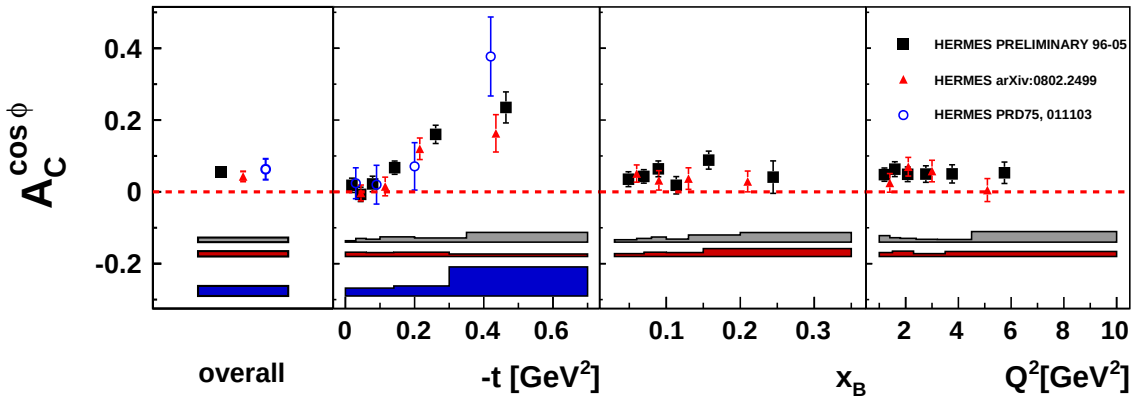

Figure 5.4: The comparison of the $A_C^{cos\phi}$ asymmetry amplitude of the BCA between the result of the present analysis (black squares) and the results from Ref. [A$^+$08c] (red triangles) and from Ref. [A$^+$07a] (blue opencircles).

5.3 DVCS azimuthal asymmetry amplitudes off an unpolarized hydrogen target

In this section the results from the present analysis are shown first binned in one dimension in $-t$, x_B and Q^2, followed by a two–dimensional binning in $-t$ and x_B, and are then compared to the recently obtained result on a deuterium target.[1]

5.3.1 One-dimensional binning

The results from the present analysis on the $A_{LU,DVCS}^{sin\phi}$ and $A_{LU,DVCS}^{sin(2\phi)}$ asymmetry amplitudes on the charge–difference BSA is shown in the first two rows of figure 5.5. This asymmetry is related to the squared amplitude of the DVCS process and thus to a bilinear combination of the CFFs. Both asymmetry amplitudes are found to be compatible with zero with a slight trend to positive values for the leading amplitude:

$$A_{LU,DVCS}^{sin\phi} = 0.043 \pm 0.028\ (\text{stat.}). \pm 0.006\ (\text{syst.}). \tag{5.4}$$

The $A_{LU,DVCS}^{sin(2\phi)}$ asymmetry amplitude is not originating from an underlying Fourier coefficient s_2^{DVCS} that does not exist for an unpolarized target as can be seen from Eq. 2.45. Though it might arise from the interplay of the coefficient s_1^{DVCS} with the BH coefficients in the denominator of the asymmetry (see Eq. 2.54). Also, the not shown constant term that has been included in the fit function Eq. 4.24 was in agreement with zero inside its statistical uncertainties, as expected. In the bottom row the fractional contributions from the associated BH process are shown. The impact of this contribution on this asymmetry is unknown.

No theory calculations are shown for these asymmetry amplitudes as the existing models do not include the full twist–3 sector and thus do not completely describe the $A_{LU,DVCS}^{sin\phi}$ asymmetry amplitude.

The $A_{LU,I}^{sin\phi}$ and $A_{LU,I}^{sin(2\phi)}$ asymmetry amplitudes of the charge–averaged BSA sensitive to the interference term, are shown in Fig 5.6 in the top two rows. While the $A_{LU,I}^{sin\phi}$ leading–twist amplitude is significantly negative

$$A_{LU,I}^{sin\phi} = -0.224 \pm 0.028\ (\text{stat.}). \pm 0.020\ (\text{syst.}), \tag{5.5}$$

the $A_{LU,I}^{sin(2\phi)}$ is approximately zero. The latter is expected to have the same sign and a smaller magnitude, which is in agreement to the present result. Neither of the two asymmetry amplitudes exhibits a significant dependence on the three kinematic variables $-t, x_B$ and Q^2.

Also shown in figure 5.6 are GPD model calculations based on the 'VGG' code formulated in a double distribution representation as described in [VGG99, GPV01]

[1] The asymmetry amplitudes are only shown within plots. Tables with exact numbers will be provided on an internet accessible database soon. In the meantime please contact the author or directly a member of the HERMES management.

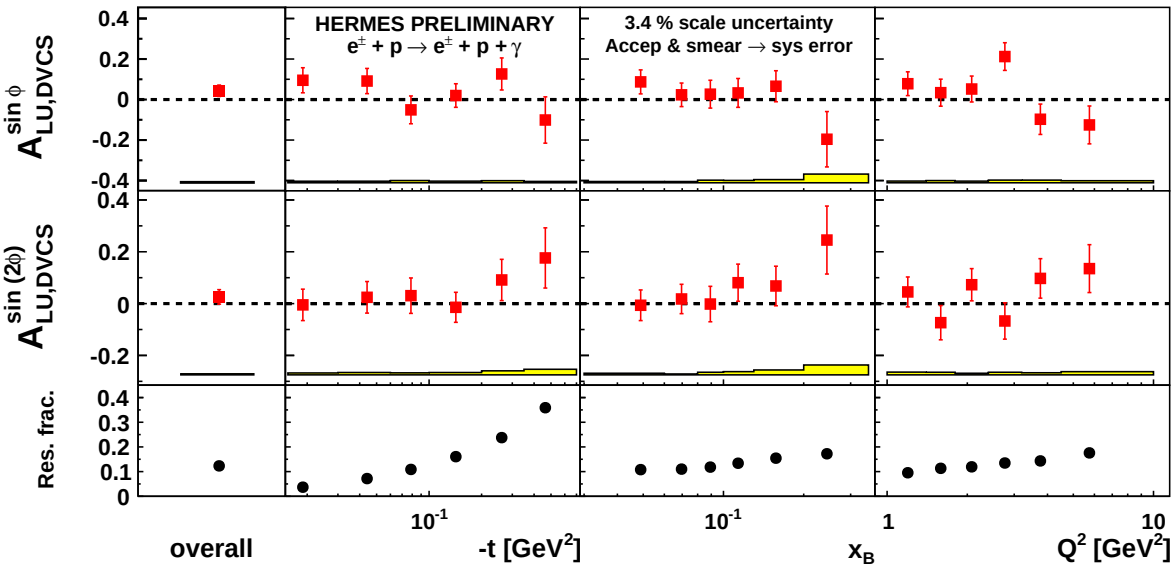

Figure 5.5: In the first two rows the $A^{sin(n\phi)}_{LU,DVCS}$ asymmetry amplitudes of the charge–difference BSA are displayed. In the first column the integrated results are displayed, in the second to fourth column the amplitudes in the usual kinematic binning are shown. The statistical uncertainties are represented in the error bars, while the systematic ones are shown as error bands. In the last row the fractional contributions of the associated process in the respective bins are given.

(see section 2.4.2). The two bands were obtained for two different approaches of the t–dependence of the GPD H: a Regge inspired t–dependence ('VGG Regge') and a factorized t–dependence ('VGG Fact.'). The bands were produced by varying the skewness parameters b_{val} and b_{sea} in the profile function [MR00] between unity and nine. In the latter case the skewness part of the GPD is negligibly small. For the $A^{sin\phi}_{LU,I}$ amplitude two broad bands are observed, showing its sensitivity to the skewness parameters. The inclusion of a D–term does not change the result on either BSA, as it only contributes to the real part of the CFF.

In addition, a model based on dual parameterization [PS02] with a Regge–inspired t–dependence ('Dual–GT Regge') [GT06] is shown (see section 2.4.3). Note, that the corrected version of this model [GT09] was used. All model variants overestimate the absolute size of the leading–twist amplitude by approximately a factor of two. Though, the model calculations involve only the elastic processes, while the data contains a 12 % contribution from the associated processes in the integrated result. The rather large systematic uncertainties reflect partially the large negative estimates from the models due to the Four–in–one error. The not shown constant term of the fit function was found to be compatible with zero.

In figure 5.7 the two leading–twist sine amplitudes of both BSAs are compared to the $A^{sin\phi}_{LU,\pm}$ and $A^{sin2\phi}_{LU,\pm}$ asymmetry amplitudes from the single–charge BSAs defined in

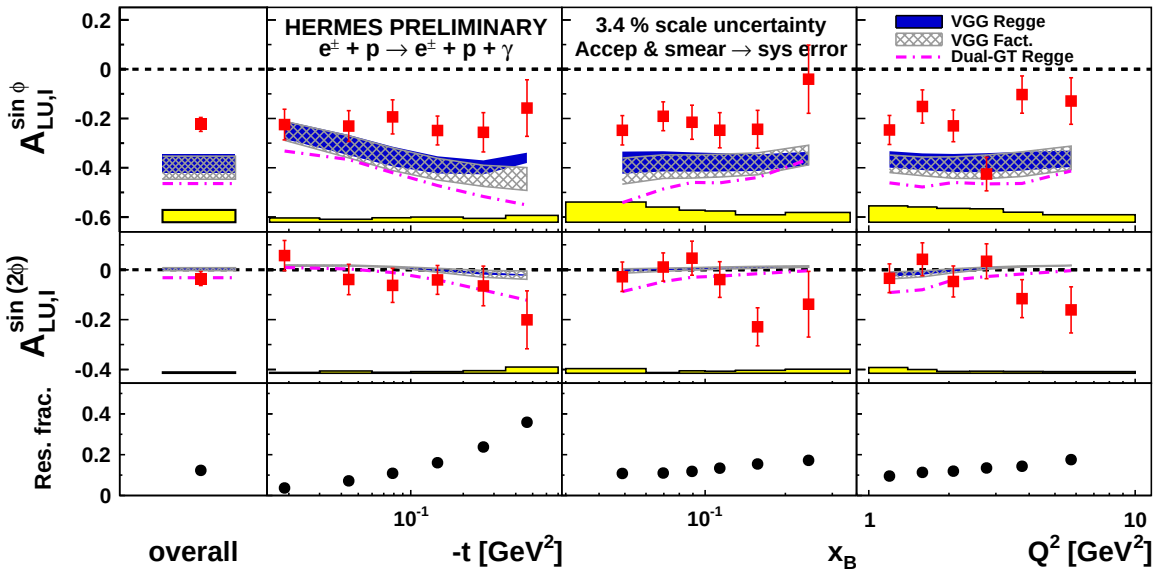

Figure 5.6: In the first two rows the $A_{\mathrm{LU,I}}^{sin\phi}$ asymmetry amplitudes of the charge–averaged BSA are displayed. The first column gives the integrated results, the second to forth column show the amplitudes in the usual kinematic binning. The blue (grey hatched) bands are calculated from the VGG–model with a Regge inspired (t–factorized) included. The magenta dash–dotted line represents a model based on dual parameterization with a Regge–inspired t–dependence. The statistical uncertainties are represented in the error bars, while the systematic ones are shown in error bands. The last row shows the fractional contributions of the associated process in the respective bins.

Eq. 2.49. For better comparability the electron data BSA was multiplied by a factor -1 and is represented by the blue filled symbols. The BSA from the positron data is displayed by the open green symbols.

As can be seen from the upper two rows of the figure, the magnitudes of the single–charge BSAs and the charge–averaged BSA are compatible, while the small differences of the BSAs from the two charges can be attributed to the charge–difference BSA that is related to the squared DVCS amplitude. This explanation is in full agreement with the definition of the three asymmetries in Eqs. 2.49, 2.50 and 2.54 as can be seen from Eq. 2.55, if the cosine coefficients related to the interference term in the denominator of Eq. 2.49 is negligible. In addition, Eq. 2.55 can be used to deduce the asymmetry amplitudes of the single–charge BSA for both beam charges. This exercise yields in the following results

$$A_{\mathrm{LU},e^+}^{sin\phi} = -0.181 \pm 0.046\ (\mathrm{stat.}), \tag{5.6}$$

$$A_{\mathrm{LU},e^-}^{sin\phi} = +0.267 \pm 0.065\ (\mathrm{stat.}), \tag{5.7}$$

which are in full agreement with the extracted results from the present analysis on

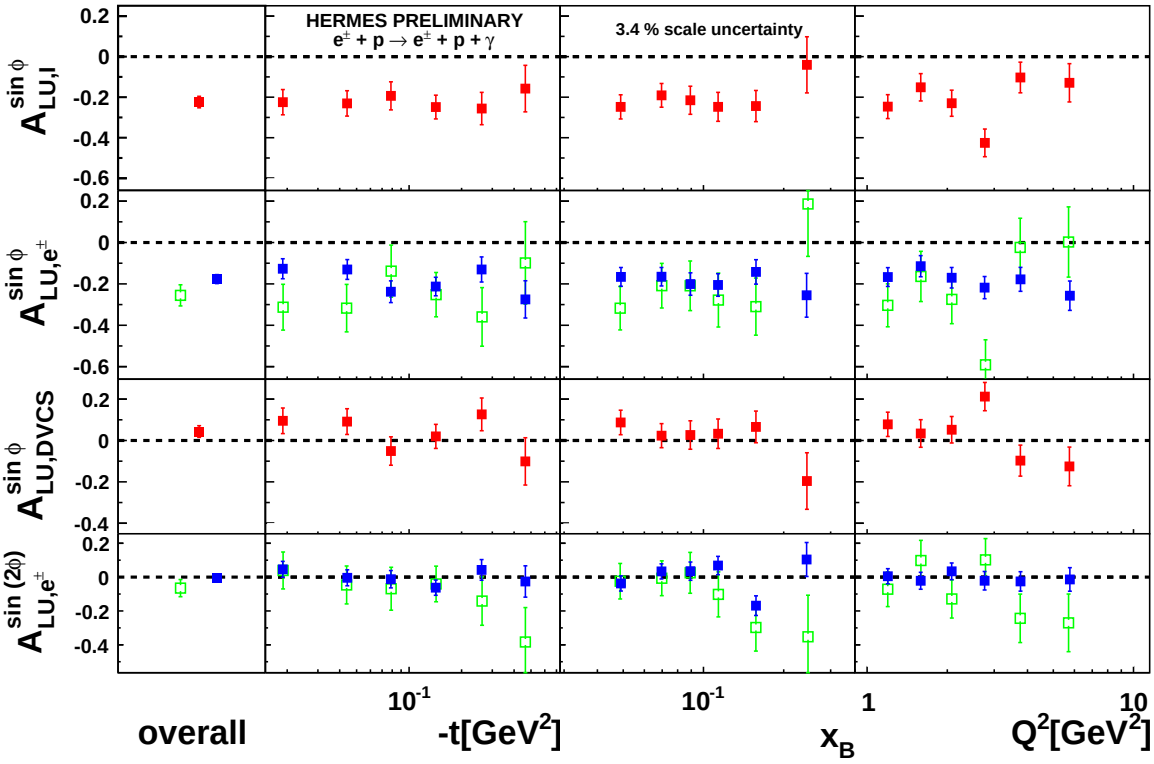

Figure 5.7: In the first (third) row the $A^{sin\phi}_{LU,I/DVCS}$ asymmetry amplitudes of the BSAs are displayed. In the second and fourth row the $A^{sin(n\phi)}_{LU,\pm}$ asymmetry amplitudes of the single–charge BSAs are shown for the electron data (blue filled squares) and the positron data (green open squares). The first column gives the integrated results, the second to forth column show the amplitudes in the usual kinematic binning.

the two beam charges:

$$A^{sin\phi}_{LU,e^+} = -0.177 \pm 0.022 \text{ (stat.)}, \tag{5.8}$$

$$A^{sin\phi}_{LU,e^-} = +0.255 \pm 0.051 \text{ (stat.)}. \tag{5.9}$$

The same single–charge BSA has been extracted at CLAS [S+01] resulting in

$$A^{sin\phi}_{LU,e^-} = +0.202 \pm 0.028 \text{ (stat.)}, \tag{5.10}$$

which also agrees with the present analysis. In addition CLAS published more compatible results on the single–charge BSA with different beam energies in [G+08b, G+08a] for various points in the phase space.

Note, that in all the previous discussion the role of the remaining 12 % contribution from the associated production is unknown. A model for its description was developed in [GMV03] relating the transition GPDs to the set of familiar twist–two GPDs.

Within this ansatz a correction factor

$$A_{\mathrm{LU,\,elas.}} = R_{\mathrm{BSA}} * A_{\mathrm{LU,\,exp.}} \tag{5.11}$$

was determined between the experimentally measured single–charge BSA $A_{\mathrm{LU,\,exp.}}$ and the 'clean' asymmetry from the pure elastic process $A_{\mathrm{LU,\,elas.}}$. For HERMES kinematics and integrating in W to 1.35 GeV a correction factor of 1.1 was found.

The $A_{\mathrm{C}}^{cos(n\phi)}$ asymmetry amplitudes of the BCA sensitive to the real part of the interference term, are shown in Fig 5.8 in the top four rows. The leading–twist $A_{\mathrm{C}}^{cos(0\phi)}$ and $A_{\mathrm{C}}^{cos\phi}$ amplitudes show significant non–zero magnitudes. Both show an increase in magnitude with increasing $-t$. This, as well as the different signs of the two asymmetry amplitudes are in agreement with the expectations. The dependence of the amplitude $A_{\mathrm{C}}^{cos\phi}$ on x_{B} and Q^2 is flat, while possibly reflecting a sign change in the amplitude $A_{\mathrm{C}}^{cos(0\phi)}$. The other two displayed amplitudes are related to higher twist contributions. While the amplitude $A_{\mathrm{C}}^{cos(2\phi)}$ is appearing at twist–3, the amplitude $A_{\mathrm{C}}^{cos(3\phi)}$ relates both to gluonic degrees of freedom and twist–4. Both are found to be compatible with zero. The not shown sinusoidal term appearing in the fit function Eq. 4.26 is slightly negative, but inside the statistical uncertainties compatible with zero.

The drawn model curves are also calculated from the same models as in the previous figures. The real–part depending BCA amplitudes are sensitive to the inclusion of a D–term. Therefore two variants of the VGG model were evaluated, one with ('VGG Regge, D') and one without the D–term ('VGG Regge, no D'). The Regge–inspired t–dependence was chosen, as the factorized one is theoretically under doubt. The variants with b_{val} set to nine and b_{sea} to unity was chosen, as it best describes the data. The comparison to the leading–twist amplitudes in the first two rows clearly disfavors the inclusion of a D–term in this model. A meaningful interpretation exploiting the relation of the D–term to the energy–momentum–tensor is at least questionable. Especially the influence of the associated process needs to be addressed first.

The dual model ('Dual–GT Regge') agrees well with the BCA amplitudes except for the large x_{B} and Q^2 range in the two leading amplitudes. In this model the D–term cannot be set to zero. Note, that compared to the previous version including the mistake in the implementation (shown, e.g. in [Zei08]) the BCA decreased slightly, while the charge–averaged BSA increased by more than a factor of two. The reason is that the missing factor of two in the model mainly affects the imaginary part of the CFF $\mathcal{H}$, while the real part is almost unaffected. Thus, the small decrease in the cosine amplitude of the BCA originated from a smaller real part of the CFF $\mathcal{E}$.

Also for the BCA a correction factor for the remaining contribution from the associated processes was derived in [GMV03]. It was found to be between 1.1 and 1.8 depending on the chosen model variant. The smaller value was obtained from a variant with an included D–term, while the large value was deduced from a variant without a D–term.

In conclusion, none of the existing GPD models can describe both charge–averaged

BSA and BCA results on the same time. Especially the large discrepancy in the leading $A_{\mathrm{LU,I}}^{sin\phi}$ asymmetry amplitude of the charge–averaged BSA is troublesome. From an experimental view the leading amplitudes show large absolute magnitudes, while the higher–order amplitudes are clearly suppressed. No evidence for a strong influence of higher–twist and/or gluonic contributions can be concluded.

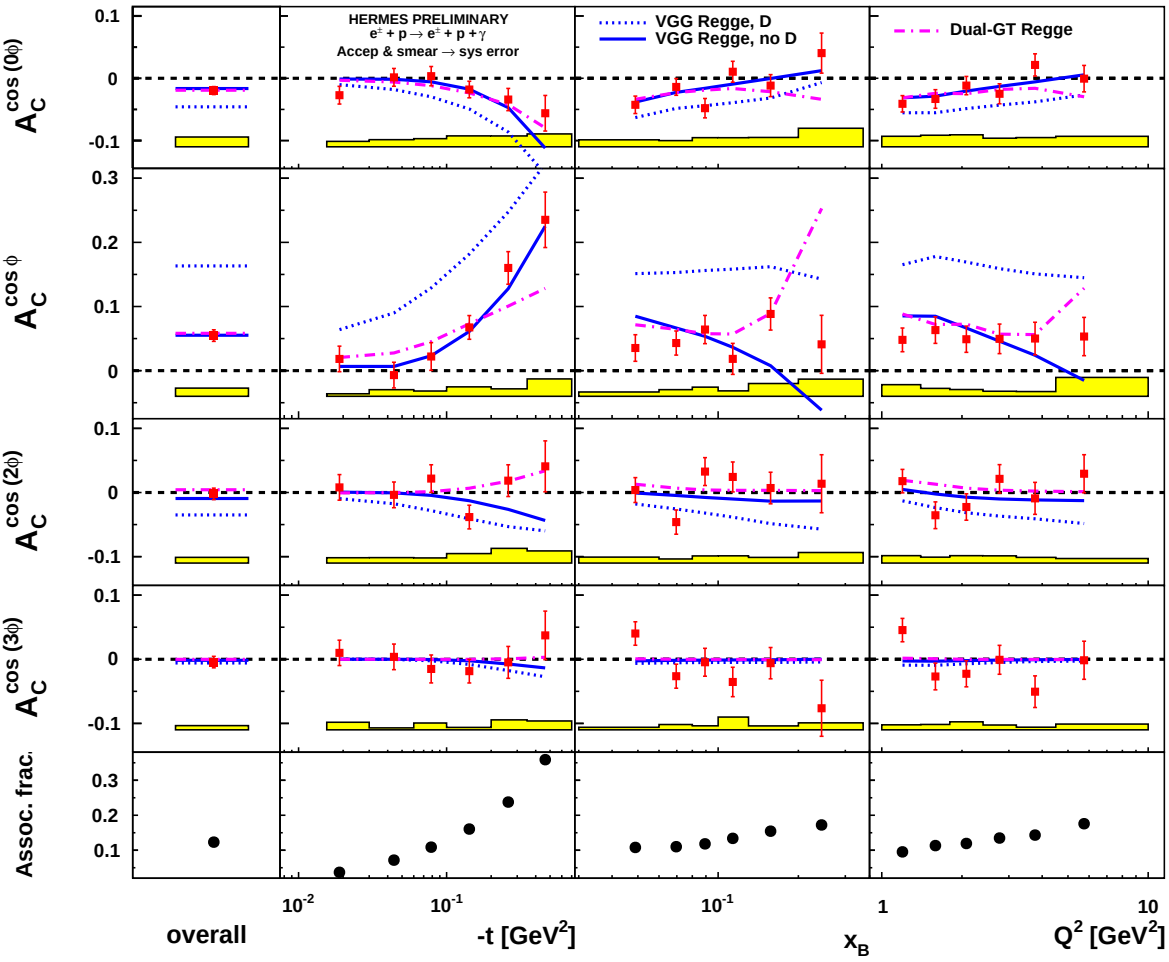

Figure 5.8: In the first four rows the $A_C^{cos(n\phi)}$ asymmetry amplitudes of the BCA are displayed. In the first column the integrated results is given, in the second to fourth column the amplitudes in the usual kinematic binning are shown. The dashed (solid) curves are calculated from a double distribution based model with (without) a D–term included. The statistical uncertainties are represented in the error bars, while the systematic ones are shown as error bands. In the last row the fractional contributions of the associated process in the respective bins are given.

5.3.2 Two-dimensional binning

As this analysis includes more data compared to previous ones, the result is also presented in a two–dimensional binning (see figures 5.9 and 5.10) to provide more data for the comparison to theoretical calculations. For this plots the usual six t-bins were chosen, this time evaluated for three different x_B–ranges as labeled in the upper rows of the plots in order to access the ξ and $-t$ dependence of the GPDs. The average x_B– and Q^2–values for the three x_B–ranges are also written on the plots. The systematic uncertainties include the same contributions as in the one–dimensional plots. This time only the uncorrected dual model was evaluated for the Four–in–One error. In certain bins the statistics for the two–photon analysis was very small and the maximum likelihood fit did not converge. Therefore the asymmetry amplitudes of the semi–inclusive background were taken from the one–dimensional case.

In the beam–helicity related asymmetry amplitudes in figure 5.9, the first bin in $-t$ is offset from the other bins in the two sinusoidal moments. Moreover, there seems to be a trend to negative $A_{LU,I}^{sin(2\phi)}$ amplitudes in the largest x_B region.

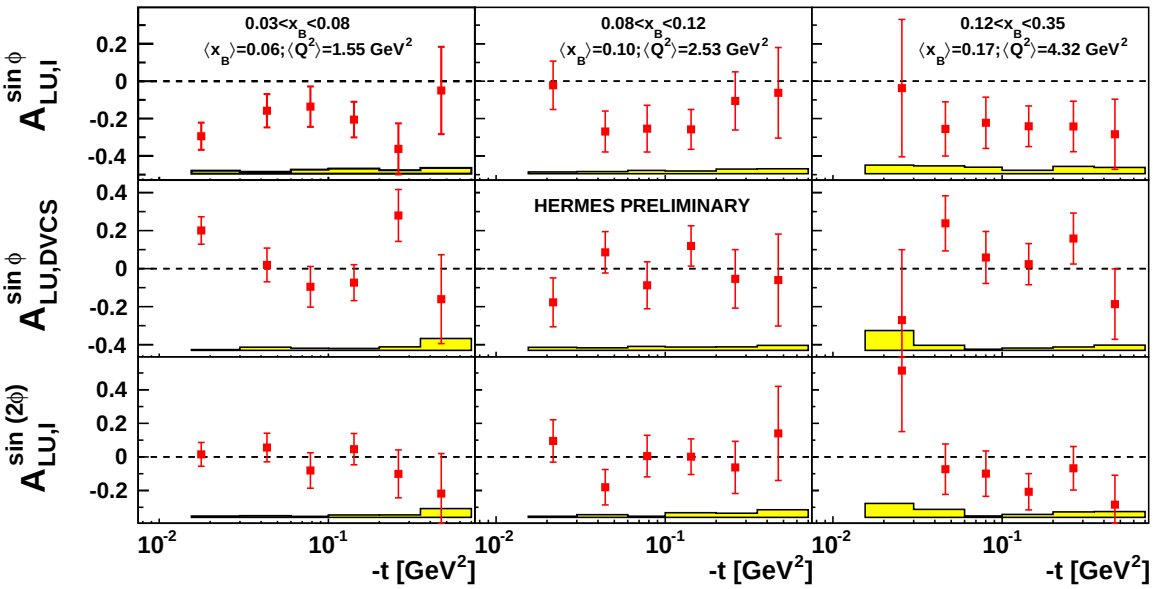

Figure 5.9: Three different $A_{LU\pm}^{sin(n\phi)}$ amplitudes of the BSAs extracted in the usual six t–bins for three different x_B–ranges (see labels in first row of the plot).

Apart from variations in the highest t–bin in the BCA amplitudes shown in figure 5.10 the results in the different x_B–ranges agree very well. Hence within the covered range of the experiment also no trend depending on the twist–defining squared momentum transfer Q^2 is observed. This is in agreement with the conclusion drawn in the previous section.

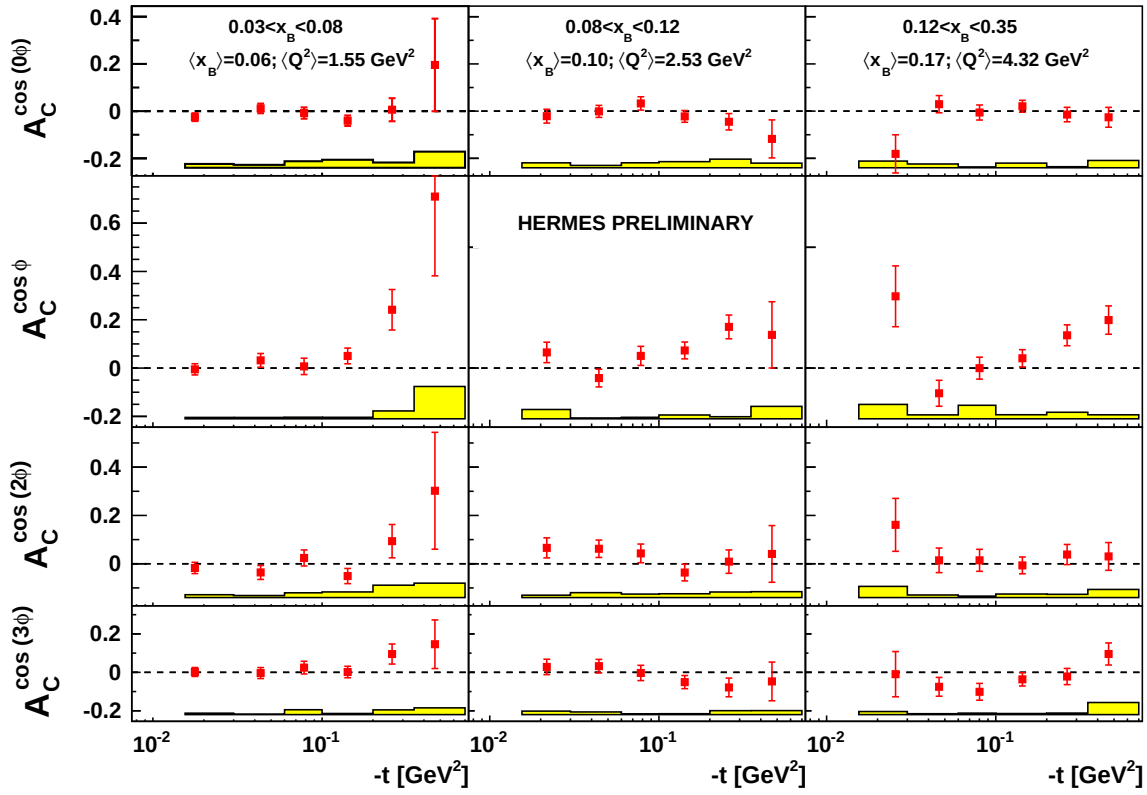

Figure 5.10: The four cosine moments of the BCA extracted in the usual six t–bins for three different x_B–ranges (see labels in first row of the plot).

5.3.3 Comparison to results off the unpolarized deuterium target

In figure 5.11 the BCA amplitudes are compared to the results obtained off an unpolarized deuterium target at the HERMES experiment [A+09a]. These results are represented by the red squares. In the case of an unpolarized deuterium target, both coherent and incoherent processes enter into the result. In the first t–bin the data contains the largest contribution from the coherent process on the deuteron of more than 40 %. Though, no deviations between the result on the hydrogen and the deuterium target were observed. The discrepancy in the highest t–bin might originate from the elastic and/or associated process off the neutron.

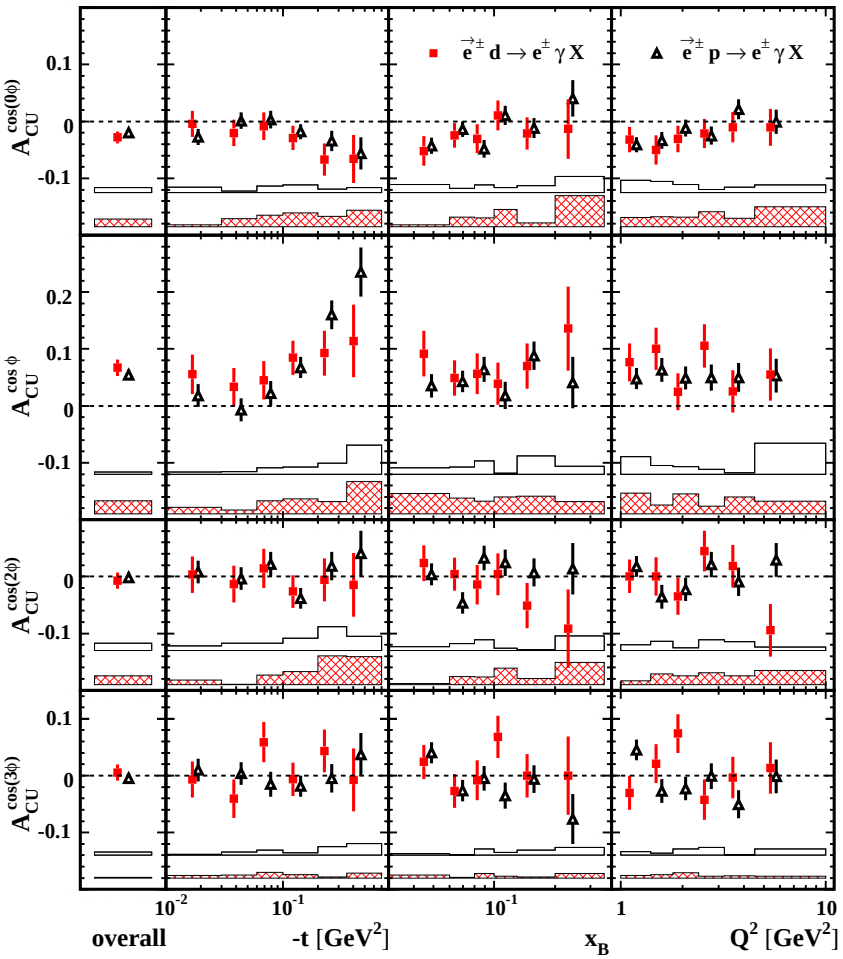

Figure 5.11: In the four rows the $A_C^{cos(n\phi)}$ asymmetry amplitudes of the BCA are displayed. The first column gives the integrated results, the second to fourth column show the amplitudes in the usual kinematic binning. The black squares represent the hydrogen analysis subject of this work and the red squares show the results from an analysis off an unpolarized deuterium target [A+09a].

Also in the amplitudes of the charge–difference BSA the results from the two targets

are compatible (not shown here). Only in the $A_{LU,I}^{sin(2\phi)}$ asymmetry amplitudes the results deviate from each other (see figure 5.12). The reason for this deviation is unclear. The leading–twist amplitudes $A_{LU,I}^{sin\phi}$ agree very well. The amplitudes $A_{LU,I}^{cos(0\phi)}$, which were included as a consistency check in the fit functions, are found to be compatible with zero for both targets, as expected.

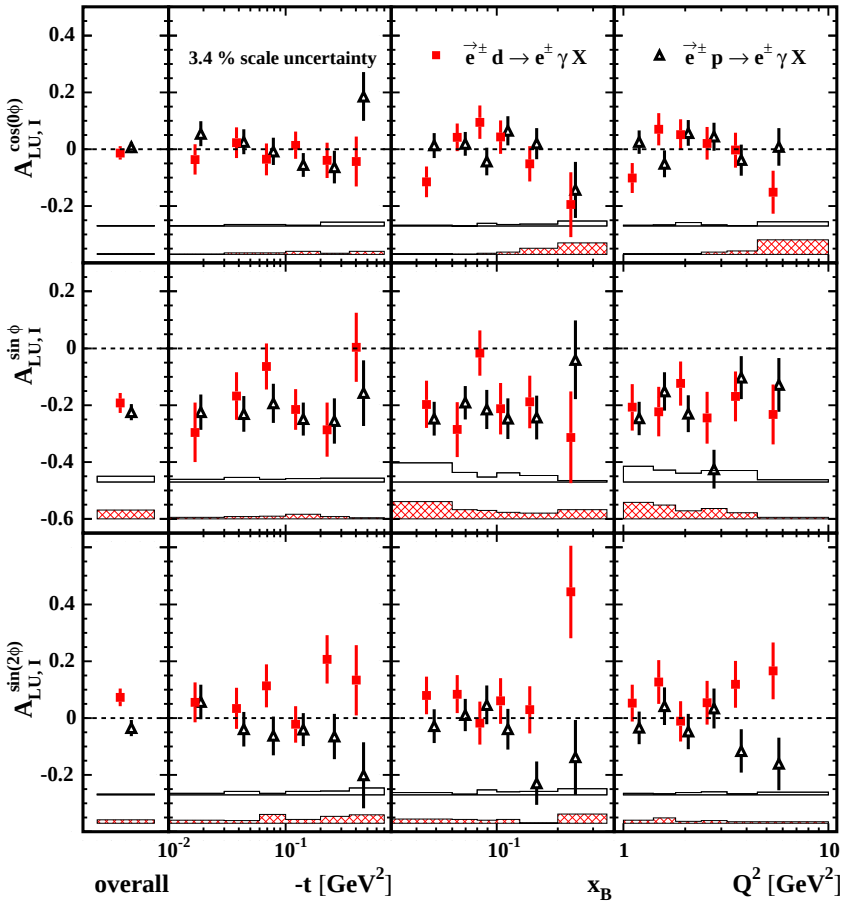

Figure 5.12: In the three rows the asymmetry amplitudes of the charge–averaged BSA are displayed. The first column gives the integrated results, the second to fourth column show the amplitudes in the usual kinematic binning. The black squares represent the hydrogen analysis subject of this work and the red squares show the results from an analysis off an unpolarized deuterium target [A$^+$09a].

5.4 Missing mass dependence

The results shown in the previous section were obtained from the whole exclusive region in the squared missing mass between $-2.79\,\mathrm{GeV}^2$ and $2.25\,\mathrm{GeV}^2$. In figures 5.13 and 5.14 the leading–twist amplitudes of the three asymmetries are shown as a function of the squared missing mass. For this study, both the data before and after applying the shift in the missing mass was used, but no background correction was performed.

The leading–twist $A_{\mathrm{LU,I}}^{\sin\phi}$ amplitude of the charge–averaged BSA is negative and flat in the whole exclusive region up to around $4\,\mathrm{GeV}^2$ and becomes zero for larger values of M_X^2. This agrees with the expectation that no charge–related asymmetry amplitude appears in the semi–inclusive region. This behavior is also compatible with the earlier result of figure 5.1, where the single–charge BSA is plotted as a function of the squared missing mass. The $A_{\mathrm{LU,DVCS}}^{\sin\phi}$ amplitude is found to be zero, both in the exclusive and semi–inclusive region.

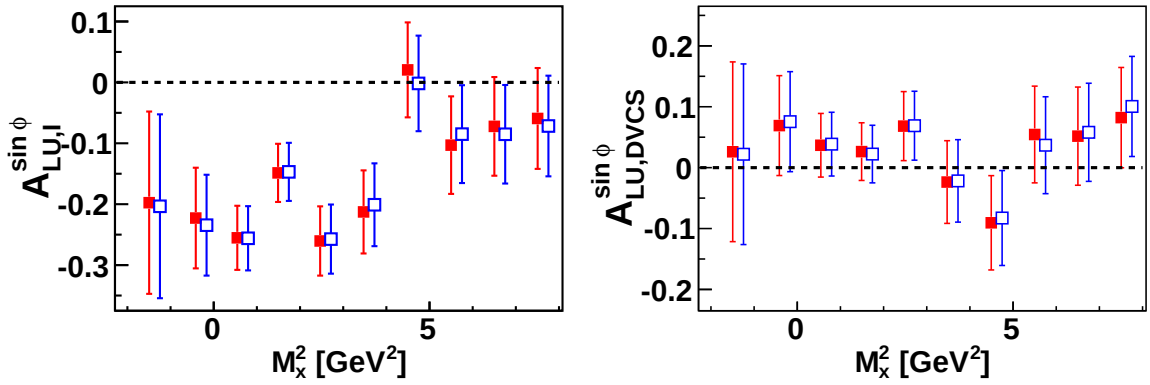

Figure 5.13: The leading–twist amplitudes of the BSAs in bins of the squared missing mass. The data was not corrected for any background process. The filled red (open blue) symbols show the data before (after) applying the missing mass shift. The open symbols were artificially shifted for a better optical comparison.

In figure 5.14 the $A_{\mathrm{C}}^{\cos(0\phi)}$ and the $A_{\mathrm{C}}^{\cos\phi}$ amplitude of the BCA are shown. While the $A_{\mathrm{C}}^{\cos\phi}$ amplitude exhibits positive values up to around $M_X^2 = 4\,\mathrm{GeV}^2$, the $A_{\mathrm{C}}^{\cos(0\phi)}$ amplitude shows an unexpected sign change in the exclusive region. As this sign change is not visible if the same amplitude is binned in the constrained t, the effect is expected to originate from the photon energy reconstruction. Another less likely explanation is the influence of the associated production that increases from 8 % fractional contribution in the range between $1\,\mathrm{GeV}^2 < M_X^2 < 2\,\mathrm{GeV}^2$ to 24 % in the range between $3\,\mathrm{GeV}^2 < M_X^2 < 4\,\mathrm{GeV}^2$. However, this could not explain, why the amplitude remains non–zero up to $6\,\mathrm{GeV}^2$, where the fractional contribution from the

semi–inclusive processes is dominant (79 %). It has been verified that this effect is not arising from:

- ⋆ the normalization to DIS events by using the information from the luminosity monitors as an alternative method for normalization;
- ⋆ the choice of the fit function by extracting the BCA for the absolute value of ϕ;
- ⋆ too restrictive exclusive cuts by opening the upper t–cut to -1 GeV^2 and the upper $\theta_{\gamma^*\gamma}$–cut to 70 mrad;
- ⋆ the magnitude of the missing mass shift by varying the amount of the shift and checking that the deviation from zero in the non–exclusive region did not change significantly.

The $A_C^{cos\phi}$ amplitude is found to be compatible with zero in the semi–inclusive region, which is in agreement with the expectations and the former HERMES publication [A+07a] as shown in figure 5.2.

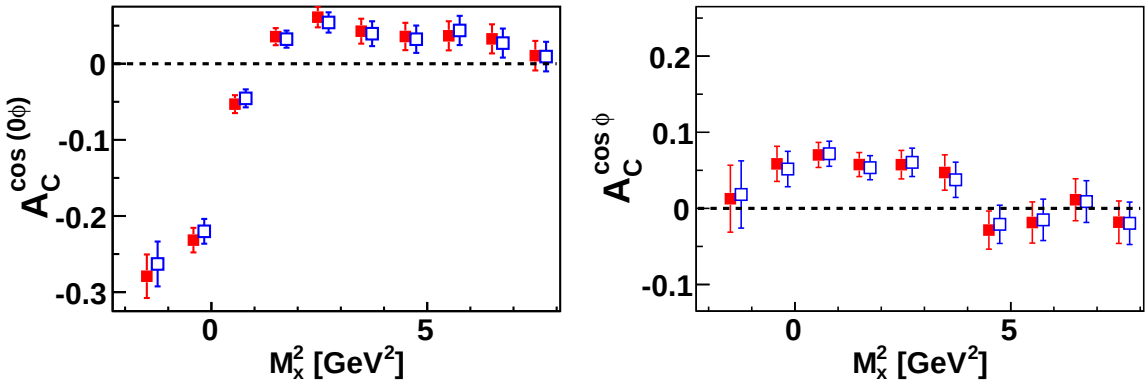

Figure 5.14: The leading–twist amplitudes of the BCA in bins of the squared missing mass. The data was not corrected for any background process. The filled red (open blue) symbols show the data before (after) the applied missing mass shift. The open symbols were artificially shifted for a better optical comparison.

The asymmetry amplitudes displayed in figures 5.13 and 5.14 receive contributions from all participating processes weighted by their fractional contributions:

$$\begin{aligned} A_{\text{meas.}} &= f_{\text{elas. BH/DVCS}} \cdot A_{\text{elas. BH/DVCS}} \\ &+ f_{\text{assoc. BH/DVCS}} \cdot A_{\text{assoc. BH/DVCS}} \\ &+ f_{\text{SIDIS}} \cdot A_{\text{SIDIS}} \\ &+ f_{\text{excl.}\cdot\pi^0} A_{\text{excl.}\pi^0}. \end{aligned} \tag{5.12}$$

The only unknown fractional contribution is the one from the DVCS process. By using different assumptions on this quantity, it has been tried to fit the asymmetry

Asymmetry		$A_{LU,I}^{sin\phi}(p \to p')$	$A_{LU,I}^{sin\phi}(p \to \Delta)$	$A_{C}^{cos\phi}(p \to p')$	$A_{C}^{cos\phi}(p \to \Delta)$
std. cuts	std. fractions	-0.21 ± 0.05	-0.29 ± 0.26	0.07 ± 0.02	0.01 ± 0.08
open cuts		-0.19 ± 0.07	-0.49 ± 0.31	0.06 ± 0.02	0.06 ± 0.10
std. cuts	no asso.	-0.22 ± 0.03	0.00 ± 0.00	0.06 ± 0.01	0.00 ± 0.00
open cuts		-0.24 ± 0.03	0.00 ± 0.00	0.06 ± 0.01	0.00 ± 0.00
std. cuts	double asso.	-0.21 ± 0.05	-0.25 ± 0.11	0.07 ± 0.02	0.04 ± 0.04
open cuts		-0.19 ± 0.07	-0.34 ± 0.14	0.06 ± 0.02	0.06 ± 0.04

Table 5.1: Fit result from fitting amplitudes in missing mass bins between −2.5 and +5. GeV^2. χ^2–values around 1.

amplitudes in bins of the squared missing mass in order to extract some limit on the asymmetries from the elastic and associated BH/DVCS processes. In the following discussion, the asymmetries from the SIDIS and the exclusive π^0 background processes were always treated as dilutions.

In the first approach the fractional contributions of the elastic and the associated BH process (along with the background contributions) were extracted by a MC study. It was assumed that the fractional contributions of the elastic and associated DVCS contributions behave like the BH contributions. This assumption can neither be proven nor disproven from basic considerations. With the fractional contributions at hand, the amplitudes $A_{LU,I}^{sin\phi}$ and $A_{C}^{cos\phi}$ were fit in the range between −2.5 and 5 GeV^2. The results for the elastic and associated asymmetries are given in the first row of table 5.1 ('std. cuts' and 'std. fractions'). The means and the statistical uncertainties of the asymmetries of the elastic processes are compatible with the asymmetries in the integrated exclusive region of the missing mass. The asymmetries of the associated process are deviating from these results and show an increased statistical uncertainty. The reduced χ^2 of the fit was around unity. The fit has been repeated twice: First with the fractional contribution of the associated process set to zero ('std cuts' and 'no asso.') and second with the fractional contribution of the associated process multiplied by a factor of two ('std cuts' and 'double asso.'). In both cases the sum of the fractional contributions of the elastic and associated production was kept constant. Only in the case of no associated production an impact on the results of the elastic process is seen. This effect is a direct result from the chosen variation of the contributions in units of the associated contributions. The rows in table 5.1 labeled with 'open cuts' are obtained from a study, in which the upper requirements on the exclusive variables t and $\theta_{\gamma^*\gamma}$ were opened to 1 GeV^2 and 70 mrad, respectively. The results are compatible to those extracted with the standard cuts.

In a second approach the exclusive region of the missing mass distribution was split into two bins (−2.5–0 GeV^2 and 0–3 GeV^2). In this case the problem can be solved numerically, if the fractional contributions of the DVCS processes were known. Again the fractional contributions from the BH processes were used as an estimate for the DVCS contributions, but were then varied in steps of 0.1 %. The results are

plotted in figure 5.15. The left (right) plots show the asymmetry amplitudes $A_{LU,I}^{sin\phi}$ and $A_C^{cos\phi}$ for the elastic (associated) processes. On the horizontal axis the fractional contributions in the lower missing mass bin are displayed. Only the mean values of the $A_C^{cos\phi}$(elas.) amplitude vary depending on the fractional contributions. The propagated statistical uncertainties of the amplitudes from the associated process are huge and constant. They are governed by the statistical uncertainty in the measured asymmetry amplitudes $A_{meas.}$.

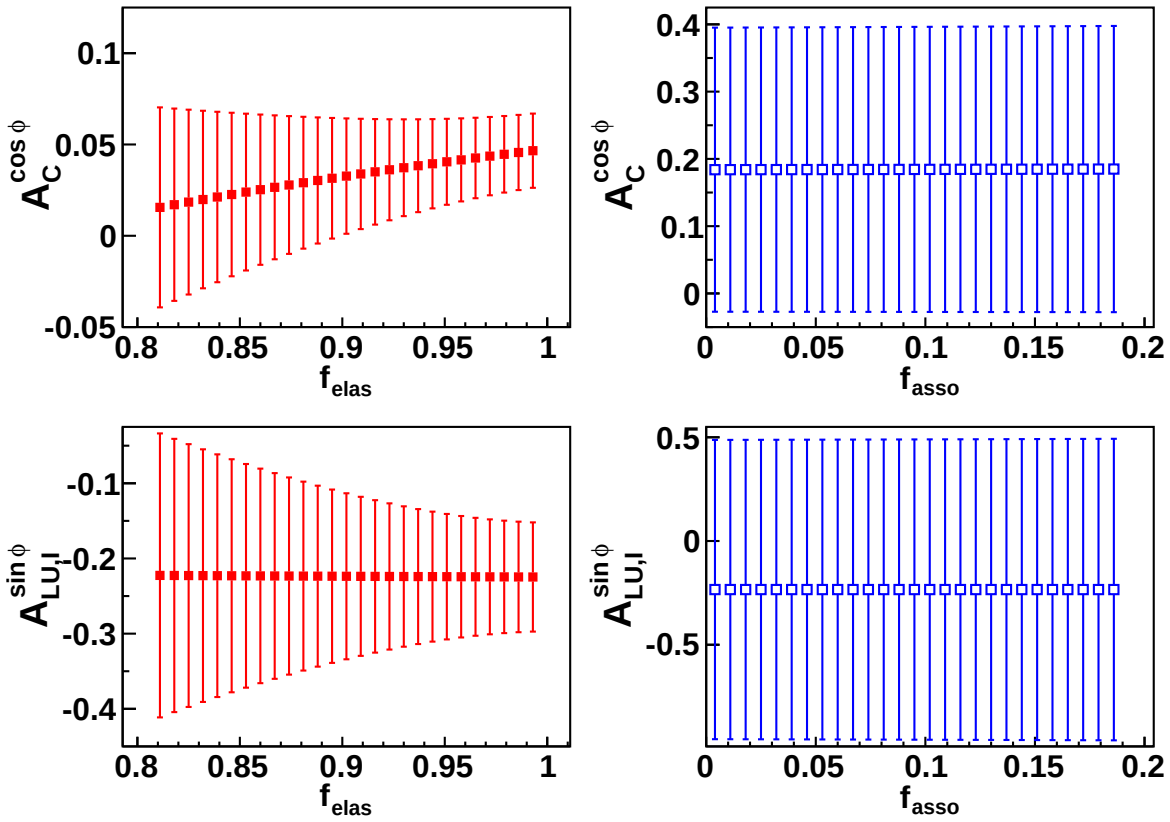

Figure 5.15: The separated asymmetry amplitudes from the elastic (left panels) and the associated processes (right panels) as a function of the fractional contributions in the lower missing mass bin. The error bars reflect (propagated) pure statistical uncertainties.

Both approaches resulted in similar observations:

- ⋆ The mean values of the amplitudes from the elastic processes vary by less than 0.03.
- ⋆ The statistical uncertainties of the amplitudes from the elastic processes increase with decreasing elastic contribution.

- ⋆ The statistical uncertainties of the amplitudes from the associated processes are too large to allow for any meaningful estimate of the size of the amplitude.

Thus, it seems safe to state that the observed asymmetry amplitudes obtained at the HERMES experiment are governed by the elastic processes. This result is in agreement to the theoretical calculations in [GMV03] for the BSA. However, in the case of the BCA the discussed experimental constraint suggests a smaller correction due to the associated contribution as was found for the GPD model that best describes the data. In any case it cannot be excluded that the impact of the associated production is sizeable and the size of its asymmetry will be an important experimental result from the data taken with the Recoil Detector.

5.5 Extraction of the CFF $\mathcal{H}$

Hard exclusive processes like DVCS can be described in the framework of GPDs, which are convolutions of CFFs. In this section an attempt to extract information on the CFF $\mathcal{H}$, which represents the leading contribution in HERMES kinematics (see Eq. 2.38), is shown.

To simplify the ansatz only the Fourier coefficients related to twist–2 GPDs were considered. The asymmetry amplitudes corresponding to three of them $\left(c_0^{\mathrm{I}},\, c_1^{\mathrm{I}}\right.$ and $\left.s_1^{\mathrm{I}}\right)$ were extracted in the present analysis. The remaining coefficient c_0^{DVCS} appearing in twist–2 cannot be accessed in asymmetry measurements.

While the two even moments are related to the real part of the photon helicity conserving amplitude $M^{1,1}$ (Eqs. 2.58 and 2.59), the odd moment depends on the imaginary part of the same amplitude (Eq. 2.53). Thus the two even moments can be directly compared as executed in Eq. 2.60, when only considering the dominant contributions in c_0^{I}. The result is shown in figure 5.16.

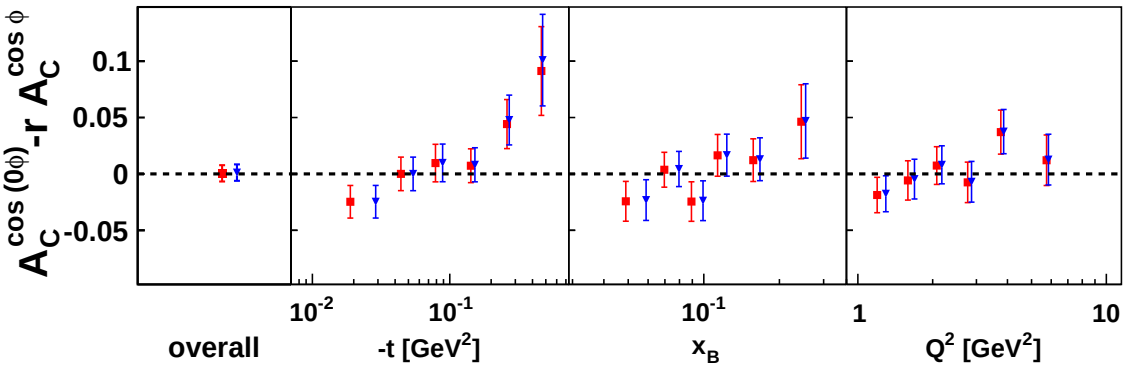

Figure 5.16: A consistency check comparing the asymmetry amplitudes $A_{\mathrm{C}}^{cos0\phi}$ and $A_{\mathrm{C}}^{cos\phi}$ using the expressions from [Bel02b] (blue triangles) and the advanced expression from [Bel09] (red squares). The result is shown in the usual kinematic binning.

For this comparison the asymmetry amplitudes corresponding to the discussed Fourier coefficients have been chosen, which is not fully equivalent as the cosine coefficient in the numerator together with a constant coefficient in the denominator might produce an additional constant. A constant fit to the weighted difference of the two asymmetry amplitudes showed that the results agree in each kinematic variable within a one–σ deviation. The larger deviation in the highest $-t$ point might be related to the increased contribution from the associated process in this bin. It has been tried to use the 'hot–fix' from [Bel09] accounting for kinematical approximations, but the effect is small even in the high t–region as can be seen from the blue triangles in the plot. It cannot be excluded that this effect originates from neglected higher twist terms.

In order to access the full CFF, the information from the even and odd twist–2 harmonics has to be combined. An ansatz to relate the real and imaginary part via a dispersion relation was explained in section 2.4.4. In this approach only the dependence on the CFF $\mathcal{H}$ was included as it is the dominant one at Hermes kinematics. In total a six parameter fit was chosen and all data points as displayed in figures 5.6 and 5.8 were included.

The fit to the asymmetry amplitudes $A_C^{cos\phi}$ and $A_{LU,I}^{sin\phi}$ converges with a reduced χ^2 below unity. This indicates that the fit exhibits no unique solution. Different starting values and ranges of the fit parameters (within a physically meaningful region) lead to significantly different results. In figure 5.17 one solution of the problem is depicted. The red squares show the results from the Hermes data and the black triangles the result from the fit to these points. Both agree very well.

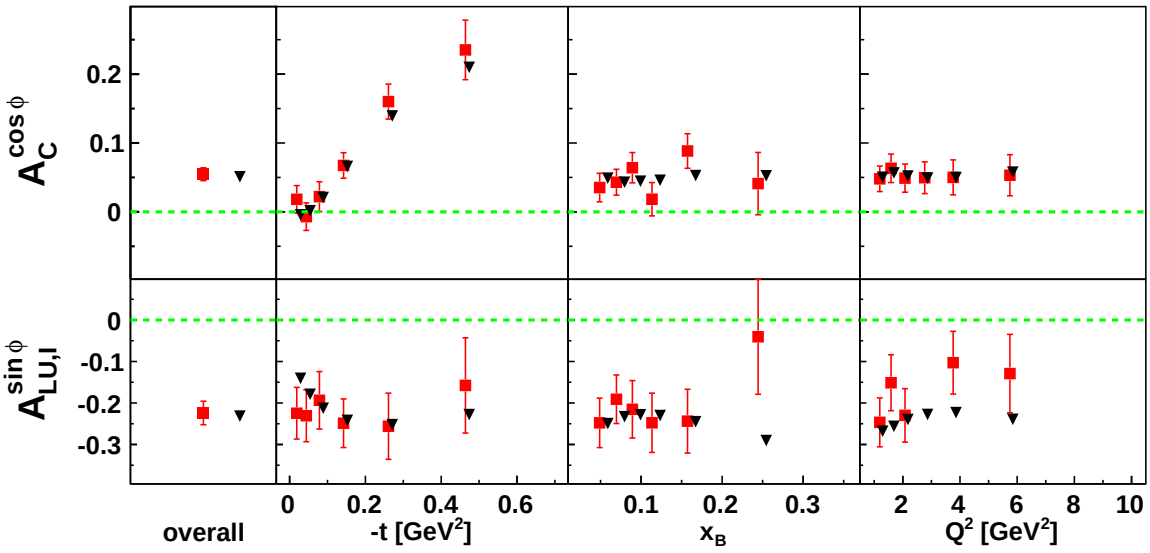

Figure 5.17: A comparison between the CFF fit results (black triangles) and the extracted Hermes data (red squares). The chosen ansatz reflected the data very well.

The inclusion of the $A_C^{cos\phi}$ amplitude degrades the reduced χ^2–value to around 4. Judging from figure 5.16 the deviation in the last t–bins might produce this effect, even though the theoretical calculations used to compare to the data in section 5.3.3 describe both asymmetry amplitudes very well.

Various conclusions can be drawn from this exercise. First, the chosen parameterization is flexible enough to describe both the leading charge–averaged BSA and BCA amplitudes contrary to the models discussed in sections 2.4.2 and2.4.3. Therefore the assumptions inherent to the approach like neglecting higher twist contributions and all three CFFs but $\mathcal{H}$ seem to be confirmed in Hermes kinematics.

Second, the data presented here is not sufficient to extract an unique solution on the CFF $\mathcal{H}$. This is most probably to the limited covered range in x_B and thus x (see

figure 5.18). Therefore the choice of the parameterization is essential for the discussed approach. The present form guarantees on the one hand a smooth transition of the imaginary part of $\mathcal{H}$ towards large x. On the other hand even strongly differing fit results produce similar shapes (see again figure 5.18). The shape of the real part of $\mathcal{H}$ is varying stronger as it includes the integration over the complete x–range (see figure 5.19).

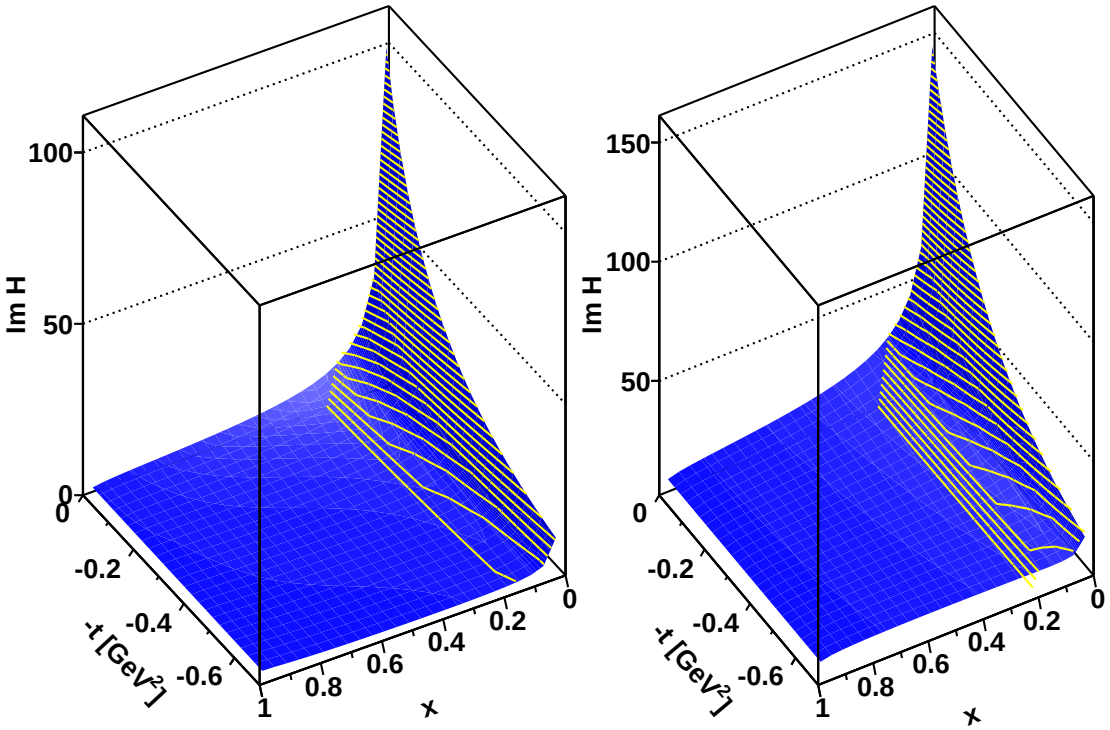

Figure 5.18: Two solutions for the imaginary part of the CFF $\mathcal{H}$ as a function of $-t$ and x are shown on the two panels. The yellow lines depict the experimentally accessible range at HERMES.

Third, an inclusion of further asymmetry amplitudes requires to give up certain simplifications like neglecting all CFFs but $\mathcal{H}$. The limited number of data points from the present analysis does not allow to proceed with this approach restrictive on the present results.

In [Kum09] the previous presented fit approach was developed. The small x–dependence was extracted from DVCS cross section data taken at H1 and ZEUS ([C$^+$03, A$^+$05, Sch07, A$^+$08a]). The authors confronted the parameterization with earlier published HERMES results on the BCA [A$^+$08c] , single–charge BSAs from CLAS [G$^+$08b] and cross section measurements from HALL A [MC$^+$06]. The former two results could be fit under the assumption of a dominance of the CFF $\mathcal{H}$ as has been

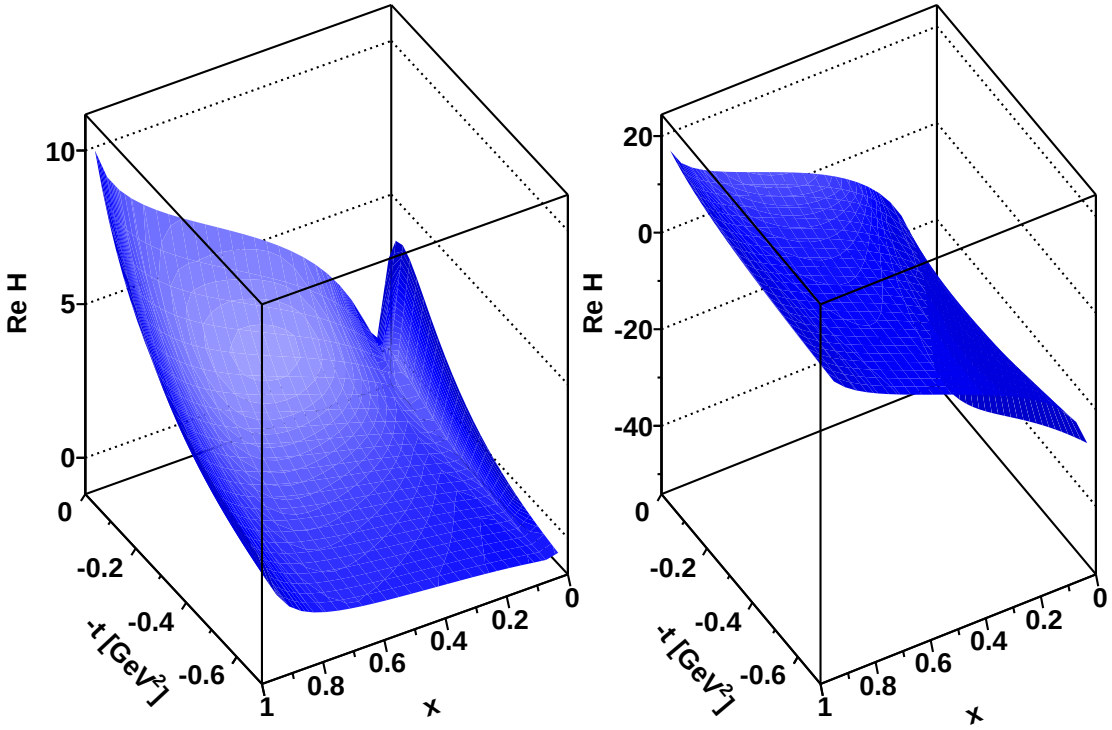

Figure 5.19: Two solutions for the real part of the CFF $\mathcal{H}$ as a function of $-t$ and x are shown on the two panels.

confirmed in the present work. In order to also describe the HALL A results a large real part of the DVCS amplitude was necessary, which was introduced by increasing the contribution from the GPD $\widetilde{H}$ [Kum09]. In addition, the results from these fits are describing earlier BSA data from HERMES [Ell07] and polarized cross section measurements from HALL A. However, the authors are emphasizing that the current results are not unique, even though very promising to become unique once more data is added into the fitting procedure.

More DVCS results are expected in the near future, e.g. the first analysis with a separation of the elastic and associated BH/DVCS contributions with the Recoil Detector at HERMES. An extension of the approach to the other leading–twist CFFs is possible via target spin asymmetries, which can be combined with different beam helicity or charge states. HERMES published various asymmetry amplitudes off a transversely polarized hydrogen target [A$^+$08c] and will publish data on a longitudinally polarized hydrogen target, which has been studied as well by the CLAS collaboration [C$^+$06]. In addition, the above explained fit procedure allows to easily combine results on various exclusive channels like meson production. A rich variety of data is already available on these channels, e.g. the HERMES results on exclusive ρ^0–production [A$^+$09c] and

π^+–production [A$^+$08b], which then allows to access also transition GPDs.

A similar strategy to fit real and imaginary parts of CFFs was outlined in [Gui08]. In the former approach the underlying GPDs are taken from the VGG code to calculate an allowed region for the variation of each CFF. The real and imaginary parts of the CFFs were not related via a dispersion integral, but taken as independent fit parameters. However, in the underlying VGG model thus relations exist and hence do lead to some coupling of the parameters. The fit procedure was confronted with HALL A data, but did not yet produce a constraint on any observable as the number of parameters exceeded the number of data points. In [GM09] the same approach was studied on the data from the present analysis and previously published HERMES data on a transversely polarized hydrogen target and compared to results from the previously discussed approach. It was found that the two approaches produce similar results, which reflects the sensitivity of the HERMES data mainly to the CFF $\mathcal{H}$. Note, that also the asymmetry amplitudes from the present analysis that do not have an underlying Fourier coefficient in the definition of the asymmetry have been introduced to the fit procedure, which only varies the obtained goodness–of–fits values. In conclusion, the discussed fit approaches are capable of describing the existing data on DVCS and might hopefully mark the starting point of a successful parameterization of CFFs once more data is added.

6 Calibration and Performance of the HERMES Recoil Silicon Detector

As discussed in the preceding chapters, at HERMES the elastic and associated BH/DVCS could not be separated before the year 2006, when the Recoil Detector was installed to detect and identify the recoiling proton and other final state particles.

The Recoil Silicon Detector served the purpose of tracking charged particles and measuring their energy depositions. The latter was of special importance for protons with low momenta that do not reach the SFT. Therefore a high accuracy in the data handling, applying corrections and the energy calibration is necessary.

Between the years 2002 and 2006 the different Recoil detector components were tested individually and together in various tests. The final calibration of the SD was extracted from the data taken in the HERMES experiment. This chapter gives a short overview of the performed studies before and during the commissioning phase and a more detailed description of the final data treatment including applied corrections, the calibration procedure and performance studies.

In the following the term 'hit' will be used to describe the impact of a particle on a detector surface. As hits create both, a low– and a high–gain signal, it will be specified which signal is meant, if necessary.

Test beams

The prototypes of the Recoil SD were confronted with bunched electron beams between 1 – 6 GeV/c momentum at the DESY–II test beam facility [GHK+04a] in October 2002. Apart from noise studies, the resolution of the detector was measured to be 222 μm confirming the expectation of $758/\sqrt{12}$ μm = 219 μm within 2 %. In addition the efficiency of a strip depending on the position of the hit was determined: For the study one strip was divided into ten bins of the same size and solely in the two outermost bins a small decrease in the efficiency for a minimum ionizing particle was found.

In December 2003 a prototype of the final design was studied at the GSI facility with a mixed hadron beam consisting of pions, protons and deuterons of momenta between 300 MeV/c and 900 MeV/c. The detector was installed rotatable in order to measure energy deposits and cluster sizes for different incident angles.

In summer 2004 nine modules were calibrated using MIPs at the DESY–II test beam facility [HMG+05]. It was encountered that defective strips might be calibrated by the mean of a group of surrounding strips. The resolution and efficiency tests with the prototype were confirmed in these measurements.

In late 2004 eight modules were tested for the first time together in form of a bench–test [Pic08]. The functionality of the whole setup was proven, also for a longer time period of about half a day, which was approximately the duration of one HERA lepton fill.

All modules were shipped to the Tandem accelerator at Erlangen University and calibrated with protons of four different kinetic energies (3.5, 4.0, 6.0 and 9.0 MeV) [BKP+05, Vog08]. Thus both gains could be studied, but due to the fixed setup and strict time restrictions only under a perpendicular incident angle. The collected data were corrected for the pedestal shift, the CMN and the cross–talk distribution. The influence of the Kapton foils was studied and calibration factors for each individual strip and both gains were determined. A list of dead and noisy strips was prepared. The exact thicknesses of all modules were found to be within $295-315$ μm. And finally, the temperature dependence of the gain of one module was tested and found to be linear.

In parallel, within a laser test–stand all modules were scanned for dead and noisy channels [GHK+04b]. Also the cross–talk between different channels was measured and found to be asymmetric. This test–stand offered a means to check very fast the response of one or various detectors after, e.g. a necessary repair on a very short time scale.

The final test stand was located in the HERA East hall, where the whole RD including the superconducting magnet was installed and running. The analysis of the taken cosmic data showed a rather big common mode noise of the SD descending with the channel number, sometimes even deviating from a linear behavior. A weighted CMN correction procedure was suggested in Ref. [Pic08].

The commissioning

In late 2005 the RD was installed in the HERMES experiment. After a short running period, the HELIX chips of the SD became very noisy due to high radio–frequency load originating from a hole in the target cell. After an inspection of the target cell and a reassemble of the beam line in front of the HERMES target, the beam was once dumped into this area. The modules were therefore completely removed and if possible repaired or else replaced by spare modules. Meanwhile only one module was kept inside the target chamber for test purposes. Before the new installation all modules were investigated in the laser test–stand. In addition, a Faraday cage to shield the modules from the high frequency radiation ('Rf–shield') from the beam was developed and installed (see figure 6.1). After the succeeded re–installation it was realized that the n–side of one outer module was broken.

After the re–installation in July of 2006 the commissioning phase took place. All electronic parameters were set and a timing scan was performed [Pic08]. From this point of time, valuable data was taken that can be used for different physics analyzes. The detector was running very stable leading to a data taking efficiency of about 95 % constant over the full data taking period. No further repairs or replacements were necessary. The leakage currents and temperature, controlled by an cooling system

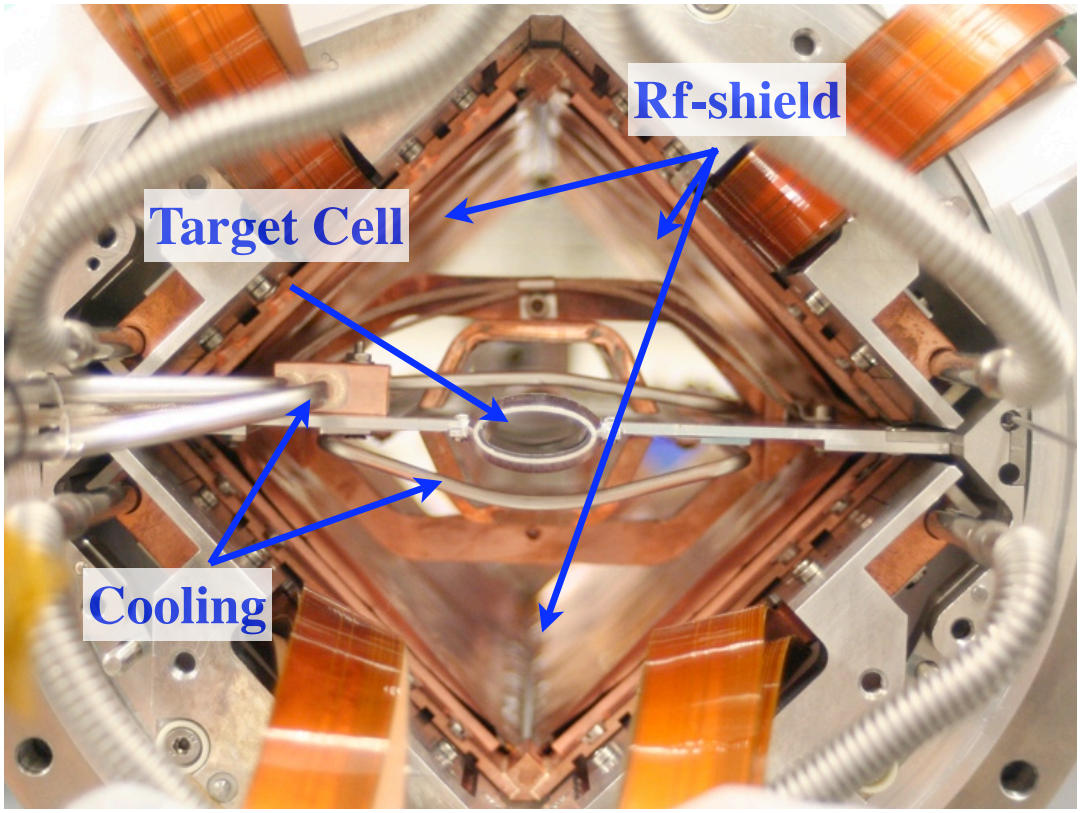

Figure 6.1: The HERMES target region during the re–installation of the RD. The thin target cell connected via the so–called wings to the target chamber is visible along with the pipes of the cooling system. The Rf–shield consisted of a copper coated Kapton foil on the inside of the modules and another nickel and gold coated Kapton foil on the outside of the modules (not visible on this picture).

using liquid ethanol, were stable during the operation time for all four inner and four outer sensors as can be seen from figure 6.2.

Until the shutdown of the HERA accelerator end of June 2007 38 million DIS events off a hydrogen and 10 million DIS events off a deuterium target were collected. Thus the total DIS statistics off an unpolarized hydrogen (deuterium) target was increased by a factor of 4.2 (1.6).

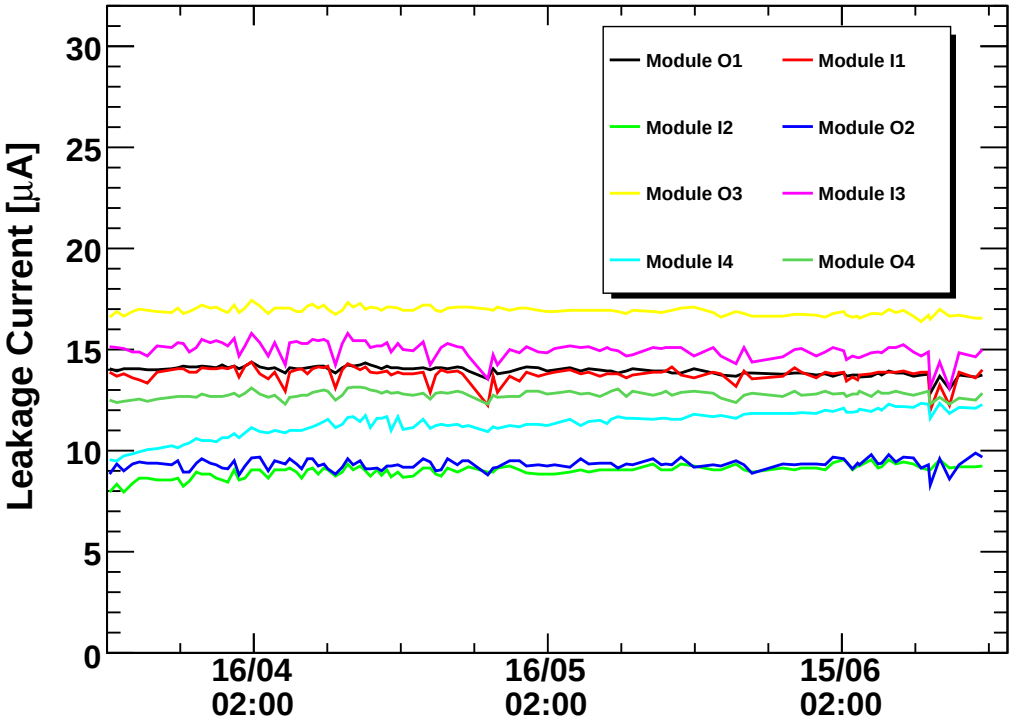

Figure 6.2: The leakage currents of the eight SSD modules are shown over a period of three months. The currents did not change severely during their whole time of operation.

6.1 Data taking and online corrections

The HELIX output signal H_i^k from event i and channel k can be decomposed into

$$H_i^k = S_i^k + P^k + N_i^k + C_i, \tag{6.1}$$

where S denotes the response to the charge created by the passing particle, P the pedestal width, N the random noise of each individual channel and C a common offset to all channels per event, usually called common mode noise.

Both, pedestal and common mode correction were done online on the HADC units. Therefore the pedestal values for each individual channel needed to be determined and loaded into the HADCs. Dedicated pedestal runs were taken every few hours, containing 5000 events each (see figure 6.3). The raw spectra for each channel were fit by a Gaussian to obtain the mean of the distribution. After each pedestal run the HADCs were re–programed. As the HADC units could not handle negative values, the pedestal positions were artificially shifted by −50 ADC counts (see figure 6.5). To reduce the amount of data only entries above a threshold of 12 ADC counts were written to disc.

For the common mode calculation those 16 channels out of the first 32 that had an entry below the so–called high threshold were averaged and then applied as a negative offset to all channels (see again figure 6.3). The high threshold is introduced to avoid the inclusion of real hits into the noise determination. If less than 16 channels fulfilled this condition, the correction failed and all data were read out and corrected by software. Furthermore the high threshold could not be adjusted for each chip individually, but always for a chain of two high– and two low–gain chips. At the beginning of data taking it was set to a compromise value of 150 ADC counts, but decreased to 100 ADC counts in October 2006. This increased the data load from the SD, but improved the common mode correction that is hampered from real hits below the high threshold. The widths of the spectra obtained from a fit with a Gaussian are also shown in figure 6.3. From the lowest panel in figure 6.3 it can be concluded that even for a pedestal run without real physics hits, the online common mode correction works only well for the first approximately 20 channels of each chip. After that the width increased with increasing channel number. This could be explained by higher frequency noise components and made an additional offline correction indispensable (see the following chapter).

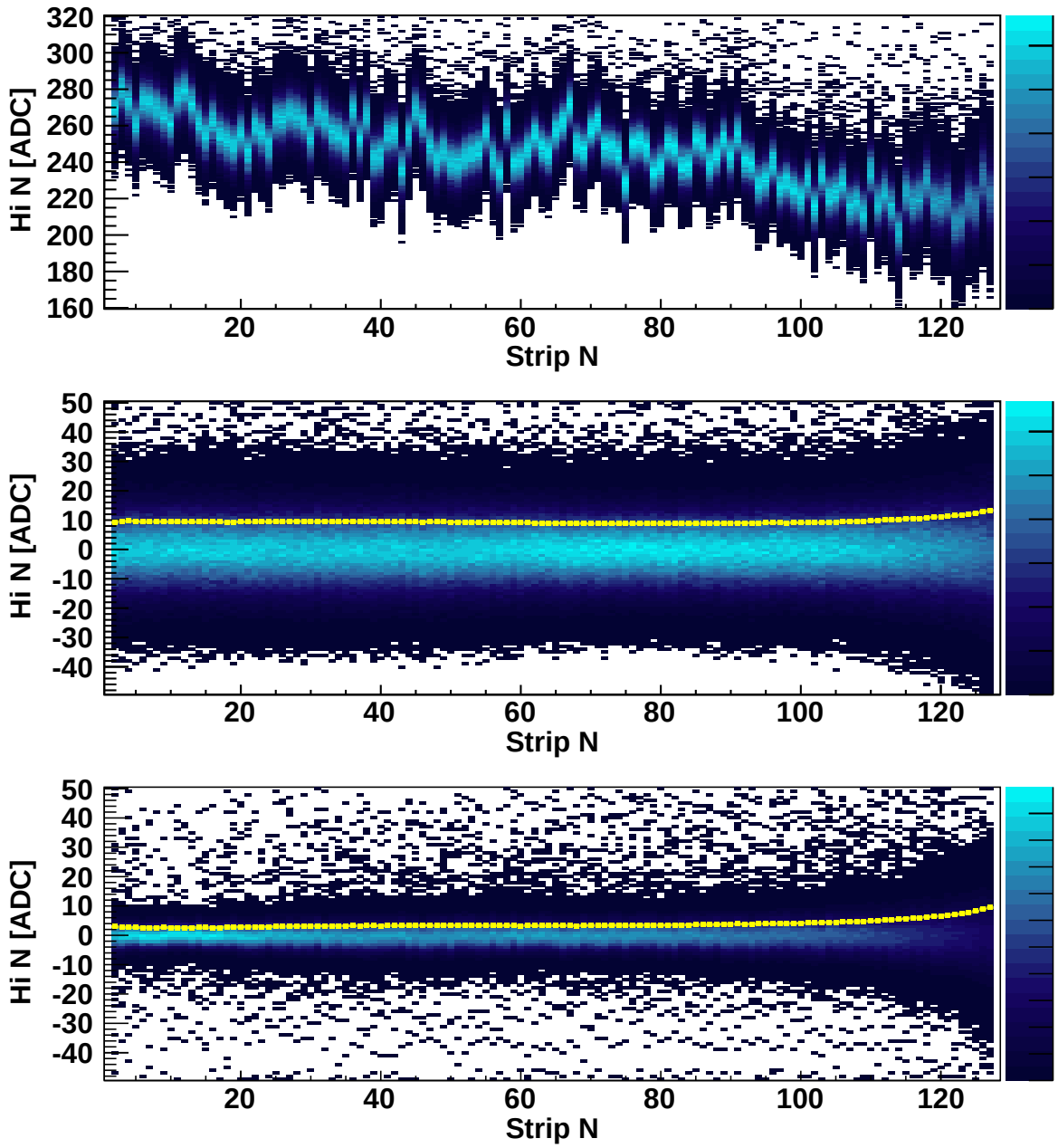

Figure 6.3: The upper plot shows the spectrum from one pedestal run for one of the n–side high–gain ('Hi N') chips versus the strip number. After the pedestal correction the width of the distributions did not change as expected, but the position of the mean was moved to zero as can be seen from the middle panel. In the lower plot also the common mode was subtracted, as calculated from the first 16 channels. The yellow squares depict the widths of the distributions obtained from channel–wise Gaussian fits. The first and the last strip were not read out.

6.2 Data processing and offline corrections

6.2.1 HERMES Decoder

The first step of the software chain is the so–called **HERMES Dec**oder (HDC), which decoded the raw data format and applied most of the detector calibrations. The HDC data was structured into ADAMO [CER95] tables with one record per event. In the case of the SD data, HDC first reversed the online common mode correction in order to be able to introduce a dynamic high threshold, followed by three correction steps:

1 Drift correction

It was realized that the pedestal position of about 15 % of the channels changed with the beam current (see figure 6.4). No pattern was found for the occurrence of those channels or the strength of their dependence. Neighboring channels showed different behavior. The functional dependence on the beam current could be described by second order polynomials, in which in most of the cases the second order contribution was small compared to the lower orders. The many taken pedestal runs allowed to get the parameterization of the beam current dependencies with an accuracy of 1 ADC count given by the integer–wise output of the HADC.

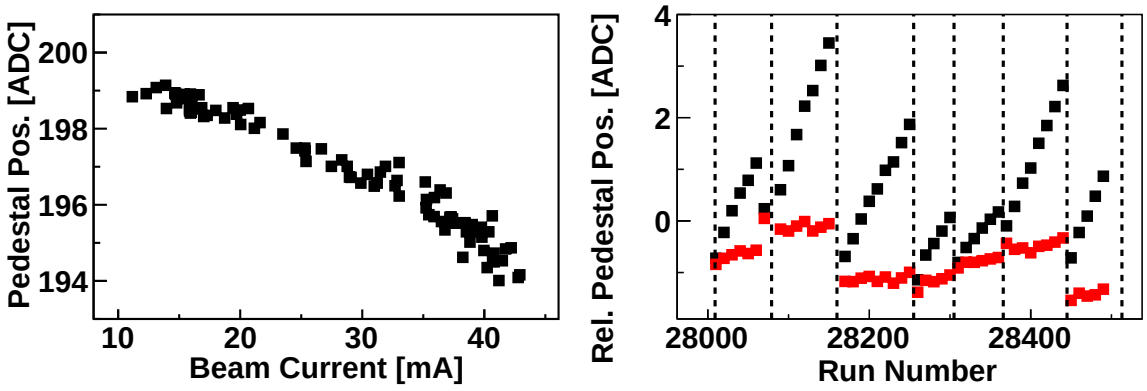

Figure 6.4: The left plot shows the dependence of the pedestal position of a particular channel on the beam current for many pedestal runs. A second order polynomial is needed for the description of this channel. The black squares in the right panel show again the pedestal position, now relative to the loaded pedestal (indicated by the vertical dashed black lines) for HERMES runs. The red squares give the relative pedestal positions after the applied correction. The horizontal axis displays the run number.

2 Offline CMN correction

In software, no requirements like a fixed high threshold for a chain of four chips exists. Therefore the offline CMN correction used a dynamic high threshold, calculated for each chip individually. This improved the correction especially when comparing the output from the low– and the high–gain chips.

3 Spline correction

In the following step a spline interpolation was applied to the data. For this correction every eighth strip starting from strip 28 was kept in the data by artificially decreasing their pedestal positions by −100 ADC counts (see figure 6.5) and therefore reducing the channels hardware threshold by 100 ADC counts. These strips produced about 90 % of the overall data load.

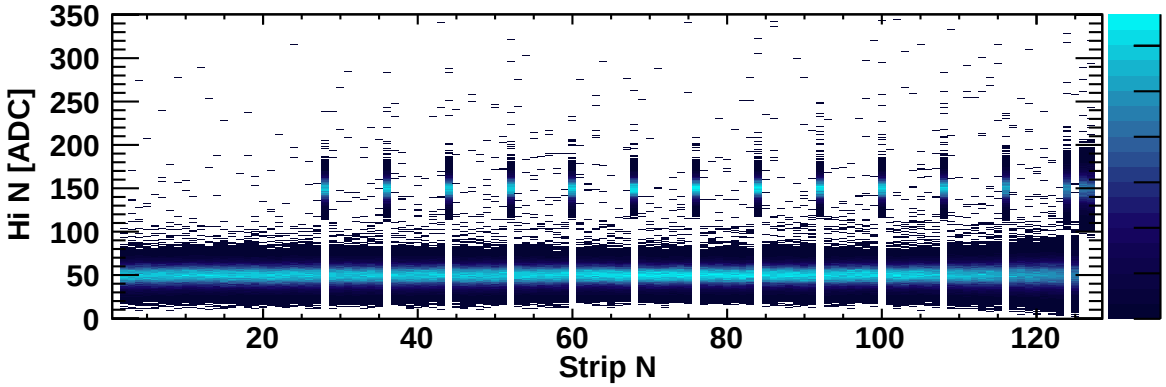

Figure 6.5: The plot shows the pedestal corrected spectrum from data taken without threshold. The means of the distributions are shifted to 50 (150) ADC counts for the (special) strips.

In the left panel of figure 6.6 a single event with a real physics hit at around channel 100 is shown after pedestal and CMN correction. The amplitude of the hit of about 100 ADC counts is artificially increased due to the correlated noise. An additional dynamic high threshold was introduced to reject real hits from the determination of the base points of the spline function. The spline interpolation is also drawn in the picture. After applying the interpolated function the hit exhibited a true amplitude of approximately 90 ADC counts and the background is flat and centered around zero (see the right panel of figure 6.6).

The spline correction reduced the noise for every channel to $3-4$ ADC counts over the full chip (see figure 6.7).

In case the online CMN correction failed, all channels were written to disc. After an offline pedestal subtraction, this data was immediately corrected with the spline interpolation and afterwards treated in the same way like the rest of the data.

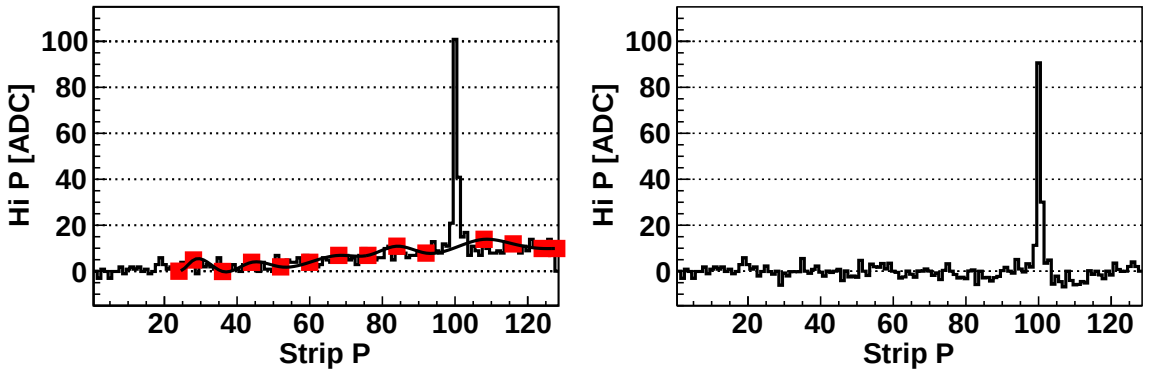

Figure 6.6: In the left plot a single event is shown after pedestal and CMN correction. The red squares display the basepoints of the spline correction, the black line indicates the interpolated function. On the right side the same event after the spline correction is shown.

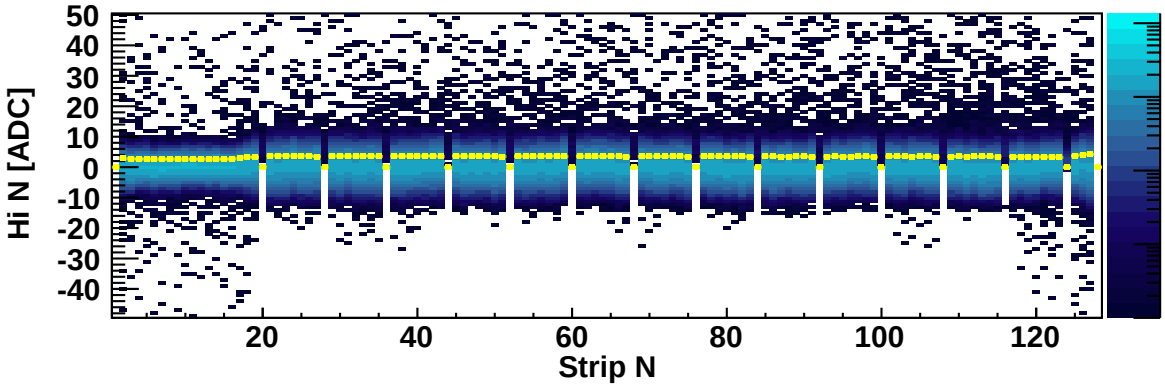

Figure 6.7: A run taken without hardware threshold after applying the spline correction is depicted. The channels used as basepoints are clearly visible as they do not reach negative values. The yellow circles visualize the widths of the distributions.

6.2.2 External Tracking Code

The output of HDC was processed with the so–called E**x**ternal **T**racking **C**ode (XTC), which was responsible for reconstructing tracks outside the regular HERMES acceptance and as such also used for the Recoil Detector. For the SD it performed the search for saturated channels, the cross–talk correction, added up the energy deposits, took care of the clustering and the space point calculation which are used in the track reconstruction algorithm.

In the case of the quadrant with the broken n–side the ϑ–angle of the track was determined by using the vertex calculated by the HRC from the Forward Spectrometer.

Saturation effects

In the first step in XTC the saturation of the read–out chip was handled. If a channel was in saturation the linear correlation from the ADC counts to the deposited energy is lost. Therefore these events had to be treated differently in the software chain. The linear range of each individual channel was determined from the comparison of the high– and low–gain signals (see section 6.3). Every event was searched for channels in saturation, which were marked accordingly along with their immediate and next neighboring channels.

Cross–talk correction algorithm

Each physics signal was smeared due to the physical and electronic cross–talk. The former one describes the migration of the produced charge carrier cloud into neighboring strips, while the latter one happens mostly on the flex foils effecting individual strips and on the chips effecting individual channels. The cross–talk complicates the energy reconstruction of a signal, as part of the signal that leaked into a neighboring channel might be lost, if it falls below the threshold. In addition, an asymmetric cross–talk might lead to a systematic offset in the position reconstruction. Moreover, the cross–talk correction can recover small signals that were below threshold.

As the problem is linear, the smearing can be formulated mathematically by a matrix $\widehat{M}$ multiplied on the cross–talk free signal $\vec{s}$:

$$\vec{t} = \widehat{M} \cdot \vec{s} = \begin{pmatrix} c_{i-2} & r_{i-2} & 0 & 0 & 0 \\ l_{i-1} & c_{i-1} & r_{i-1} & 0 & 0 \\ 0 & l_i & c_i & r_i & 0 \\ 0 & 0 & l_{i+1} & c_{i+1} & r_{i+1} \\ 0 & 0 & 0 & l_{i+2} & c_{i+2} \end{pmatrix} \cdot \vec{s}. \tag{6.2}$$

In the correction, the matrix had to be inverted and multiplied with the measured signal $\vec{t}$. The diagonal elements of the matrix give the fractions of the signal c_i that remain in the corresponding channels i. The adjacent entries give the fraction that couple in the neighboring channels $r_\mathrm{i}, l_\mathrm{i}$ and so on. In order to not violate charge

conservation with the correction, each column of the matrix is normalized to unity:

$$l_{i-1} + c_i + r_{i+1} = 1. \tag{6.3}$$

Following these basic ideas it is clear that only a small part of the 128 x 128 cells of the matrix exhibits a value significantly larger than zero. Neglecting these small entries, it is not necessary to invert the full matrix, but one can find an approximative analytical solution for the problem by writing out the middle column of the Matrix $\widehat{M}$ for an event n. In the following only the two neighboring channels will be taken into account in the correction:

$$t_{n,i} \equiv s_{n,i-1}r_{i-1} + s_{n,i}z_i + s_{n,i+1}l_{i+1} \quad \rightsquigarrow \quad s_{n,i} = \frac{t_{n,i}}{z_i} - s_{n,i-1}\frac{r_{i-1}}{z_i} - s_{n,i+1}\frac{l_{i+1}}{z_i}, \tag{6.4}$$

$$s_{n,i} = \frac{t_{n,i}}{z_i} - \left(\frac{t_{n,i-1}}{z_{i-1}} - s_{n,i-2}\frac{r_{i-2}}{z_{i-1}} - s_{n,i}\frac{l_i}{z_{i-1}}\right)\frac{r_{i-1}}{z_i} - \left(\frac{t_{n,i+1}}{z_{i+1}} - s_{n,i}\frac{r_i}{z_{i+1}} - s_{n,i+2}\frac{l_{i+2}}{z_{i+1}}\right)\frac{l_{i+1}}{z_i}$$

$$= s_{n,i-2}\frac{r_{i-2}r_{i-1}}{z_{i-1}z_i} - t_{n,i-1}\frac{r_{i-1}}{z_{i-1}z_i} + \frac{t_{n,i}}{z_i} - t_{n,i+1}\frac{l_{i+1}}{z_{i+1}z_i} + s_{n,i+2}\frac{l_{i+2}l_{i+1}}{z_{i+1}z_i} + s_{n,i}\left(\frac{l_i r_{i-1}}{z_{i-1}z_i} + \frac{r_i l_{i+1}}{z_{i+1}z_i}\right)$$

$$= \frac{\frac{t_{n,i}}{z_i} - t_{n,i-1}\frac{r_{i-1}}{z_{i-1}z_i} - t_{n,i+1}\frac{l_{i+1}}{z_{i+1}z_i} + s_{n,i-2}\frac{r_{i-2}r_{i-1}}{z_{i-1}z_i} + s_{n,i+2}\frac{l_{i+2}l_{i+1}}{z_{i+1}z_i}}{1 - \frac{l_i r_{i-1}}{z_{i-1}z_i} - \frac{r_i l_{i+1}}{z_{i+1}z_i}}$$

$$= \left(t_{n,i} - t_{n,i-1}\frac{r_{i-1}}{z_{i-1}} - t_{n,i+1}\frac{l_{i+1}}{z_{i+1}} + s_{n,i-2}\frac{r_{i-2}r_{i-1}}{z_{i-1}} + s_{n,i+2}\frac{l_{i+2}l_{i+1}}{z_{i+1}}\right)\frac{1}{z_i - \frac{l_i r_{i-1}}{z_{i-1}} - \frac{r_i l_{i+1}}{z_{i+1}}}. \tag{6.5}$$

The entry in the channels next to the neighboring ones, $s_{n,i\pm2}$, can now be set to zero. A replacement by $\left(\frac{t_{n,i\pm2}}{z_{i\pm2}}\right)$, corresponding to a correction without including the neighboring channels, will lead to an error, as it would contradict to the model assumptions:

$$s_{n,i} = \left(t_{n,i} - t_{n,i-1}\frac{r_{i-1}}{z_{i-1}} - t_{n,i+1}\frac{l_{i+1}}{z_{i+1}}\right)\frac{1}{z_i - \frac{l_i r_{i-1}}{z_{i-1}} - \frac{r_i l_{i+1}}{z_{i+1}}}. \tag{6.6}$$

Taking into account the second neighbor complicates the correction formula, but improves the stability of the correction. The same calculation as shown above results

in

$$
\begin{aligned}
s_{n,i} \quad \cdot \quad & \Big(z_i \\
& - \frac{r_{i-1}}{z_{i-1}} \left[l_i + \frac{l_i l_{i-1} r_{i-2}}{z_{i-1} z_{i-2}} - \frac{r_{i-2} ll_i}{z_{i-2} z_i} - \frac{ll_{i+1} r_i}{z_{i+1} z_i} \right] \\
& - \frac{rr_{i-2}}{z_{i-2}} \left[ll_i - \frac{l_{i-1} l_i}{z_{i-1} z_i} \right] \\
& - \frac{l_{i+1}}{z_{i+1}} \left[r_i + \frac{r_i r_{i+1} l_{i+2}}{z_{i+1} z_{i+2}} - \frac{l_{i+2} rr_i}{z_{i+2} z_i} - \frac{rr_{i-1} l_i}{z_{i-1} z_i} \right] \\
& - \frac{ll_{i+2}}{z_{i+2}} \left[rr_i - \frac{r_{i+1} r_i}{z_{i+1} z_i} \right] \Big) \\
= \quad & t_{n,i} \\
& - t_{n,i-1} \left[\frac{r_{i-1}}{z_{i-1}} \left(1 + \frac{r_{i-2} l_{i-1}}{z_{i-2} z_{i-1}} \right) - \frac{l_{i+1} rr_{i-1}}{z_{i+1} z_{i-1}} - \frac{rr_{i-2} l_{i-1}}{z_{i-2} z_{i-1}} \right] \\
& - t_{n,i-2} \left[\frac{rr_{i-2}}{z_{i-2}} - \frac{r_{i-1} r_{i-2}}{z_{i-1} l_{z-2}} \right] \\
& - t_{n,i+1} \left[\frac{l_{i+1}}{z_{i+1}} \left(1 + \frac{l_{i+2} r_{i+1}}{z_{i+2} z_{i+1}} \right) - \frac{r_{i-1} ll_{i+1}}{z_{i-1} z_{i+1}} - \frac{ll_{i+2} r_{i+1}}{z_{i+2} z_{i+1}} \right] \\
& - t_{n,i+2} \left[\frac{ll_{i+2}}{z_{i+2}} - \frac{l_{i+1} l_{i+2}}{z_{i+1} l_{z+2}} \right], \qquad (6.7)
\end{aligned}
$$

where $rr_{n,i}, ll_{n,i}$ denote the cross–talk to the second neighbor of channel i for an event n. Up to now the simple correction mode has been used for the so far completed data productions.

Extraction of cross–talk coefficients

The cross–talk coefficients were extracted from HERMES data separately for each gain. The algorithm searched for clusters of neighboring strips that each had a hit with an amplitude of more than 4 ADC counts (secondary threshold). The strip with the largest entry was labeled as the central strip of the cluster and had to exceed an amplitude of 12 ADC counts (primary threshold), which corresponded to the hardware threshold chosen throughout the data taking. The strips preceding (following) the central strip were called left (right) strip of the cluster. The ratio between the amplitude of the left neighbor and the amplitude of the central strip of a cluster for a high–gain n–side chip is shown in figure 6.8. All clusters with a size greater than one strip were included into this plot, if the left strip was above the secondary threshold. The zipper structure of the plot was already found in the Erlangen calibration measurement and is probably caused by an asymmetry in the chip design [Tru00]. Although a small increase of the coefficients with increasing strip number is visible, all even (odd) strips could be evaluated together resulting in a good estimate of the coefficient for each single strip.

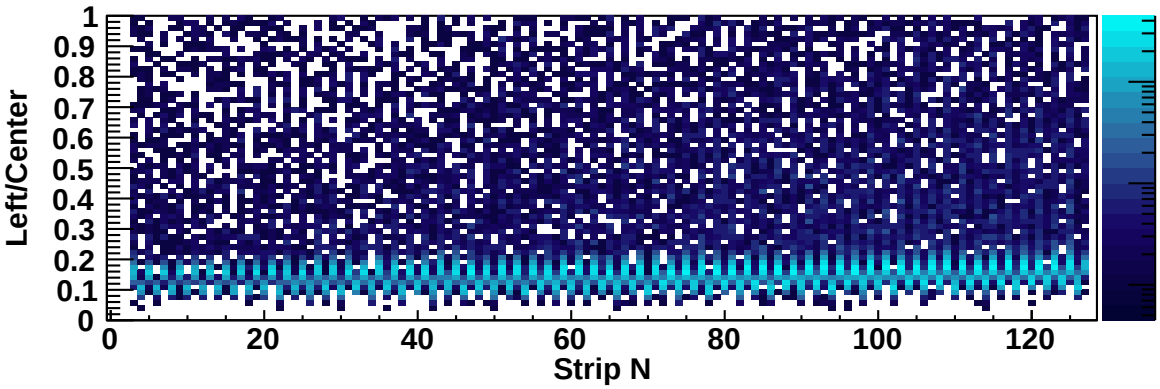

Figure 6.8: The ratio of the energy deposits between two neighboring strips is shown, where the strip with the higher strip number has the largest energy deposit within the cluster. On the horizontal axis the number of the central strip is given. A zipper structure is visible, which means that strips with even and odd numbers showed different cross–talk behavior.

The final extraction method therefore consisted of two steps. First, all even (odd) strips of each chip were evaluated together and, second, the coefficients for each individual strip were extracted. The first step is visualized in figure 6.9.

For all even (odd) strips of a chip the ratio between the amplitudes of the neighboring strips relative to the central strip was histogrammed. Again the two thresholds were applied as described above, but no restriction on the cluster size was required. Most of the clusters showed a constant ratio between the amplitudes of the neighboring strips (the bands in the four plots), but there were also entries with different ratios originating from particles physically crossing two strips of a sensor (the data points above the bands in the four plots). The band was confined by two effects: On the one side, in clusters with small overall amplitudes the neighboring strips fell under either the hardware or the secondary threshold of the algorithm. On the other side, clusters with very large amplitudes led to saturated strips. Therefore two limits were introduced and the distribution was cut at these points perpendicular to the orientation of the band (leading to the selection of data points shown in the four plots). In order to fit the resulting bands, a box indicated by the red dashed line in the plots was calculated. The coordinates of their corners were given by the limits (in x) and the center of the distribution plus/minus three times the width (in y). The yellow dashed lines represent the result of the fits.

In the second step the data was again stored in form of a histogram like figure 6.8. The algorithm now projected each strips' distribution and fit the spectrum with a Gaussian function. In order to avoid the large tails the data were limited to a ratio below 0.35. In case the error on the fit was small, the mean of the Gaussian function determined the cross–talk coefficient of the strip. Else the coefficient obtained from fitting the band was chosen. The fraction of the signal in the central strip was

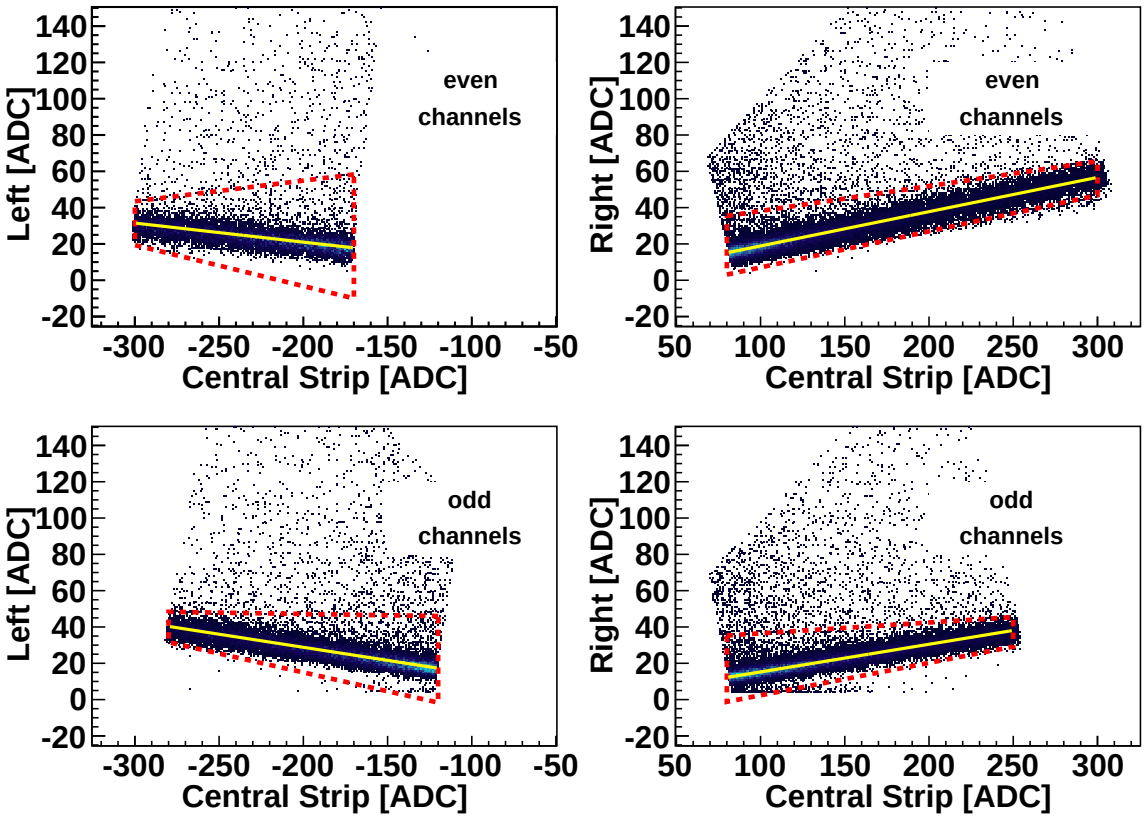

Figure 6.9: The four two–dimensional plots show the signal in the central strip of the cluster versus the signal in one of the neighboring strips. In the upper panel for all even and in the lower panel for all odd channels. See text for further details.

calculated from the fit results on the two neighbors and formula 6.3.

The cluster shapes were observed to be asymmetric with a tendency to strips with higher strip numbers, which is not explicable by the geometry of the modules. The coefficients covered a range between 6 % and 25 % except for outliers. The cross–talk to right neighbors was larger than to left ones. Some of the strips seemed to be electrically connected and divide the signal in equal parts. Those pairs along with dead strips were not treated differently, but could not create charge due to the basic assumptions of the correction.

The outcome of the correction is shown in figure 6.10. The bands are now almost horizontal with a width of around 6 ADC counts. The remaining slopes of the bands could be corrected by including the exact coefficients for the cross–talk to the second neighbors. This was tested in MC and might be included in future data productions.

The cross–talk correction failed for clusters with a saturated central strip. This was not taken care of in the cross–talk algorithm, but in the summing of the energy

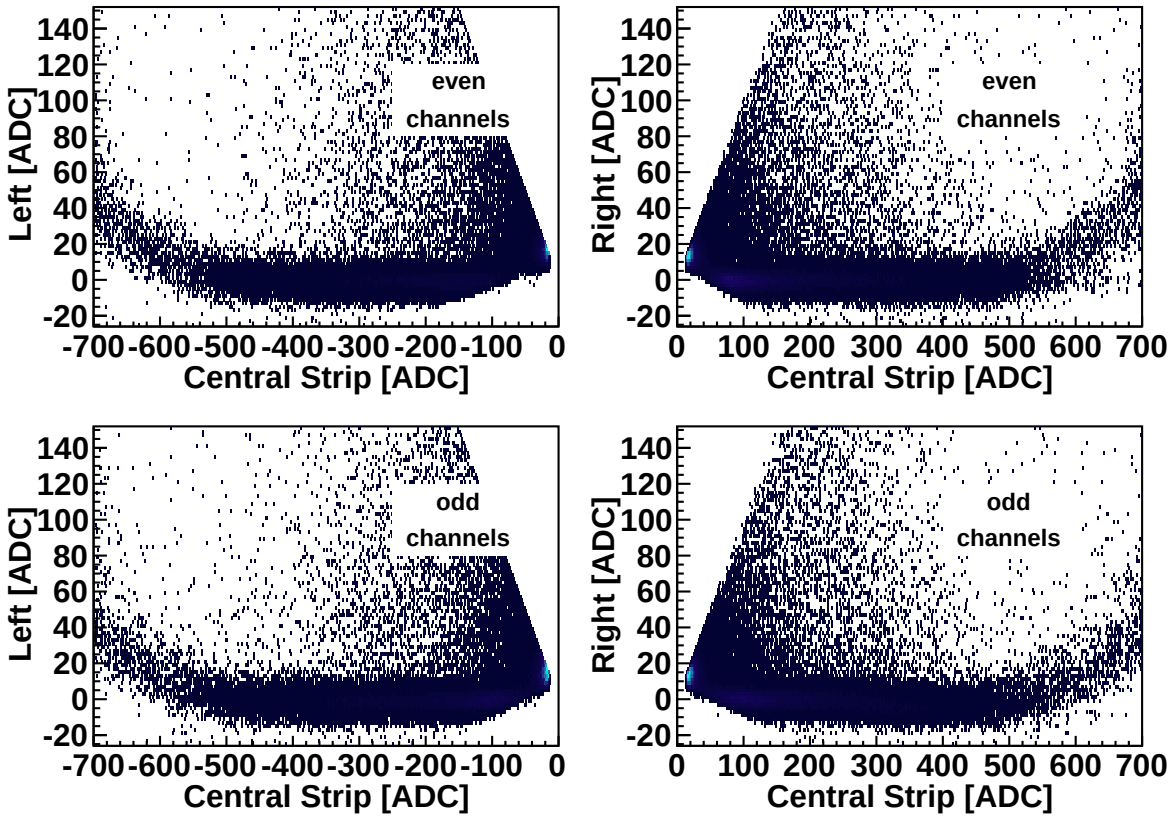

Figure 6.10: The four two–dimensional plots show the signal in the central strip of the cluster versus the signal in one of the neighboring strips after applying the cross–talk correction. In the upper panel for all even and in the lower panel for all odd channels. The light (blue) areas with large statistics at central strip values of arround 10 ADC counts originate from noise events just above the hardware threshold. See text for further details.

deposits by using the low–gain information from saturated high–gain channels and their neighbors. The ratio between immediate neighbors of a saturated channel relative to their next neighbor was not influenced. This would allow to reconstruct the energy deposit in a saturated channel from its neighbor and the known cross–talk coefficient. However, this way of reconstruction is very inefficient and was not included into the calibration procedure.

Stability of cross–talk coefficients

The SD took data for about one year, which evoked the question on the stability of all parameters. The data came in natural packets defined by the period between two pedestal runs. Therefore these entities were not split up any further. This packets

ranged between a few to about 300 HERMES runs[1]. For a stable extraction of the cross–talk coefficients the statistics of about 500 runs were necessary. An algorithm was written that summed up the packets until it reached enough data and started the extraction procedure. From this analysis sudden jumps of the cross–talk coefficients of whole chips had been found. All jumps are related to changes in the operation parameters of the corresponding chips or the conditions of the beam facility (e.g. in spring 2007 the proton beam was run in a low momentum mode). Fortunately the (very few) jumps divided the data in packets of sizes that could be handled individually.

Toy model noise simulation

A simple toy model was used to simulate the noise behavior of the cross–talk correction. A hit was distributed on five strips and each strip smeared by a Gaussian of 3 ADC counts width corresponding to the random noise for each channel. Then the advanced cross–talk correction algorithm was applied on the data. The result is shown in figure 6.11. The width of the center strip was increased to 4.8 ADC counts after the correction, which is about 2.1 ADC counts lower than the summed width of $3 \cdot \sqrt{5} = 6.7$ ADC counts of the cluster.

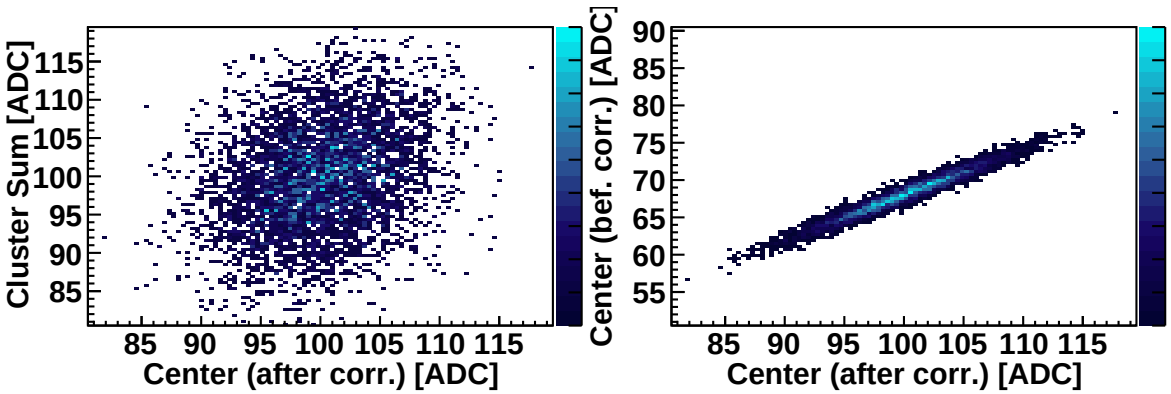

Figure 6.11: On the left the summed deposited energy of the cluster before the cross–talk correction is shown versus the energy deposit of the central strip after applying the correction. On the right the energy deposit of the central strip is compared before and after the correction.

Energy deposit calculation

The cross–talk corrected signals are used to calculate the deposited energy for each hit. If the hit amplitude of the low–gain was larger than 60 ADC counts, only the low–gain information went into the determination of the deposited energy. For hits with

[1]The HERMES data acquisition stored events in packages of 560 Mbytes called 'runs'.

smaller amplitudes the high–gain information was chosen and converted to low–gain equivalents (see Eq. 6.8). Below a threshold of 8 ADC counts in the high–gain, the hits were omitted to avoid any effects from the applied corrections. In addition it was also ensured that the high–gains of the neighboring and the next-to neighboring strips were not saturated. The low–gain equivalents were converted to an energy by multiplying with a factor obtained from the calibration described in section 6.3.

Clustering

In the first step of the clustering algorithm a hit above a primary energy threshold was searched. It then scanned for additional hits above a secondary threshold in the direct vicinity of the started cluster. Each hit that had not been used in another cluster and that was separated by at most one strip below the secondary threshold was added to the cluster's amplitude. If the cluster contained several local amplitude minima, it was split into different clusters, if each cluster exceeded a third threshold required for the sum of the hits.

Calculation of space points

A space point combines the hits originating from one passing particle to form a point with both the position and energy deposition measurement.

For the space point calculation usually p– and n–side information were combined and the space point energy was averaged from both clusters, except the independent energy measurements showed too large discrepancies to originate from one particle. The position of the space point was determined from the hits on the two detector sides.

The n–side of one module was found to be dead immediately after the installation. In this case only the other side was used in the algorithm. In the position reconstruction these events have one unconstrained coordinate. In addition, a check was performed for sides with lower efficiency for small signals and in case were handled in the same way as the dead side.

6.3 Energy calibration

The silicon energy calibration served for two purposes: First, to improve the momentum resolution and PID of particles passing through at least three of the four inner detector layers. Second, to allow a momentum reconstruction for particles not reaching the inner SFT layer. The second class of particles was split up into further categories as can be seen in figure 6.12, where the energy deposits of protons and deuterons in the two silicon layers are shown. Both particle types show a characteristic triangular shape with two branches. The upper one describes particles that got stopped in the outer silicon layer, while the particles in the lower branch traverse both layers. In the low energy deposit region the distinction between protons and deuterons will be most difficult, because the curves are converging. As the deuterons in this momentum range are not used in an analysis so far, this point has not been addressed yet.

The red point in the figure marks the punch–through point of the inner layer for protons. In the upper branch between 125 MeV/c and 145 MeV/c (green point) the protons got stopped in the second layer and the momentum was obtained as the sum of the energy deposits in both layers under the assumption of a certain particle type. Above this momentum the dE/dx behavior was used for the momentum reconstruction. From around 200 MeV/c (magenta point) the protons traversed also the target chamber and reached the inner layer of the SFT. Their momenta were reconstructed from the bending in the magnetic field. However, the inclusion of the energy deposits in the SD in the momentum reconstruction improved the resolution of the momentum measurement.

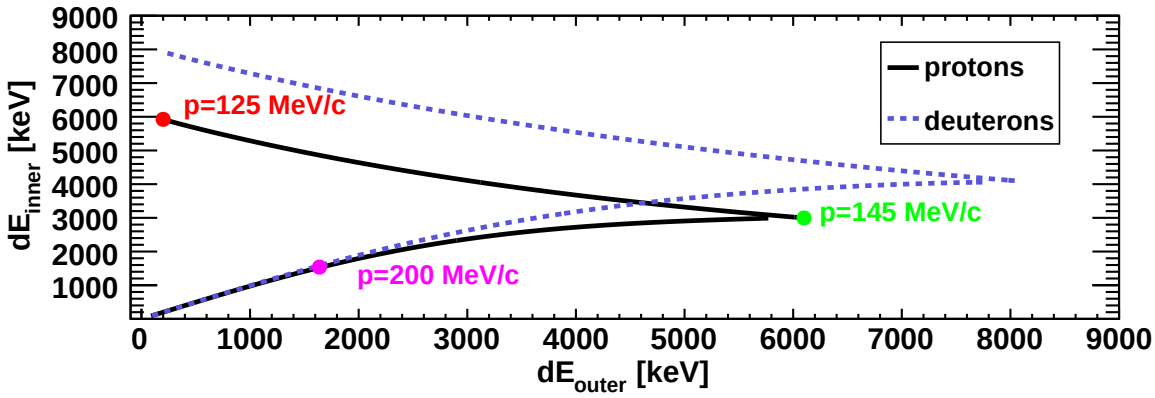

Figure 6.12: The energy deposits of proton (black line) and deuterons (blue dashed line) in the inner layer of the SD against the deposits in the outer layer. The curves are the results from a Geant4 simulation [A+03]. The colored points give the position of protons of certain momenta as labeled on the plot.

The chips of the SD covered a very large dynamic range to measure both protons

with large energy deposits (up to 6.2 MeV) and charged particles with a energy deposit **M**ost **P**robable **V**alue (MPV) of 84 keV in 300 μm thick silicon sensors (see figure 6.13). As the pions always reached the SFT layers, the SD energy measurement in the low energy deposit region was off less importance as the sensitivity of the dE/dx–behavior is lower in this region of the Bethe–Bloch curve. Thus, the focus of the SD energy calibration was put on the large energy deposits starting from an energy deposition of about 1.5 MeV.

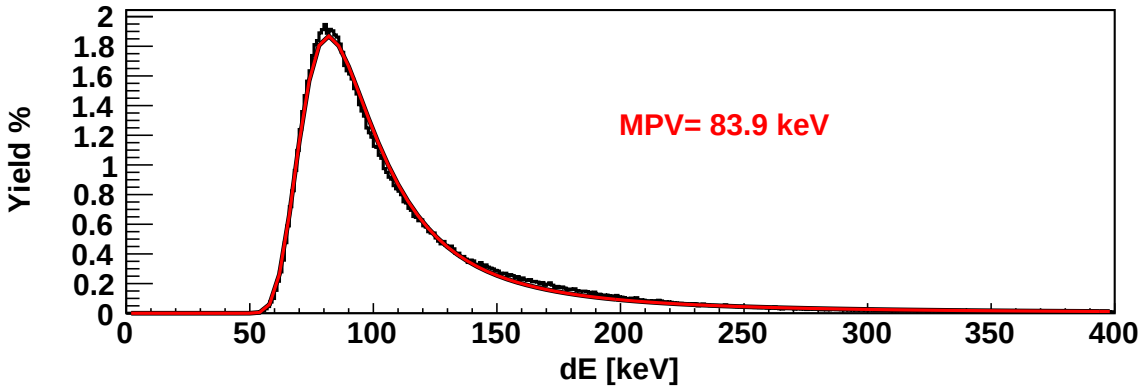

Figure 6.13: The energy deposit distribution in the SD for pions of 200 MeV/c momentum calculated from a GEANT4 simulation. The red line describes a Landau curve with a MPV of 83.9 keV.

The calibration consisted of a relative calibration of the two gains and an absolute calibration described in the following two sections.

Extraction of high–low gain ratios

The high–low–gain ratio of a particular strip is shown in figure 6.14. After the cutoff (given by the hardware threshold) a linear behavior was observed until the high–gain chip started to saturate. The linear range is larger on the n–side. On the p–side it was difficult to find the point of transition from the linear range in the saturation region. From these plots no conclusion could be drawn on the linearity of the low– or high–gain chips as any non–linearities could compensate each other.

Like for the cross–talk coefficients also for the extraction of the high–low gain ratios the data was subdivided into packets defined by the taken pedestal runs. To extract the linear range various packets had to be merged to about 5000 runs. Contrary to the expectations a second parameter c_2 had to be introduced in the fitting function:

$$Lo = c_1 \cdot Hi + c_2 \cdot Hi^2. \tag{6.8}$$

The time stability of the ratio parameter c_1 showed jumps at the same points in time as the cross–talk coefficients. In addition a small slope was observed, which resulted in about 1 % change over a range of 1000 runs.

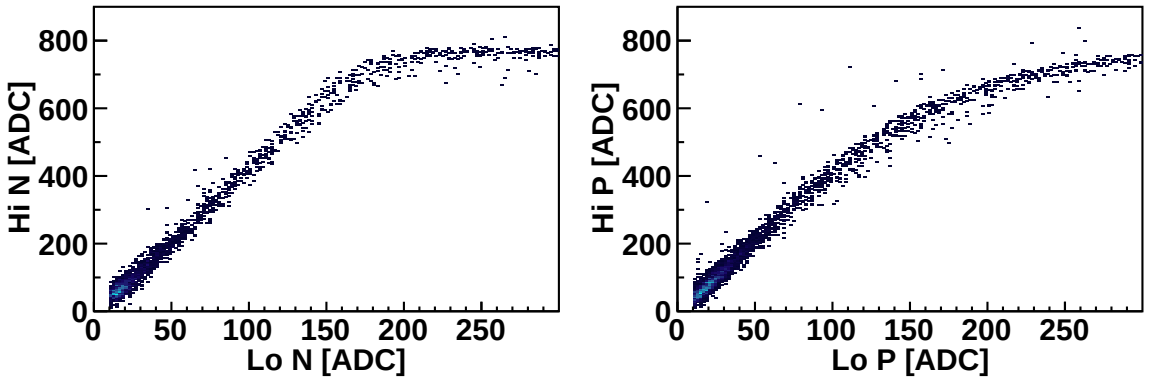

Figure 6.14: The high–low–gain ratios of one n–side (left plot) and one p–side strip (right plot).

Even though the non–linearities in the gain distributions are not extractable from these plots, the knowledge of the coefficients appearing in Eq. 6.8 together with an upper limit of their validity are sufficient for an absolute energy calibration.

Absolute energy calibration

All protons with momenta below approximately 200 MeV/c did not reach the SFT. The characteristical triangular shape of the energy deposits of protons and deuterons in the two silicon layers (see figure 6.12) was used as basis for a first calibration. The upper branches were built from the stopped particles and the lower branches from the particles passing through the first silicon layer.

In figure 6.15 the energy deposit for six different sensor side combinations on data from both a hydrogen and a deuterium target after a correction for the incident angle can be seen. The two left columns show combinations of the corresponding inner and outer detector layers with the familiar shape, where each point represents one track. While the right plots display the correlation between n– and p–side of each silicon layer and each point represents one space point. In each of the six plots a combination of all 128×128 strips of a sensor is shown. The red curves were obtained from a Geant4 simulation for particles hitting the SD under an angle of 90°. The black markers depict the position of the different branches in data obtained from a fit to the projection of the branches on the vertical axis. In the calibration procedure the difference between the measured branch positions and the simulated curves was minimized.

In the first iteration the four inner–outer combinations were minimized simultaneously. This was achieved by multiplying the energy deposits in both layers each with a constant and calculating the difference from the simulated behavior. The obtained constants were used to calibrate the data assuming a linear correlation to the cluster

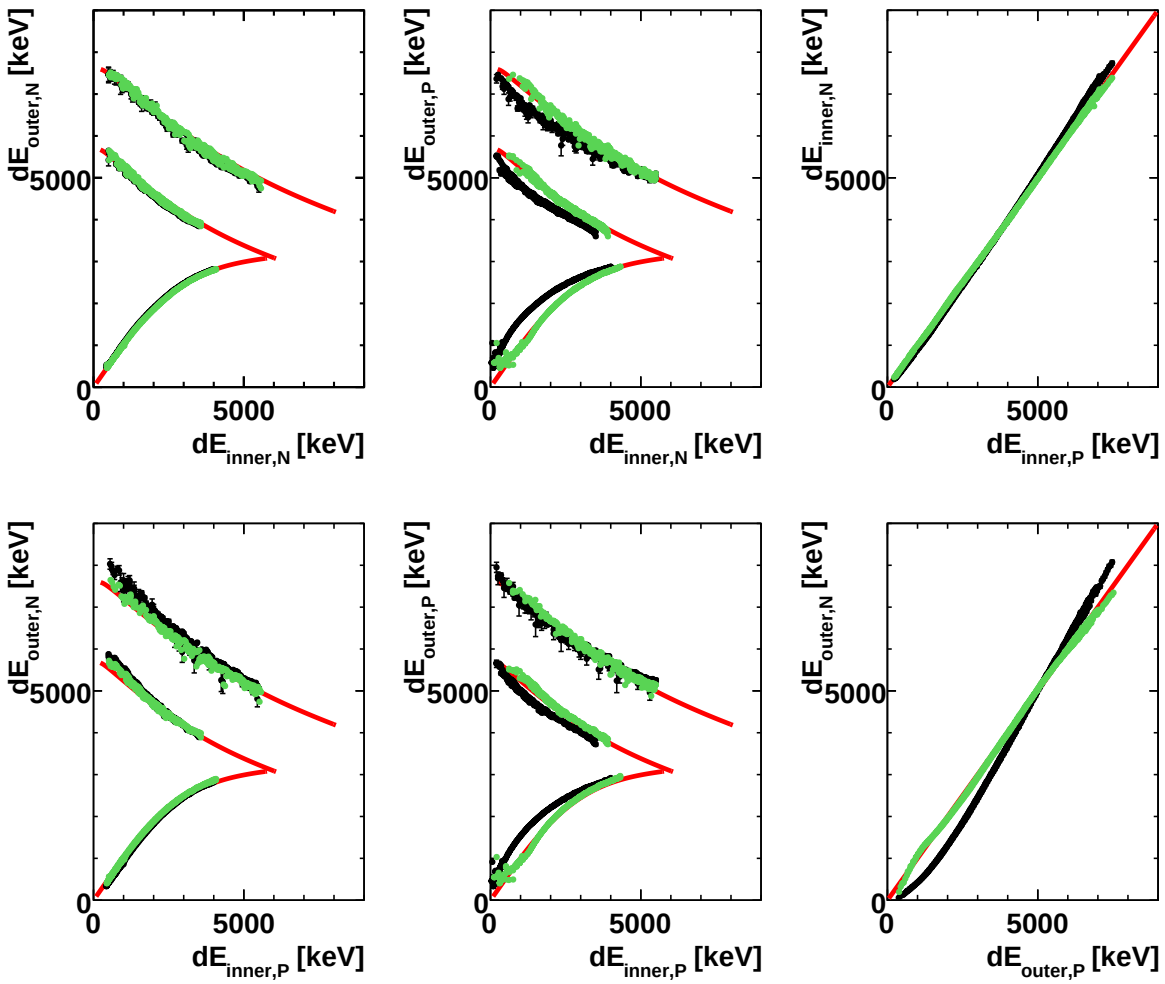

Figure 6.15: Energy deposits for different sensor side combinations on a deuterium target. See text for further details.

amplitudes:

$$\begin{aligned} dE_{\text{inner}} &= c_{\text{inner}} \cdot Cluster_{\text{inner}}, \\ dE_{\text{outer}} &= c_{\text{outer}} \cdot Cluster_{\text{outer}}. \end{aligned} \tag{6.9}$$

In a second step all six sensor side combination shown in figure 6.15 were fit simultaneously with a combination of two functions. From the origin to a connection point a second order polynomial was used and continued by a first order polynomial. At the connection point the two functions were required to result in the same value and the same first derivative. For this purpose the different branches needed to be weighted in the minimization algorithm to get stable results. The choice of the fit function allowed to account for non–linearities of the system.

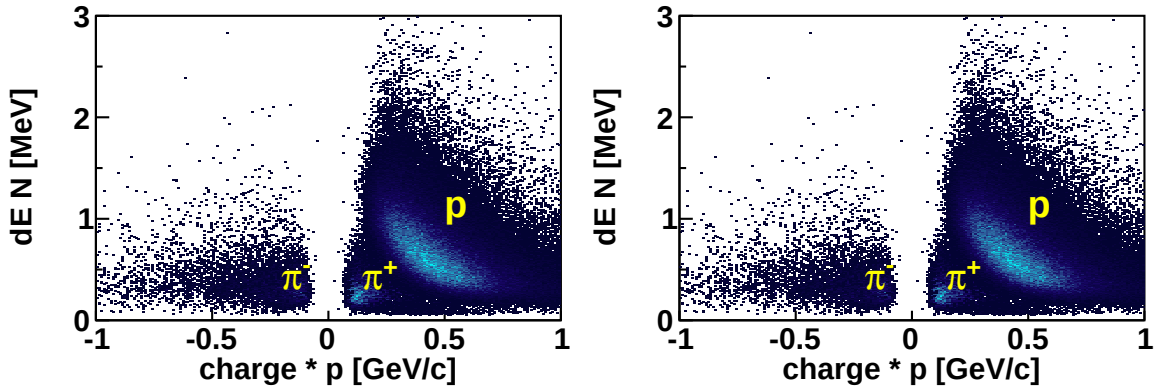

Figure 6.16: The energy deposits of protons and pions versus the momentum multiplied by the charge of the particle. On the left (right) side one inner (outer) sensor is shown.

In figure 6.16 the energy deposits on the n–side of one inner (outer) silicon sensor against the particles' momentum multiplied by the charge of the particle are shown. Thus the negative momenta correspond to negative pions (π^-). A similar distribution on the positive side originated from positive pions (π^+), while the protons (p) show larger energy deposits for the same momenta.

6.4 Performance of the SD

6.4.1 Recoil tracking algorithm

The RD was installed to detect particles leaving the interaction area under large polar angles not covered by the acceptance of the Forward Spectrometer. Special reconstruction algorithms were included into XTC to find and fit/reconstruct these particles.

The algorithm searched for tracks separately in the four ϕ–quadrants. It first looked for tracks with four space points in the SD and the SFT and tried to fit them. Space points from tracks with a reasonable χ^2 were removed from the search. Then three–space point tracks with any possible combination were identified and finally tracks with a space point in both silicon layers.

In the track fitting the algorithm treated proton and pion tracks differently. For the latter only the coordinates were used to calculate the fit result, while for the proton hypothesis also the measured energy deposits were included in the fit. The XY- and the RZ-plane were chosen for the fits. Depending on the choice of the track parameterization the algorithm assumed a(n) (in)homogeneous magnetic field. The energy losses of particles traversing any material before hitting the outer sensors was accounted for by momentum dependent corrections in the reconstruction algorithms taking into account the energy loss in the SD layers. A MC study showed no improvement of the momentum resolution or fit errors by including effects from multiple scattering into the error estimation.

From a MC simulation a lookup table was produced that contains the dependence of the energy deposits of protons with respect to their path length in the detector layer and their kinetic energy before the crossing. The values from the lookup table were used as starting values for the reconstruction procedure. Thus the thickness of each layer was taken into account and the reconstruction algorithm was accelerated.

An example for a reconstructed track is shown in figure 6.17. It contains four space points and was fit using a proton hypothesis.

To improve exclusivity in the measurement of the DVCS process certain requirements were claimed. The distinction between the elastic and associated process was ensured by a sufficient angular resolution to be able to identify each track and a good momentum resolution needed for the PID. The obtained momentum resolution matched the requirements from the technical design report [TDR02] (see figure 6.18). The impact of the energy depositions is clearly visible comparing the black points and the green points, where in the latter only the coordinate information from the spacepoints was used. The absolute energy calibration of the SD is reflected in the mean of the momentum resolution for protons below 200 MeV/c. The width of the momentum resolution in the low momentum region could be improved by a strip–by–strip calibration of the SD. The resolution in the azimuthal angle ϕ was found to be around 0.12 % dominated by the SDT position resolution. In the polar angle θ the resolution improved to below 1 % with increasing θ. This quantity is dominated by the resolution in the SD.

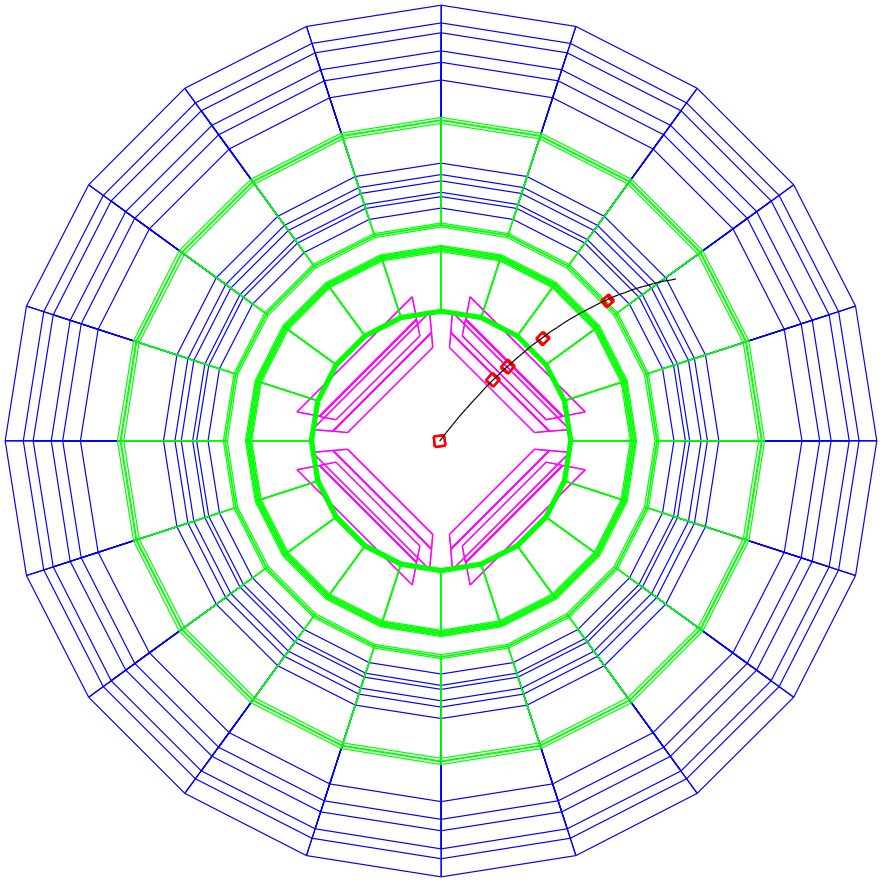

Figure 6.17: A three–dimensional drawing of the RD viewed in beam direction with a proton track (black line) containing four space points (red squares) in the four inner layers of the RD and the vertex position. From inside out: the vertex, the SD in magenta, the two layers of the SFT in green and the three PD layers in blue.

The handling of the pion tracks was complicated by the low MIP efficiency of parts of the SD. Therefore tracks with three space points were also considered. In this case the reduction of ghost track became more difficult. In a physics analysis the kinematics of the process might be used to select real tracks.

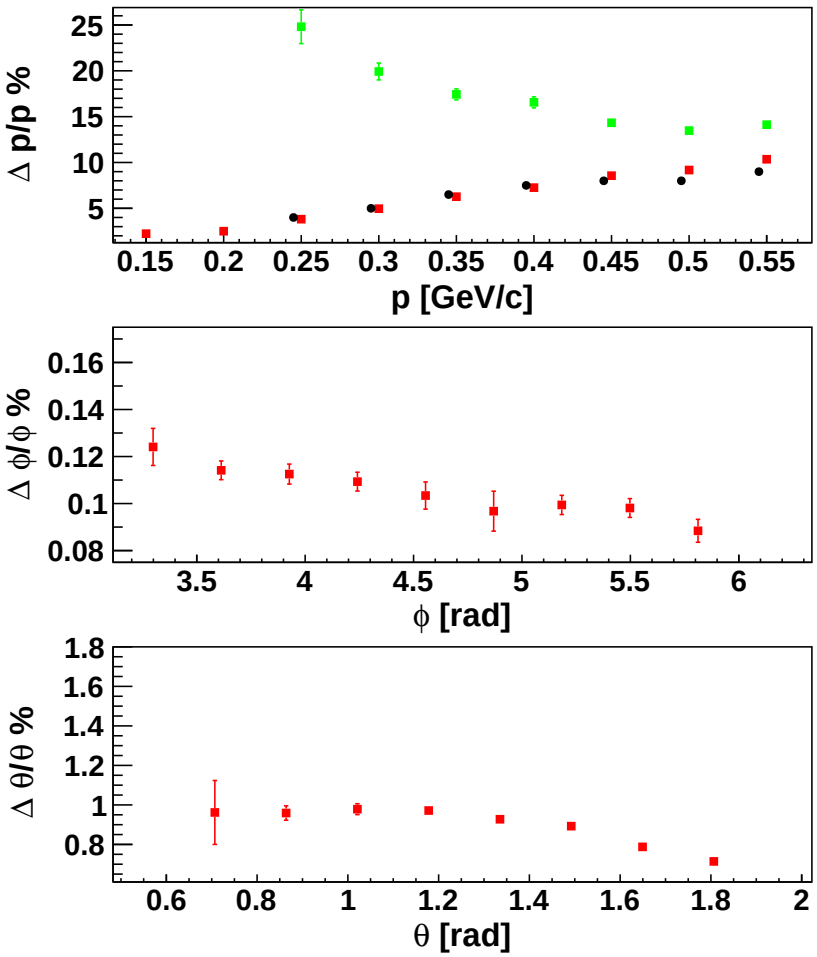

Figure 6.18: The red squares visualize the momentum (upper panel) and angular resolutions (lower two panels) of the RD obtained for protons with space points in either all four layers or only the two SD layers. In black the expected resolutions from the technical design report [TDR02] are shown. The green squares show the momentum resolution as obtained when only using the coordinate information from the four spacepoints.

6.4.2 Recoil PID

Like for the PID detectors of the Forward Spectrometer (see formula 3.2) also for the RD detectors parent distributions were used. The main purpose was to distinguish between protons and pions:

$$PID = \log_{10} \frac{P_p(dE, p)}{P_\pi(dE, p)}. \tag{6.10}$$

Flux factors were not studied yet. The parent distributions were obtained from data. For each layer hard cuts on the dE–p–distributions for the three other layers were introduced to provide clean proton and pion samples. For future productions a denser grid will be included as will be the information from the PD for the higher momentum range above 0.6 GeV/c.

The resulting sepraration between positive pions and protons can be seen in figure 6.19. Negative values correspond to a higher probability for pions and positive values for protons. The obtained values from the Silicon Detector and the SFT do agree nicely. The efficiencies of the identification of a proton decreases slightly with higher momenta, but is found to be above 95 % for a typical threshold of $PID > 1$. The purity of the proton sample for such a PID–value is approximately one, except for the very large momentum range above 0.7 GeV/c, where the puritiy starts to decrease slightly.

The distinction between protons and deuterons will be more difficult as the dE–p–distributions do not differ too much. The deuterons stopped before reaching the SFT could be identified by their dE/dx–behavior in the two silicon layers (see figure 6.15). Deuterons with higher momenta might be selected by requiring kinematical constraints or improved track residuals.

6.4.3 Efficiency

The efficiency of the SD was studied for each layer. For the innermost layer tracks produced by minimum ionizing pions (with a momentum between 0.1 and 0.7 GeV/c) exhibit a high probability to pass through all four sub–detector layers of the RD. Each track not containing a space point in the layer under study was selected and the intersection of the track with the inner silicon layer was determined, with a straight line in the RZ–plane and a circle in the XY–plane. For each sensor side deviations between the calculated position and the true cluster positions of typically 1.5 strip pitches were found. A cluster matched the track, if it agreed with the calculated position within ten strips around the offset.

The obtained cluster efficiencies for protons ($p < 0.5$ GeV/c) in the inner silicon layer are shown in figure 6.20. An overall efficiency of more than 99 % for each sensor and side was found. Similar numbers were extracted for the outer silicon sensors for both particle types. The data yields are also displayed in the figure. The dips were identified as acceptance holes and dead strips in other detector layers. In rare cases

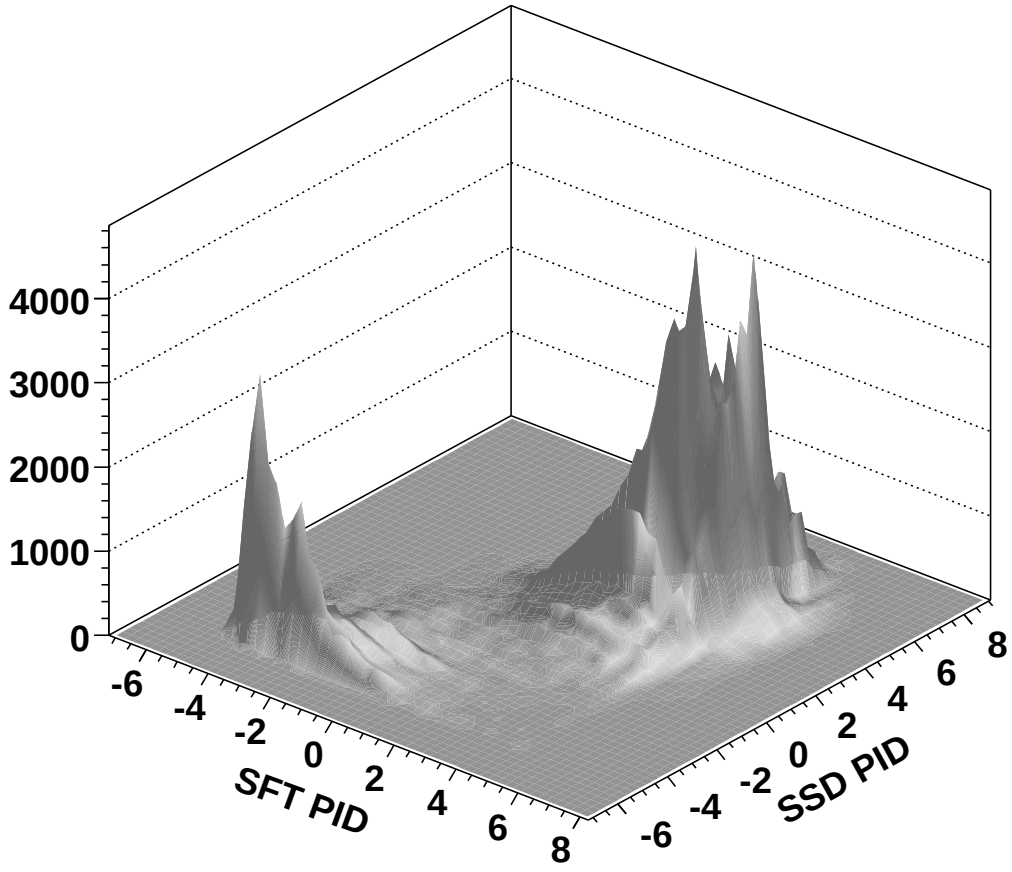

Figure 6.19: The comparison of the PID values obtained from the Silicon Detector ('SSD') and the SFT. Positive (negative) values correspond to a higher probability for a proton (positive pion).

the online hit threshold cut into the MIP peak, thus reducing the cluster efficiency for high proton momenta.

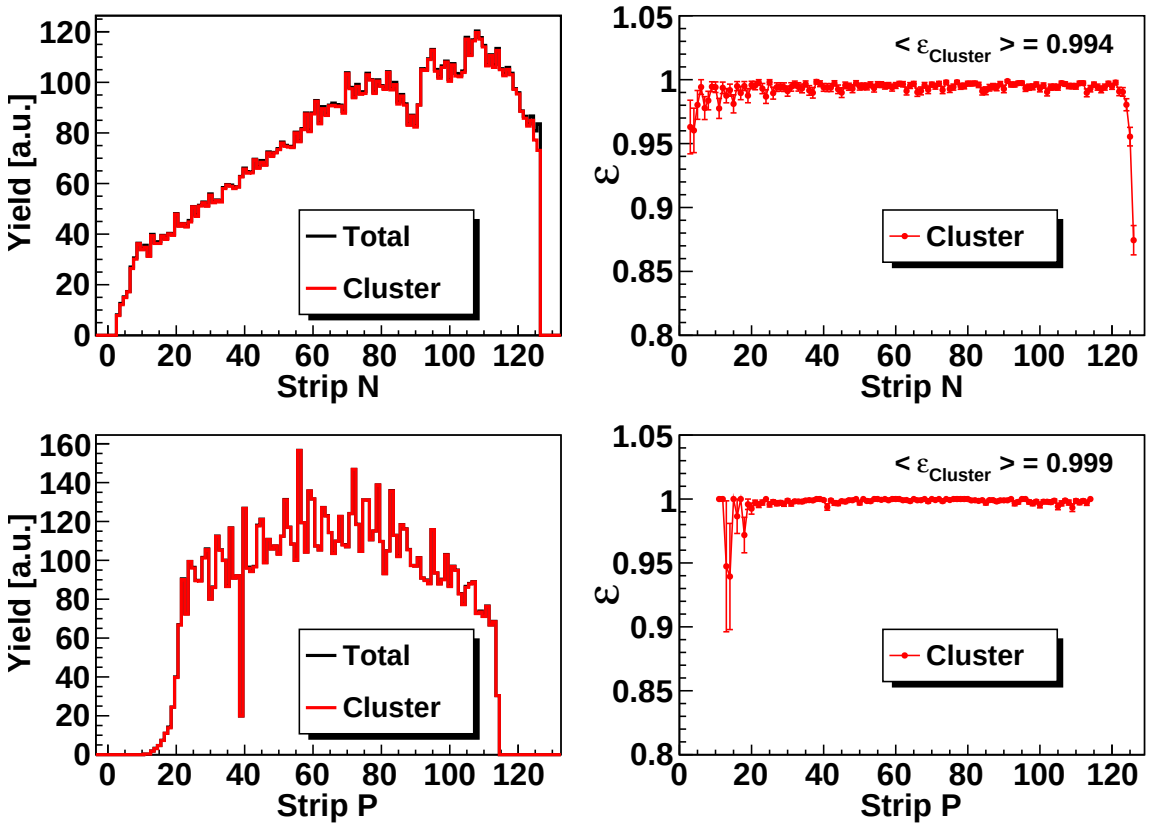

Figure 6.20: The left side shows the yields of high–gain hits and clusters on the n– and p–side of one silicon sensor versus the strip number. The right side gives the efficiencies ε as a function of the strip number together with a mean value obtained from a constant fit.

7 Outlook

The Recoil Detector was installed by the HERMES collaboration with the aim to detect recoiling protons in exclusive processes. In case of DVCS this allows to separate the elastic and associated process types. As discussed in the previous chapters, this might be the biggest remaining issue in the understanding of the DVCS data. In the following basic ideas of this separation will be outlined.

Figure 7.1 shows the squared missing mass distribution separated for all contributing processes as obtained from a MC sample. In the upper panel the black solid line represents the yield for elastic BH events with the DVCS cuts described in this analysis. For the distribution represented by the red dashed curve some of the exclusive cuts were opened. The green solid and dashed line show yields for the associated BH process. The blue dashed line shows the semi–inclusive background with opened cuts. By opening some of the exclusive cuts approximately 6 % of elastic BH data is gained. For the real data a larger effect is expected as the requirement on the preshower signal can be loosened, which presently reduces the statistics by about 20 %. The effect on the associated BH process is marginal.

The red lines in the lower panel represent the yield of elastic BH events in the acceptance of the Recoil Detector. The dotted, dash–dotted and long–dashed lines correspond to the recoiling proton in the acceptance of the outer SD layer, the outer SFT layer and in the combined acceptance of the inner four sub–layers of the RD. The dashed line has the same meaning as in the upper panel, namely all elastic BH events detected by the FS with the loosened exclusive cuts. From these plots it can be concluded that in about two third of the elastic BH events the recoiling proton is detected in the SD. The coverage of the SFT detector is around one half, while requiring a hit in all four sub–layers reduces the number by additional 10 %.

The green lines represent the yields of the associated BH events. For this process type only one third of the events produce a recoiling proton in the acceptance of the outer SD. Hence, the existence of a signal in the RD is already substantially increasing the probability of an elastic event.

The semi–inclusive background processes (blue lines) exhibit an expected very low probability for a proton in the acceptance of the RD. Thus, the new set of exclusive requirements needs to get rid of the remaining contribution from the associated BH process.

The currently most promising candidates are comparisons of the transverse components of the missing momentum $\vec{p}_{\mathrm{miss}}$ obtained from the FS and the reconstructed momentum $\vec{p}_{\mathrm{rec}}$ of the recoiling particle in the RD. In the technical design report [TDR02] the ratio of the absolute values of the transverse parts of the two momenta R and the

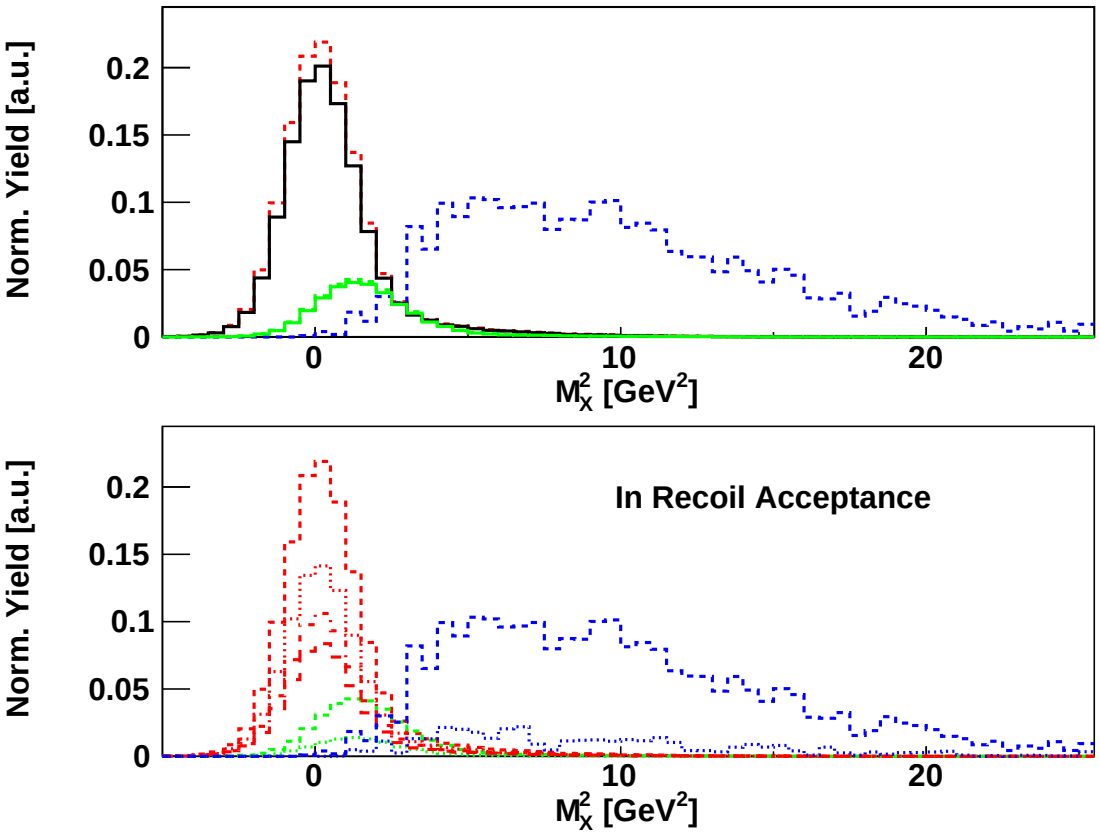

Figure 7.1: The squared missing mass distribution separated for all contributing processes. See text for details.

angle ω between both components were proposed:

$$R \equiv \frac{\left|\vec{p}_{\mathrm{t,miss}}\right|}{\left|\vec{p}_{\mathrm{rec,t}}\right|}, \tag{7.1}$$

$$\omega \equiv \angle(\vec{p}_{\mathrm{t,miss}}, \vec{p}_{\mathrm{t,rec}}). \tag{7.2}$$

By using the transverse components the impact of the large z–component introduced by the beam is minimized.

This can be seen from figure 7.2, in which the ϕ distribution between the reconstructed proton momentum in the Recoil Detector and the missing momentum calculated from the FS is compared. In this study data taken in the year 2007 has been included with loosened requirements on the exclusive quantities and without a cut on the squared missing mass. A nice correlation in the ϕ–distribution is visible, which further improves when applying an additional cut on the squared missing mass.

The R and ω distributions as shown in figure 7.3 exhibit peaks at unity and zero. An additional cut on the squared missing mass slightly reduces the statistics in the

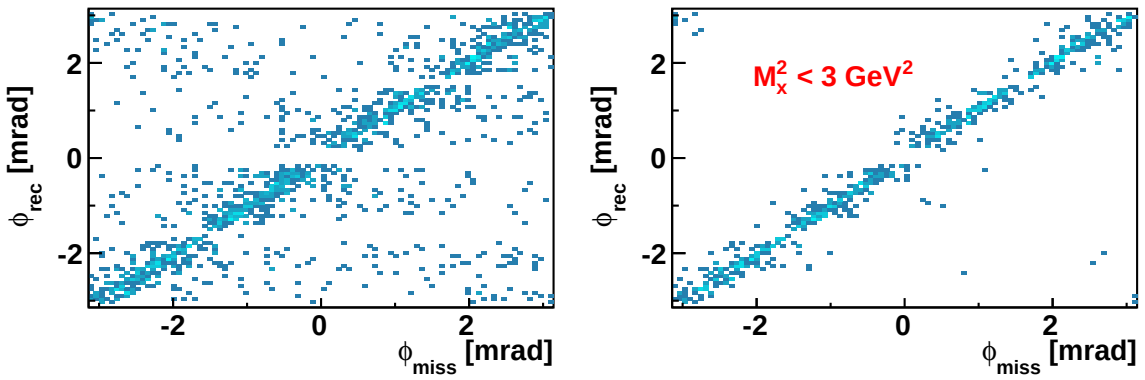

Figure 7.2: A comparison between the reconstructed proton ϕ–distribution in the Recoil Detector and the calculated one from the FS is shown. On the right side an additional cut on the squared missing mass value is applied ($M_X^2 > 3$ GeV^2).

peaks, but removes essentially all events in the tails. This shows that the Recoil Detector information is successfully exploited for both detecting and reconstructing recoiling protons. The best set of cuts to distinguish between the elastic and associated DVCS/BH processes is still under investigation. However, it is clear that this separation will be possible and hence a first measurement of the purely elastic single–charge BSA.

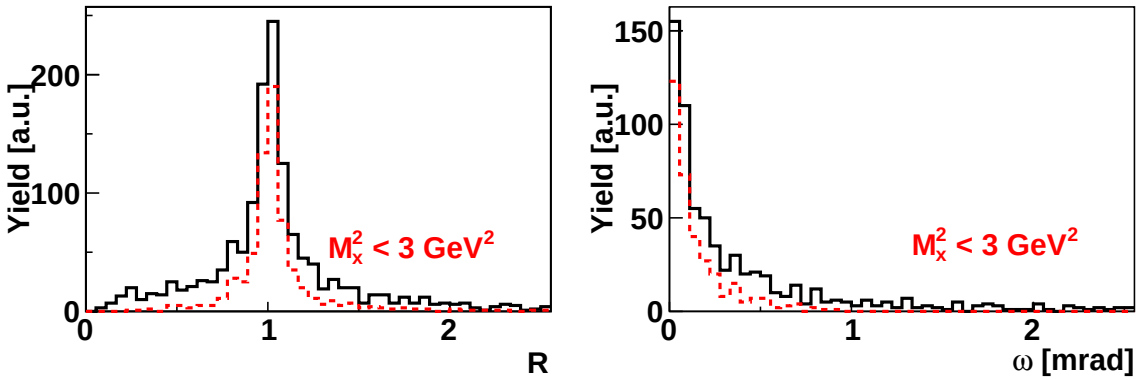

Figure 7.3: A comparison between the reconstructed proton momentum in the Recoil Detector and the missing momentum calculated from the FS is shown. The quantities ω and R are defined in the text. The red dashed lines show the same distribution with an additional cut applied on the squared missing mass value ($M_X^2 > 3$ GeV^2).

8 Summary

In summary, all data taken at the HERMES experiment off a hydrogen target before the installation of the Recoil Detector was examined. The analysis combined data with different beam charge and helicity states and thus allowed to extract three azimuthal asymmetries simultaneously.

The newly defined charge–difference beam–helicity asymmetry is sensitive to the squared DVCS amplitude. It is found to be compatible with zero. This implies that the twist–3 sector is suppressed at HERMES kinematics.

The leading amplitude $A_{\mathrm{LU,I}}^{sin\phi}$ of the charge–averaged beam–helicity asymmetry sensitive to the interference of DVCS and BH amplitudes has a large negative value. No dependence on either of the variables $-t, x_{\mathrm{B}}$ and Q^2 is observed. A comparison to different model calculations exhibits a large discrepancy, which cannot be solved by changing any of the free parameters within the models. The higher twist amplitude $A_{\mathrm{LU,I}}^{sin(2\phi)}$ is found to be compatible with zero.

The leading amplitudes $A_{\mathrm{C}}^{cos\phi}$ and $A_{\mathrm{C}}^{cos(0\phi)}$ of the beam–charge asymmetry were found to exhibit sizeable magnitudes, but opposite signs as expected from theory. Their magnitudes both increase with increasing $-t$. In contrast, the amplitudes related to higher cosine moments are compatible with zero in the whole kinematic space. In this case various model variants were found that nicely agree with the data. The results on the beam–charge asymmetry and the single–charge beam–helicity asymmetry are in agreement to previous results published by the HERMES collaboration.

In addition, the asymmetry amplitudes were extracted in a two–dimensional binning in $-t$ and x_{B}. The three different ranges in Bjorken–x do not differ strongly.

A comparison with the asymmetry amplitudes obtained from the analysis of a deuterium target shows a nice agreement, except for the $A_{\mathrm{LU,I}}^{sin(2\phi)}$ amplitude. In conclusion, both the DVCS processes on the hydrogen and deuterium target seem to be dominated by the leading–twist amplitudes.

However, the asymmetry amplitudes are still uncorrected for the contribution of the associated processes. The fractional contributions are estimated using a MC study and vary between 3.6 % and 35 %. The disentanglement of the contributions will be possible with the additional information from the Recoil Detector. A first attempt has been made to extract the asymmetry amplitudes separately for elastic and associated processes from the current analysis.

Finally, the leading amplitudes were fit with a parameterization of the Compton Form Factor $\mathcal{H}$. The used model allows to describe both leading–twist amplitudes together for the first time. Unfortunately the covered phase space does not allow to obtain an unique solution for the set of free parameters within the ansatz. The success

of this approach again shows that the data in HERMES kinematics is dominated by the leading–twist amplitudes.

In addition, the data processing and calibration procedure of the Recoil Silicon Detector has been outlined in detail. Several examples showed how well the full Recoil Detector was working. A short glimpse in data collected with the Recoil Detector demonstrated that it will allow to separate between elastic and associated processes.

A List of Figures

B List of Tables

C List of Acronyms

ADCs **A**nalog **D**igital **C**onverter

ABS **A**tomic **B**eam **S**ource

BCA **B**eam–**C**harge **A**symmetry

BH **B**ethe–**H**eitler

BSA **B**eam–**S**pin **A**symmetry

BC **B**ack **C**hambers

CFF **C**ompton **F**orm **F**actors

CLAS **C**EBAF **L**arge **A**cceptance **S**pectrometer

CMN **C**ommon **M**ode **N**oise

DESY **D**eutsches **E**lektronen–**Sy**nchrotron

DIS **D**eep **I**nelastic **S**cattering

DVC **D**rift **V**ertex **C**hamber

DVCS **D**eeply **V**irtual **C**ompton **S**cattering

EML **E**xtended **M**aximum **L**ikelihood

FC **F**ront **C**hambers

GPD **G**eneralised **P**arton **D**istributions

HADCs **H**ELIX **a**nalog–to–**d**igital **c**onverters

HDC **H**ERMES **Dec**oder

HERA **H**adron–**E**lektron–**R**ing–**A**nlage

HERMES **HER**A **me**asurement of **s**pin

HRC **H**ERMES **r**econstruction **c**ode

MCs **M**agnet **C**hambers

ML **M**aximum **L**ikelihood

MC **M**onte **C**arlo

MIP **M**inimum **I**onizing **P**article

MPV **M**ost **P**robable **V**alue

PDF **P**arton **D**istribution **F**unction

PID **P**article **I**dentification

PD **P**hoton **D**etector

PMTs **P**hoto**m**ultiplier **T**ubes

PDF **P**robability **D**ensity **F**unctions

QED **Q**uantum **E**lectro–**D**ynamics

QCD **Q**uantum **C**hromo–**D**ynamics

RD **R**ecoil **D**etector

RICH **R**ing **I**mage **Č**erenkov Counter

SIDIS **S**emi–**i**nclusive **DIS** processes

SD **S**ilicon **D**etector

SFT **S**cintillating **F**iber **T**racker

TRD **T**ransition **R**adiation **D**etector

VCS **V**irtual **C**ompton **S**cattering

XTC External **T**racking **C**ode

D Bibliography

[A+88] J. Ashman et al. A measurement of the spin asymmetry and determination of the structure function g_1 in deep inelastic muon proton scattering. *Phys. Lett.*, B206:364, 1988.

[A+98a] K. Ackerstaff et al. The HERMES spectrometer. *Nucl. Instrum. Meth.*, A417:230, 1998, hep-ex/9806008.

[A+98b] H. Avakian et al. Performance of the electromagnetic calorimeter of the HERMES experiment. *Nucl. Instrum. Meth.*, A417:69–78, 1998, hep-ex/9810004.

[A+01] A. Airapetian et al. Measurement of the beam spin azimuthal asymmetry associated with deeply–virtual Compton scattering. *Phys. Rev. Lett.*, 87:182001, 2001, hep-ex/0106068.

[A+03] S. Agostinelli et al. GEANT4: A simulation toolkit. *Nucl. Instrum. Meth.*, A506:250–303, 2003.

[A+05] A. Aktas et al. Measurement of deeply virtual Compton scattering at HERA. *Eur. Phys. J.*, C44:1–11, 2005, hep-ex/0505061.

[A+07a] A. Airapetian et al. The Beam–Charge Azimuthal Asymmetry and Deeply Virtual Compton Scattering. *Phys. Rev.*, D75:011103, 2007, hep-ex/0605108.

[A+07b] A. Airapetian et al. Using the HERA polarization measurements. *Internal Note, 07-016*, 2007.

[A+08a] F. D. Aaron et al. Measurement of Deeply Virtual Compton Scattering and its t–dependence at HERA. *Phys. Lett.*, B659:796–806, 2008, arXiv:0709.4114.

[A+08b] A. Airapetian et al. Cross sections for hard exclusive electroproduction of π^+ mesons on a hydrogen target. *Phys. Lett.*, B659:486–492, 2008, arXiv:0707.0222.

[A+08c] A. Airapetian et al. Measurement of Azimuthal Asymmetries With Respect To Both Beam Charge and Transverse Target Polarization in Exclusive Electroproduction of Real Photons. *JHEP*, 06:066, 2008, arXiv:0802.2499.

[A+08d] C. Amsler et al. Review of particle physics. *Phys. Lett.*, B667:1, 2008.

[A+09a] A. Airapetian et al. Measurement of azimuthal asymmetries associated with deeply virtual compton scattering on an unpolarized deuterium target. *To be published*, 2009.

[A+09b] A. Airapetian et al. Nuclear–mass dependence of beam–helicity and beam–charge azimuthal asymmetries in deeply virtual compton scattering. *To be published*, 2009.

[A+09c] A. Airapetian et al. Spin Density Matrix Elements in Exclusive ρ^0 Electroproduction on ^{1}H and ^{2}H Targets at 27.5 GeV Beam Energy. 2009, arXiv:0901.0701.

[AGIS83] B. Andersson, G. Gustafson, G. Ingelman, and T. Sjostrand. Parton Fragmentation and String Dynamics. *Phys. Rept.*, 97:31–145, 1983.

[B+76] F. W. Brasse et al. Parametrization of the Q**2 Dependence of Virtual gamma p Total Cross–Sections in the Resonance Region. *Nucl. Phys.*, B110:413, 1976.

[B+94] D. P. Barber et al. High spin polarization at the HERA Electron Storage Ring. *Nucl. Instrum. Meth.*, A338:166–184, 1994.

[B+01] T. Benisch et al. The luminosity monitor of the HERMES experiment at DESY. *Nucl. Instrum. Meth.*, A471:314–324, 2001.

[B+02a] C. Baumgarten et al. An atomic beam polarimeter to measure the nuclear polarization in the HERMES gaseous polarized hydrogen and deuterium target. *Nucl. Instrum. Meth.*, A482:606–618, 2002.

[B+02b] M. Beckmann et al. The longitudinal polarimeter at HERA. *Nucl. Instrum. Meth.*, A479:334–348, 2002, physics/0009047.

[B+03] C. Baumgarten et al. A gas analyzer for the internal polarized target of the HERMES experiment. *Nucl. Instrum. Meth.*, A508:268–275, 2003.

[Bar90] R. J. Barlow. Extended maximum likelihood. *Nucl. Instrum. Meth.*, A297:496–506, 1990.

[BDDM04] A. Bacchetta, U. D'Alesio, M. Diehl, and C. A. Miller. Single–spin asymmetries: The Trento conventions. *Phys. Rev.*, D70:117504, 2004, hep-ph/0410050.

[BDS+75] V. G. Bagrov, O. F. Dorofeev, A. A Sokolov, I. M. Ternov, and V. R. Khalilov. On the radiation selfpolarization of electrons moving in a magnetic field. (in russian). *Dokl. Akad. Nauk Ser. Fiz.*, 221:312, 1975.

[Bel98] Belitsky, A. V. and Müller, D. Predictions from conformal algebra for the deeply virtual Compton scattering. *Phys. Lett.*, B417:129–140, 1998, hep-ph/9709379.

[Bel00a] Belitsky, A. V. and Freund, A. and Müller, D. NLO evolution kernels for skewed transversity distributions. *Phys. Lett.*, B493:341–349, 2000, hep-ph/0008005.

[Bel00b] Belitsky, A. V. and Müller, D. Off–forward gluonometry. *Phys. Lett.*, B486:369–377, 2000, hep-ph/0005028.

[Bel00c] Belitsky, A. V. and Müller, D. Twist–three effects in two–photon processes. *Nucl. Phys.*, B589:611–630, 2000, hep-ph/0007031.

[Bel00d] Belitsky, A. V. and Müller, D. and Niedermeier, L. and Schäfer, A. Deeply virtual Compton scattering in next–to–leading order. *Phys. Lett.*, B474:163–169, 2000, hep-ph/9908337.

[Bel01] Belitsky, A. V. and Müller, D. and Niedermeier, L. and Schäfer, A. Leading twist asymmetries in deeply virtual Compton scattering. *Nucl. Phys.*, B593:289–310, 2001, hep-ph/0004059.

[Bel02a] Belitsky, A. V. and Müller, D. Nucleon hologram with exclusive leptoproduction. *Nucl. Phys.*, A711:118–126, 2002, hep-ph/0206306.

[Bel02b] Belitsky, A. V. and Müller, D. and Kirchner, A. Theory of deeply virtual compton scattering on the nucleon. *Nucl. Phys.*, B629:323, 2002, hep-ph/0112108.

[Bel09] Belitsky, A. V. and Müller, D. Refined analysis of photon leptoproduction off spinless target. *Phys. Rev.*, D79:014017, 2009, arXiv:0809.2890.

[BKP+05] S. Balashov, B. Krauss, N. Pickert, K. Rith, F. Stinzing, and C. Vogel. Energy Calibration of the Silicon Modules for the Recoil Detector with the Tandem Facility. *Internal Note, 05-020*, 2005.

[Blu99] Blumlein, J. and Geyer, B. and Robaschik, D. The virtual Compton amplitude in the generalized Bjorken region: Twist–2 contributions. *Nucl. Phys.*, B560:283–344, 1999, hep-ph/9903520.

[BR97] R. Brun and F. Rademakers. ROOT: An object oriented data analysis framework. *Nucl. Instrum. Meth.*, A389:81–86, 1997.

[Bur00] M. Burkardt. Impact parameter dependent parton distributions and off–forward parton distributions for zeta $\to$ 0. *Phys. Rev.*, D62:071503, 2000, hep-ph/0005108.

[C+03] S. Chekanov et al. Measurement of deeply virtual Compton scattering at HERA. *Phys. Lett.*, B573:46–62, 2003, hep-ex/0305028.

[C+06] S. Chen et al. Measurement of deeply virtual Compton scattering with a polarized proton target. *Phys. Rev. Lett.*, 97:072002, 2006, hep-ex/0605012.

[CER95] CERN. Adamo. World Wide Web electronic publication, 1995.

[CF99] J. C. Collins and A. Freund. Proof of factorization for deeply virtual compton scattering in QCD. *Phys. Rev.*, D59:074009, 1999, hep-ph/9801262.

[Dem07] M. Demey. *The polarization of Lambda0 hyperons in quasi–real photoproduction*. Universiteit van Amsterdam, 2007. DESY-THESIS-2007-005.

[DGPR97] M. Diehl, T. Gousset, B. Pire, and J. P. Ralston. Testing the handbag contribution to exclusive virtual Compton scattering. *Phys. Lett.*, B411:193–202, 1997, hep-ph/9706344.

[DHKT99] D. Drechsel, O. Hanstein, S. S. Kamalov, and L. Tiator. A unitary isobar model for pion photo– and electroproduction on the proton up to 1-GeV. *Nucl. Phys.*, A645:145–174, 1999, nucl-th/9807001.

[Die06] M. Diehl. Generalized parton distributions from form factors. *Nucl. Phys. Proc. Suppl.*, 161:49–58, 2006, hep-ph/0510221.

[dN01] L. de Nardo. Trigger efficiencies for 98 and 99 data. *Internal Note, 01-005*, 2001.

[Duf68] Dufner, A. J. and Tsai, Y.-S.of the γ N N* Form–Factors. *Phys. Rev.*, 168:1801–1809, 1968.

[Ell04] F. Ellinghaus. *Beam charge and beam spin azimuthal asymmetries in deeply– virtual Compton scattering*. Humboldt-Universität Berlin, 2004. DESY-THESIS-2004-005.

[Ell07] F. Ellinghaus. DVCS at Hermes: Recent Results. 2007, arXiv:0710.5768 [hep-ex].

[Ely02] J. H. Ely. Measurement of the single spin azimuthal asymmetry in the predominantly exclusive electroproduction of photons from the proton. 2002. DESY-THESIS-2002-014.

[G+08a] G. Gavalian et al. Beam Spin Asymmetries in DVCS with CLAS at 4 .8 GeV. 2008, arXiv:0812.2950.

[G+08b] F. X. Girod et al. Deeply Virtual Compton Scattering Beam–Spin Asymmetries. *Phys. Rev. Lett.*, 100:162002, 2008, arXiv:0711.4805.

[Gab08] D. D. Gabbert. *Determination of the structure function F(2) at HERMES*. Dissertation Universität Hamburg, 2008. DESY-THESIS-2008-041.

[GHK+04a] I.M. Gregor, I. Hristova, M. Kopytin, W. Lange, M. Reinecke, C. Shearer, J. Stewart, and A. Vandenbroucke. Study of the First Prototype for the Hermes Silicon Recoil Detector with the Zeus Beam Telescope. *Internal Note, 04-019*, 2004.

[GHK+04b] I.M. Gregor, I. Hristova, M. Kopytin, W. Lange, M. Reinecke, J. Stewart, and A. Vandenbroucke. A Laser test–stand for the new Hermes Silicon Recoil Detector. *Internal Note, 04-016*, 2004.

[GM09] M. Guidal and H. Moutarde. Generalized Parton Distributions from Deeply Virtual Compton Scattering at HERMES. 2009, arXiv:0905.1220.

[GMV03] P. A. M. Guichon, L. Mosse, and M. Vanderhaeghen. Pion production in deeply virtual Compton scattering. *Phys. Rev.*, D68:034018, 2003, hep-ph/0305231.

[GPV01] K. Goeke, Maxim V. Polyakov, and M. Vanderhaeghen. Hard exclusive reactions and the structure of hadrons. *Prog. Part. Nucl. Phys.*, 47:401–515, 2001, hep-ph/0106012.

[GT06] V. Guzey and T. Teckentrup. The dual parameterization of the proton generalized parton distribution functions H and E and description of the DVCS cross sections and asymmetries. *Phys. Rev.*, D74:054027, 2006, hep-ph/0607099.

[GT09] V. Guzey and T. Teckentrup. On the mistake in the implementation of the minimal model of the dual parameterization and resulting inability to describe the high–energy DVCS data. *Phys. Rev.*, D79:017501, 2009, arXiv:0810.3899.

[Gui08] M. Guidal. A fitter code for Deep Virtual Compton Scattering and Generalized Parton Distributions. *Eur. Phys. J.*, A37:319–332, 2008, arXiv:0807.2355.

[GV03] M. Guidal and M. Vanderhaeghen. Double deeply virtual Compton scattering off the nucleon. *Phys. Rev. Lett.*, 90:012001, 2003, hep-ph/0208275.

[Hil05] A. Hillenbrand. *Measurement and simulation of the fragmentation process at HERMES*. Dissertation Universität Erlangen-Nürnberg, 2005. DESY-THESIS-2005-035.

[HMG+05] I. Hristova, M.J. Murray, I.M. Gregor, W.D. Nowak, M. Reinecke, J. Stewart, and A. Vandenbroucke. Hermes Silicon Recoil Detector Calibration to MIPS at T22 at Desy. *Internal Note, 05-014*, 2005.

[Hoe06] M. Hoek. *Design and construction of a scintillating fibre tracker for measuring hard exclusive reactions at* Hermes. Dissertation Universität Giessen, 2006. DESY-THESIS-2006-027.

[IER97] G. Ingelman, A. Edin, and J. Rathsman. LEPTO 6.5 - A Monte Carlo Generator for Deep Inelastic Lepton–Nucleon Scattering. *Comput. Phys. Commun.*, 101:108–134, 1997, hep-ph/9605286.

[Jaf96] R. L. Jaffe. Spin, twist and hadron structure in deep inelastic processes. 1996, hep-ph/9602236.

[Ji97a] X.-D. Ji. Deeply–virtual compton scattering. *Phys. Rev.*, D55:7114, 1997, hep-ph/9609381.

[Ji97b] X.-D. Ji. Gauge invariant decomposition of nucleon spin. *Phys. Rev. Lett.*, 78:610–613, 1997, hep-ph/9603249.

[Ji98] X.-D. Ji. Off–forward parton distributions. *J. Phys.*, G24:1181, 1998, hep-ph/9807358.

[JM90] R. L. Jaffe and A. Manohar. The G(1) Problem: Fact and Fantasy on the Spin of the Proton. *Nucl. Phys.*, B337:509–546, 1990.

[JO98] X.-D. Ji and J. Osborne. One–loop corrections and all order factorization in deeply virtual Compton scattering. *Phys. Rev.*, D58:094018, 1998, hep-ph/9801260.

[JR75] F. James and M. Roos. Minuit: A System for Function Minimization and Analysis of the Parameter Errors and Correlations. *Comput. Phys. Commun.*, 10:343–367, 1975.

[Ker08] T. Keri. *Detection of exclusive reactions in the* Hermes *Recoil Fiber Tracker*. Dissertation Universität Giessen, 2008. DESY-THESIS-2008-021.

[Kis07] A. Kisselev. Survey of tracking detectors at Hermes. *Internal* Hermes *talk*, 2007.

[KM01] N. Kivel and L. Mankiewicz. Twist–4 photon helicity–flip amplitude in DVCS on a nucleon in the Wandzura–Wilczek approximation. *Eur. Phys. J.*, C21:621–629, 2001, hep-ph/0106329.

[KN02] V. A. Korotkov and W. D. Nowak. Future measurements of deeply virtual compton scattering at Hermes. *Eur. Phys. J.*, C23:455, 2002, hep-ph/0108077.

[KPV01] N. Kivel, Maxim V. Polyakov, and M. Vanderhaeghen. DVCS on the nucleon: Study of the twist–3 effects. *Phys. Rev.*, D63:114014, 2001, hep-ph/0012136.

[Kra05] B. Krauss. *Deeply virtual Compton scattering and the* HERMES *recoil– detector*. Dissertation Universität Erlangen-Nürnberg, 2005. DESY-THESIS-2005-008.

[Kum08a] Kumericki, K. and Müller, D. and Passek-Kumericki, K. Sum rules and dualities for generalized parton distributions: Is there a holographic principle? *Eur. Phys. J.*, C58:193–215, 2008, arXiv:0805.0152.

[Kum08b] Kumericki, K. and Müller, D. and Passek-Kumericki, K. Towards a fitting procedure for deeply virtual Compton scattering at next–to–leading order and beyond. *Nucl. Phys.*, B794:244–323, 2008, hep-ph/0703179.

[Kum09] Kumericki, K. and Müller, D. Deeply virtual Compton scattering at small x_B and the access to the GPD H. 2009, arXiv:0904.0458.

[LY07] X.-G. Lu and Z. Ye. Simultaneous Extraction of the BSAs and the BCA Associated with DVCS with the Extended Maximum Likelihood Method. *Internal Note, 07-001*, 2007.

[M+03] B. A. Mecking et al. The CEBAF Large Acceptance Spectrometer (CLAS). *Nucl. Instrum. Meth.*, A503:513–553, 2003.

[MC+06] C. Munoz Camacho et al. Scaling tests of the cross section for deeply virtual Compton scattering. *Phys. Rev. Lett.*, 97:262002, 2006, nucl-ex/0607029.

[MPW98] L. Mankiewicz, G. Piller, and T. Weigl. Hard exclusive meson production and nonforward parton distributions. *Eur. Phys. J.*, C5:119–128, 1998, hep-ph/9711227.

[MR00] I. V. Musatov and A. V. Radyushkin. Evolution and models for skewed parton distributions. *Phys. Rev.*, D61:074027, 2000, hep-ph/9905376.

[MRST98] A. D. Martin, R. G. Roberts, W. J. Stirling, and R. S. Thorne. Parton distributions: A New global analysis. *Eur. Phys. J.*, C4:463–496, 1998, hep-ph/9803445.

[MT69] L. W. Mo and Y. Tsai. Radiative corrections to elastic and inelastic e p and mu p scattering. *Rev. Mod. Phys.*, 41:205, 1969.

[Mul94] Muller, D. and Robaschik, D. and Geyer, B. and Dittes, F. M. and Horejsi, J. Wave functions, evolution equations and evolution kernels from light–ray operators of QCD. *Fortschr. Phys.*, 42:101, 1994, hep-ph/9812448.

[N+03] A. Nass et al. The HERMES polarized atomic beam source. *Nucl. Instrum. Meth.*, A505:633–644, 2003.

[Pic08] N. C. Pickert. *Commissioning of the recoil silicon detector for the* HERMES *experiment*. Dissertation Universität Erlangen-Nürnberg, 2008. DESY-THESIS-2008-005.

[PS02] M. V. Polyakov and A. G. Shuvaev. On 'dual' parametrizations of generalized parton distributions. 2002, hep-ph/0207153.

[PSTS09] M. V. Polyakov and K. M. Semenov-Tian-Shansky. Dual parametrization of GPDs versus double distribution Ansatz. 2009, arXiv:0811.2901.

[PW99] M. V. Polyakov and C. Weiss. Skewed and double distributions in pion and nucleon. *Phys. Rev.*, D60:114017, 1999, hep-ph/9902451.

[Rad96] A. V. Radyushkin. Scaling limit of deeply virtual compton scattering. *Phys. Lett.*, B380:417, 1996, hep-ph/9604317.

[Rad99] A. V. Radyushkin. Double distributions and evolution equations. *Phys. Rev.*, D59:014030, 1999, hep-ph/9805342.

[RP02] J. P. Ralston and B. Pire. Femto-photography of protons to nuclei with deeply virtual Compton scattering. *Phys. Rev.*, D66:111501, 2002, hep-ph/0110075.

[S+98] T. A. Shibata et al. A high precision laser alignment monitoring system for HERMES tracking detectors. *Nucl. Instrum. Meth.*, A411:75–80, 1998.

[S+01] S. Stepanyan et al. First observation of exclusive deeply virtual Compton scattering in polarized electron beam asymmetry measurements. *Phys. Rev. Lett.*, 87:182002, 2001, hep-ex/0107043.

[Sch07] L. Schoeffel. Deeply Virtual Compton Scattering at HERA II. 2007, arXiv:0705.2925.

[Sjo95] T. Sjostrand. PYTHIA 5.7 and JETSET 7.4: Physics and manual. 1995, hep-ph/9508391.

[Tai05] P. Tait. *Beam–Induced Depolarisation at the* HERMES *Transversely–Polarised Hydrogen Target.* Dissertation Universität Erlangen-Nürnberg, 2005. DESY-THESIS-2006-060.

[TDR02] The HERMES recoil detector. *Internal Note, 02-003*, 2002.

[Tru00] U. Trunk. *Development and Characterisation of the Radiation tolerant HELIX128–2 Readout Chip for the HERA–B Microstrip Detectors*. Dissertation Universität Heidelberg, 2000.

[Van07] A. Vandenbroucke. *Exclusive pi0 production at HERMES: Detection - simulation - analysis*. Dissertation Universiteit Gent, 2007. DESY-THESIS-2007-003.

[VGG99] M. Vanderhaeghen, P. A. M. Guichon, and M. Guidal. Deeply virtual electroproduction of photons and mesons on the nucleon: Leading order amplitudes and power corrections. *Phys. Rev.*, D60:094017, 1999, hep-ph/9905372.

[vH07] Y. van Haarlem. *The* Hermes *recoil photon-detector and nuclear p(t)– broadening at* Hermes. Dissertation Universiteit Gent, 2007. DESY-THESIS-2007-033.

[Vog08] C. Vogel. *Kalibration von Siliziumdetektoren für den* Hermes *Rückstoßdetektor (In German)*. Dissertation Universität Erlangen–Nürnberg, 2008.

[Wan97] W. Wander. *Reconstruction of High Energy Scattering Events in the HERMES Experiment*. Dissertation Universität Erlangen–Nürnberg, 1997. DESY-THESIS-1997-031.

[WW77] S. Wandzura and F. Wilczek. Sum Rules for Spin Dependent Electroproduction: Test of Relativistic Constituent Quarks. *Phys. Lett.*, B72:195, 1977.

[Ye07] Z. Ye. *Transverse target–spin asymmetry associated with deeply virtual Compton scattering on the proton and a resulting model–dependent constraint on the total angular momentum of quarks in the nucleon*. Dissertation Universität Hamburg, 2007. DESY-THESIS-2007-005.

[Zei05] D. Zeiler. *Investigations on deep inelastic virtual Compton scattering at the HERMES experiment. (In German)*. Diplomarbeit Universität Erlangen-Nürnberg, 2005. DESY-THESIS-2005-31.

[Zei08] D. Zeiler. Azimuthal asymmetries in Deeply Virtual Compton Scattering on an unpolarized proton target. 2008, arXiv:0810.5007.

[ZL08] D. Zeiler and X.-G. Lu. Combined Analysis of the Deeply Virtual Compton Scattering Process on the Proton. Hermes *release report (unpublished)*, 2008.

Zusammenfassung

Als tiefinelastische virtuelle Compton–Streuung bezeichnet man den Prozess, in dem ein einlaufendes Lepton mittels eines virtuellen Photons mit einem Quark wechselwirkt, das hierbei ein reelles Photon emittiert. Das Nukleon kann dabei intakt bleiben oder in einen Resonanzzustand angeregt werden. Die Beschreibung dieses Prozesses mit Hilfe von sogenannten Generalisierten Parton–Verteilungsfunktionen erlaubt eine experimentelle Bestimmung des Gesamtdrehimpulses der Quarks innnerhalb eines polarisierten Nukleons. Diese Information wird das Verständnis der Zusammensetzung des Spins des Nukleons aus dessen Bestandteilen verbessern.

In dieser Arbeit wurden Daten untersucht, die am Hermes–Experiment an der Speicherringanlage Hera in Hamburg am Desy in den Jahren 1996 bis 2005 genommen wurden. Bei Hermes werden polarisierte Leptonstrahlen an einem polarisierbaren Gastarget gestreut. In der vorliegenden Analyse wurde die Daten analysiert, die an einem Wasserstofftarget genommen wurden. Dabei wurden alle Ereignisse so kombiniert, dass es sich effektiv um einen unpolarisierten Datensatz handelte.

Der Prozess der tiefinelastischen virtuellen Compton–Streuung konkuriert mit dem Bethe–Heitler Prozess, in dem das reelle Photon von dem ein– oder auslaufenden Lepton emittiert wird. Die experimentelle Ununterscheidbarkeit der beiden Prozesse führt zur Interferenz derer Amplituden. Diese Interferenz erzeugt azimutale Asymmetrien in der Verteilung der reellen Photonen um die Richtung des virtuellen Photons relativ zum Spin– und/oder Ladungszustand der Strahlleptonen. In der vorliegenden Arbeit wurde diese azimutalen Asymmetrien extrahiert.

Dazu wurden zunächst die entsprechenden Ereignisse aus den am Hermes–Experiment genommenen Daten gefiltert und dann auf ihre Konsistenz untersucht. Verschiedene systematische Untersuchungen teils mit Hilfe von Monte Carlo Studien wurden durchgeführt und eine Abschätzung der systematischen Fehler vorgenommen.

Die resultierenden Asymmetrien wurden mit verschiedenen Modellrechnungen verglichen. Keines der vorhandenen Modelle kann alle extrahierten Asymmetrien gleichzeitig beschreiben. Daher wurden erste Schritte unternommen, eine Parameterisierung der den Generalisierten Parton–Verteilungsfunktionen zu Grunde liegenden Compton Formfaktoren zu finden, die die erzielten Resultate beschreiben können. Der abgedeckte Phasenraum durch das Hermes–Experiment erlaubt es jedoch nicht, die freien Variablen einer solchen Parameterisierung alleine festzulegen. Dazu müssen weitere experimentelle Ergebnisse mit den hier Erzielten kombiniert werden.

Im untersuchten Datensatz wurde das Proton im Endzustand nicht nachgewiesen. Daher war es nicht möglich, zwischen Ereignissen zu unterscheiden, in denen sich dieses Proton im Grundzustand oder einer Resonanz befand. Deshalb wurde das Hermes–Experiment im Jahr 2006 um den Rückstoß–Detektor erweitert. Dieser bestand u.a. aus einem Silizium–Streifen–Zähler. Die Untersuchungen vor der Installation dieses Detektors, sowie die Inbetriebnahme und Kalibration desselben waren Bestandteil dieser Arbeit. Die Datenaufbereitung und Kalibration des Detektors sind daher ausführlich beschrieben.

Acknowledgements

First, I want to thank my supervisor Prof. Dr. Klaus Rith for offering me this interesting topic for the present work. I enjoyed his way of guiding me through the last years, both, because he encouraged me to work on my own (when possible) and offered valuable advice (when needed).

Second, I very much benefited from the knowledge and experience of Dr. Andreas Mussgiller both on hardware and software. I would like to thank him for the great working atmosphere and his continuous support. In addition, I very much enjoyed the discussions with my other (almost) office-mates Martin, Markus D. and Christian on physics, politics, programming and many other topics.

Lots of people were involved in the installation of the Recoil Detector and the development of the DVCS analysis. In many instructive discussions I learned a lot from numerous colleagues. I am especially grateful for the support I experienced during the release and the (ongoing) publishing process of my results. Many thanks go to my theory colleague Dieter for his explanations providing me insight into the underlying theory and his new fitting approach.

Most of the time I spent in Erlangen and deeply appreciated the very friendly atmosphere between the group members permanently working in Erlangen and those visiting from Hamburg.

I owe many thanks to my family for their support throughout the past years.

This work is dedicated to my wife. She suffered the most from the (sometimes) cruel working hours, but never complained. Instead she always gave me confidence and motivation. The perfect harmony in our relation carried me through all troubles that crossed my path.